Eur. Phys. J. C (2020) 80:1104
https://doi.org/10.1140/epjc/s10052-020-08477-8

THE EUROPEAN PHYSICAL JOURNAL C

Regular Article - Experimental Physics

Determination of jet calibration and energy resolution in proton–proton collisions at $\sqrt{s} = 8$ TeV using the ATLAS detector

ATLAS Collaboration[*]

CERN, 1211 Geneva 23, Switzerland

Received: 11 October 2019 / Accepted: 13 September 2020

Abstract The jet energy scale, jet energy resolution, and their systematic uncertainties are measured for jets reconstructed with the ATLAS detector in 2012 using proton–proton data produced at a centre-of-mass energy of 8 TeV with an integrated luminosity of 20 fb^{-1}. Jets are reconstructed from clusters of energy depositions in the ATLAS calorimeters using the anti-k_t algorithm. A jet calibration scheme is applied in multiple steps, each addressing specific effects including mitigation of contributions from additional proton–proton collisions, loss of energy in dead material, calorimeter non-compensation, angular biases and other global jet effects. The final calibration step uses several in situ techniques and corrects for residual effects not captured by the initial calibration. These analyses measure both the jet energy scale and resolution by exploiting the transverse momentum balance in γ+jet, Z+jet, dijet, and multijet events. A statistical combination of these measurements is performed. In the central detector region, the derived calibration has a precision better than 1% for jets with transverse momentum 150 GeV $< p_{\mathrm{T}} <$ 1500 GeV, and the relative energy resolution is $(8.4 \pm 0.6)\%$ for $p_{\mathrm{T}} = 100$ GeV and $(23 \pm 2)\%$ for $p_{\mathrm{T}} = 20$ GeV. The calibration scheme for jets with radius parameter $R = 1.0$, for which jets receive a dedicated calibration of the jet mass, is also discussed.

Contents

[*] e-mail: atlas.publications@cern.ch

Published online: 01 December 2020

1 Introduction

Collimated sprays of energetic hadrons, known as jets, are the dominant final-state objects of high-energy proton–proton (pp) interactions at the Large Hadron Collider (LHC) located at CERN. They are key ingredients for many physics measurements and for searches for new phenomena. This paper describes the reconstruction of jets in the ATLAS detector [1] using 2012 data. Jets are reconstructed using the anti-k_t [2] jet algorithm, where the inputs to the jet algorithm are typically energy depositions in the ATLAS calorimeters that have been grouped into "topological clusters" [3]. Jet radius parameter values of $R = 0.4$, $R = 0.6$, and $R = 1.0$ are considered. The first two values are typically used for jets initiated by gluons or quarks, except top quarks. The last choice of $R = 1.0$ is used for jets containing the hadronic decays of massive particles, such as W/Z/Higgs bosons and top quarks. The same jet algorithm can also be used to form jets from other inputs, such as inner-detector tracks associated with charged particles or simulated stable particles from the Monte Carlo event record.

Calorimeter jets, which are reconstructed from calorimeter energy depositions, are calibrated to the energy scale of jets created with the same jet clustering algorithm from stable interacting particles. This calibration accounts for the following effects:

- **Calorimeter non-compensation** Different energy scales for hadronic and electromagnetic showers.
- **Dead material** Energy lost in inactive areas of the detector.
- **Leakage** Showers reaching the outer edge of the calorimeters.
- **Out-of-calorimeter jet** Energy contributions which are included in the stable particle jet but which are not included in the reconstructed jet.
- **Energy depositions below noise thresholds** Energy from particles that do not form calorimeter clusters or have energy depositions not included in these clusters due to the noise suppression in the cluster formation algorithm.
- **Pile-up** Energy deposition in jets is affected by the presence of multiple pp collisions in the same pp bunch crossing as well as residual signals from other bunch crossings.

A first estimate of the jet energy scale (JES) uncertainty of 5%−9% was based on information available prior to pp collision data and initial analysis of early data taken in 2010 [4]. An improved jet calibration with an uncertainty evaluated to be about 2.5% for jets with pseudorapidity[1] $|\eta| < 0.8$ over a wide range of transverse momenta (p_{T}) was achieved with the full 2010 dataset using test-beam measurements, single-hadron response measurements, and in situ techniques [5]. A much larger dataset, recorded during the 2011 data-taking period, improved the precision of JES measurements to 1−3% for jets with $p_{\mathrm{T}} > 40$ GeV within $|\eta| < 2.5$ using a statistical combination of several in situ techniques [6].

This paper describes the derivation of the ATLAS jet calibration and jet energy resolution using the full 2012 pp collision dataset, which is more than four times larger than the 2011 dataset used for the previous calibration [6]. Due to the increased instantaneous luminosity, the beam conditions in 2012 were more challenging than those in 2011, and the ability to mitigate the effects of additional pp interactions is of major importance for robust performance, especially for jets with low p_{T}. The jet calibration is derived using a combination of methods based both on Monte Carlo (MC) simulation and on in situ techniques. The jet energy resolution (JER), which previously was studied using events with dijet topologies [7], is determined using a combination of several in situ JER measurements for the first time. A subset of these jet calibration techniques were subsequently used for $R = 0.4$ jets recorded during the 2015 data-taking period [8], and for $R = 1.0$ jets recorded during the 2015-2016 data-taking period [9].

The outline of the paper is as follows. Section 2 describes the ATLAS detector and the dataset used. The MC simulation framework is presented in Sect. 3, and the jet reconstruction and calibration strategy is summarized in Sect. 4. Section 5 describes the global sequential calibration method, which exploits information from the tracking system (including the muon chambers) and the topology of the energy depositions in the calorimeter to improve the JES uncertainties and

[1] ATLAS uses a right-handed coordinate system with its origin at the nominal interaction point (IP) in the centre of the detector and the z-axis along the beam pipe. The x-axis points from the IP to the centre of the LHC ring, and the y-axis points upward. Cylindrical coordinates (r, ϕ) are used in the transverse plane, ϕ being the azimuthal angle around the z-axis. The pseudorapidity η is an approximation of rapidity $y \equiv 0.5 \ln\left[(E + p_z)/(E - p_z)\right]$ in the high-energy limit and is defined in terms of the polar angle θ as $\eta \equiv -\ln\tan(\theta/2)$.

the JER. The in situ techniques based on a p_{T} balance are described in Sects. 6–8. First, the intercalibration between the central and forward detector, using events with dijet-like topologies, is presented in Sect. 6. The methods based on the p_{T} balance between a jet and a well-calibrated photon or Z boson are discussed in Sect. 7, while the study of the balance between a high-p_{T} jet and a system of several low-p_{T} jets is presented in Sect. 8. The combination of the JES in situ results and the corresponding uncertainties are discussed in Sect. 9, while the in situ combination and the results for the JER are presented in Sect. 10.

2 The ATLAS detector and data-taking conditions

The ATLAS detector consists of an inner tracking detector, sampling electromagnetic and hadronic calorimeters, and muon chambers in a toroidal magnetic field. A detailed description of the ATLAS detector is in Ref. [1].

The inner detector (ID) has complete azimuthal coverage and spans the pseudorapidity range of $|\eta| < 2.5$. It consists of three subdetectors: a high-granularity silicon pixel detector, a silicon microstrip detector, and a transition radiation tracking detector. These are placed inside a solenoid that provides a uniform magnetic field of 2 T. The ID reconstructs tracks from charged particles and determines their transverse momenta from the curvature in the magnetic field.

Jets are reconstructed from energy deposited in the ATLAS calorimeter system. Electromagnetic calorimetry is provided by high-granularity liquid argon (LAr) sampling calorimeters, using lead as an absorber, which are split into barrel ($|\eta| < 1.475$) and endcap ($1.375 < |\eta| < 3.2$) regions, where the endcap is further subdivided into outer and inner wheels. The hadronic calorimeter is divided into the barrel ($|\eta| < 0.8$) and extended barrel ($0.8 < |\eta| < 1.7$) regions, which are instrumented with tile scintillator/steel modules, and the endcap region ($1.5 < |\eta| < 3.2$), which uses LAr/copper modules. The forward calorimeter region ($3.1 < |\eta| < 4.9$) is instrumented with LAr/copper and LAr/tungsten modules to provide electromagnetic and hadronic energy measurements, respectively. The electromagnetic and hadronic calorimeters are segmented into layers, allowing a determination of the longitudinal profiles of showers. The electromagnetic barrel, the electromagnetic endcap outer wheel, and tile calorimeters consist of three layers. The electromagnetic endcap inner wheel consists of two layers. The hadronic endcap calorimeter consists of four layers. The forward calorimeter has one electromagnetic and two hadronic layers. There is also an additional thin LAr presampler, covering $|\eta| < 1.8$, dedicated to correcting for energy loss in material upstream of the calorimeters.

The muon spectrometer surrounds the ATLAS calorimeter. A system of three large air-core toroids with eight coils each, a barrel and two endcaps, generates a magnetic field in the pseudorapidity range $|\eta| < 2.7$. The muon spectrometer measures muon tracks with three layers of precision tracking chambers and is instrumented with separate trigger chambers.

Events are retained for analysis using a trigger system [10] consisting of a hardware-based level-1 trigger followed by a software-based high-level trigger with two levels: level-2 and subsequently the event filter. Jets are identified using a sliding-window algorithm at level-1 that takes coarse-granularity calorimeter towers as input. This is refined with an improved jet reconstruction based on trigger towers at level-2 and on calorimeter cells in the event filter [11].

The dataset consists of pp collisions recorded from April to December 2012 at a centre-of-mass energy ($\sqrt{s}$) of 8 TeV. All ATLAS subdetectors were required to be operational and events were rejected if any data quality issues were present, resulting in a usable dataset with a total integrated luminosity of 20 fb^{-1}. The LHC beams were operated with proton bunches organized in bunch trains, with bunch crossing intervals (bunch spacing) of 50 ns. The average number of pp interactions per bunch crossing, denoted μ, was typically between 10 and 30 [12].

The typical electron drift time within the ATLAS LAr calorimeters is 450 ns [13]. Thus, it is not possible to read out the full detector signal from one event before the next event occurs. To mitigate this issue, a bipolar shaper [14] is applied to the output, creating signals with a pulse sufficiently short to be read between bunch crossings. After bipolar shaping, the average energy induced by pile-up interactions should be zero in the ideal situation of sufficiently long bunch trains with the same luminosity in each pair of colliding bunches. A bunch-crossing identification number dependent offset correction is applied to account for the finite train length such that the average energy induced by pileup is zero for every crossing. However, fluctuations in pile-up activity, both from in-time and out-of-time collisions, contribute to the calorimeter energy read out of the collision of interest. Multiple methods to suppress the effects of pile-up are discussed in subsequent sections.

3 Simulation of jets in the ATLAS detector

Monte Carlo event generators simulate the type, energy, and direction of particles produced in pp collisions. Table 1 presents a summary of the various event generators used to determine the ATLAS jet calibration. A detailed overview of the MC event generators used in ATLAS analyses can be found in Ref. [15].

The baseline simulation samples used to obtain the MC-based jet calibration were produced using Pythia version 8.160 [24]. Pythia uses a $2 \rightarrow 2$ matrix element interfaced

Table 1 Summary of the simulated samples used to derive the jet calibration and to assess systematic uncertainties

Process	Event generator	PDF set	MPI/shower tune set
Dijet & multijet	PYTHIA 8.160	CT10 [16]	AU2 [17]
	HERWIG++ 2.5.2	CTEQ6L1 [18]	EE3 MRST LO** [19]
	POWHEG + PYTHIA 8.175	CT10	AU2
	POWHEG + HERWIG 6.520.2	CT10	AUET2 [20]
	SHERPA 1.4.5	CT10	SHERPA-default [21]
Z + jet	POWHEG + PYTHIA8	CT10	AU2
	SHERPA	CT10	SHERPA-default
γ + jet	PYTHIA8	CTEQ6L1	AU2
	HERWIG++	CTEQ6L1	UE-EE-3 [19]
Pile-up	PYTHIA8	MSTW2008LO [22]	AM2 [23]

with a parton distribution function (PDF) to model the hard process. Additional radiation was modelled in the leading-logarithm approximation using p_{T}-ordered parton showers. Multiple parton–parton interactions (MPI), also referred to as the underlying event (UE), were also simulated, and modelling of the hadronization process was based on the Lund string model [25].

Separate samples produced using other generators were used to derive the final jet calibration and resolution and associated uncertainties using in situ techniques. The HERWIG [26] and HERWIG++ [27] event generators use a $2 \to 2$ matrix element convolved with a PDF for the hard process just as PYTHIA8 does, but use angle-ordered parton showers and a different modelling of the UE and hadronization. The SHERPA event generator [28] was used to produce multi-leg $2 \to N$ matrix elements matched to parton showers using the CKKW [29] prescription. Fragmentation was simulated using the cluster-hadronization model [30], and the UE was modelled using the SHERPA AMISIC model based on Ref. [21]. Samples were also produced using the POWHEG BOX [31–34] software that is accurate to next-to-leading order (NLO) in perturbative QCD. Parton showering and modelling of the hadronization and the UE were provided by either PYTHIA8 or HERWIG, resulting in separate samples referred to as POWHEG + PYTHIA8 and POWHEG + HERWIG, respectively. Tuned values of the modelling parameters affecting the parton showering, hadronization, and the UE activity were determined for each generator set-up to match various distributions in data as summarized in Table 1 and references therein.

The generated stable particles, defined as those with a lifetime τ such that $c\tau > 10$ mm, were input to the detector simulation that models the particles' interactions with the detector material. Such particles are used to build jets as explained in Sect. 4. Most MC samples were generated with a full detector simulation of the ATLAS detector [35] based on GEANT4 [36], in which hadronic showers are simulated with the QGSP BERT model [37]. Alternative samples were produced using the Atlfast-II (AFII) fast detector simulation based on a simplified modelling of particle interactions with the calorimeter, yielding a factor of ten more events produced for the same CPU time [38]. The output of the detector simulation were detector signals with the same format as those from real data.

Pile-up events, i.e. additional pp interactions that are not correlated with the hard-scatter event of interest, were simulated as minimum-bias events produced with PYTHIA8 using the AM2 tuned parameter set [23] and the MSTW2008LO PDF [22]. The simulated detector signals from these events were overlaid with the detector signals from the hard-scatter event based on the pile-up conditions of the 2012 data-taking period. Pile-up events were overlaid both in the hard-scatter bunch crossing (in-time pile-up) and in nearby bunch crossings (out-of-time pile-up) with the detector signals offset in time accordingly. These out-of-time pile-up signals are overlaid in such a manner as to cover the full read-out window of each of the ATLAS calorimeter sub-detectors. The number of pile-up events to overlay in each bunch crossing was sampled from a Poisson distribution with a mean μ corresponding to the expected number of additional pp collisions per bunch crossing.

4 Overview of ATLAS jet reconstruction and calibration

4.1 Jet reconstruction and preselection

Jets are reconstructed with the anti-k_t algorithm [2] using the FASTJET software package [39,40] version 2.4.3. Jets are formed using different inputs: stable particles from the event generator record of simulated events resulting in *truth-particle jets*; reconstructed calorimeter clusters, producing *calorimeter jets*; or inner-detector tracks to form *track jets*.

The generated stable particles used to define truth-particle jets are required to originate (either directly or via a decay

chain) from the hard-scatter vertex, and hence do not include particles from pile-up interactions. Muons and neutrinos are excluded to ensure that the truth-particle jets are built from particles that leave significant energy deposits in the calorimeters.

Calorimeter jets are built from clusters of adjacent calorimeter read-out cells that contain a significant energy signal above noise levels, referred to as topological clusters or *topo-clusters*. Details of the formation of topo-clusters are provided in Ref. [3]. In its basic definition, a topo-cluster is assigned an energy equal to the sum of the associated calorimeter cell energies calibrated at the *electromagnetic scale* (EM-scale) [41–44], which is the basic signal scale accounting correctly for the energy deposited in the calorimeter by electromagnetic showers. The direction (η and ϕ) of a topo-cluster is defined from the centre of the ATLAS detector to the energy-weighted barycentre of the associated calorimeter cells, and the mass is set to zero. Topo-clusters can further be calibrated using the local cell signal weighting (LCW) method [3] designed to give the correct scale for charged pions produced in the interaction point. The LCW method reduces fluctuations in energy due to the non-compensating nature of the ATLAS calorimeters, out-of-cluster energy depositions, and energy deposited in dead material, improving the energy resolution of the reconstructed jets in comparison with jets reconstructed using EM-scale clusters [5].

The calorimeter jet four-momentum directly after jet finding is referred to as the *constituent scale* four-momentum p^{const} and is defined as the sum of the constituent topo-cluster four-momenta p_i^{topo}:

$$p^{\text{const}} = \left(E^{\text{const}}, \mathbf{p}^{\text{const}}\right) = \sum_{i=1}^{N_{\text{const}}} p_i^{\text{topo}} = \left(\sum_{i=1}^{N_{\text{const}}} E_i^{\text{topo}}, \sum_{\text{i=1}}^{N_{\text{const}}} \mathbf{p}_i^{\text{topo}}\right). \quad (1)$$

The constituent scales considered in this paper are EM or LCW depending on the calibration of the constituent topo-clusters. At this stage, all angular coordinates are defined from the centre of the ATLAS detector, and the *detector pseudorapidity* $\eta_{\text{det}} \equiv \eta^{\text{const}}$ and *detector azimuth* $\phi_{\text{det}} \equiv \phi^{\text{const}}$ are recorded for each jet. The most common choice in ATLAS analyses of the anti-k_t radius parameter is $R = 0.4$, but $R = 0.6$ is also used frequently. Analyses that search for hadronic decays of highly boosted (high p_{T}) massive objects often use larger values of R than these since the decay products of the boosted objects can then be contained within the resulting *large-R jets*. Due to the larger radius parameter, this class of jets spans a larger solid angle and hence are more sensitive to pile-up interactions than jets with $R \leq 0.6$. To mitigate the influence of pile-up and hence improve the sensitivity of the analyses, several jet grooming algorithms have been designed and studied within ATLAS [45–48]. In this paper, the trimming algorithm [49] (one type of grooming method) is applied to anti-k_t jets built with $R = 1.0$. This grooming procedure starts from the constituent topo-clusters of a given $R = 1.0$ anti-k_t jet to create *subjets* using the k_t jet algorithm [50] with radius parameter $R_{\text{sub}} = 0.3$. The topo-clusters belonging to subjets with $f_{\text{cut}} \equiv {p_{\text{T}}}^{\text{subjet}}/{p_{\text{T}}}^{\text{jet}} < 0.05$ are discarded, and the jet four-momentum is then recalculated from the remaining topo-clusters.

For each in situ analysis, jets within the full calorimeter acceptance $|\eta_{\text{det}}| < 4.5$ with calibrated $p_{\text{T}} > 8$ GeV ($p_{\text{T}} > 25$ GeV in case of the multijet analysis) are considered. These p_{T} thresholds do not bias the kinematic region of the derived calibration, which is $p_{\text{T}} \geq 17$ GeV ($p_{\text{T}} \geq 300$ GeV for the multijet analysis). The jets are also required to satisfy "Loose" quality criteria, designed to reject fake jets originating from calorimeter noise bursts, non-collision background, or cosmic rays [6], and to fulfil a requirement designed to reject jets originating from pile-up vertices. The latter criterion is based on the jet vertex fraction (JVF), computed as the scalar sum $\sum p_{\text{T}}^{\text{track}}$ of the tracks matched to the jet that are associated with the hard-scatter primary vertex divided by $\sum p_{\text{T}}^{\text{track}}$ using all tracks matched to the jet (see Ref. [51] for further details). The default hard-scatter vertex is the primary vertex with the largest $\sum_{\text{tracks}} p_{\text{T}}^2$, but other definitions are used for certain analyses [52]. Each jet with $p_{\text{T}} < 50$ GeV within the tracking acceptance $|\eta_{\text{det}}| < 2.4$ is required to have JVF > 0.25, which effectively rejects pile-up jets in ATLAS 2012 pp data [51].

Jets with a radius parameter of $R = 0.4$ or $R = 0.6$ have been built using both EM- and LCW-scale topo-clusters as inputs. These four jet reconstruction options have been studied in similar levels of detail, but for brevity the paper will focus on presenting the results for jets built using EM-scale topo-clusters with a radius parameter of $R = 0.4$, which better demonstrates the importance of the GS calibration as described in Sect. 5. Key summary plots will present the results for all four jet definitions thus showing the final performance of each of the different options. In contrast, jets with a radius parameter of $R = 1.0$ have only been studied in detail using LCW-scale topo-clusters as inputs. This choice is motivated by the common usage of such jets for tagging of hadronically-decaying particles, where the energy and angular distribution of constituents within the jet is important. For such a situation, LCW topo-clusters are advantageous because they flatten the detector response, and thus the tagging capabilities are less impacted by where a given energy deposit happens to be within the detector.

4.2 Matching between jets, jet isolation, and calorimeter response

To derive a calibration based on MC simulation, it is necessary to match a truth-particle jet to a reconstructed jet. Two methods are used for this: a simple, angular matching as well as a more sophisticated approach known as *jet ghost association* [53]. For the angular matching, a $\Delta R < 0.3$ requirement is used, where ΔR is the pseudorapidity and azimuthal angle separation between the two jets added in quadrature, i.e. $\Delta R = \Delta\eta \oplus \Delta\phi \equiv \sqrt{(\Delta\eta)^2 + (\Delta\phi)^2}$. The angular criterion $\Delta R < 0.3$ is chosen to be smaller than the jet radius parameter used for ATLAS analyses ($R = 0.4$ or larger) but much larger than the jet angular resolution (Sect. 4.3.2). Jet matching using ghost association treats each MC simulated particle as a *ghost particle*, which means that they are assigned an infinitesimal p_{T}, leaving the angular coordinates unchanged. The calorimeter jets can now be built using both the topo-clusters and ghost particles as input. Since the ghost particles have infinitesimal p_{T}, the four-momenta of the reconstructed jets will be identical to the original jets built only from topo-clusters, but the new jets will also have a list of associated truth particles for any given reconstructed jet. A truth-particle jet is matched to a reconstructed jet if the sum of the energies of the truth-particle jet constituents which are ghost-associated with the reconstructed jet is more than 50% of the truth-particle jet energy, i.e. the sum of the energies of all constituents. This ensures that only one reconstructed jet is matched to any given truth-particle jet. If several truth-particle jets fulfil the matching requirement, the truth-particle jet with the largest energy is chosen as the matched jet. Matching via ghost association results in a unique match for each truth-particle jet and hence performs better than the simple angular matching in cases where several jets have small angular separation from each other.

The simulated jet energy response is defined by

$$\mathcal{R}_E = \left\langle \frac{E_{\mathrm{reco}}}{E_{\mathrm{truth}}} \right\rangle,$$

where E_{reco} is the reconstructed energy of the calorimeter jet, E_{truth} is the energy of the matching truth-particle jet, and the brackets denote that $\mathcal{R}_E$ is defined from the mean parameter of a Gaussian fit to the response distribution $E_{\mathrm{reco}}/E_{\mathrm{truth}}$. The p_{T} and mass responses are defined analogously as the Gaussian means $\langle p_{\mathrm{T,reco}}/p_{\mathrm{T,truth}}\rangle$ and $\langle m_{\mathrm{reco}}/m_{\mathrm{truth}}\rangle$ of the reconstructed quantity divided by that of the matching truth-particle jet. When studying the jet response for a population of jets, both the reconstructed and the truth-particle jets are typically required to fulfil isolation requirements. For the analyses presented in this paper, reconstructed jets are required to have no other reconstructed jet with $p_{\mathrm{T}} > 7$ GeV within $\Delta R < 1.5R$, where R is the anti-k_t jet radius parameter used. Truth-particle jets are similarly required to have no jets with $p_{\mathrm{T}} > 7$ GeV within $\Delta R < 2.5R$. After requiring the particle and reconstructed jets to be isolated, the jet energy response distributions for jets with fixed E_{truth} and η have nearly Gaussian shapes, and $\mathcal{R}_E$ and the jet resolution $\sigma_{\mathcal{R}}$ are defined as the mean and width parameters of Gaussian fits to these distributions, respectively. For all results presented in this paper, the mean jet response is defined from the mean parameter of a fit to a jet response or momentum balance distribution as appropriate rather than the mean or median of the underlying distribution, as the fit mean is found to be significantly more robust against imperfect modelling of the tails of the underlying distribution.

4.3 Jet calibration

An overview of the ATLAS jet calibration applied to the 8 TeV data is presented in Fig. 1. This is an extension of the procedure detailed in Ref. [6] that was applied to the 7 TeV data collected in 2011. The calibration consists of five sequential steps. The derivation and application of the first three calibration steps are described in this section, while the global sequential calibration (GS) is detailed in Sect. 5, and the relative in situ correction and the associated uncertainties are described in Sects. 6–9.

4.3.1 Jet origin correction

The four-momentum of the initial jet is defined according to Eq. (1) as the sum of the four-momenta of its constituents. As described in Sect. 4.1, the topo-clusters have their angular directions (η, ϕ) defined from the centre of the ATLAS detector to the energy-weighted barycentre of the cluster. This direction can be adjusted to originate from the hard-scatter vertex of the event. The jet origin correction first redefines the (η, ϕ) directions of the topo-clusters to point to the selected hard-scatter vertex, which results in a updated set of topo-cluster four-momenta. The origin-corrected calorimeter jet four-momentum p^{orig} is the sum of the updated topo-cluster four-momenta,

$$p^{\mathrm{orig}} = \sum_{i=1}^{N_{\mathrm{const}}} p_i^{\mathrm{topo,orig}}.$$

Since the energies of the topo-clusters are not affected, the energy of the jet also remains unchanged. Figure 2 presents the impact of the jet origin correction on the jet angular resolution by comparing the axis of the calorimeter jet $(\eta_{\mathrm{reco}}, \phi_{\mathrm{reco}})$ with the axis of the matched truth-particle jet $(\eta_{\mathrm{truth}}, \phi_{\mathrm{truth}})$. A clear improvement can be seen for the pseudorapidity resolution, while no change is seen for the azimuthal resolution. This is expected as the spread of the beamspot is significantly larger along the beam axis ($\sim$50 mm) than in the transverse plane ($\ll 1$ mm).

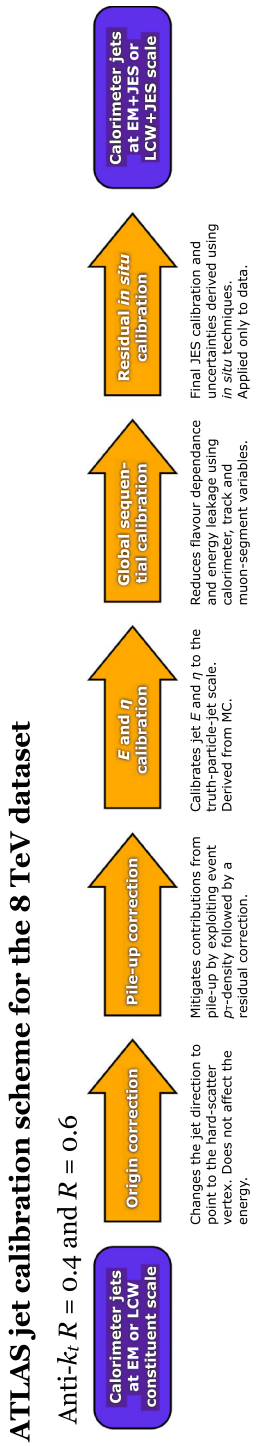

Fig. 1 Overview of the ATLAS jet calibration described in this paper. All steps are derived and applied separately for jets built from EM-scale and LCW calibrated calorimeter clusters, except for the global sequential calibration, which is only partially applied to LCW-jets (Sect. 5). The notations EM+JES and LCW+JES typically refer to the fully calibrated jet energy scale; however, in the sections of this paper that detail the derivations of the GS and the in situ corrections, these notations refer to jets calibrated by all steps up to the correction that is being described

4.3.2 Pile-up correction

The reconstruction of the jet kinematics is affected by pile-up interactions. To mitigate these effects, the contribution from pile-up is estimated on an event-by-event and jet-by-jet basis as the product of the event p_{T}-density ρ [53] and the jet area A in (y, ϕ)-space, where y is the rapidity of the jet [54]. The jet area is determined with the FastJet 2.4.3 program [39,40] using the active-area implementation, in which the jets are rebuilt after adding randomly distributed ghost particles with infinitesimal p_{T} and randomly selected y and ϕ from uniform distributions. The active area is estimated for each jet from the relative number of associated ghost particles (Sect. 4.2). As can be seen in Fig. 3a, the active area for a given anti-k_t jet tends to be close to πR^2. The event p_{T}-density ρ is estimated event-by-event by building jets using the k_t jet-finding algorithm [50] due to its tendency to naturally include uniform soft background into jets [53]. Resulting k_t jets are only considered within $|\eta| < 2$ to remain within the calorimeter regions with sufficient granularity [51]. No requirement is placed on the p_{T} of the jets, and the median of the p_{T}/A distribution is taken as the value of ρ. The median is used to reduce the sensitivity of the method to the hard-scatter activity in the tails. The ρ distributions of events with average interactions per bunch crossing μ in the narrow range of $20 < \mu < 21$ and several fixed numbers of primary vertices N_{PV} are shown in Fig. 3b. It can be seen that ρ increases with N_{PV} as expected, but for a fixed N_{PV}, ρ still has sizeable event-by-event fluctuations. A typical value of the event p_{T}-density in the 2012 ATLAS data is $\rho = 10$ GeV, which for a $R = 0.4$ jet corresponds to a subtraction in jet p_{T} of $\rho A \approx 5$ GeV.

After subtracting the pile-up contribution based on ρA, the pileup dependence of $p_{\mathrm{T}}^{\mathrm{jet}}$ is mostly removed, especially within the region where the value of ρ is derived. However, the value of $p_{\mathrm{T}}^{\mathrm{jet}}$ has a small residual dependence on N_{PV} and μ, particularly in the region beyond where ρ is derived and where the calorimeter granularity changes. To mitigate this, an additional correction is derived, parameterized in terms of N_{PV} and μ, which is the same approach and parameterization as was used for the full pile-up correction of the ATLAS 2011 jet calibration [6]. A typical value for this correction is ± 1 GeV for jets in the central detector region. The full pile-up correction to the jet p_{T} is given by

$$p_{\mathrm{T}} \mapsto p_{\mathrm{T}} - \rho A - \alpha (N_{\mathrm{PV}} - 1) - \beta \mu, \tag{2}$$

where the α and β parameters depend on jet pseudorapidity and the jet algorithm, and are derived from MC simulation. Further details of this calibration, including evaluation of the associated systematic uncertainties, are in Ref. [51]. No pile-up corrections are applied to the trimmed large-R jets

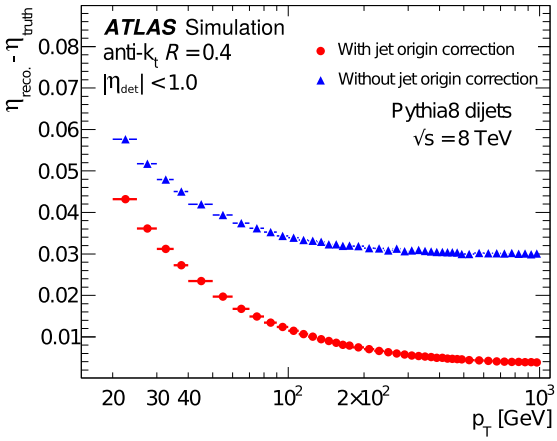

Fig. 2 Jet angular resolution as a function of transverse momentum for anti-k_t jets with $R = 0.4$. The resolutions are defined by the spread of the difference between the reconstructed jet axis ($\eta_{\text{reco}}, \phi_{\text{reco}}$) and the axis of the matched truth-particle jet ($\eta_{\text{truth}}, \phi_{\text{truth}}$) (see Sect. 4.2 for matching details) in simulated events and are shown both with (circles) and without (triangles) the jet origin correction, which adjusts the direction of the reconstructed jet to point to the hard-scatter vertex instead of the geometrical centre of the detector

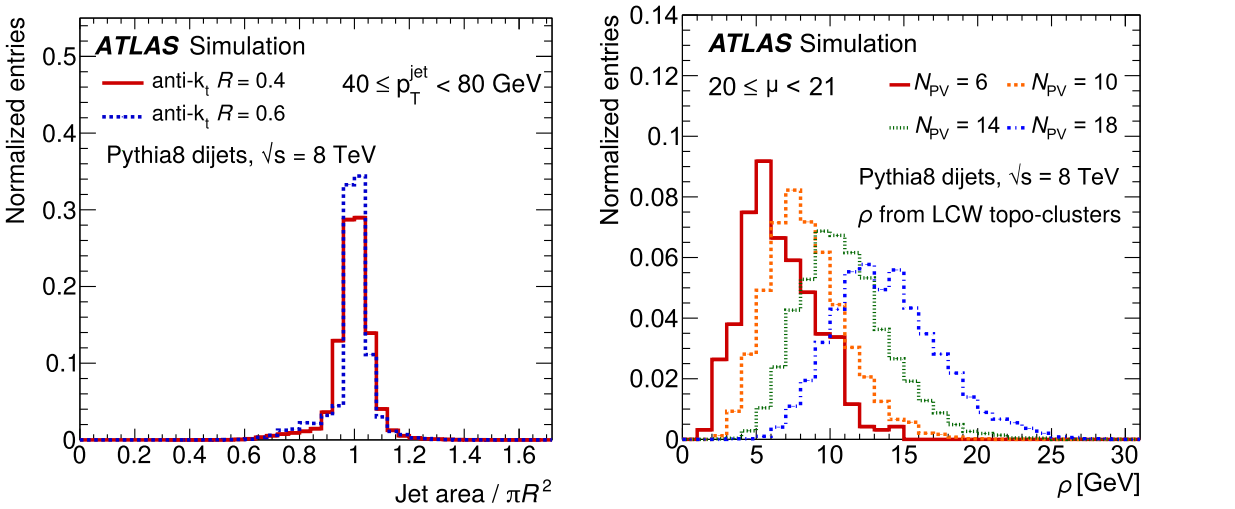

(a) Jet area **(b)** Event p_T-density, ρ

Fig. 3 **a** Ratio of the jet active area to πR^2, where R is the jet radius parameter and **b** the event p_T-density ρ. The jet area ratio is shown separately for $R = 0.4$ and $R = 0.6$ jets reconstructed with the anti-k_t algorithm, and ρ is shown for different numbers of reconstructed primary vertices N_{PV} in events with average number of pp interactions in the range $20 \le \mu < 21$

since this is found to be unnecessary after applying the trimming procedure.

4.3.3 Monte Carlo-based jet calibration

After the origin and pile-up corrections have been employed, a baseline jet energy scale calibration is applied to correct the reconstructed jet energy to the truth-particle jet energy. This calibration is derived in MC-simulated dijet samples following the same procedure used in previous ATLAS jet calibrations [5,6]. Reconstructed and truth-particle jets are matched and required to fulfil the isolation criteria as described in Sect. 4.2. The jets are then subdivided into narrow bins of η_{det} of the reconstructed jet and energy of the truth-particle jet E_{truth}, and $\mathcal{R}_E$ is determined for each such bin from the mean of a Gaussian fit (Sect. 4.2). The average reconstructed jet energy $\langle E_{\text{reco}} \rangle$ (after pile-up correction) is also recorded for each such bin. A calibration function $c_{\text{JES},1}(E_{\text{reco}}) = 1/\mathcal{R}_1(E_{\text{reco}})$ is determined for each η_{det} bin by fitting a smooth function $\mathcal{R}_1(E_{\text{reco}})$ to a graph of $\mathcal{R}_E$ versus $\langle E_{\text{reco}} \rangle$ measurements for all E_{truth} bins within the given η_{det} bin. After applying this correction ($E_{\text{reco}} \mapsto c_{\text{JES},1}\, E_{\text{reco}}$)

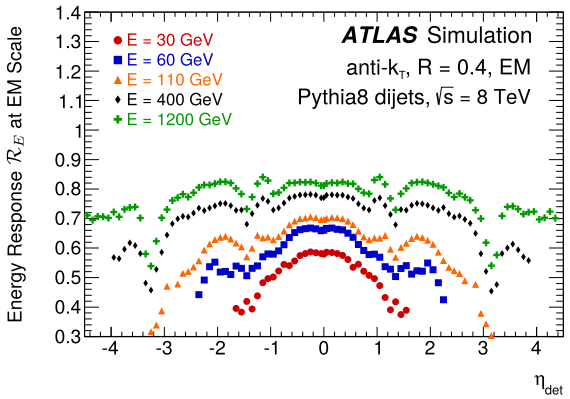

(a) Jet energy response $\mathcal{R}_E$, EM scale, $R = 0.4$

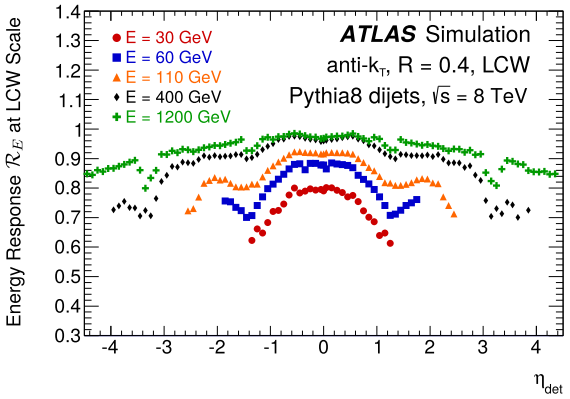

(b) Jet energy response $\mathcal{R}_E$, LCW scale, $R = 0.4$

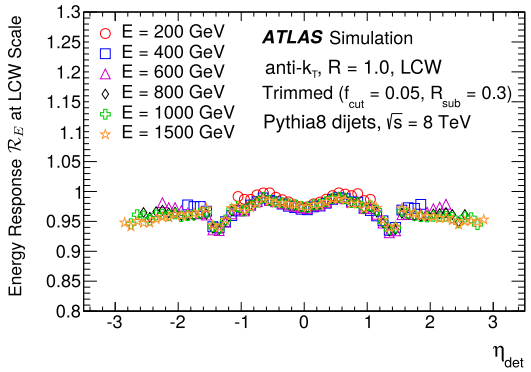

(c) Jet energy response $\mathcal{R}_E$, LCW scale, $R = 1.0$

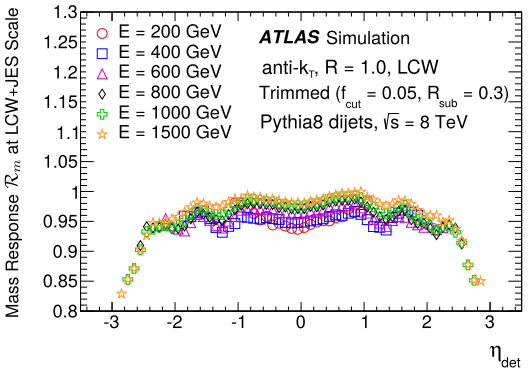

(d) Jet mass response $\mathcal{R}_m$, LCW scale, $R = 1.0$

Fig. 4 Jet energy and mass responses as a function of η_{det} for different truth-particle jet energies. The energy responses $\mathcal{R}_E$ for anti-k_t jets with $R = 0.4$ at the **a** EM scale and the **b** LCW scale and **c** for trimmed anti-k_t $R = 1.0$ jets are presented. Also, **d** the jet mass response $\mathcal{R}_m$ for the latter kind of jets is given

and repeating the derivation of the calibration factor, the jet response does not close perfectly. The derived calibration factor from the second iteration $c_{\text{JES},2}$ is close to but not equal to unity. The calibration improves after applying three such iterative residual corrections $c_{\text{JES},i}$ ($i \in \{2, 3, 4\}$) such that the final correction factor $c_{\text{JES}} = \prod_{i=1}^{4} c_{\text{JES},i}$ achieves a jet response close to unity for each $(E_{\text{truth}}, \eta_{\text{det}})$ bin.

For the large-R jets (trimmed anti-k_t $R = 1.0$), a subsequent jet mass calibration is also applied, derived analogously to the energy calibration. Figure 4 shows the energy and jet mass responses for jets with $R = 0.4$ and $R = 1.0$. Jets reconstructed from LCW-calibrated topo-clusters have a response closer to unity than jets built from EM-scale topo-clusters. Figure 5 shows the jet E, p_{T}, and m response plots after the application of the MC-based jet calibration. Good closure is demonstrated across the pseudorapidity range, but there is some small non-closure for low-p_{T} jets primarily due to imperfect fits arising from the non-Gaussian energy response and threshold effects.

A small, additive correction $\Delta\eta$ is also applied to the jet pseudorapidity to account for biased reconstruction close to regions where the detector technology changes (e.g. the barrel–endcap transition region). The magnitude of this correction is very similar to that of the previous calibrations (Figure 11 of Ref. [5]) and can reach values as large as 0.05 near the edge of the forward calorimeters around $|\eta| = 3$, but is typically much smaller in the well-instrumented detector regions.

4.4 Definition of the calibrated jet four momentum

For small-R jets, i.e. jets built with a radius parameter of $R = 0.4$ or $R = 0.6$, the fully calibrated jet four-momentum is specified by

$$(E, \eta, \phi, m) = \left(c_{\text{calib}}\, E^{\text{orig}},\ \eta^{\text{orig}} + \Delta\eta,\ \phi^{\text{orig}},\ c_{\text{calib}}\, m^{\text{orig}}\right), \tag{3}$$

where the quantities denoted "orig" are the jet four-vector after the origin correction discussed in Sect. 4.3.1, $\Delta\eta$ is the

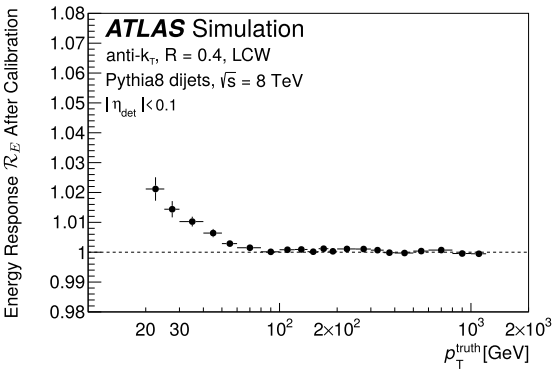

(a) Jet energy response $\mathcal{R}_E$ vs p_{T}, $R = 0.4$

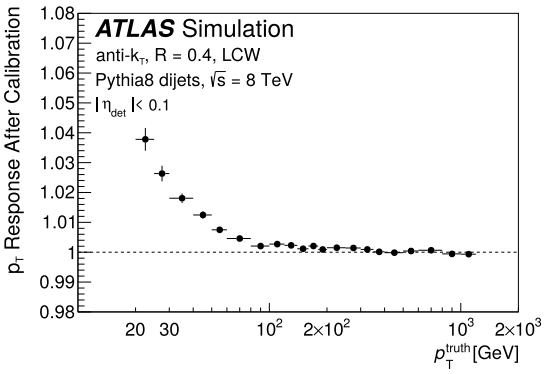

(b) Jet p_{T} response vs p_{T}, $R = 0.4$

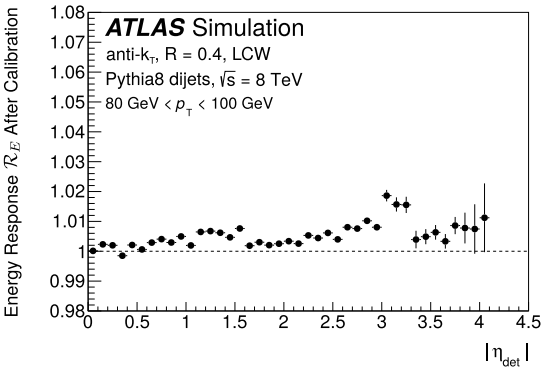

(c) Jet energy response $\mathcal{R}_E$ vs $|\eta_{\mathrm{det}}|$, $R = 0.4$

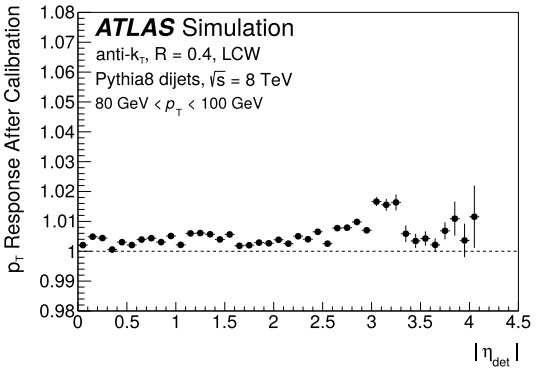

(d) Jet p_{T} response vs $|\eta_{\mathrm{det}}|$, $R = 0.4$

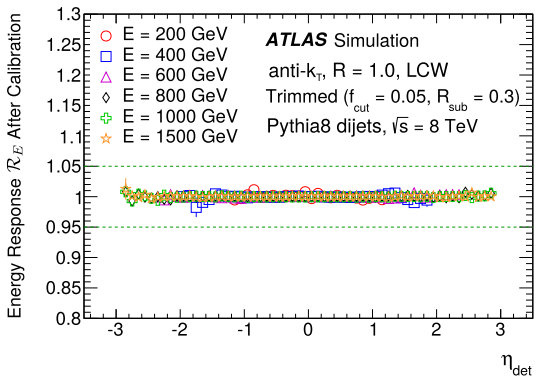

(e) Jet energy response $\mathcal{R}_E$ vs η_{det}, $R = 1.0$

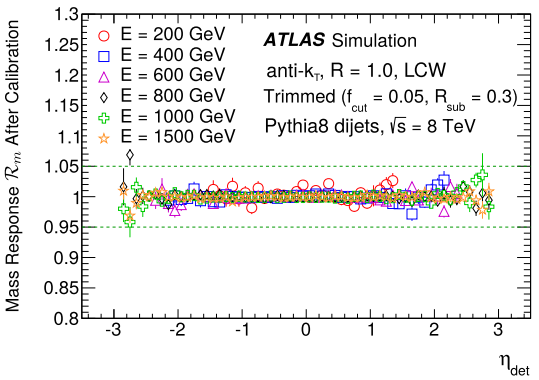

(f) Jet mass response $\mathcal{R}_m$ vs η_{det}, $R = 1.0$

Fig. 5 Jet energy, p_{T}, and mass response after the MC-based jet calibration has been applied for $R = 0.4$ and $R = 1.0$ anti-k_t jets reconstructed from LCW calibrated topo-clusters

MC-based pseudorapidity calibration reported in Sect. 4.3.3, and c_{calib} is a four-momentum scale factor that combines the other calibration steps:

$$c_{\mathrm{calib}} = \begin{cases} c_{\mathrm{PU}} \cdot c_{\mathrm{JES}} \cdot c_{\mathrm{GS}} \cdot c_{\eta} \cdot c_{\mathrm{abs}} & \text{for data} \\ c_{\mathrm{PU}} \cdot c_{\mathrm{JES}} \cdot c_{\mathrm{GS}} & \text{for MC simulation.} \end{cases} \quad (4)$$

Here, the pile-up correction factor is defined as

$$c_{\mathrm{PU}} = \frac{p_{\mathrm{T}} - \rho\, A - \alpha(N_{\mathrm{PV}} - 1) - \beta\mu}{p_{\mathrm{T}}}$$

in accordance with Eq. (2) ($p_{\mathrm{T}} \mapsto c_{\mathrm{PU}}\, p_{\mathrm{T}}$), c_{JES} is derived as explained in Sect. 4.3.3, c_{GS} is the global sequential calibration that is discussed in Sect. 5, and the pseudorapidity intercalibration c_{η} and the absolute in situ calibration c_{abs} are

detailed in Sects. 6–9. As given in Eq. (4), the MC-derived calibrations c_{JES} and c_{GSC} correct simulated jets to the truth-particle jet scale, but jets in data need the in situ corrections c_η and c_{abs} to reach this scale. JES systematic uncertainties are evaluated for the in situ terms.

The calibration procedure is slightly different for the large-R jets used in this paper (Sect. 4.1). These jets do not receive any origin correction or global sequential calibration as the precision needs of the overall scale are not the same as for $R = 0.4$ and $R = 0.6$ jets. Further, no pile-up correction is applied since the trimming algorithm detailed in Sect. 4.1 mitigates the pile-up dependence. However, large-R jets do receive a MC-derived jet mass calibration c_{mass}. The calibrated large-R jet four-momentum is given by

$$(E, \eta, \phi, m) = \left(c_{\mathrm{JES}}\, E^{\mathrm{const}},\ \eta^{\mathrm{const}} + \Delta\eta,\ \phi^{\mathrm{const}},\ c_{\mathrm{mass}}\, m^{\mathrm{const}}\right). \tag{5}$$

By expressing the jet transverse momentum in terms of energy, mass, and pseudorapidity, it can be seen that all calibration terms of Eqs. (3) and (5) affect p_{T}, for example

$$p_{\mathrm{T}} = \frac{E \ominus m}{\cosh\eta} = \frac{c_{\mathrm{JES}}\, E^{\mathrm{const}} \ominus c_{\mathrm{mass}}\, m^{\mathrm{const}}}{\cosh\left(\eta^{\mathrm{const}} + \Delta\eta\right)},$$

where the symbol $\ominus$ denotes subtraction in quadrature, i.e. $a \ominus b \equiv \sqrt{a^2 - b^2}$.

5 Global sequential calibration

The global sequential (GS) calibration scheme exploits the topology of the energy deposits in the calorimeter as well as tracking information to characterize fluctuations in the jet particle content of the hadronic shower development. Correcting for such fluctuations can improve the jet energy resolution and reduce response dependence on the so-called "jet flavour", meaning dependence on the underlying physics process in which the jet was produced. Jets produced in dijet events tend to have more constituent particles, a wider transverse profile and a lower calorimeter energy response than jets with the same p_{T} and η produced in the decay of a W boson or in association with a photon (γ+jet) or Z boson (Z+jet). This can be attributed to differences in fragmentation between "quark-initiated" and "gluon-initiated" jets. The GS calibration also exploits information related to the activity in the muon chamber behind uncontained calorimeter jets, for which the reconstructed energy tends to be smaller with a degraded resolution. The calibration is applied in sequential steps, each designed to flatten the jet energy response as a function of a jet property without changing the mean jet energy.

5.1 Description of the method

Any variable x that carries information about the jet response can be used for the GS calibration. A multiplicative correction to the jet energy measurement is derived by inverting the jet response as a function of this variable: $c(x) = k/R(x)$, where the constant k is chosen to ensure that the average energy is not affected by the calibration, and the average jet response $R(x)$ is determined using MC simulation as described in Sect. 4.2. After a successful application, the jet response should no longer depend on x. As a result, the spread of reconstructed jet energy is reduced, thus improving the resolution.

Each correction is performed separately in bins of η_{det}, in order to account for changes in the jet p_{T} response in different detector regions and technologies. The corrections are further parameterized as a function of p_{T} and jet property x: $c(p_{\mathrm{T}}, x)$, except for the correction for uncontained calorimeter jets, which is constructed as a function of jet energy E and the logarithm of the number of muon segments reconstructed in the muon chambers behind the jet: $c(E, \log N_{\mathrm{segments}})$. The uncontained calorimeter jet correction is constructed using the jet E rather than the p_{T} to better represent the probability of a jet penetrating the full depth of the calorimeter, which depends on $\log E$. The two-dimensional calibration function is constructed using a two-dimensional Gaussian kernel [6] for which the kernel-width parameters are chosen to capture the shape of the response across η_{det} and p_{T}, and at the same time provide stability against statistical fluctuations.

Several variables can be used sequentially to achieve the optimal resolution. The jet p_{T} after N GS calibration steps is given by the initial jet p_{T} multiplied by the product of the N corrections:

$$\begin{aligned} p_{\mathrm{T}}^{\mathrm{GS}} &= p_{\mathrm{T},0}\, c_{\mathrm{GS}} = p_{\mathrm{T},0} \prod_{j=1}^{N} c_j(\, p_{\mathrm{T},j-1},\, x_j\,), \\ p_{\mathrm{T},i} &= p_{\mathrm{T},i-1}\, c_i(p_{\mathrm{T},i-1}, x_i), \end{aligned} \tag{6}$$

where $p_{\mathrm{T},0}$ is the jet p_{T} prior to the GS calibration. Hence, when deriving correction j, one needs to start by calibrating the jets with the previous $j-1$ correction factors. This method assumes there is little to gain from non-linear correlations of the variables used and this has been demonstrated in simulation.

5.2 Jet observables sensitive to the jet calorimeter response

The GS calibration relies on five jet properties that were identified empirically to have a significant effect on the jet energy response. This empirical study was conducted primarily using EM jets, while a reduced scan was performed for LCW jets given that they already exploit some of the following variables as part of the LCW procedure. Two of the variables characterize the longitudinal shower structure

of a jet, namely the fractions of energy deposited in the third electromagnetic calorimeter layer, f_{LAr3}[2], and in the first hadronic Tile calorimeter layer, f_{Tile0}. These fractions are defined according to

$$f_{\mathrm{LAr3}} = E_{\mathrm{EM}}^{\mathrm{LAr3}} / E_{\mathrm{EM}}^{\mathrm{jet}}, \text{ and } f_{\mathrm{Tile0}} = E_{\mathrm{EM}}^{\mathrm{Tile0}} / E_{\mathrm{EM}}^{\mathrm{jet}}, \tag{7}$$

where the subscript EM refers to the electromagnetic scale. The next two of the five jet properties rely on reconstructed tracks from the selected primary vertex that are matched to the calorimeter jets using ghost association (Sect. 4.2). The tracks are required to fulfil quality criteria relating to their impact parameter and the number of hits in the different inner-detector layers, and to have $p_{\mathrm{T}} > 1$ GeV and $|\eta| < 2.5$. The track-based observables are the number of tracks associated with a given jet n_{trk}, and the jet width $\mathcal{W}_{\mathrm{trk}}$ defined as

$$\mathcal{W}_{\mathrm{trk}} = \sum_{i=1}^{N_{\mathrm{trk}}} p_{\mathrm{T},i}\, \Delta R(i, \mathrm{jet}) \Big/ \sum_{i=1}^{N_{\mathrm{trk}}} p_{\mathrm{T},i}, \tag{8}$$

where N_{trk} are the number of tracks associated with the jet, $p_{\mathrm{T},i}$ is the p_{T} of the ith track, and $\Delta R(i, \mathrm{jet})$ is the ΔR distance in (η, ϕ)-space between the ith track and the calorimeter jet axis. The jet width $\mathcal{W}_{\mathrm{trk}}$ quantifies the transverse structure of the jet, which is sensitive to the "jet flavour". The final variable used in the GS calibration is N_{segments}, the number of muon segments behind the jet, which quantifies the activity in the muon chambers. Muon segments are partial tracks constructed from hits in the muon spectrometer chambers [55], and are matched to the jet of interest in two stages. Based on jets built using anti-k_t with $R = 0.6$, N_{segments} is defined by the number of matching muon segments within a cone of size $\Delta R = 0.4$ around the jet axis. For anti-k_t $R = 0.4$ jets, the closest $R = 0.6$ jet is found (fulfilling $\Delta R < 0.3$), and N_{segments} is assigned to the $R = 0.4$ jets according to the corresponding value for the $R = 0.6$ jet.

Figures 6 and 7 show distributions comparing data with MC simulations for f_{Tile0}, f_{LAr3}, n_{trk}, $\mathcal{W}_{\mathrm{trk}}$ and N_{segments} for jets with $|\eta_{\mathrm{det}}| < 0.6$ produced in dijet events selected as described in Sect. 6.3. Predictions are provided using the default Pythia8 sample with full detector simulation from which the GS calibration is derived, and also using the AFII fast simulation, which is often used in physics analyses (Sect. 3). For the AFII detector simulation, there is no complete implementation of the muon segments produced behind high-energy uncontained jets. Therefore, this correction is not applied to AFII samples, and no AFII prediction is provided in Fig. 7e. It can be seen that the simulation predicts the general shapes of the data, although there are visible differences. Similar results are found in the other η_{det} regions. Disagreements in the distributions of the jet properties have little impact on the GS calibration performance as long as the response dependence $R(x)$ of the jet properties x is well described by the simulation (Sect. 5.6).

5.3 Derivation of the global sequential jet calibration

The jet observables used for the GS calibration and their order of application are summarized in Table 2. The first four corrections are determined separately in η_{det}-bins of width 0.1 and are parameterized down to $p_{\mathrm{T}} = 15$ GeV. For jets at the LCW+JES scale, only the tracking and uncontained calorimeter jets corrections are applied since the LCW calibration already takes into account shower shape information. No further improvement in resolution is thus achieved through the use of f_{Tile0} and f_{LAr3} for LCW jets.

The calorimeter response for EM+JES calibrated anti-k_t $R = 0.4$ jets with $p_{\mathrm{T}}^{\mathrm{truth}}$ in three representative intervals is presented as a function of the different jet property variables used by the GS calibration in Fig. 8. For all properties, a strong dependence of the response as a function of the property is observed. The n_{trk} and $\mathcal{W}_{\mathrm{trk}}$ show a stronger p_{T} dependence than the other properties and this is extensible for other p_{T} and η_{det} bins and jet collections. The corresponding distributions after the GS calibration are shown in Fig. 9. The jet response dependence on the jet properties is removed to within 2% after applying the GS calibration for all observables. Deviations from unity are expected since the correlations between the variables are not accounted for in the GS calibration procedure.

5.4 Jet transverse momentum resolution improvement in simulation

Figure 10 shows the jet transverse momentum resolution as a function of $p_{\mathrm{T}}^{\mathrm{truth}}$ in simulated Pythia8 dijet events. While the response remains unchanged, the jet resolution improves as more corrections are added. The relative improvement[3] for EM+JES calibrated anti-k_t $R = 0.4$ jets with central rapidity is found to be 10% at $p_{\mathrm{T}} = 30$ GeV, rising to 40% at 400 GeV. This is equivalent to removing an absolute uncorrelated resolution source $\Delta\sigma$ of 10% or 5%, respectively, as can be seen

[2] The ATLAS calorimeters have three electromagnetic layers in the pseudorapidity interval $|\eta| < 2.5$, but only two in $2.5 < |\eta| < 3.2$. f_{LAr3} includes energy deposits with $|\eta| < 2.5$ in the third EM layer and contributions with $2.5 < |\eta| < 3.2$ in the second EM layer. Energy deposits with $|\eta| > 3.2$ are not included, however a jet with $|\eta| \gtrsim 3.2$ will most often have topo-clusters with $|\eta| < 3.2$ that leave contributions to the second EM layer.

[3] The relative improvement in the jet p_{T} resolution in comparison with the baseline (no-GS) calibration is calculated as $\frac{(\sigma_{p_{\mathrm{T}}}/p_{\mathrm{T}})_{\text{no-GS}} - (\sigma_{p_{\mathrm{T}}}/p_{\mathrm{T}})_{\mathrm{GS}}}{(\sigma_{p_{\mathrm{T}}}/p_{\mathrm{T}})_{\text{no-GS}}}$, where the label no-GS refers to the jet prior to the GS calibration, i.e. directly after the MC-based calibration (Fig. 1) and GS refers to the jet after the GS calibration.

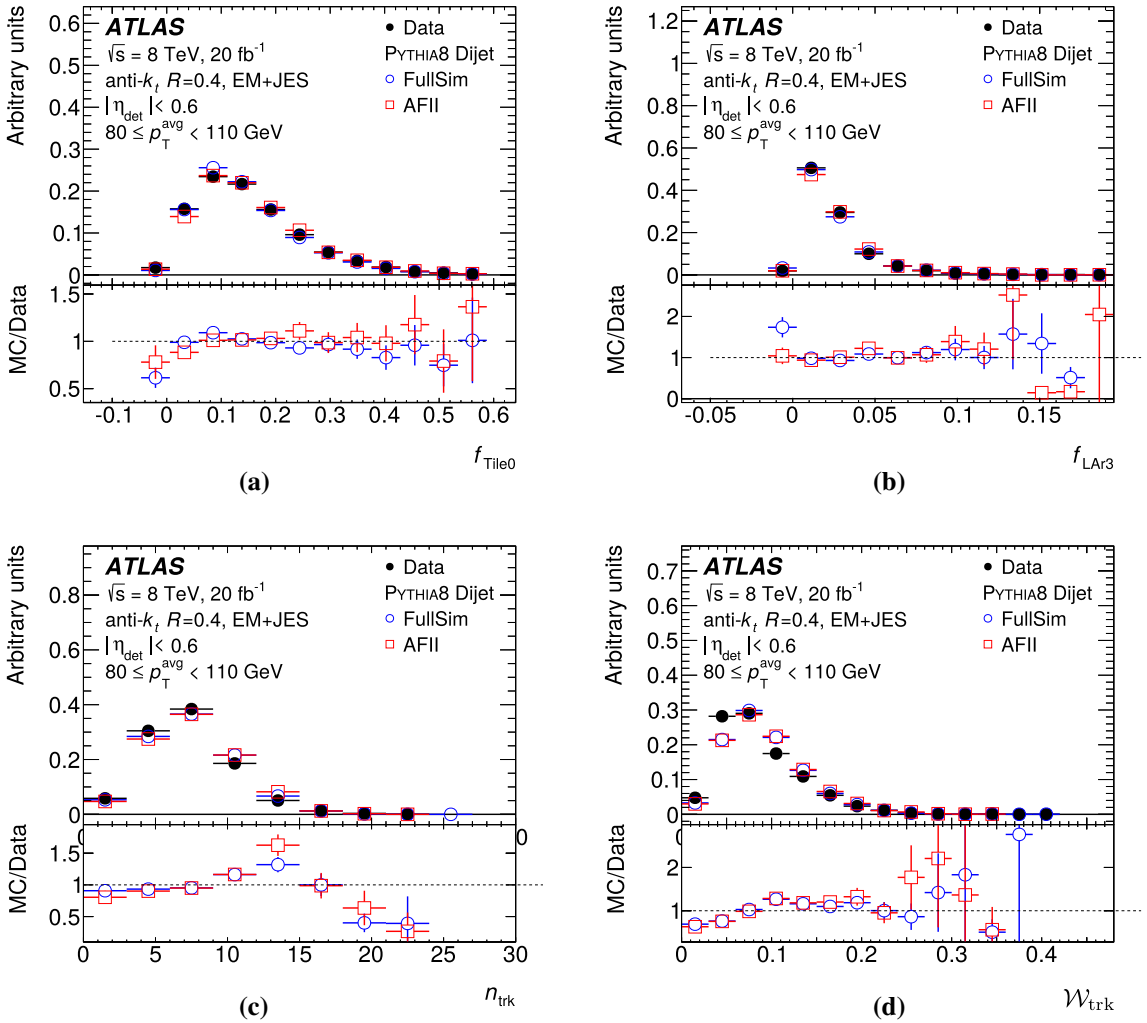

Fig. 6 Normalized distributions of f_{Tile0}, f_{LAr3}, n_{trk}, and $\mathcal{W}_{\text{trk}}$ for jets $|\eta_{\text{det}}| < 0.6$ in dijet events with $80\,\text{GeV} < p_{\text{T}}^{\text{avg}} < 110\,\text{GeV}$ in data (filled circles) and PYTHIA8 MC simulation with both full (empty circles) and fast (empty squares) detector simulation. All jets are reconstructed with anti-k_t $R = 0.4$ and calibrated with the EM+JES scheme. The quantity $p_{\text{T}}^{\text{avg}}$ is the average p_{T} of the leading two jets in an event, and hence represent the p_{T} scale of the jets being probed. N_{segments} is not shown since the vast majority of jets in this p_{T} range have $N_{\text{segments}} = 0$

in the lower part of Fig. 10a. The quantity $\Delta\sigma$ is calculated by subtracting in quadrature the relative jet p_{T} resolution:

$$\Delta\sigma = \begin{cases} -\left((\sigma_{p_{\text{T}}}/p_{\text{T}})_{\text{no-GS}} \ominus (\sigma_{p_{\text{T}}}/p_{\text{T}})_{\text{GS}}\right) & \text{if } (\sigma_{p_{\text{T}}}/p_{\text{T}})_{\text{no-GS}} > (\sigma_{p_{\text{T}}}/p_{\text{T}})_{\text{GS}} \\ +\left((\sigma_{p_{\text{T}}}/p_{\text{T}})_{\text{GS}} \ominus (\sigma_{p_{\text{T}}}/p_{\text{T}})_{\text{no-GS}}\right) & \text{otherwise.} \end{cases} \tag{9}$$

The improvement observed for jets initially calibrated with the LCW+JES scheme is found to be smaller, which is expected as only tracking and non-contained jet corrections are applied to these jets. For both EM+JES and LCW+JES calibrated jets, improvements to the JER is observed across the full p_{T} range probed ($25\,\text{GeV} \leq p_{\text{T}} < 1200\,\text{GeV}$). The fact that JER reduction is observed at high jet p_{T} means that also the constant term of the calorimeter resolution (Eq. (24)) is reduced by the GS calibration. This improvement can be explained by considering the jet resolution distributions for different values of the jet properties. As is evident in Fig. 8, the mean of these distributions have a strong dependence on the jet property, while the width of the distributions (JER) are not expected to have any such dependence at high jet p_{T}. The GS calibration can hence be seen as aligning several similarly shaped response distributions, which each have a biased mean, towards the desired truth-particle jet scale.

The conclusions from this section can generally be extended to the whole η_{det} range, although close to the calorimeter transition regions where the detector instrumen-

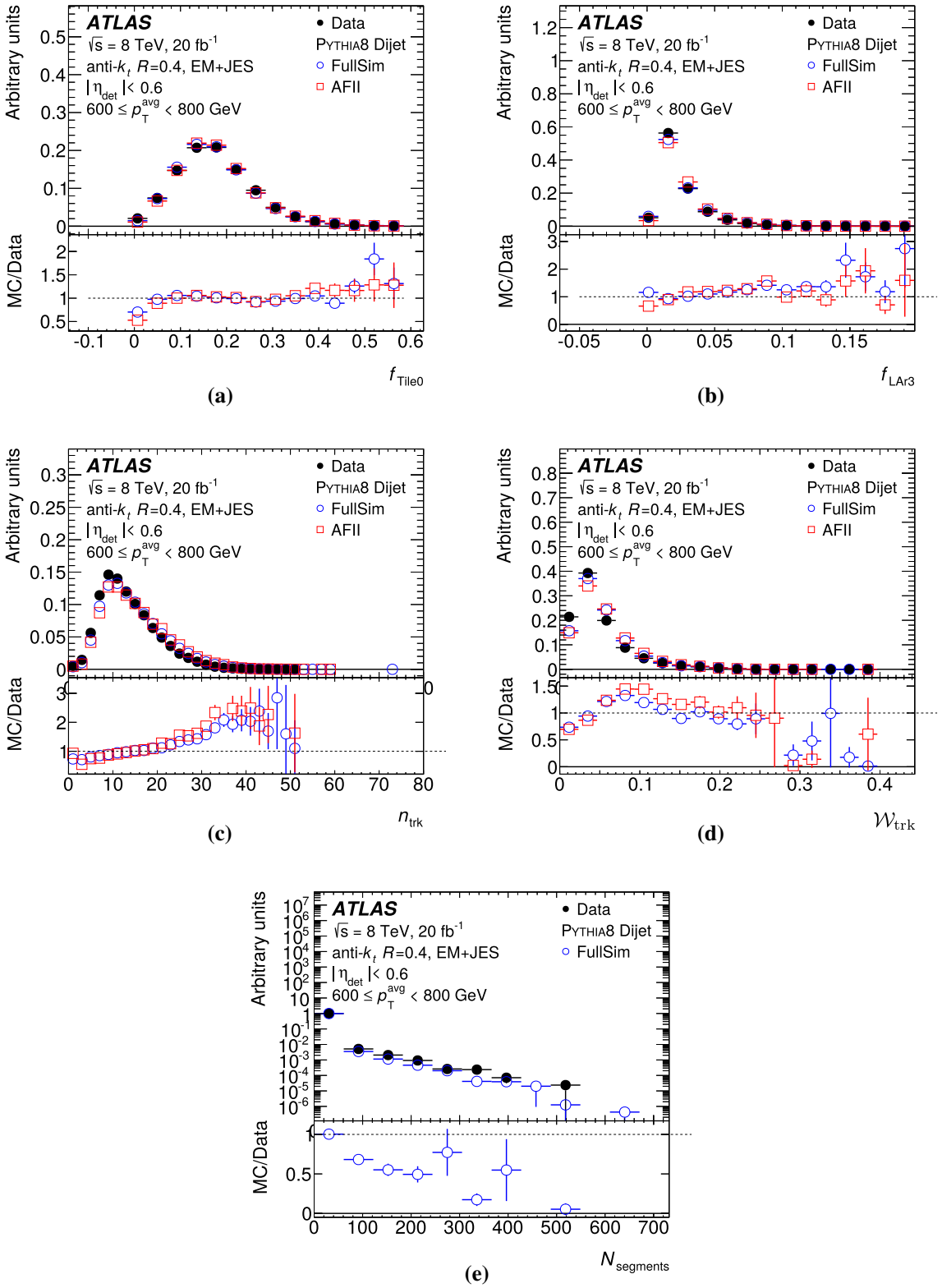

Fig. 7 Normalized distributions of f_{Tile0}, f_{LAr3}, n_{trk}, $\mathcal{W}_{\mathrm{trk}}$ and N_{segments} for jets $|\eta_{\mathrm{det}}| < 0.6$ in dijet events with 600 GeV $< p_{\mathrm{T}}^{\mathrm{avg}} <$ 800 GeV in the data (filled circles) and Pythia8 MC simulation with both full (empty circles) and fast (empty squares) simulation. All jets are reconstructed with anti-k_t $R = 0.4$ and calibrated with the EM+JES scheme. The quantity $p_{\mathrm{T}}^{\mathrm{avg}}$ is the average p_{T} of the leading two jets in an event, and hence represent the p_{T} scale of the jets being probed

Table 2 Sequence of GS corrections used to improve the jet performance in each η_{det} region. For jets at the LCW+JES scale, only the tracking and uncontained calorimeter jet corrections are applied

$\lvert\eta\rvert$ Region	Correction 1	Correction 2	Correction 3	Correction 4	Correction 5
[0, 1.7]	f_{Tile0}	f_{LAr3}	n_{trk}	$\mathcal{W}_{\text{trk}}$	N_{segments}
[1.7, 2.5]		f_{LAr3}	n_{trk}	$\mathcal{W}_{\text{trk}}$	N_{segments}
[2.5, 2.7]		f_{LAr3}			N_{segments}
[[2.7, 3.5]		f_{LAr3}			

tation is reduced (Fig. 4), the track-based observables introduce an even stronger improvement. The enhancement in JER due to the GS calibration is found to be similar for different MC generators.

Only a small improvement is observed after applying the last GS correction for uncontained calorimeter jets in the inclusive jet sample since only a small fraction of energetic jets are uncontained. Figure 11 presents a measure of the improvement in jet energy resolution from applying the fifth GS correction both to inclusive jets and to jets with at least 20 associated muon segments, which are less likely to be fully contained in the calorimeters. The resolution metric is the standard deviation (RMS) of the jet response distribution divided by the arithmetic mean. This quantity is used instead of the normal resolution definition (from the σ of a Gaussian fit as described in Sect. 4.2) since it gives information about the reduction in the low response tail. While the improvement observed is small for an inclusive jet sample, the impact is significant for uncontained jets. A relative resolution improvement of 10% is seen for jets with $p_{\text{T}} \approx 100$ GeV, while the improvement is 20% for jets with $p_{\text{T}} \approx 1$ TeV. This corresponds to removing an absolute resolution source of 8% or 4%, respectively.

5.5 Flavour dependence of the jet response in simulation

The internal structure of a jet, and thereby also its calorimeter response, depends on how the jet was produced. Jets produced in dijet events are expected to originate from gluons more often than jets with the same p_{T} and η produced in the decay of a W boson or in association with a photon or Z boson. The hadrons of a quark-initiated jet will tend to be of higher energy and hence penetrate further into the calorimeter, while the less energetic hadrons in a gluon-initiated jet will bend more in the magnetic field in the inner detector. It is desirable that such flavour dependence of the calibrated jet should be as small as possible to mitigate sample-specific systematic biases in the jet energy scale (Sect. 9.2.3 for discussion of the associated uncertainty).

The flavour dependence of the response is studied in simulated dijet events by assigning a flavour label to each calorimeter jet using an angular matching to the particles in the MC event record. If the jet matches a b- or a c-hadron, it is labelled a b-jet or c jet, respectively. If it matches both a b- and a c-hadron, it is labelled a b-jet. If it does not match any such heavy hadron, the jet is labelled "light quark" (LQ) or gluon initiated, based on the type of the highest-energy matching parton. The matching criterion used is $\Delta R < R$, where R is the radius parameter of the jet algorithm (0.4 or 0.6). The p_{T} responses before and after GS calibration for jets in different flavour categories are presented in Fig. 12. For each flavour category, results are shown for two representative pseudorapidity regions. The response for LQ jets is larger than unity since the MC-derived baseline calibration (Sect. 4.3) is derived in dijet events that contain a large fraction of gluon jets. For gluon-initiated jets the response is lower than that of LQ jets, as expected, and b-jets have a p_{T} response between that of LQ and gluon jets. In all cases, the GS calibration brings the response closer to unity and hence reduces the flavour dependence, which is important as analyses do not know the flavour of each jet. The change in p_{T} response introduced by the GS calibration for jets with $p_{\text{T}} = 80$ GeV with $|\eta| < 0.3$ is -4%, $+1\%$ and -2% for LQ jets, gluon jets and b-jets, respectively.

5.6 In situ validation of the global sequential calibration

The GS correction is validated in situ with dijet events using the tag-and-probe technique, using the event selection described in Sect. 6, with only one modification: both jets are required to be in the same $|\eta_{\text{det}}|$ region to avoid biases from any missing η-dependent calibration factors. The jet whose response dependence is studied is referred to as the probe jet, while the other is referred to as the reference jet. The choice of reference jet and probe jet is arbitrary when studying the response dependence on the jet properties, and the events are always used twice, alternating the roles of reference and probe. The response for the probe jet is measured through the dijet p_{T} asymmetry variable $\mathcal{A}$ (Eq. (10) and Sect. 6.1) in bins of the average p_{T} of the probe and the reference jet $p_{\text{T}}^{\text{avg}}$, and is studied as a function of the jet property of the probe jet.

Results for all variables used in the GS calibration are shown in Fig. 13 for jets with $|\eta_{\text{det}}| < 0.6$ in two representative p_{T} ranges. No GS calibration is applied to either the probe or the reference jet. It can be seen that the reference Pythia8 dijet MC sample agrees with the data within 1% (4%) for 600 GeV $< p_{\text{T}}^{\text{avg}} <$ 800 GeV (80 GeV $< p_{\text{T}}^{\text{avg}} <$

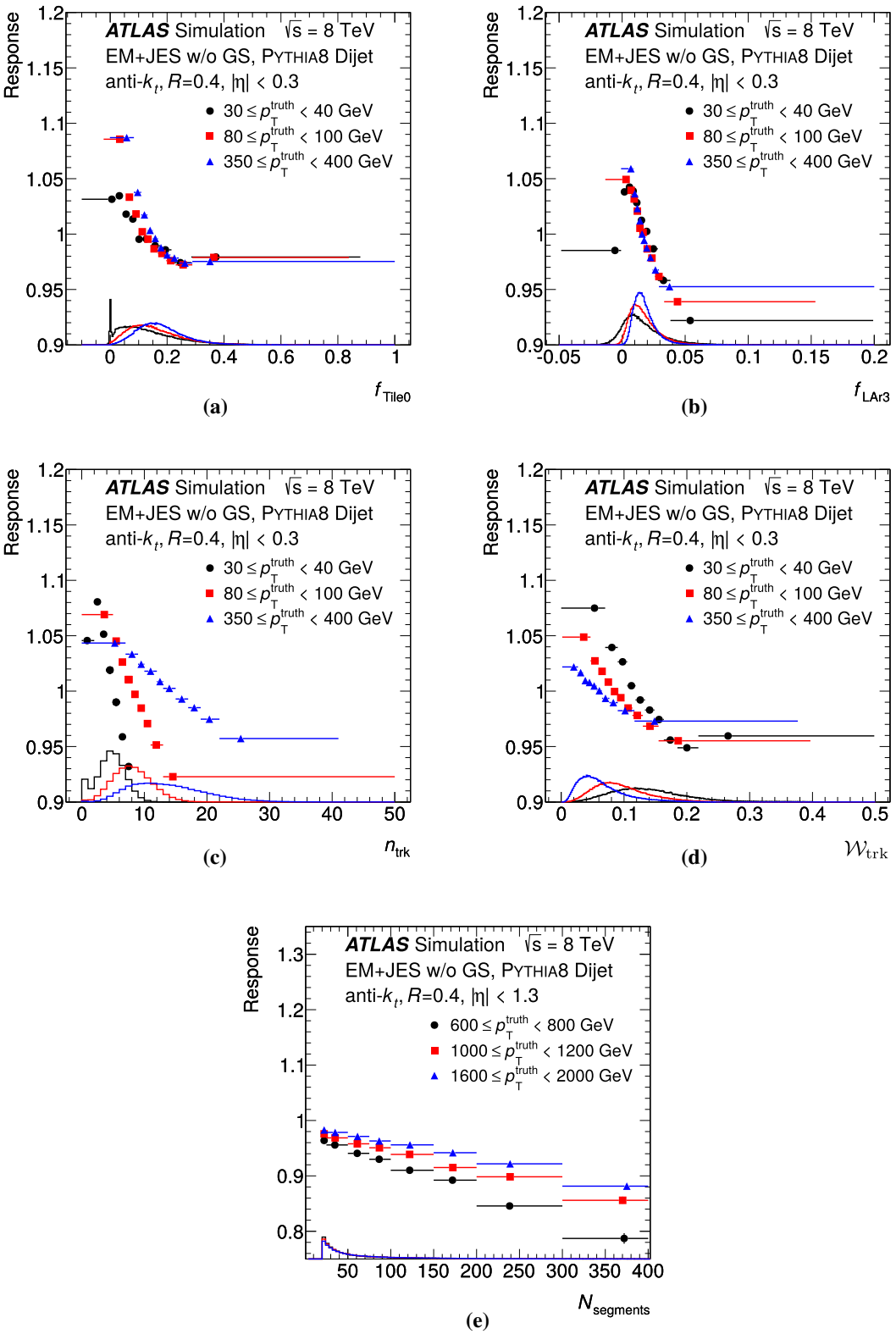

Fig. 8 Jet p_{T} response as a function of f_{Tile0}, f_{LAr3}, n_{trk}, $\mathcal{W}_{\mathrm{trk}}$ and N_{segments} for jets with $|\eta_{\mathrm{det}}| < 0.3$ ($|\eta_{\mathrm{det}}| < 1.3$ for N_{segments}) in different $p_{\mathrm{T}}^{\mathrm{truth}}$ ranges. All jets are reconstructed with anti-k_t $R = 0.4$ and calibrated with the EM+JES scheme without global sequential corrections. The horizontal line associated with each data point indicates the bin range, and the position of the marker corresponds the centroid within this bin. The underlying distributions of the jet properties for each $p_{\mathrm{T}}^{\mathrm{truth}}$ bin normalized to the same area are also shown as histograms at the bottom of the plots

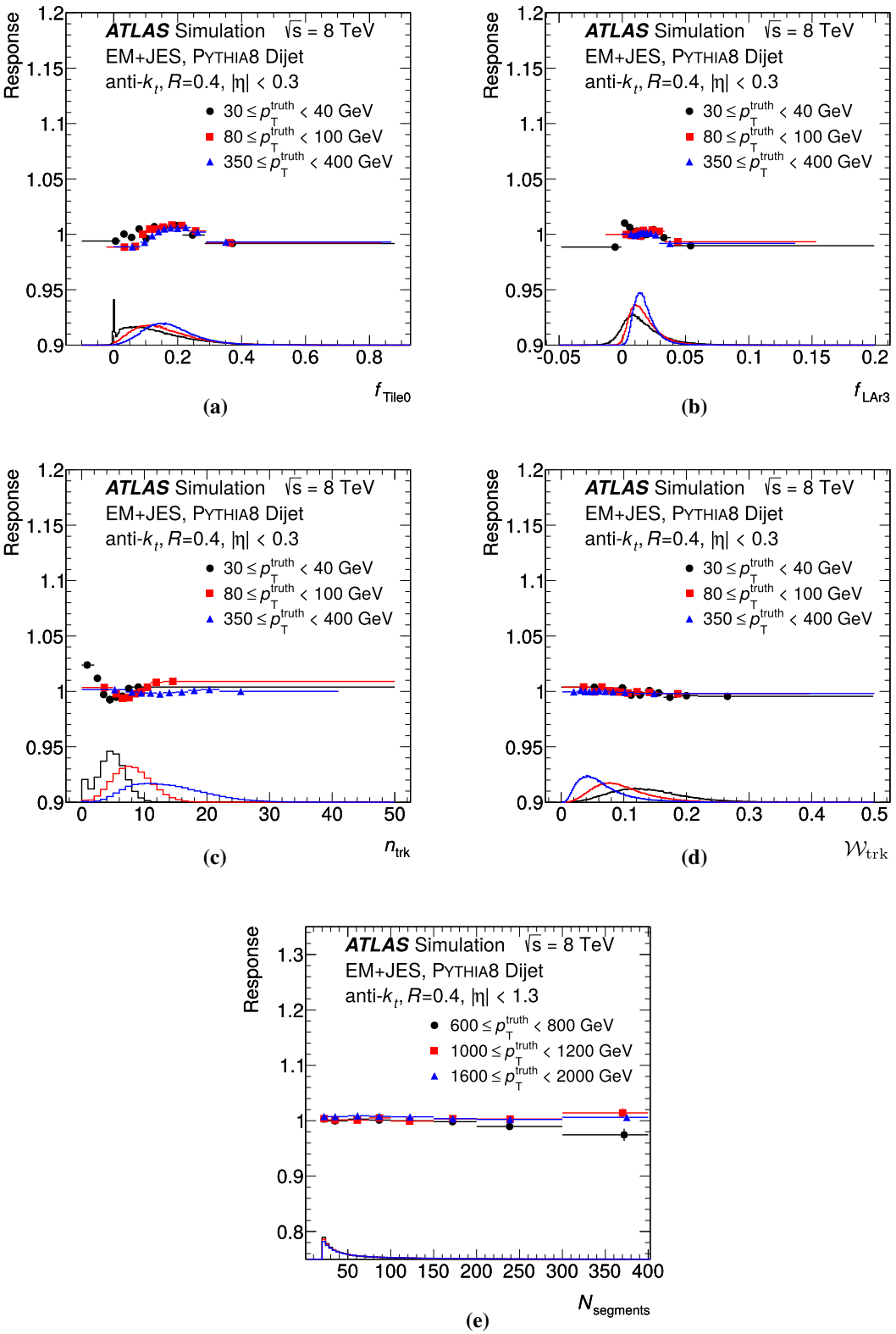

Fig. 9 Jet p_T response as a function of f_{Tile0}, f_{LAr3}, n_{trk}, $\mathcal{W}_{trk}$ and $N_{segments}$ for jets with $|\eta_{det}| < 0.3$ ($|\eta_{det}| < 1.3$ for $N_{segments}$) in different p_T^{truth} ranges. All jets are reconstructed with anti-k_t $R = 0.4$ and calibrated with the EM+JES scheme including global sequential corrections. The horizontal line associated with each data point indicates the bin range, and the position of the marker corresponds the centroid within this bin. The underlying distributions of the jet properties for each p_T^{truth} bin normalized to the same area are also shown as histograms at the bottom of the plots

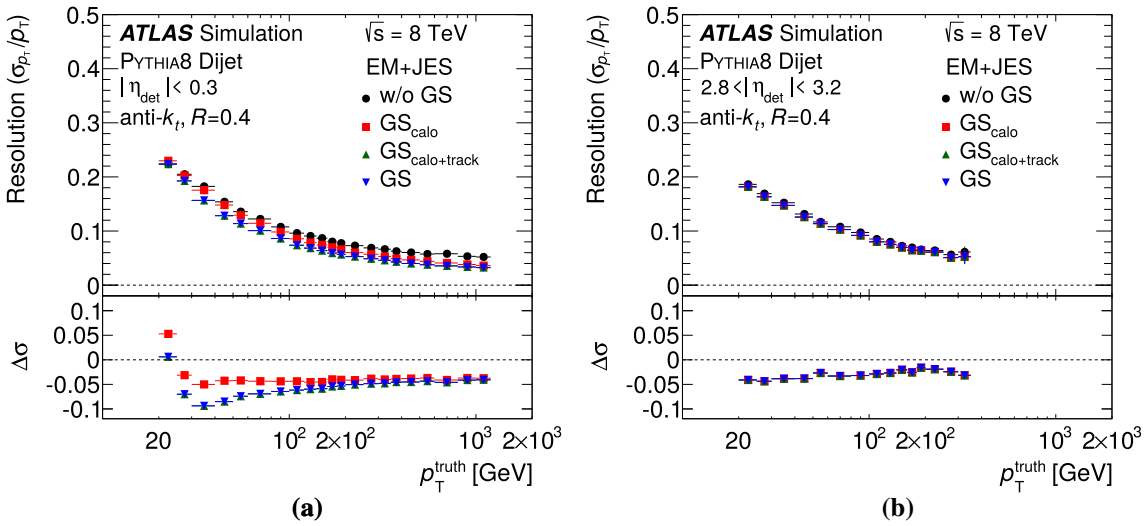

Fig. 10 Jet p_{T} resolution as a function of $p_{\mathrm{T}}^{\mathrm{truth}}$ in the nominal Pythia8 MC sample for jets with **a** $|\eta_{\mathrm{det}}| < 0.3$ and **b** $2.8 < |\eta_{\mathrm{det}}| < 3.2$. The jets are reconstructed with anti-k_t $R = 0.4$. Curves are shown after the EM+JES calibration without global sequential corrections (black circles), with calorimeter-based global sequential corrections only (red squares), with calorimeter- and track-based corrections only (green upward triangles) and including all the global sequential corrections (blue downward triangles). The lower panels show the improvement relative to the EM+JES scale without global sequential corrections obtained using subtraction in quadrature (Eq. (9))

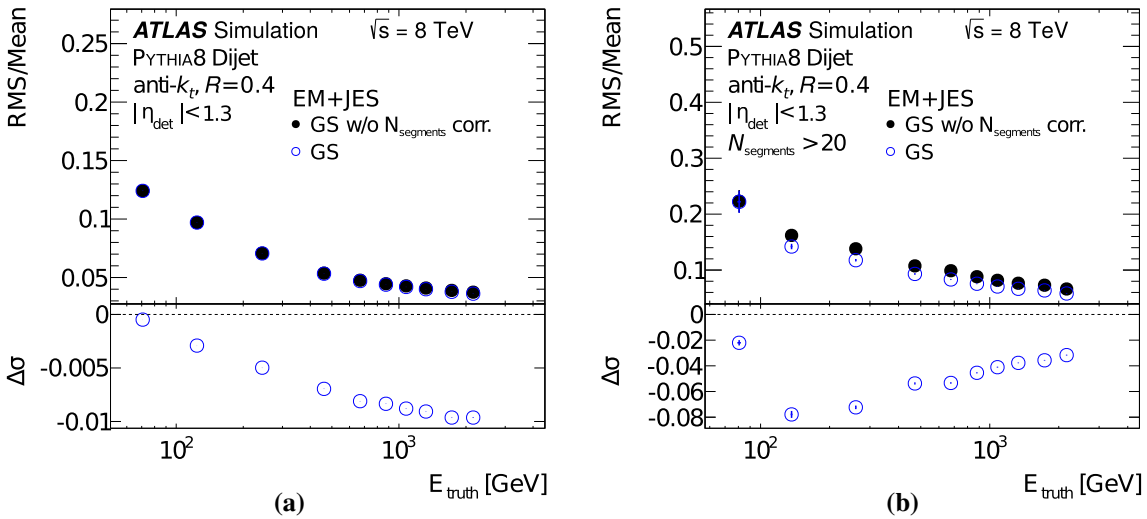

Fig. 11 Standard deviation over arithmetic mean of the jet energy response as a function of E^{truth} for $|\eta_{\mathrm{det}}| < 1.3$ before (filled circles) and after (empty circles) the fifth global sequential correction for **a** all jets and **b** calorimeter jets with $N_{\mathrm{segments}} > 20$ in the nominal Pythia8 dijet MC sample. All jets are reconstructed with anti-k_t $R = 0.4$ and initially calibrated at the EM+JES scale. The requirement $N_{\mathrm{segments}} > 20$ selects a large fraction of "uncontained" jets, i.e. jets for which some of the particles produced in the hadronic shower travel into the muon spectrometers behind the calorimeters. The bottom panels show the improvement introduced by the corrections quantified using subtraction in quadrature (Eq. (9))

110 GeV) for the calorimeter-based variables, and slightly better for the track-based observables. A similar level of agreement is seen in other jet p_{T} and η_{det} ranges. These differences impact the average jet p_{T} weighted by the fraction of jets with corresponding values of the GS property in question; given that these differences occur in the tails of the distributions, the impact on the average jet p_{T} is thus minimal. Results using MC samples produced with the AFII fast detector simulation are also shown and demonstrate similar agreement with data, although these samples have larger statistical uncertainties. The relative data–MC agreement stays the same after the GS calibration is applied for both full and fast detector simulation.

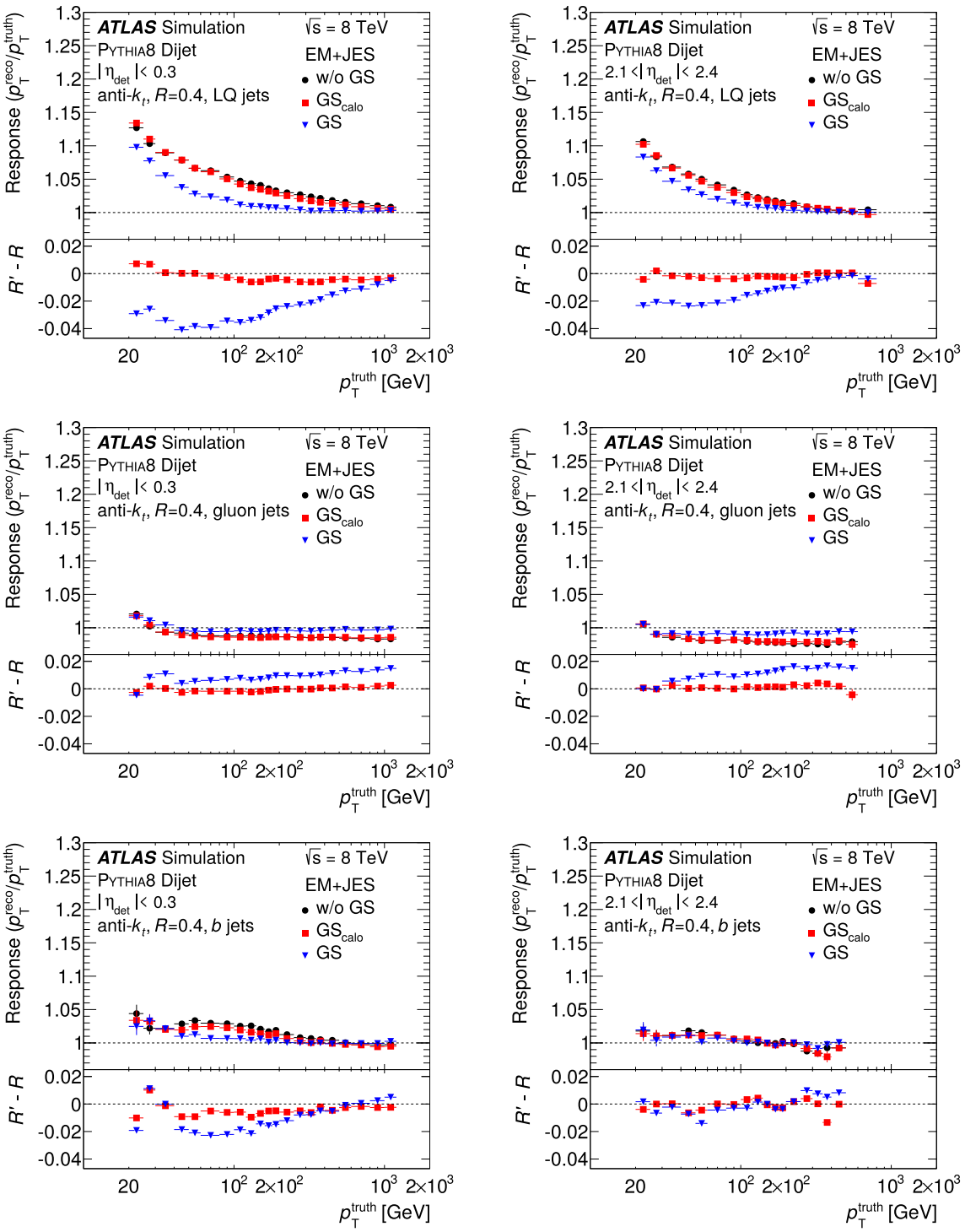

Fig. 12 The p_{T} response for anti-k_t $R = 0.4$ jets as a function of $p_{\mathrm{T}}^{\mathrm{truth}}$ for light quark (LQ) jets (top), gluon jets (middle) and b-jets (bottom) with $|\eta_{\mathrm{det}}| < 0.3$ (left) and $2.1 < |\eta_{\mathrm{det}}| < 2.4$ (right) regions in the PYTHIA8 MC sample. The p_{T} response after the EM+JES calibration without GS corrections (circles), with calorimeter-based GS corrections only (squares) and including all the GS corrections (triangles) are shown. The lower box of each plot shows the impact on the jet response, subtracting the response before the GS corrections (R) from the response after applying the GS corrections (R')

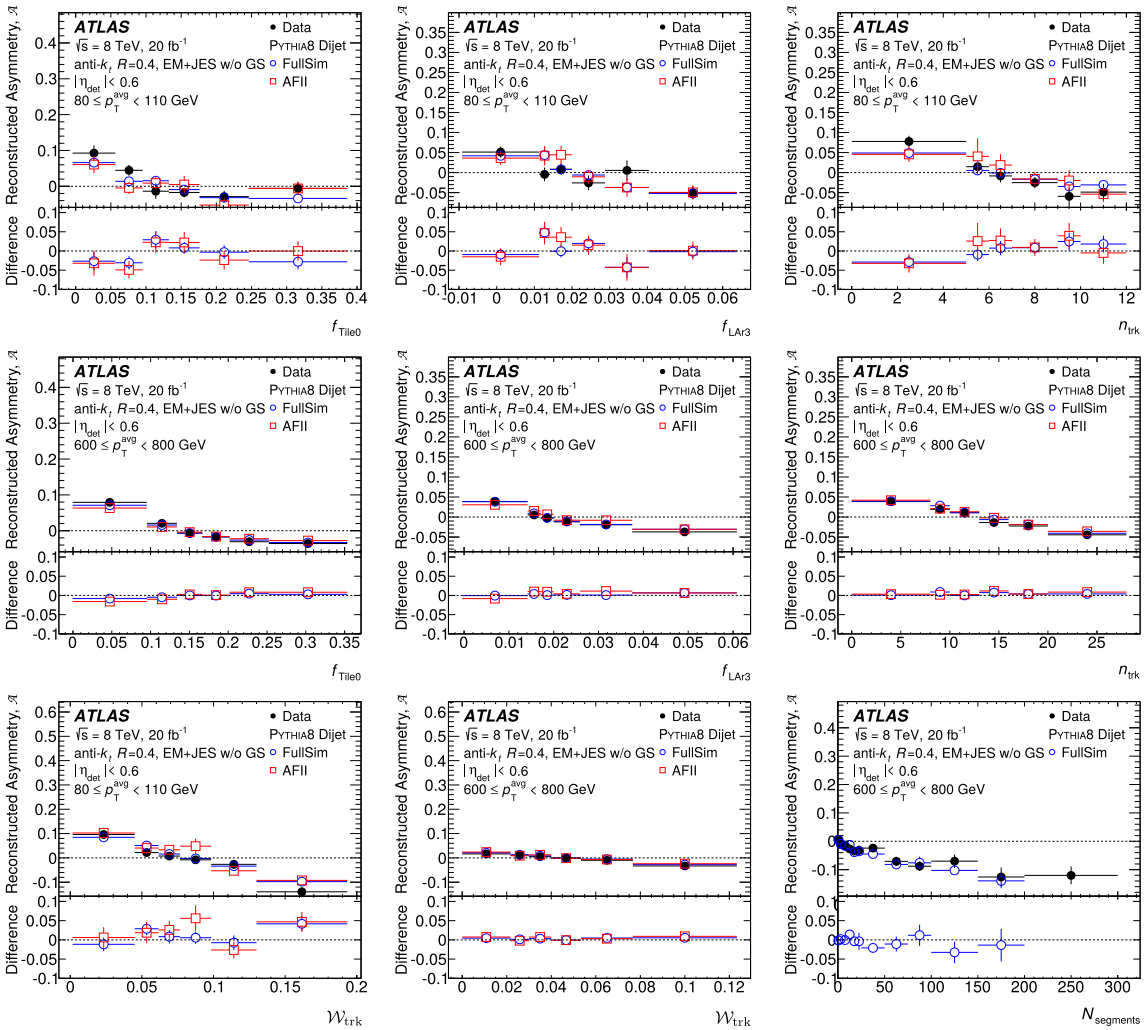

Fig. 13 Dijet in situ validation of jet response as a function of f_{Tile0}, f_{LAr3} and n_{trk} for jets with 80 GeV $< p_{\text{T}}^{\text{avg}} <$ 110 GeV and $|\eta_{\text{det}}| < 0.6$ (top) and for jets with 600 GeV $< p_{\text{T}}^{\text{avg}} <$ 800 GeV and $|\eta_{\text{det}}| < 0.6$ (middle) and the same quantity as a function of $\mathcal{W}_{\text{trk}}$ and N_{segments} (bottom). Each set of measurements are shown for data (filled circles) and for Pythia8 MC simulation with both full (empty circles) and fast (empty squares) detector modelling. All jets are reconstructed with anti-k_t $R = 0.4$ and calibrated with the EM+JES scheme without any global sequential corrections

5.7 Comparison of jet resolution and flavour dependence between different event generators

Figure 14 presents comparisons of p_{T} resolution and response dependence on jet flavour between three MC event generators, namely Pythia8, Herwig++, and Sherpa, each with a different implementation of parton showering, multiple parton–parton interactions and hadronization (Sect. 3). These quantities are shown as a function of jet p_{T} both with and without GS calibration applied in two representative η_{det} regions. Pythia8 tends to predict a slightly worse jet p_{T} resolution for jets with $p_{\text{T}} < 50$ GeV compared with the jet resolution in Herwig++ and Sherpa, but the improvement introduced by the GS correction is compatible between the different generators. The reduction of jet flavour dependence is studied by taking the difference between the jet responses for LQ and gluon jets, determined as discussed in Sect. 5.5 and as used for light-quark vs gluon discrimination [56]. The overall flavour dependence of the jet response is found to be smaller for Herwig than for Pythia8 and Sherpa, and in general, the LQ jet response is quite similar between the generators, while the response for gluon jets varies more. For jets with $p_{\text{T}} > 40$ GeV, the response difference between LQ and gluon jets is reduced by at least a factor of two after applying the GS correction.

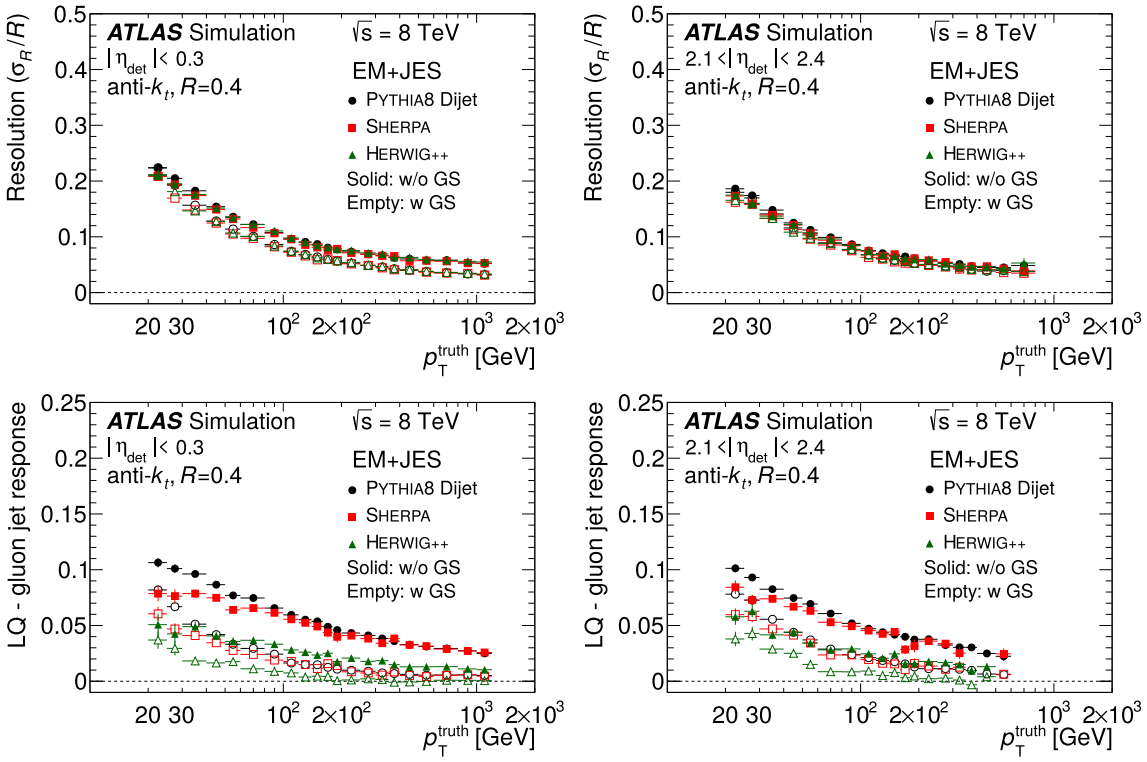

Fig. 14 Jet p_{T} resolution (top) and difference in jet response between gluon and light quark (LQ) initiated jets (bottom) as a function of $p_{\mathrm{T}}^{\mathrm{truth}}$ for two representative $|\eta_{\mathrm{det}}|$ regions. Results are shown both before (closed markers) and after (open markers) the global sequential corrections is applied, and separately for jets in the PYTHIA8 (circles), SHERPA (squares), and HERWIG++ (triangles) dijet MC samples. All jets are reconstructed with anti-k_t $R = 0.4$. Jets are labelled LQ- or gluon-initiated, based on the highest-energy parton in the MC event record which fulfils an angular matching to the jet as further detailed in Sect. 5.5

6 Intercalibration and resolution measurement using dijet events

Following the determination and application of MC-based jet calibration factors, it is important to measure the jet response and resolution in situ, quantify the level of agreement between data and simulation, and correct for any discrepancy. The first step is to investigate the jet response dependence across the detector in terms of pseudorapidity. All results presented in this section are obtained with jets calibrated with the calibration chain up to, and including, the GS calibration (Sect. 4.4).

6.1 Techniques to determine the jet calibration and resolution using dijet asymmetry

The jet energy resolution (JER) and the relative response of the calorimeter as a function of pseudorapidity are determined using events with dijet topologies [6,7]. The p_{T} balance is quantified by the dijet asymmetry

$$\mathcal{A} = \frac{p_{\mathrm{T}}^{\mathrm{probe}} - p_{\mathrm{T}}^{\mathrm{ref}}}{p_{\mathrm{T}}^{\mathrm{avg}}}, \tag{10}$$

where $p_{\mathrm{T}}^{\mathrm{ref}}$ is the transverse momentum of a jet in a well-calibrated reference region, $p_{\mathrm{T}}^{\mathrm{probe}}$ is the transverse momentum of the jet in the calorimeter region under investigation, and $p_{\mathrm{T}}^{\mathrm{avg}} = (p_{\mathrm{T}}^{\mathrm{probe}} + p_{\mathrm{T}}^{\mathrm{ref}})/2$. The average calorimeter response relative to the reference region, $1/c$, is then defined as

$$\frac{1}{c} \equiv \frac{2 + \langle\mathcal{A}\rangle}{2 - \langle\mathcal{A}\rangle} \approx \frac{\left\langle p_{\mathrm{T}}^{\mathrm{probe}}\right\rangle}{\left\langle p_{\mathrm{T}}^{\mathrm{ref}}\right\rangle}, \tag{11}$$

where $\langle\mathcal{A}\rangle$ is the mean of the asymmetry distribution in a given bin of $p_{\mathrm{T}}^{\mathrm{avg}}$ and η_{det}, and the last equality of Eq. (11) can be obtained by inserting the expectation value of a first-order Taylor expansion of Eq. (10), giving $\langle\mathcal{A}\rangle = \left(\langle p_{\mathrm{T}}^{\mathrm{probe}}\rangle - \langle p_{\mathrm{T}}^{\mathrm{ref}}\rangle\right)/\langle p_{\mathrm{T}}^{\mathrm{avg}}\rangle$.

Two versions of the analysis are performed. In the *central reference method*, the calorimeter response is measured as a function of $p_{\mathrm{T}}^{\mathrm{avg}}$ and η_{det} relative to the region defined by $|\eta_{\mathrm{det}}| < 0.8$. Jets in this region are precisely calibrated using Z+jet, γ+jet and multijet data (Sects. 7 and 8). In the *matrix method*, multiple η_{det} regions are chosen and the calorimeter response in a given region is measured relative to all other regions. For a given $p_{\mathrm{T}}^{\mathrm{avg}}$ bin, $\langle\mathcal{A}\rangle$ is determined

for each of a large number of combinations of η_{det} regions of the two jets involved. The calorimeter response relative to the central region is then obtained by solving a set of linear equations based on this matrix of dijet asymmetries [6]. A constraint is applied that sets the average response for jets with $|\eta_{\text{det}}| < 0.8$ to unity. The advantage of the matrix method is that a much larger fraction of events can be used, since events with both jets outside $|\eta_{\text{det}}| < 0.8$ are considered, thus reducing the statistical uncertainty of the final result. Statistical uncertainties in the matrix method result are estimated using pseudo-experiments. Each pseudo-experiment generates a new matrix of dijet asymmetries by sampling the average asymmetry $\langle\mathcal{A}\rangle$ of each bin (matrix element) according to their statistical uncertainty. The intercalibration factors are then derived for each pseudo-experiment, and the statistical uncertainty of the calibration is obtained from the spread. In this paper, the main results are obtained using the matrix method, and the simpler central reference method is used for validation.

The asymmetry distribution also probes the jet energy resolution. The standard deviation of the asymmetry distribution $\sigma_{\mathcal{A}}^{\text{probe}}$ in a given $\left(p_{\text{T}}^{\text{avg}}, \eta_{\text{det}}^{\text{probe}}\right)$ bin can be expressed as

$$\sigma_{\mathcal{A}}^{\text{probe}} = \frac{\sigma_{p_{\text{T}}}^{\text{probe}} \oplus \sigma_{p_{\text{T}}}^{\text{ref}}}{p_{\text{T}}^{\text{avg}}} = \left\langle \frac{\sigma_{p_{\text{T}}}}{p_{\text{T}}} \right\rangle_{\text{probe}} \oplus \left\langle \frac{\sigma_{p_{\text{T}}}}{p_{\text{T}}} \right\rangle_{\text{ref}} = \left\langle \frac{\sigma_E}{E} \right\rangle_{\text{probe}} \oplus \left\langle \frac{\sigma_E}{E} \right\rangle_{\text{ref}}, \tag{12}$$

where $\sigma_{p_{\text{T}}}^{\text{probe}}$ and $\sigma_{p_{\text{T}}}^{\text{ref}}$ are the standard deviations of $p_{\text{T}}^{\text{probe}}$ and $p_{\text{T}}^{\text{ref}}$, respectively. The first two equalities of Eq. (13) follow from error propagation of Eq. (10) and from the fact that after calibration $\langle p_{\text{T}}^{\text{probe}} \rangle = \langle p_{\text{T}}^{\text{ref}} \rangle = \langle p_{\text{T}}^{\text{avg}} \rangle$ in a given $p_{\text{T}}^{\text{avg}}$ bin. The energy and p_{T} resolutions are approximately the same since contributions of the jet angular resolution are negligible (Fig. 2). The standard deviation of the asymmetry distribution $\sigma_{\mathcal{A}}$ is obtained from a Gaussian fit to the core of the distribution.

The standard deviation of the probe jet p_{T} is derived from Eq. (13) as

$$\left\langle \frac{\sigma_{p_{\text{T}}}}{p_{\text{T}}} \right\rangle_{\text{probe}} = \sigma_{\mathcal{A}}^{\text{probe}} \ominus \left\langle \frac{\sigma_{p_{\text{T}}}}{p_{\text{T}}} \right\rangle_{\text{ref}}, \tag{13}$$

where the latter term is derived from events where both jets fall in the central reference region ($|\eta_{\text{det}}| < 0.8$). In this case, the reference region is being probed, and the first and last terms in Eq. (13) are hence equal, which gives $\left\langle \sigma_{p_{\text{T}}}/p_{\text{T}} \right\rangle_{\text{ref}} = \sigma_{\mathcal{A}}/\sqrt{2}$. When calculating the asymmetry, the jets are fully calibrated including all data-driven correction factors.

The p_{T} balance strictly holds only for $2 \to 2$ partonic events. In reality, the p_{T} balance between two jets is affected on an event-by-event basis by additional quark/gluon radiation outside of the jets, as well as hadronization and MPI effects that cause particle losses and additions to the jets, respectively. To account for the impact of such effects, the dijet asymmetry standard deviation $\sigma_{\mathcal{A}}$ is measured separately for reconstructed and truth-particle jets, and the standard deviation due to detector smearing $\sigma_{\mathcal{A}}^{\text{det}}$ is obtained by subtracting the truth-particle quantity from the observed quantity in quadrature:

$$\sigma_{\mathcal{A}}^{\text{det}} = \sigma_{\mathcal{A}}^{\text{reco}} \ominus \sigma_{\mathcal{A}}^{\text{truth}}. \tag{14}$$

This final jet energy resolution measurement $\left\langle \sigma_{p_{\text{T}}}/p_{\text{T}} \right\rangle$ is calculated according to Eq. (13) after first correcting the asymmetry width $\sigma_{\mathcal{A}}$ according to Eq. (14).

6.2 Determining the jet resolution using the dijet bisector method

The bisector method attempts to separate the desired part of the dijet p_{T} imbalance that is due to fluctuations in the jet calorimeter response from contributions from other effects such as soft parton radiation and the underlying event. In the same way as for the central reference method, selection criteria are applied to select events with dijet topology, and at least one of the two jets is required to have $|\eta_{\text{det}}| < 0.8$. This jet is referred to as the "reference jet", while the other jet is labelled "probe jet". If both jets fulfil $|\eta_{\text{det}}| < 0.8$, the labels are assigned randomly. The p_{T} (imbalance) of the dijet system in the transverse plane is defined as the vectorial sum of the p_{T} vectors of the leading two jets: $\mathbf{p}_{\text{T}}^{jj} = \mathbf{p}_{\text{T}}^{\text{probe}} + \mathbf{p}_{\text{T}}^{\text{ref}}$. This vector is projected onto a Cartesian coordinate system in the transverse plane (ψ, υ), where the υ-axis is defined to be along the direction that bisects the angle $\Delta\phi_{12}$ between the two jets, and the ψ-axis is defined to have a direction that minimizes the angle to the probe jet as illustrated in Fig. 15. Both effects from the detector (response and resolution) and from physics (e.g. radiation) are present in the ψ component of the p_{T} balance that is oriented "towards" the probe jet axis, whereas detector effects should be significantly smaller than physics effect in the υ component, oriented "away" from both the probe and the reference jet. As a result [7], the jet energy resolution for events in a given $p_{\text{T}}^{\text{avg}}$ bin where both jets are in the reference region ($|\eta_{\text{det}}^{\text{probe}}| < 0.8$) is given by

$$\left\langle \frac{\sigma_{p_{\text{T}}}}{p_{\text{T}}} \right\rangle_{\text{ref}} = \frac{\sigma_\psi \ominus \sigma_\upsilon}{p_{\text{T}}^{\text{avg}} \sqrt{2\,\langle|\cos\Delta\phi_{12}|\rangle}}, \tag{15}$$

and for events where the probe jet is outside the reference region it is given by

$$\left\langle \frac{\sigma_{p_{\text{T}}}}{p_{\text{T}}} \right\rangle_{\text{probe}} = \frac{\sigma_\psi \ominus \sigma_\upsilon}{p_{\text{T}}^{\text{avg}} \sqrt{\langle|\cos\Delta\phi_{12}|\rangle}} \ominus \left\langle \frac{\sigma_{p_{\text{T}}}}{p_{\text{T}}} \right\rangle_{\text{ref}}. \tag{16}$$

The standard deviations σ_υ and σ_ψ are evaluated as the width parameters of Gaussian fits to the $p_{\text{T}\upsilon}$ and $p_{\text{T}\psi}$ distributions, respectively.

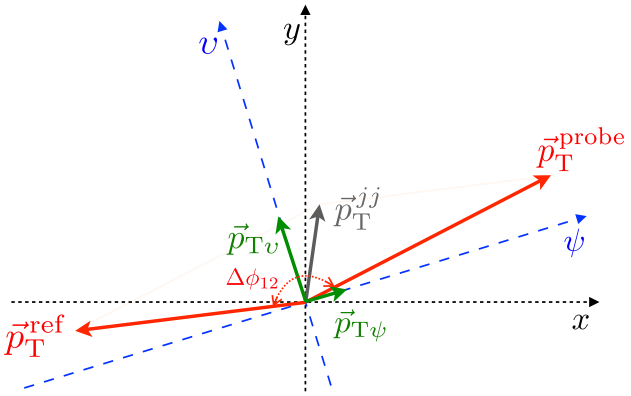

Fig. 15 Illustration of observables used in the dijet bisector technique. The (ψ, υ)-coordinate system is defined such that the υ-axis bisects the azimuthal angle $\Delta\phi_{12}$ between the leading two jets while the ψ-axis minimizes the angle to the probe jet. The vectorial sum of the transverse momenta of the probe and the reference jets define the dijet transverse momentum $\mathbf{p}_{\mathrm{T}}^{jj}$. Its components along the ψ- and υ-axes ($p_{\mathrm{T}\psi}$ and $p_{\mathrm{T}\upsilon}$) are used to extract a measurement of the jet energy resolution

Although the bisector observables in Eqs. (15) and (16) have less dependence on soft quark or gluon emission than the asymmetry-based jet resolution measurement of Eq. (13), the approach relies on the assumption that the physics effects are the same in the ψ and υ components. Corrections to the measured σ_ψ and σ_υ are made by subtracting the corresponding quantities derived using truth-particle jets in quadrature from the measured quantity, analogously to what is done for the central reference method (Eq. (14)).

6.3 Dijet selection

Dijet events are selected using a combination of central ($|\eta_{\mathrm{det}}| < 3.2$) and forward ($|\eta_{\mathrm{det}}| > 3.2$) jet triggers. For this selection, the trigger efficiency for each region of $p_{\mathrm{T}}^{\mathrm{avg}}$ is greater than 99% and approximately independent of the pseudorapidity of the probe jet. The jet triggers used have different *prescales*, downscaling factors used to meet bandwidth constraints on the recording of data. Larger prescales are used for data recorded when the instantaneous luminosity is high or for triggers that require lower jet p_{T}. Due to the different prescales for the central and forward jet triggers, the data collected by the different triggers correspond to different integrated luminosities. Each data event is assigned a trigger based on the $p_{\mathrm{T}}^{\mathrm{avg}}$ and η_{det} of the more forward jet. The data is hence split into different categories, and each is weighted according to the integrated luminosity of the dedicated trigger used following the "exclusion method" [57]. Events are selected in which there are at least two jets with $p_{\mathrm{T}} > 25$ GeV and $|\eta_{\mathrm{det}}| < 4.5$. To select events with a dijet topology, the azimuthal angle between the two leading jets (i.e., the reference and probe jets) is required to be $\Delta\phi_{12} > 2.5$ and events are rejected if they contain a third jet with $p_{\mathrm{T}}^{\mathrm{j3}} > 0.4\, p_{\mathrm{T}}^{\mathrm{avg}}$. The jets are also required to fulfil the preselection described in Sect. 4.1.

6.4 Method for evaluating in situ systematic uncertainties

The in situ techniques rely on assumptions that are only approximately fulfilled, and simulation is used to account for these approximations. For example, the momentum balance between the jet and the reference object is altered to varying degrees by the presence of additional radiation. The impact from such radiation is reduced by event topology selection criteria. Since the choice of the exact threshold values is arbitrary, systematic uncertainties are evaluated by rederiving the final result, which is a data-to-MC ratio, after varying these selection criteria. Other systematic uncertainties are evaluated by altering choices used by the method, such as a parameter used in a fit or changing the MC generator. In the case of the γ+jet, Z+jet, and multijet techniques (Sects. 7 and 8), uncertainties are also established by adjusting the kinematic properties (energy, p_{T}, etc.) of the reference object according to their associated uncertainties. These variations test the ability of the MC simulation to model the physics effects since they either reduce or amplify their importance.

Many potential effects are considered as systematic uncertainty sources. As explained above, each of these is evaluated by introducing a variation to the analysis. However, due to limited statistics in both the data and MC samples, these variations have an associated statistical uncertainty (i.e. an "uncertainty on the uncertainty"). For example, an introduced variation that has no impact on the measured calibration factor (or resolution) still produces changes consistent with statistical fluctuations. Thus, it is important to only include statistically significant variations as systematic uncertainties. This is achieved with a two-step procedure outlined below.

In the first step, the statistical uncertainty of the systematic variations is evaluated in each p_{T} bin using pseudo-experiments, following the "bootstrapping" method [58]. Each such pseudo-experiment is constructed by altering the data and MC samples. Each event is counted n times, where n is sampled from a Poisson distribution with a mean of unity. For each pseudo-experiment i, both the nominal $c_{\mathrm{nom},i}$ and varied $c_{\mathrm{var},i}$ results are extracted, and the uncertainty is evaluated as the difference between these results $\Delta c_{\mathrm{var},i} = c_{\mathrm{var},i} - c_{\mathrm{nom},i}$. If the variation is a change in the selection criteria or a change of the calibration or resolution smearing of any of the objects, the random fluctuations of the events that stay in the same bin are the same between the nominal and varied samples, while the events that migrate between bins will have independent fluctuations. The statistical uncertainty of the systematic uncertainty amplitude is evaluated as the standard deviation of the systematic uncertainty (difference between varied and nominal result) of the pseudo-experiments.

In a second step, adjacent p_{T} bins might iteratively be combined until the observed variation is statistically significant. If the variation already is significant with the original binning, it is recorded as a systematic uncertainty. Otherwise, neighbouring bins are merged, which results in improved statistical precision. After each bin-merging, it is checked if the systematic variation is significant, and if so, it is recorded as a systematic uncertainty. If after all bins are merged, the variation is still not significant, the systematic effect is considered consistent with zero and is discarded.

For some systematic variations, there are physics reasons for the response to depend on p_{T}, such as the out-of-cone effects being relatively larger at low p_{T}. In such cases, the bin merging step is not performed for the nominal uncertainty evaluation, but it is considered within alternative uncertainty scenarios (Sect. 9.4).

The use of the pseudo-experiments and the bin merging procedure strongly reduces the effect of statistical fluctuations when evaluating systematic uncertainties. This procedure is used for all the in situ methods discussed in this paper.

6.5 Relative jet energy scale calibration using dijet events

The following sections detail the determination of the intercalibration aimed at achieving a uniform scale for jets as a function of pseudorapidity.

6.5.1 Comparison of matrix and central reference methods

Figure 16 compares the relative jet response calculated using the matrix method with that obtained from the central reference method. The relative response obtained from the matrix method differs slightly from that from the central reference method, most notably in the forward regions where the difference is up to 4%. This is not surprising since the matrix method uses a significantly larger pool of events that have different kinematics (smaller rapidity separation) than the ones used by the central reference method. The same shift appears in both data and MC simulation, resulting in consistent data-to-MC ratios between the two methods. For 25 GeV $\leq p_{\mathrm{T}}^{\mathrm{avg}} <$ 40 GeV the statistical precision of the matrix method generally exhibits a 40% improvement compared with the precision of the central reference method. The level of improvement decreases with increasing $p_{\mathrm{T}}^{\mathrm{avg}}$ and is typically less than 10% for $p_{\mathrm{T}}^{\mathrm{avg}} >$ 400 GeV. Since the final η intercalibration is derived using data-to-MC ratios that are found to be consistent between the methods and the matrix method gives significantly smaller uncertainties, the matrix method is chosen, and hereafter all η intercalibration results presented are derived using this method.

6.5.2 Comparison of data with simulation

Figure 17 shows the relative response as a function of η_{det} for data and the MC simulations for four $p_{\mathrm{T}}^{\mathrm{avg}}$ regions. Figure 18 shows the relative response as a function of $p_{\mathrm{T}}^{\mathrm{avg}}$ for two representative η_{det} bins, namely $-1.5 \leq \eta_{\mathrm{det}} < -1.2$ and $2.1 \leq \eta_{\mathrm{det}} < 2.4$. The general features of the response in data are reproduced reasonably well by the SHERPA and POWHEG + PYTHIA8 predictions. Furthermore, the theoretical predictions are in good agreement with each other, with a much smaller spread than that observed in the previous studies using PYTHIA8 and HERWIG++ [6], because the new theoretical predictions are accurate to leading order in perturbative QCD for variables sensitive to the third jet's activity, such as the dijet balance, whereas the PYTHIA8 and HERWIG++ predictions rely on the leading-logarithm accuracy of the parton shower algorithms.

6.5.3 Derivation of residual jet energy scale correction

The residual calibration factor c_η is derived from the ratio of data and SHERPA η-intercalibration factors, i.e. $c_{\eta,i} = c_i^{\mathrm{data}}/c_i^{\mathrm{SHERPA}}$. The calibration factors from many bins of $p_{\mathrm{T}}^{\mathrm{avg}}$ and η_{det} are combined into a smooth function using a two-dimensional Gaussian kernel [6]. The kernel-width parameters of this function are chosen to capture the shape of the MC-to-data ratio across p_{T} and η_{det}, and at the same time provide stability against statistical fluctuations. The resulting residual correction c_η is shown as a black line in the lower panels of Figs. 17 and 18. In these panels, it can also be seen that the calibration function is fixed for η_{det} and p_{T} regions that extend beyond the data measurements. The same freezing of the calibration is also done for $|\eta_{\mathrm{det}}| > 2.7$ since the generator dependence becomes larger in this region. Measurements in these forward regions are not used to derive the intercalibration but are used when assessing the uncertainty.

6.5.4 Systematic uncertainties

All intercalibration systematic uncertainties are derived as a function of p_{T} and $|\eta_{\mathrm{det}}|$ with no uncertainty assigned in the reference region ($|\eta_{\mathrm{det}}| < 0.8$). No statistically significant difference is observed for positive and negative η_{det} for any of the uncertainties, justifying the parameterization versus $|\eta_{\mathrm{det}}|$, which increases the statistical power in the uncertainty evaluation.

The difference between SHERPA and POWHEG + PYTHIA8 is used to assess the physics modelling uncertainty. Both of these generators are accurate to leading order in QCD for variables sensitive to the modelling of the third jet (such as the dijet balance). Since there is no a priori reason to trust one generator over the other, the difference between the two

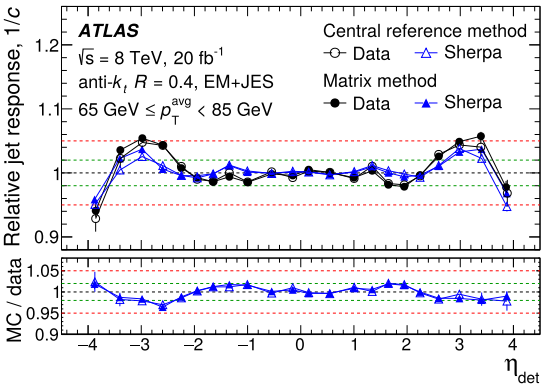

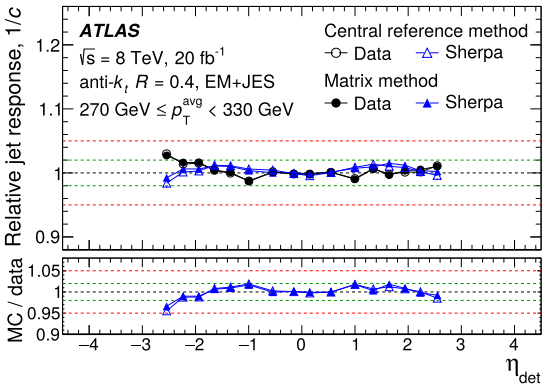

Fig. 16 Relative jet response measured using the matrix and central reference methods for anti-k_t jets with $R = 0.4$ calibrated with the EM+JES scheme as a function of the probe jet pseudorapidity. Results are presented for $65\text{GeV} \leq p_{\mathrm{T}}^{\mathrm{avg}} < 85$ GeV and $270\text{GeV} \leq p_{\mathrm{T}}^{\mathrm{avg}} < 330\text{GeV}$ for data (circles) and SHERPA (triangles) using the central reference method (empty symbols) and the matrix method (filled symbols). Only statistical uncertainties are shown. The dashed lines in the lower panels indicate 1 ± 0.02 and 1 ± 0.05

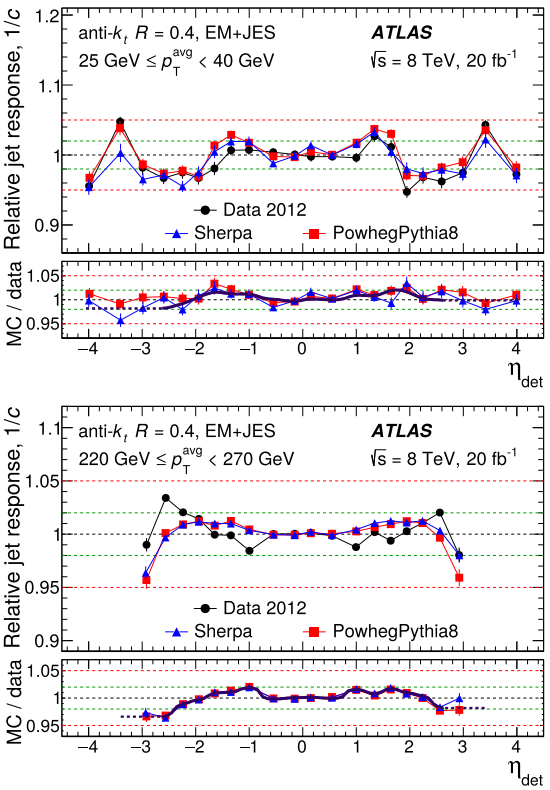

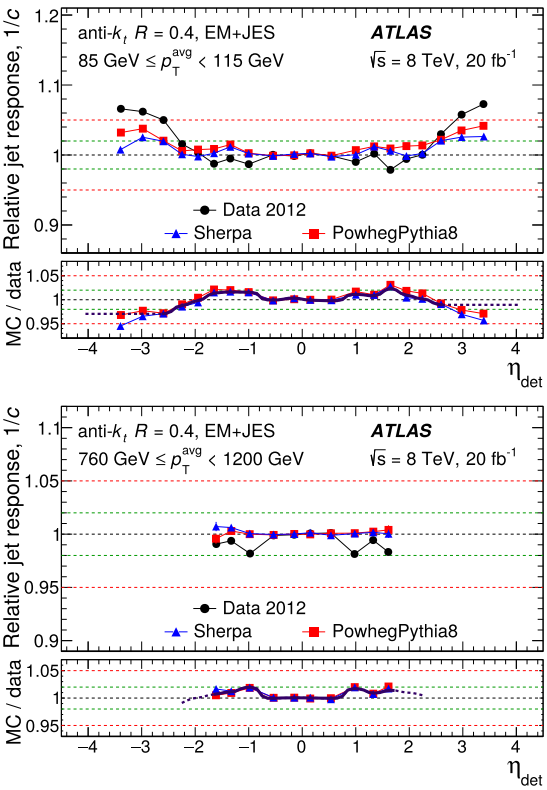

Fig. 17 Relative jet response, $1/c$, as a function of the jet pseudorapidity for anti-k_t jets with $R = 0.4$ calibrated with the EM+JES scheme, for data (black circles), SHERPA (blue triangles) and POWHEG+PYTHIA8 (red squares). Results are shown separately for 25 GeV $< p_{\mathrm{T}}^{\mathrm{avg}} <$ 40 GeV, 85 GeV $< p_{\mathrm{T}}^{\mathrm{avg}} <$ 115 GeV, 220 GeV $< p_{\mathrm{T}}^{\mathrm{avg}} <$ 270 GeV and 760 GeV $< p_{\mathrm{T}}^{\mathrm{avg}} <$ 1200 GeV with associated statistical uncertainties. The lower part of each figure shows the ratio of relative response in MC simulation to that in data, while the thick line indicates the resulting residual correction. The dashed part of this line represents the extrapolation of the ratio into regions which are either statistically limited or probe $|\eta_{\mathrm{det}}| > 2.7$. These measurements are performed using the matrix method. The dashed lines in the lower panels indicate 1 ± 0.02 and 1 ± 0.05

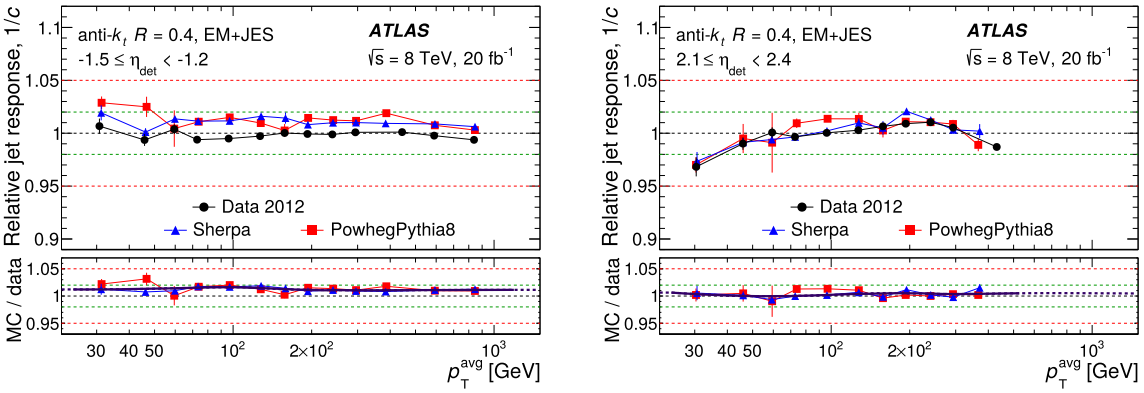

Fig. 18 Relative jet response, $1/c$, as a function of the jet p_T for anti-k_t jets with $R = 0.4$ calibrated with the EM+JES scheme, separately for $-1.5 \leq \eta_{det} < -1.2$ and $2.1 \leq \eta_{det} < 2.4$, for data (black circles), SHERPA (blue triangles) and POWHEG+PYTHIA8 (red squares). The lower parts of the figures show the ratios of MC simulation to data relative response, while the thick line indicates the resulting residual correction. The dashed part of this line represents the extrapolation of the ratio into regions which are statistically limited. The dashed lines in the lower panels indicate 1 ± 0.02 and 1 ± 0.05

predictions is used to estimate the modelling uncertainty. For $0.8 \leq |\eta_{det}| < 2.7$, where data are corrected to the SHERPA predictions, the full difference between POWHEG+PYTHIA8 and SHERPA is taken as the uncertainty.[4] For $|\eta_{det}| \geq 2.7$, where the calibration is frozen, the uncertainty is taken as the maximum difference between the extrapolated calibration and the prediction from either POWHEG+PYTHIA8 or SHERPA. The use of these event generators results in a substantial improvement in the agreement between the theoretical predictions, thus reducing the modelling-based uncertainty by a factor of approximately two relative to the previous result [6]. Despite the improvement, this modelling uncertainty remains the largest systematic uncertainty in the measurement.

The physics modelling uncertainty in the relative response is cross-checked using truth-particle jets by varying the POWHEG+PYTHIA8 predictions. The QCD renormalization and factorization scales in the POWHEG BOX are each varied by factors of 0.5 and 2.0, which has a significantly smaller impact on the relative response than the difference between the POWHEG+PYTHIA8 and SHERPA predictions. A comparison of the relative response between the POWHEG+HERWIG sample and the POWHEG+PYTHIA8 sample is also performed and is similar to the truth-particle jet relative response between POWHEG+PYTHIA8 and SHERPA. The assigned uncertainty from the difference between SHERPA and POWHEG+PYTHIA8 is a good reflection of the underlying physics modelling uncertainty.

The event topology selection requires $\Delta\phi_{12} > 2.5$ and $p_T^{j3} < 0.4\, p_T^{avg}$. To assess the influence of these selection criteria on the MC modelling of the p_T balance, the residual calibration is rederived after shifting the $\Delta\phi_{12}$ selection by ± 0.3 radians and the radiation criteria based on the fractional p_T of a potential third jet by ± 0.1. The maximum difference between the rederived calibration after the up and down shifts to the nominal is taken as uncertainty. To assess the impact of pile-up, the calibration is rederived in subsets split into high and low μ ($\mu < 14$ and $\mu \geq 17$), and high and low N_{PV} subsets ($N_{PV} < 9$ and $N_{PV} \geq 11$). The uncertainty due to pile-up effects is taken to be the maximum fractional difference between the varied and nominal calibrations. Similarly, an uncertainty due to the JVF requirement is derived by redoing the calibration after tightening and loosening the JVF criteria following the procedure defined in Ref. [51]. These variations account for the extent to which JVF is mis-modelled for jets originating from the primary interaction vertex. An uncertainty due to imperfect modelling of the jet energy resolution is also assigned by smearing the jet four-momenta in MC simulation using Gaussian random sampling with a standard deviation calculated from the JER data-to-MC difference. The difference between the calibrations obtained with nominal and smeared simulation is taken as the uncertainty due to JER effects.

The total systematic uncertainty is the sum in quadrature of the various components mentioned. Figure 19 presents a summary of the uncertainties as a function of $|\eta_{det}|$ for two representative values of jet transverse momentum, namely $p_T = 35$ GeV and $p_T = 300$ GeV. The uncertainties have a strong pseudorapidity dependence, increasing with η_{det}, and have a weaker p_T-dependence, decreasing with increasing jet p_T.

[4] The full difference between the generators is considered the uncertainty amplitude of a two-sided systematic uncertainty. All uncertainty components discussed in this paper are treated as two-sided uncertainties.

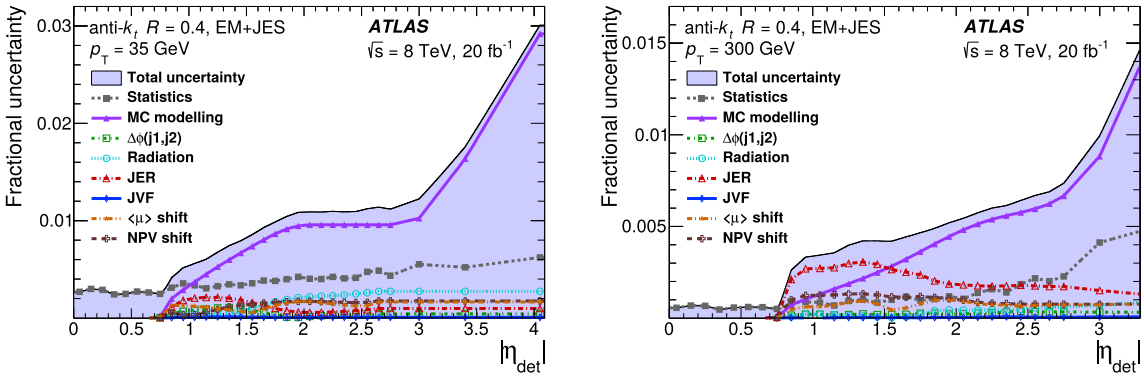

Fig. 19 Summary of uncertainties in the intercalibration as a function of the jet η_{det} for anti-k_t jets with $R = 0.4$ calibrated with the EM+JES scheme, separately for $p_{\text{T}} = 35$ GeV (left) and $p_{\text{T}} = 300$ GeV (right). The individual components are added in quadrature to obtain the total uncertainty. The MC modelling uncertainty is the dominant component for jets with $|\eta_{\text{det}}| > 1.5$

6.6 Jet energy resolution determination using dijet events

Figure 20 shows the measured relative jet energy resolution as a function of $p_{\text{T}}^{\text{avg}}$ for EM+JES calibrated jets in different η_{det} regions of the calorimeter. The results are presented for both the dijet balance and bisector methods, and there is good agreement between the methods for all values of $p_{\text{T}}^{\text{avg}}$ and $|\eta_{\text{det}}|$. The jet energy resolution in simulated events, determined as described in Sect. 4.2, is also shown as a dotted line and is in agreement with the measured JER in data.

6.6.1 Systematic uncertainties

The JER is determined in data by subtracting the truth-particle jet asymmetry from the measured asymmetry as discussed in Sect. 6.1. The truth-particle jet asymmetry is defined as the weighted average of the truth-particle jet asymmetries obtained for each of the SHERPA, POWHEG + PYTHIA8, PYTHIA8, and HERWIG++ event samples. The uncertainty in this weighted average is taken to be the RMS deviation of the truth-particle jet asymmetries obtained from the four event generators. This source of uncertainty is typically 0.02 at low $p_{\text{T}}^{\text{avg}}$ for both methods, falling to less than 0.01 at the highest $p_{\text{T}}^{\text{avg}}$.

Non-closure is defined as the difference between the jet resolution measured by the in situ method and the truth-particle jet resolution obtained by matching truth-particle and calorimeter jets (Sect. 4.2). This is treated as a systematic uncertainty in the method. The weighted average of the truth-particle jet asymmetries predicted by SHERPA, POWHEG + PYTHIA8, PYTHIA8, and HERWIG++ is subtracted in quadrature from the weighted average of the asymmetries evaluated for reconstructed calorimeter jets. The non-closure is typically about 10–15% for the bisector method, but it is larger for the dijet balance method, reaching 25% in some regions.

Finally, there are a number of systematic uncertainties that arise from experimental sources. The uncertainty in the JES calibration is investigated by shifting the energy of the jets by the $\pm 1\sigma$ uncertainty, with a typical effect between 5% and 10% at low $p_{\text{T}}^{\text{avg}}$. The uncertainty due to the choice of JVF selection has a less than 2% effect for both methods. The uncertainty due to the criterion on the azimuthal angle between the jets is investigated by changing the requirement by ± 0.3, with a negligible effect at high $p_{\text{T}}^{\text{avg}}$ for both methods, a small ($< 4\%$) effect on the dijet balance results at low $p_{\text{T}}^{\text{avg}}$ and a larger effect (5–15%) on the bisector results at low $p_{\text{T}}^{\text{avg}}$. The impact of the veto on the third jet is investigated by changing the selection criteria by ± 4 GeV, and is found to have a 10–15% effect at low $p_{\text{T}}^{\text{avg}}$ for both methods, falling to a few percent at higher $p_{\text{T}}^{\text{avg}}$ values.

The total systematic uncertainty, which is taken as the sum in quadrature of all sources discussed above, is shown as a dashed band around the points in Fig. 20.

7 Calibration and resolution measurement using γ + jet and Z + jet events

This section describes the determination of the final jet calibration that corrects the absolute energy scale of the jets to achieve a data-to-MC agreement within the associated uncertainties. The jet calibration is based on measurements conducted by in situ techniques that exploit the transverse momentum balance between a well-calibrated object and the hadronic recoil (jet). The well-calibrated object is either a photon or a Z boson that decays leptonically, either $Z \to ee$ or $Z \to \mu\mu$. Three separate datasets are used: $(Z \to ee)$+jet, $(Z \to \mu\mu)$+jet and γ+jet, and two different in situ techniques are used for each dataset, namely the *direct balance technique* (DB) and the *missing projection fraction method* (MPF). The three independent datasets and the two analy-

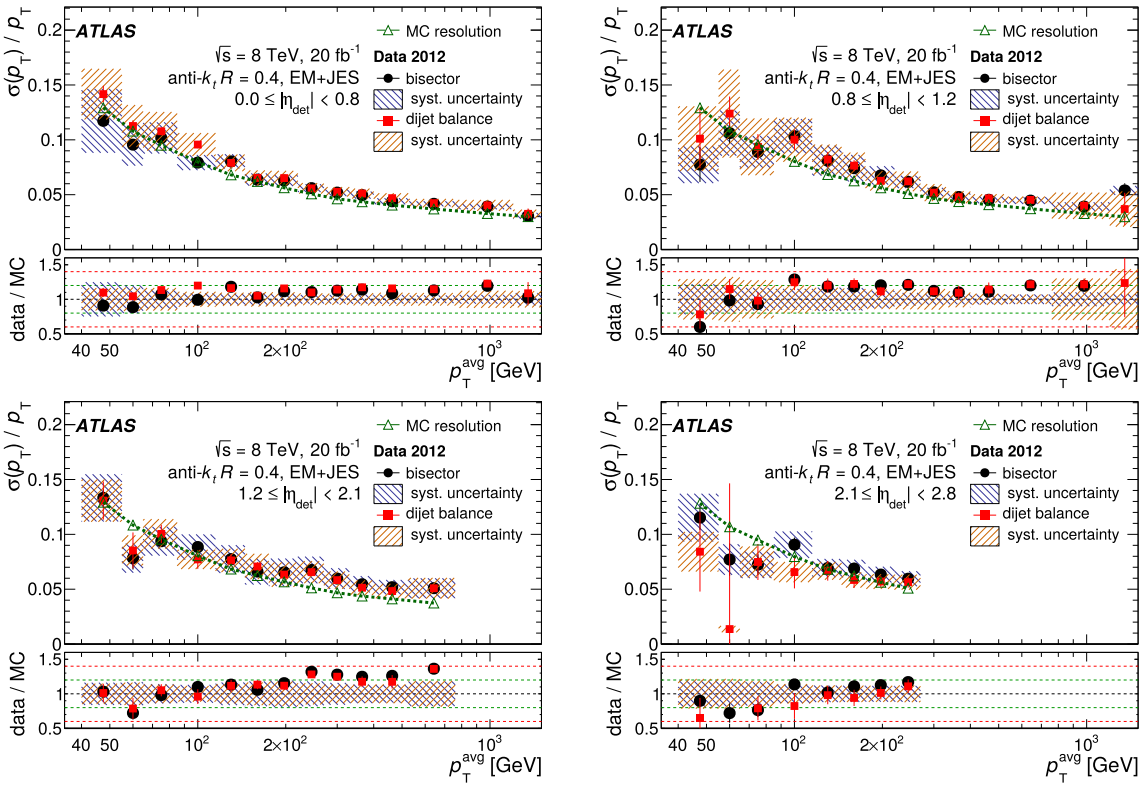

Fig. 20 Relative jet energy resolution obtained for EM+JES calibrated jets using the bisector (filled circles) and dijet balance (filled squares) methods, respectively. The MC simulated resolution derived from matching truth-particle jets with calorimeter jets is presented by the open triangles connected by dashed lines. The error bars reflect the statistical uncertainty while the hashed band indicates the total systematic uncertainty. Results are shown as a function of the jet p_{T} in four regions of detector pseudorapidity: $|\eta_{\mathrm{det}}| < 0.8$, $0.8 \leq |\eta_{\mathrm{det}}| < 1.2$, $1.2 \leq |\eta_{\mathrm{det}}| < 2.1$, and $2.1 \leq |\eta_{\mathrm{det}}| < 2.8$. The lower panels show the data-to-MC ratio, and the thin dashed lines indicate 1 ± 0.2 and 1 ± 0.4

sis methods provide six separate measurements of the jet calorimeter response that can be cross-checked with each other, allowing detailed studies of systematic uncertainties. For each dataset, the method that gives the smallest overall uncertainty is chosen and is used as input to the final combination of the absolute jet calibration (Sect. 9).

Due to the steeply falling Z boson p_{T} spectrum, the Z+jet data provide sufficient statistics to calibrate jets at lower p_{T} and are used in the range $17\,\mathrm{GeV} \leq p_{\mathrm{T}} < 250\,\mathrm{GeV}$. The Z boson four-momentum is reconstructed by four-vector addition of its decay products (leptons). The γ+jet process has a higher cross section and covers the jet p_{T} range $25\,\mathrm{GeV} \leq p_{\mathrm{T}} < 800\,\mathrm{GeV}$. However, at low p_{T} the photon sample has a large contamination from events that do not contain any true prompt photon and hence a sizeable systematic uncertainty. As discussed in Sect. 9.1, a combination of both the Z+jet and γ+jet channels covers the full momentum range $17\,\mathrm{GeV} \leq p_{\mathrm{T}} < 800\,\mathrm{GeV}$.

7.1 The direct balance and missing projection fraction methods

Both the DB and MPF methods exploit the momentum balance in events with γ+jet or Z+jet topology to study the jet calorimeter response. Both methods benefit from accurate knowledge of the energy scale and resolution of the boson (i.e. the photon or the dilepton system). The calibration of electrons and photons is accurately known through measurements using $Z \to ee$ data and other final states [44], while the muon reconstruction is determined to high precision through studies of $J/\Psi \to \mu\mu$, $Z \to \mu\mu$, and $\Upsilon \to \mu\mu$ [59].

The DB response R_{DB} is

$$R_{\mathrm{DB}} = \left\langle p_{\mathrm{T}}^{\mathrm{j1}} \,/\, p_{\mathrm{T}}^{\mathrm{ref}} \right\rangle, \quad \text{where } p_{\mathrm{T}}^{\mathrm{ref}} = p_{\mathrm{T}}^{Z/\gamma} \,|\cos\Delta\phi|\,, \tag{17}$$

where $p_{\mathrm{T}}^{\mathrm{j1}}$ is the p_{T} of the leading jet being probed and $\Delta\phi$ is the azimuthal angle between this jet and the boson (Z or γ). If the jet includes all the particles that recoil against the Z boson or γ and all particles are perfectly measured, then $p_{\mathrm{T}}^{\mathrm{j1}} \,/\, p_{\mathrm{T}}^{\mathrm{ref}} = 1$ and $\cos\Delta\phi = \cos\pi = -1$. In reality, there is always additional QCD radiation not captured by the jet,

which skews the balance. This radiation, referred to as out-of-cone radiation (OOC), tends to be in the same hemisphere as the jet and hence biases the DB to values below unity. The reference transverse momentum $p_{\mathrm{T}}^{\mathrm{ref}}$ used in the denominator of R_{DB} is the boson momentum projected onto the jet axis in the transverse plane in order to attempt to at least partially reduce OOC effects. The DB is also affected by uncertainties in the reconstructed photon, electron, or muon momenta, as well as contributions from pile-up and multiple parton–parton interactions (the underlying event).

The MPF method [5,60] is an alternative to the DB technique. Rather than balancing the jet object itself against the well-measured boson, the whole hadronic recoil is used. The MPF measures the response for the full hadronic recoil, which is significantly less sensitive to OOC radiation and effects due to pile-up and the underlying event. The logic of the MPF method is detailed below for γ+jet events. The case of Z+jet is the same with the Z boson replacing the photon.

From conservation of transverse momentum, the p_{T} vector of the system of all hadrons produced in a γ+jet event, $\mathbf{p}_{\mathrm{T}}^{\mathrm{recoil}}$, will perfectly balance the photon $\mathbf{p}_{\mathrm{T}}^{\gamma}$ at the truth-particle level. In a perfect $2 \to 2$ process, $\mathbf{p}_{\mathrm{T}}^{\mathrm{recoil}}$ would be equal to the $\mathbf{p}_{\mathrm{T}}$ of the parton, which in turn is that of the jet. At reconstruction level, the p_{T} of the photon (or Z boson) is well calibrated and hence accurately reconstructed, while the hadronic response is low prior to calibration, primarily due to the non-compensating nature of the ATLAS calorimeters.[5]. There is hence a momentum imbalance, which defines the missing transverse momentum $\mathbf{E}_{\mathrm{T}}^{\mathrm{miss}}$:

$$\begin{aligned} \mathbf{p}_{\mathrm{T,truth}}^{\gamma} + \mathbf{p}_{\mathrm{T,truth}}^{\mathrm{recoil}} &= \mathbf{0} \quad \text{(truth-particle level)} \\ \mathbf{p}_{\mathrm{T}}^{\gamma} + \mathbf{p}_{\mathrm{T}}^{\mathrm{recoil}} + \mathbf{E}_{\mathrm{T}}^{\mathrm{miss}} &= \mathbf{0} \quad \text{(detector level)}. \end{aligned} \tag{18}$$

Projecting the vector quantities of Eq. (18) onto the direction of the photon $\hat{n}_{\gamma}$ and dividing the result by p_{T}^{γ} gives the MPF observable r_{MPF}, whose mean is the MPF response R_{MPF}, where

$$r_{\mathrm{MPF}} = -\frac{\hat{n}_{\gamma} \cdot \mathbf{p}_{\mathrm{T}}^{\mathrm{recoil}}}{p_{\mathrm{T}}^{\gamma}} = 1 + \frac{\hat{n}_{\gamma} \cdot \mathbf{E}_{\mathrm{T}}^{\mathrm{miss}}}{p_{\mathrm{T}}^{\gamma}} \quad \text{and}$$
$$R_{\mathrm{MPF}} = \left\langle 1 + \frac{\hat{n}_{\gamma} \cdot \mathbf{E}_{\mathrm{T}}^{\mathrm{miss}}}{p_{\mathrm{T}}^{\gamma}} \right\rangle. \tag{19}$$

The $E_{\mathrm{T}}^{\mathrm{miss}}$ definition used in Eqs. (18) and (19) is based on the calibrated momentum of the photon (or dilepton system for Z+jet data) using topo-clusters at the constituent scale, either at the EM-scale when studying the EM+JES calibration or at the LCW-scale for the LCW+JES calibration. Details of the ATLAS $E_{\mathrm{T}}^{\mathrm{miss}}$ reconstruction are in Ref. [61].

[5] The hadronic recoil is reconstructed at the constituent scale, for which the calorimeter response can have a significant energy dependance as can be seen in Fig. 4.

The MPF response R_{MPF} provides a measure of the p_{T} response of the calorimeter to the hadronic recoil for a given p_{T}^{γ}. A feature of this method is that it is almost independent of the jet algorithm as the jet definition enters only in the event selection criteria applied (Sect. 7.2). Except for two relatively small corrections known as the *topology* and *showering corrections* (Sect. 7.3.4.2), the R_{MPF} determined in γ+jet or Z+jet events can be used as an estimator of the calorimeter jet response at pile-up-subtracted scale (Sect. 4.3.2). This is because pile-up is independent of both the hard interaction and the azimuth ϕ, and so its contribution to $\hat{n}_{\gamma} \cdot E_{\mathrm{T}}^{\mathrm{miss}}$ will be zero on average, meaning that R_{MPF} already effectively subtracts the pile-up as is done for jets using Eq. (2). Since R_{MPF} is an approximation of the pile-up-subtracted jet response, it can be compared with the corresponding quantity of the MC-derived calibration in Fig. 4 that defines $1/c_{\mathrm{JES}}$.

The R_{DB} and R_{MPF} parameters are determined in bins of $p_{\mathrm{T}}^{\mathrm{ref}}$ (Eq. (17)) from the mean parameter extracted from fits to the balance distributions ($p_{\mathrm{T}}^{\mathrm{j1}}/p_{\mathrm{T}}^{\mathrm{ref}}$ and r_{MPF}) using a *Modified Poisson* distribution, which was also used in the previous ATLAS jet calibration [6]. This distribution starts from a standard Poisson distribution $f_{\mathrm{P}}(n;\nu)$ and is extended to non-integer values using a Gamma function $\Gamma(n+1)$, followed by the introduction of a new parameter s used to redefine the argument using $x = s^2 n$ and defining $\mu \equiv E[x] = s^2 \nu$, giving

$$f_{\mathrm{MP}}(x;\mu,s) = \frac{(\mu/s^2)^{x/s^2}}{\Gamma(x/s^2+1)} \frac{\mathrm{e}^{-\mu/s^2}}{s^2}. \tag{20}$$

This distribution has the same shape as a "smoothed" Poisson distribution with $\nu = \mu/s^2$ and has mean μ and standard deviation $\sqrt{\mu}\,s$. For larger values of μ/s^2 ($\gtrapprox 15$), it is very similar to a Gaussian distribution, while for lower values ($\mu/s^2 \lessapprox 5$) the longer upper tail of a Poisson distribution is prominent. The Modified Poisson function better describes the balance distributions and is motivated by the Poisson nature of sampling calorimeters.

The MPF and DB methods probe the calorimeter response to jets in a different way and are sensitive to different systematic effects. They therefore provide complementary measurements of the jet-energy scale. The explicit use of jets in the measurement of the jet response from DB makes this technique dependent on the jet reconstruction algorithm while the MPF technique is mostly independent of the jet algorithm, as explained above. Thus, in the following, when presenting MPF results, no jet algorithm is explicitly mentioned.

7.2 Event and object selection

This section outlines the event selection used for the DB and MPF analyses separately for the γ+jet and Z+jet datasets. The two methods have similar selections, but the restriction

on the subleading jet p_{T} (Sect. 7.2.3) is less stringent for the MPF method because it is less sensitive to QCD radiation.

7.2.1 Photon selection

The γ+jet data was collected using six different single-photon triggers, each with a different associated photon p_{T} threshold. The five lower-threshold triggers were prescaled, while only the highest-threshold trigger was not prescaled. A given γ+jet event was assigned to one of these triggers, based on the p_{T} of the leading photon reconstructed by the algorithm used in the high-level trigger. This mapping was created such that the trigger efficiency for each p_{T} range was at least 99%. The lowest-threshold trigger data has the largest associated prescale factor and is used for photons between 20 and 40 GeV, while the highest-threshold trigger, which was not prescaled, is used for $p_{\mathrm{T}} > 120$ GeV.

Reconstructed photons are required to satisfy strict identification criteria ensuring that the pattern of energy deposition in the calorimeter is consistent with that expected for a photon [62]. Photons are calibrated following the procedure in Ref. [44] and are required to have $p_{\mathrm{T}} > 25$ GeV and $|\eta| < 1.37$ such that they are fully contained within the electromagnetic barrel calorimeter. In order to suppress backgrounds from calorimeter signatures of hadrons misidentified as photons, an isolation criterion is further applied to all photons. The isolation transverse energy of a photon $E_{\mathrm{T}}^{\mathrm{iso}}$ is calculated from calorimeter energy deposits in a cone of size $\Delta R = 0.4$ around the photon, excluding the photon itself and the expected contribution from pile-up [62]. Photons are initially required to fulfil $E_{\mathrm{T}}^{\mathrm{iso}} < 3.0$ GeV. However, for events where the leading photon has p_{T} below 85 GeV, the contamination from misidentified photons is still large. Hence, more stringent criteria are applied as follows: $E_{\mathrm{T}}^{\mathrm{iso}} < 0.5$ GeV if $p_{\mathrm{T}}^{\gamma} < 45$ GeV, or else $E_{\mathrm{T}}^{\mathrm{iso}} < 1.0$ GeV if $p_{\mathrm{T}}^{\gamma} < 65$ GeV, and otherwise $E_{\mathrm{T}}^{\mathrm{iso}} < 2.0$ GeV if $p_{\mathrm{T}}^{\gamma} < 85$ GeV. Each event is required to have at least one photon fulfilling these criteria. In the very rare case of two such photons, the leading one is used.

7.2.2 Z boson selection

A typical Z boson selection is applied, starting by requiring dilepton triggers that were not prescaled during the data-taking period. For the $Z{\to}ee$ channel, the dielectron triggers requires two "`loose`" electrons, defined in Ref. [63], with $E_{\mathrm{T}} > 12$ GeV and $|\eta| < 2.5$. For the $Z{\to}\mu\mu$ channel, the trigger requires one "`tight`" and one "`loose`" muon, defined in Ref. [64], with $p_{\mathrm{T}} > 18$ GeV and $p_{\mathrm{T}} > 8$ GeV, respectively. The reconstructed electrons are required to fulfil "`medium`" quality requirements [65] and are calibrated as detailed in Ref. [44]. Electrons are required to have $p_{\mathrm{T}} > 20$ GeV and $|\eta| < 2.37$, excluding the barrel–endcap transition region $1.37 < |\eta| < 1.52$. Muons are reconstructed through the combination of trajectories and energy-loss information in several detector systems [59] and are required to have $|\eta| < 2.5$ and $p_{\mathrm{T}} > 20$ GeV. Each event is required to have exactly two reconstructed electrons or two muons with opposite charge. The invariant mass of the dilepton system $m_{\ell\ell}$ must then fulfil 80 GeV $< m_{\ell\ell} <$ 116 GeV, ensuring high $Z \to \ell\ell$ purity.

7.2.3 Jet and boson+jet topology selection

Jets are reconstructed and a preselection is applied, including standard JVF requirements, as described in Sect. 4.1. They are calibrated with all steps prior to the absolute in situ correction (Sect. 4.3). To avoid double counting of energy depositions, jets are required to be $\Delta R > 0.35$ from a photon for the γ+jet analysis or from any of the leptons in the Z+jet analysis for jets reconstructed with $R = 0.4$. The corresponding criterion is $\Delta R > 0.5$ for $R = 0.6$ jets.

The leading jet is required to have $|\eta_{\mathrm{det}}| < 0.8$ and p_{T} greater than 10 GeV for the Z+jet analysis and 12 GeV for the γ+jet analysis. To enforce a "boson+jet" topology and hence suppress additional QCD radiation, criteria are imposed on the azimuthal angle $\Delta\phi(Z/\gamma, \mathrm{j1})$ between the Z boson or photon and the leading jet and on the subleading jet transverse momentum $p_{\mathrm{T}}^{\mathrm{j2}}$, if such a jet is present. The DB analysis requires $\Delta\phi(Z/\gamma, \mathrm{j1}) > 2.8$ and $p_{\mathrm{T}}^{\mathrm{j2}} < \max(8\ \mathrm{GeV}, 0.1\, p_{\mathrm{T}}^{\mathrm{ref}})$ while the MPF analysis uses the criteria $\Delta\phi(Z/\gamma, \mathrm{j1}) > 2.9$ and $p_{\mathrm{T}}^{\mathrm{j2}} < \max(8\ \mathrm{GeV}, 0.3\, p_{\mathrm{T}}^{\mathrm{ref}})$. The subleading jet p_{T} is always defined using the jet collection reconstructed using $R = 0.4$, even when studying jets built using $R = 0.6$ or $R = 1.0$. For jets built using $R = 1.0$, $p_{\mathrm{T}}^{\mathrm{j2}}$ is defined as the p_{T} of the leading $R = 0.4$ jet that fulfils $\Delta R(\mathrm{j1}, \mathrm{j2}) > 0.8$, where "j1" refers to the leading $R = 1.0$ jet, i.e. the jet that is being probed. This ensures that the "j2" jet will have a significant proportion of its energy depositions outside of the large-R jet.

7.3 Jet response measurements using Z+jet and γ+jet data

Measurements of R_{DB} and R_{MPF} using both of the individual $Z \to \ell\ell$ datasets and the γ+jet dataset are discussed below. The subsequent combination of the $Z \to \ell\ell$ and γ+jet results into the final in situ calibration is detailed in Sect. 9.1.

The $Z{\to}ee$ and $Z{\to}\mu\mu$ analyses probe jets over the same kinematic space and use exactly the same $p_{\mathrm{T}}^{\mathrm{ref}}$ binning. Within each bin, the balance distributions $p_{\mathrm{T}}^{\mathrm{j1}}/p_{\mathrm{T}}^{\mathrm{ref}}$ and r_{MPF} agree between the channels for both the cores of the distributions (including their means) and their tails (including their standard deviations). The two datasets are combined into a $Z \to \ell\ell$ channel, which increases the statistical power of the

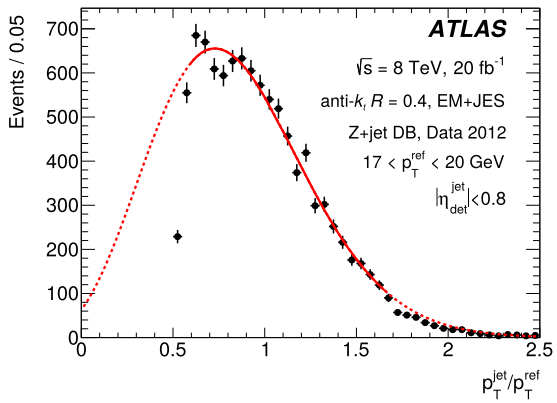

(a) Z+jet, $17\,\text{GeV} \leq p_{\text{T}}^{\text{ref}} < 20\,\text{GeV}$

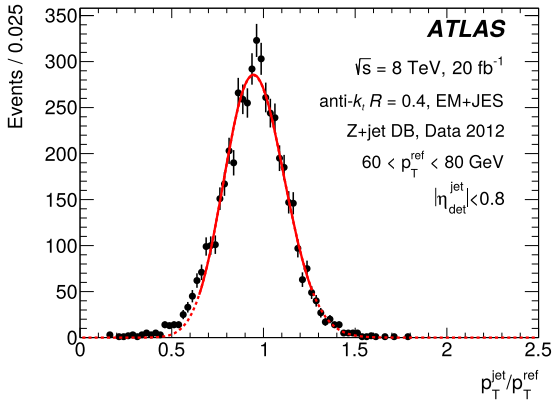

(b) Z+jet, $60\,\text{GeV} \leq p_{\text{T}}^{\text{ref}} < 80\,\text{GeV}$

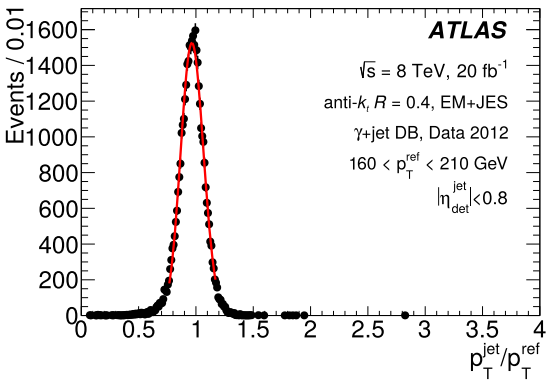

(c) γ+jet, $160\,\text{GeV} \leq p_{\text{T}}^{\text{ref}} < 210\,\text{GeV}$

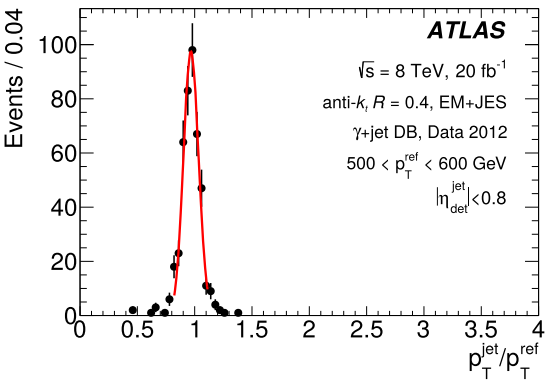

(d) γ+jet, $500\,\text{GeV} \leq p_{\text{T}}^{\text{ref}} < 600\,\text{GeV}$

Fig. 21 Distributions of $p_{\text{T}}^{\text{j1}}/p_{\text{T}}^{\text{ref}}$ for **a** $17\,\text{GeV} \leq p_{\text{T}}^{\text{ref}} < 20\,\text{GeV}$, **b** $60\,\text{GeV} \leq p_{\text{T}}^{\text{ref}} < 80\,\text{GeV}$, **c** $160\,\text{GeV} \leq p_{\text{T}}^{\text{ref}} < 210\,\text{GeV}$, and **d** $500\,\text{GeV} \leq p_{\text{T}}^{\text{ref}} < 600\,\text{GeV}$ using anti-k_t jets with $R = 0.4$ calibrated with the EM+JES scheme in data from the **a**, **b** Z+jet and **c**, **d** γ+jet analyses. The dashed lines in **a**, **b** show the fitted Modified Poisson distributions of Eq. (20), from which the means are taken as the DB response measurements R_{DB}. The solid lines indicate the fitting ranges. The lack of data at low $p_{\text{T}}^{\text{j1}}/p_{\text{T}}^{\text{ref}}$ visible in **a** is due to the $p_{\text{T}}^{\text{j1}} > 10\,\text{GeV}$ criterion. The markers are the data counts with error bars corresponding to the statistical uncertainties

measurement. This combination is done consistently for data and MC simulation, and also for systematic variations.

7.3.1 Direct balance results

Figure 21 presents four DB $p_{\text{T}}^{\text{j1}}/p_{\text{T}}^{\text{ref}}$ distributions in representative $p_{\text{T}}^{\text{ref}}$ bins from the Z+jet and γ+jet analyses using anti-k_t jets with $R = 0.4$ calibrated with the EM+JES scheme. Good fit quality using the Modified Poisson parameterization of Eq. (20) is observed. This is true for the other $p_{\text{T}}^{\text{ref}}$ bins considered, both for data and for all MC samples considered.

The value of R_{DB} is extracted for each $p_{\text{T}}^{\text{ref}}$ bin for both data and simulation. Figure 22 shows the measurements of R_{DB} in data compared with predictions from the different MC generators as a function of $p_{\text{T}}^{\text{ref}}$ for anti-k_t $R = 0.4$ jets calibrated with the EM+JES scheme. The different MC generators agree with data within 1% for $p_{\text{T}} > 40\,\text{GeV}$ with slightly worse agreement at lower p_{T}. The worst data-to-MC agreement is for EM+JES calibrated $R = 0.4$ jets in the $17\,\text{GeV} \leq p_{\text{T}}^{\text{ref}} < 20\,\text{GeV}$ bin (Fig. 22a), for which the POWHEG MC sample predicts ∼5% higher R_{DB} than what is observed in data. For LCW+JES calibrated $R = 0.4$ jets and $R = 0.6$ jets using both calibration schemes, the data-to-MC agreement is within 3% across the full $p_{\text{T}}^{\text{ref}}$ range probed.

For the γ+jet analysis, the measured responses agree within 1% with the MC predictions for $p_{\text{T}}^{\text{ref}} < 100$ GeV for both $R = 0.4$ and $R = 0.6$ jets using both calibration schemes. For jets with $p_{\text{T}}^{\text{ref}} > 100$ GeV, the MC simulation systematically tends to overestimate the measured response by approximately 1%.

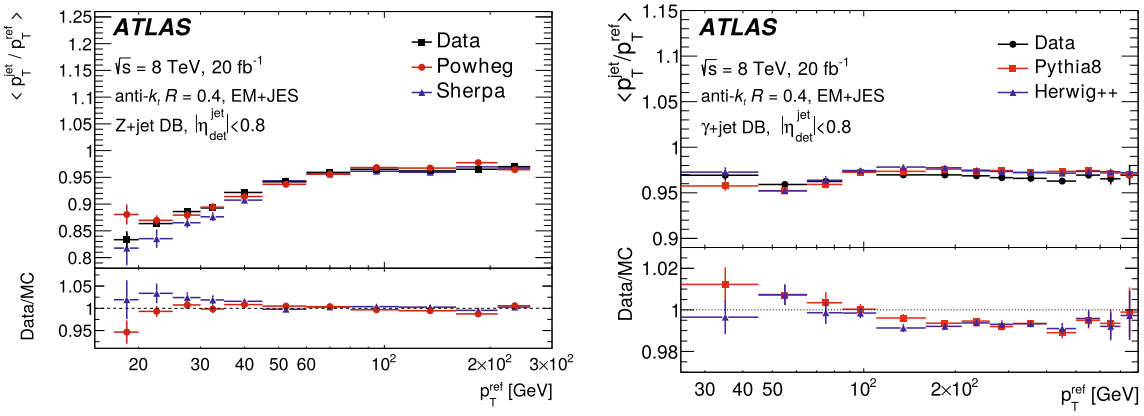

(a) $Z \to \ell\ell$+jet, anti-k_t $R = 0.4$ **(b)** γ+jet, anti-k_t $R = 0.4$

Fig. 22 R_{DB} for anti-k_t jets with $R = 0.4$ and calibrated with the EM+JES scheme from the **a** Z+jet and **b** γ+jet analyses in the data and for two MC simulations. Only statistical uncertainties are shown

7.3.2 *Validation of intercalibration of forward jets using Z+jet data*

The derived intercalibration in Sect. 6 corrects jets with forward rapidities $|\eta_{\mathrm{det}}| > 0.8$ by about 1−3% (Fig. 17). The total uncertainty in this calibration is presented in Fig. 19 and is typically below 1% for jets with $|\eta_{\mathrm{det}}| < 3$, increasing to about 3.5% for low-p_{T} jets with $|\eta_{\mathrm{det}}| > 4$.

To validate this calibration, the DB analysis is repeated for the jets with $0.8 \leq |\eta_{\mathrm{det}}| < 4.5$ using Z+jet events. As in the standard analysis (Sect. 7.2.3), the intercalibration is applied to the jets, and hence the data-to-MC ratio of R_{DB} is expected to be uniform versus η_{det} within the uncertainty assigned to the intercalibration. Results of this analysis for EM+JES calibrated anti-k_t $R = 0.4$ jets are presented in Fig. 23. The prediction of both MC generators agree with the data within the assigned uncertainties for jets with $0.8 \leq |\eta_{\mathrm{det}}| < 2.8$. For the region $|\eta_{\mathrm{det}}| > 2.8$, differences can be up to 7% as shown in Fig. 23; however, the statistical uncertainties of the $Z \to \ell\ell$ measurements are of similar magnitude. Hence, the results validate the derived dijet intercalibration.

7.3.3 *MPF results*

Figure 24 presents R_{MPF} calculated at both the EM and LCW scales as a function of $p_{\mathrm{T}}^{\mathrm{ref}}$ extracted using both the Z+jet and γ+jet events. As mentioned in Sect. 7.1, R_{MPF} is a measurement of the hadronic response of the calorimeter and does not include the MC-derived calibration c_{JES} nor the GS calibration c_{GS} (see Sects. 7.3.4.2 and 7.3.4.6 for further discussion on this). The "upturn" of R_{MPF} at low values of $p_{\mathrm{T}}^{\mathrm{ref}}$ visible in Fig. 24 is an expected artefact of the jet reconstruction threshold. Since a jet is required to be present in the event (Sect. 7.2.3), when this jet's p_{T} fluctuates low the event might fail the selection. For such an event, r_{MPF} will also tend to be low. And similarly, events with jets that fluctuate high in p_{T} will have high r_{MPF} and will pass the selection.

For the Z+jet analysis, the R_{MPF} measured in data is systematically about 1% below the prediction of POWHEG+PYTHIA8, considered the reference MC sample. For the γ+jet analysis, the predictions of R_{MPF} from both MC simulations agree across the full $p_{\mathrm{T}}^{\mathrm{ref}}$ range within the statistical precision. Both simulations systematically overestimate the R_{MPF} value measured in data by about 1% for $p_{\mathrm{T}}^{\mathrm{ref}} > 85$ GeV at the EM scale and by about 1% for $p_{\mathrm{T}}^{\mathrm{ref}} > 50$ GeV at the LCW scale.

7.3.4 *Systematic uncertainties*

The final JES calibration that is described in Sect. 9 is based on the data-to-MC ratio of the response measurements. As explained in detail in Sect. 6.4, systematic uncertainties in this quantity are evaluated by introducing variations to the analysis. The following seven sections present the evaluation of in total 17 uncertainty sources that affect the data-to-MC ratio of R_{DB} and R_{MPF}. These uncertainties assess various effects that can affect the response measurement, such as impact of additional QCD radiation, choice of MC generator, effects from out-of-cone radiation and pile-up, and the precision of the p_{T} scale of the reference objects (photons, electrons, or muons).

7.3.4.1 Suppression of additional radiation As explained in Sect. 7.2.3, a "boson+jet" topology is selected by imposing constraints on the azimuthal angle $\Delta\phi$ between the boson and the jet and by restricting the p_{T} of any subleading jet. These criteria reduce the impact from additional QCD radiation on the momentum balance between the jet and the boson. Systematic uncertainties from two sources are evaluated, one through varying the $\Delta\phi$ requirement and one through varia-

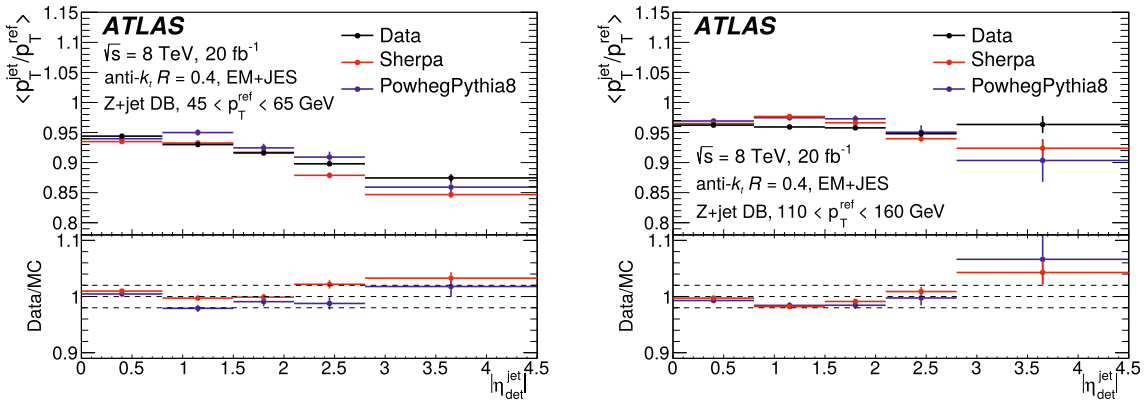

(a) $45\,\text{GeV} \leq p_{\text{T}}^{\text{ref}} < 65\,\text{GeV}$ **(b)** $110\,\text{GeV} \leq p_{\text{T}}^{\text{ref}} < 160\,\text{GeV}$

Fig. 23 R_{DB} as a function of η_{det} for anti-k_t jets with $R = 0.4$ calibrated with the EM+JES scheme in data (black), as well as in SHERPA (red) and POWHEG+PYTHIA8 (blue) simulation, for **a** $45\,\text{GeV} \leq p_{\text{T}}^{\text{ref}} < 65\,\text{GeV}$ and **b** $110\,\text{GeV} \leq p_{\text{T}}^{\text{ref}} < 160\,\text{GeV}$. Only statistical uncertainties are shown

tions of the p_{T}^{j2} selection. Constructing a single uncertainty component from variation in simulations of the two criteria is also considered (as was done previously [5]); however, the two-component approach is sufficient.

The $\Delta\phi$ selection is varied by ± 0.1 around the nominal values of 2.9 for MPF and 2.8 for DB (Sect. 7.2.3). The p_{T}^{j2} requirement for the DB analysis is similarly tightened to $\max(7\,\text{GeV}, 0.05\,p_{\text{T}}^{\text{ref}})$ and loosened to $\max(9\,\text{GeV}, 0.15\,p_{\text{T}}^{\text{ref}})$. The MPF selection is varied by similar amounts around the nominal selection. The resulting uncertainty from the $\Delta\phi$ variation is generally negligible. The uncertainty due to the p_{T}^{j2} requirement is 0.4% or smaller for $p_{\text{T}}^{\text{ref}} < 50\,\text{GeV}$ and is negligible above this value.

7.3.4.2 Systematic uncertainties due to out-of-cone radiation For the DB method, the p_{T} of a jet, even if perfectly calibrated, will always tend to be smaller than that of the photon or Z boson due to the out-of-cone radiation (Fig. 21). The impact of the out-of-cone radiation on R_{DB} is studied in both data and simulation by measuring the average p_{T} density of tracks as a function of the angular distance (ΔR) between the track direction and the leading jet axis. Based on this p_{T} profile, the fraction of the radiation outside the jet cone is estimated (see Section 9.4 of Ref. [6] for details), and an out-of-cone systematic uncertainty is evaluated on the basis of the simulation's ability to model the measured value of this quantity. The resulting uncertainty is as large as 2% at $p_{\text{T}}^{\text{ref}} = 40\,\text{GeV}$ and is smaller at higher $p_{\text{T}}^{\text{ref}}$.

In principle, the MPF technique does not depend on the OOC correction because the calorimeter response is integrated over the whole detector. However, two effects related to the OOC contribution must be considered. The "showering correction" quantifies the migration of energy across the jet boundary of the calorimeter jet relative to the truth-particle jet and is difficult to measure with data. This effect is included in the DB analysis by design since it is based on reconstructed jets but is not included for the MPF method since it measures the entire hadronic recoil. In addition, the hadronic response in the periphery of the jet is different than in the core because of the different energy densities and particle compositions. This "topology correction" is also difficult to extract from data but is expected to be small since the average p_{T} density around the jet axis decreases fairly rapidly, and only a small fraction of the p_{T} is outside the jet radius. MC studies have shown that the uncertainty in each of these corrections is significantly smaller than the DB OOC uncertainty. As a conservative approach, the OOC uncertainty measured in data for the DB case is used to estimate the contributions from showering and jet topology to the uncertainty in the JES determined using the MPF technique. The use of this larger uncertainty does not significantly affect the total systematic uncertainty in the JES from this analysis over most of the p_{T} range.

7.3.4.3 Impact of the Monte Carlo generator For each final state, predictions of the response observables (R_{DB} and R_{MPF}) are produced with two different MC generators: POWHEG and SHERPA for Z+jet and PYTHIA8 and HERWIG++ for γ+jet. As detailed in Sect. 3, these generators use different modelling of the parton shower, jet fragmentation, and multiple parton interactions. The difference in the data-to-MC ratio of the response between the generators is taken as a "generator" systematic uncertainty source. This is a reasonable estimate of the dependence of the pp collision modelling on R_{DB} and R_{MPF}, but a possible compensation by competing modelling effects cannot be excluded. This generator modelling constitutes the largest systematic uncertainty source for Z+jet for $p_{\text{T}}^{\text{ref}} \lesssim 50\,\text{GeV}$, where it can be as large as 2.5%.

7.3.4.4 Uncertainties associated with the reference objects The definitions of R_{DB} and R_{MPF} both have the p_{T} of the reference object in the denominator and are hence sensitive to

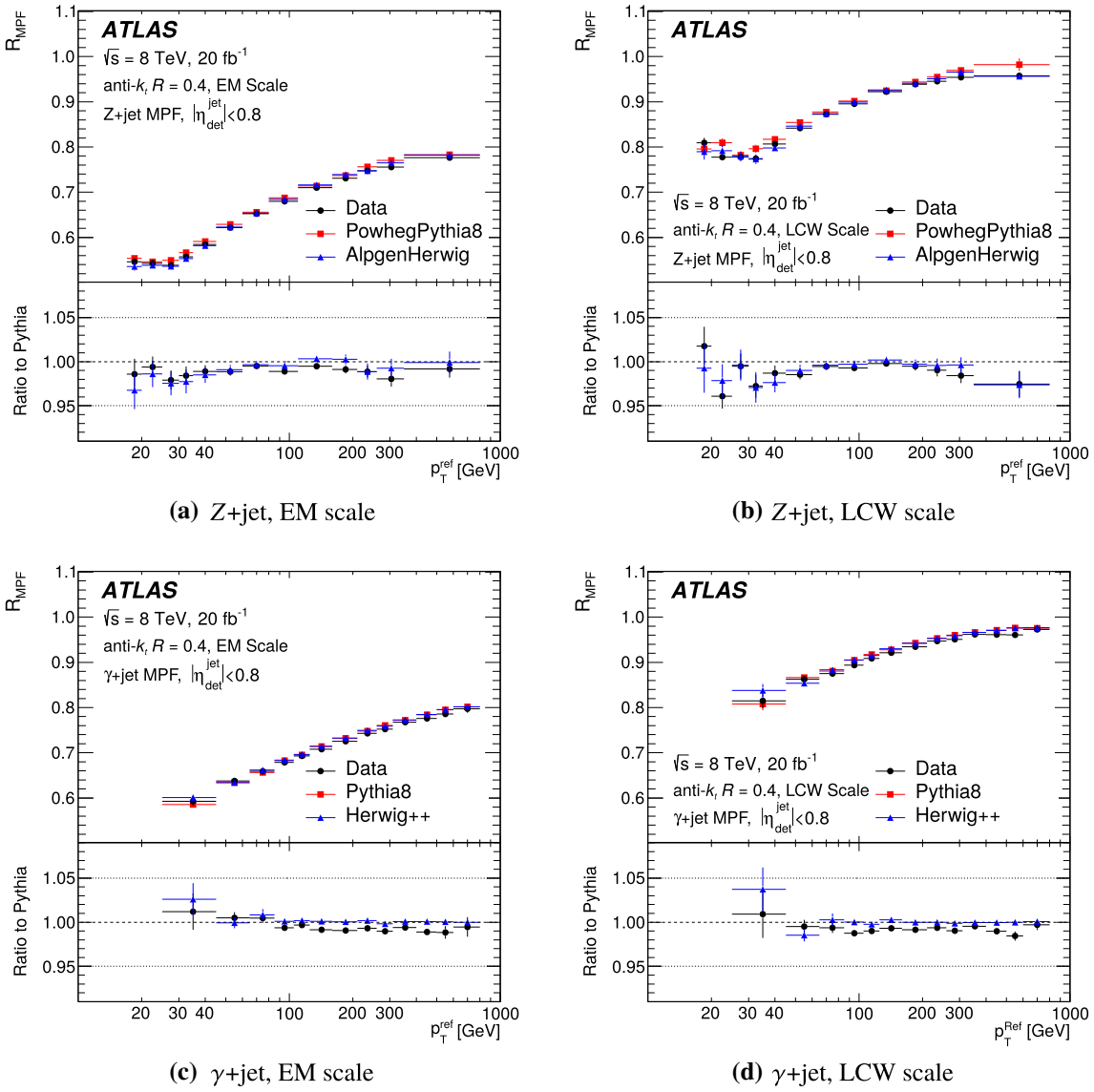

(a) Z+jet, EM scale **(b)** Z+jet, LCW scale

(c) γ+jet, EM scale **(d)** γ+jet, LCW scale

Fig. 24 The MPF response R_{MPF} in **a**, **b** $Z+$jet and **c**, **d** $\gamma+$jet events for jets calibrated **a**, **c** at the EM scale and **b**, **d** using the LCW scheme, for both data and MC simulation, as a function of $p_{\mathrm{T}}^{\mathrm{ref}}$. Only statistical uncertainties are shown

knowledge of its energy scale and resolution. For the $Z+$jet analyses, uncertainties in $p_{\mathrm{T}}^{\mathrm{ref}}$ arise from the precision of the electron energy scale (EES) and energy resolution (EER) and from the muon momentum scale (MMS) and resolution (MMR), while for $\gamma+$jet, uncertainties arise from the precision of the photon energy scale (PES) and energy resolution (PER).

The EES is measured in data [44] and has three uncertainty components: MC modelling of the $Z \rightarrow ee$ decay; the material description in simulation; and the response of the calorimeter's presampler. These are treated statistically independent of each other. The EER uncertainty is parameterized by a single component. The MMS and MMR are determined in data [59] and have one and two associated uncertainty components, respectively. Finally, the PES and PER are evaluated using extrapolation of EES and EER, and are hence affected by the same uncertainty sources. Hence, they have the same four uncertainty sources, but these affect photons and electrons quite differently.

Each of the 11 uncertainty sources are propagated to the simulated samples by adjusting the four-momenta of the reconstructed electron, muon, or photon. The uncertainties in R_{DB} and R_{MPF} are then evaluated following the procedure described in Sect. 6.4. For all objects, the resolution uncertainties are found to be negligible (0.1% or less). For $\gamma+$jet, the PES uncertainties are reasonably independent of $p_{\mathrm{T}}^{\mathrm{ref}}$ and their sum in quadrature amounts to 0.5–0.6%. The magnitudes of the EES and MMS uncertainties are less than 0.3%.

7.3.4.5 Impact of additional pile-up **interactions**
Jets produced in additional pile-up interactions are present in both data and simulation and might impact the response measurements. To study this effect, the JVF criterion is varied around its nominal value of 0.25 (Sect. 4.1). The JVF criteria used for this variation are based on studies presented in Ref. [51] and are 0.24 and 0.27 for EM+JES calibrated jets and are 0.21 and 0.28 for jets calibrated using LCW+JES.

Studies of the dependence of R_{DB} and R_{MPF} on the number of primary vertices N_{PV} in the event and on the average number of interactions per beam bunch crossing μ were also performed. Figure 25 presents results from these studies for the MPF method for a representative selection of $p_{\mathrm{T}}^{\mathrm{ref}}$ bins. The data-to-MC ratio of R_{MPF} is found to be independent of both N_{PV} and μ for all $p_{\mathrm{T}}^{\mathrm{ref}}$ bins. The same conclusion is reached for the DB analysis. Hence, only one pile-up uncertainty component is assigned, due to the pile-up mitigation using the JVF criterion.

7.3.4.6 Impact of lack of GS correction for the MPF method
The GS correction (Sect. 5) is based on the properties of jets. Since the MPF does not use jets directly, applying the GS correction in the standard way will have no impact on R_{MPF}. Instead, the GS correction factor c_{GSC} is extracted from the leading jet in each event and is used to adjust R_{MPF}. Two methods were tested: simply scaling R_{MPF} with c_{GSC} and recalculating R_{MPF} after adjusting $\mathbf{E}_{\mathrm{T}}^{\mathrm{miss}}$ by adding the change of the jet momentum vector due to the GS correction $(c_{\mathrm{GSC}}-1)\mathbf{p}_{\mathrm{T}}^{j1}$. Both methods result in a negligible change to the data-to-MC ratio of R_{MPF}, and no uncertainty is assigned for this effect.

7.3.4.7 Impact of background in the γ+jet **sample**
The γ+jet dataset suffers from non-negligible contamination from dijet events where one of the jets is misreconstructed as a photon. The purity, i.e. the fraction of actual γ+jet events, after the nominal selection is estimated using a "sideband" technique based on the event yields in different control regions defined by alternative photon isolation and identification criteria. This technique is described in detail in Refs. [5,62]. The purity increases with p_{T}^{γ}, being about 80% at $p_{\mathrm{T}}^{\gamma} = 85$ GeV and rising above 90% for $p_{\mathrm{T}}^{\gamma} \gtrsim 200$ GeV. The misreconstructed events tend to have higher $p_{\mathrm{T}}^{\mathrm{j1}}/p_{\mathrm{T}}^{\mathrm{ref}}$ and r_{MPF}. The difference in DB and MPF response between true γ+jet events and misreconstructed events is estimated by varying the photon identification criteria. The γ+jet MC samples used have perfect purity by definition. The uncertainty due to the contamination from dijet events in the γ+jet analyses was estimated by multiplying the fraction of misreconstructed events by the relative difference in response between γ+jet and misreconstructed events. The resulting uncertainty decreases with $p_{\mathrm{T}}^{\mathrm{ref}}$. For the DB analysis, it is ~3.5% at $p_{\mathrm{T}}^{\mathrm{ref}} = 35$ GeV, decreasing to 1% at $p_{\mathrm{T}}^{\mathrm{ref}} = 100$ GeV and to < 0.4% for $p_{\mathrm{T}}^{\mathrm{ref}} > 250$ GeV. For MPF, this uncertainty is smaller by approximately a factor of 2. This reduction is due to the definition of the observable, where R_{MPF} is inherently more stable against stochastically-oriented effects (pileup, fake photons, etc) compared to R_{DB} due to such contributions cancelling in R_{MPF} when averaged over many events.

7.3.4.8 Summary of the systematic uncertainties Figure 26 presents the JES uncertainties from various sources, evaluated for both the DB and MPF methods with anti-k_t $R = 0.4$ jets calibrated with the EM+JES using the Z+jet dataset. The total uncertainty is obtained by addition in quadrature of the uncertainties from different sources. Overall, the DB and MPF methods achieve similar levels of precision. The MC generator uncertainties dominate for $p_{\mathrm{T}}^{\mathrm{ref}} \lesssim 50$ GeV and the out-of-cone uncertainty is also significant for $p_{\mathrm{T}}^{\mathrm{ref}} \lesssim 80$ GeV. The statistical uncertainty is the major uncertainty for the Z+jet analyses at $p_{\mathrm{T}}^{\mathrm{ref}} > 200$ GeV.

Figure 27 shows the uncertainties for the corresponding γ+jet analyses. Here, the photon purity systematic uncertainty is the dominant uncertainty for the DB method for $p_{\mathrm{T}}^{\mathrm{ref}} < 100$ GeV, while it is significantly smaller and subdominant for MPF. The other systematic uncertainties are of similar magnitude for the two methods. For the range $100\,\mathrm{GeV} \le p_{\mathrm{T}}^{\mathrm{ref}} < 400\,\mathrm{GeV}$, the photon energy scale contributes the dominant uncertainty.

7.4 Calibration of large-R jets

For analyses based on pre-2012 data, the JES uncertainty of large-R jets has been evaluated in situ using track jets (Sect. 4.1) [45]. This method, discussed further in Sect. 9.5, is limited to 2–7% precision due to tracking uncertainties and the uncertainty in the charged-particle component of the jet. Furthermore, this method is restricted to the central calorimeter region $|\eta_{\mathrm{det}}| < 1.2$, since at more forward η_{det}, the large-R jet will not be fully contained in the acceptance of tracking detectors. This section presents an improved large-R jet JES uncertainty evaluation using γ+jet events.

7.4.1 R_{DB} measurements using γ + large-R jet events

The DB analysis is performed for large-R jets using the same approach as for small-R jets. The binning in $p_{\mathrm{T}}^{\mathrm{ref}}$ and η_{det} is different, chosen to account for the available data statistics, and $p_{\mathrm{T}}^{\mathrm{ref}}$ is defined simply as $p_{\mathrm{T}}^{\mathrm{ref}} \equiv p_{\mathrm{T}}^{\gamma}$ instead of projecting onto the jet axis (Eq. (17)). Examples of $p_{\mathrm{T}}^{\mathrm{j1}}/p_{\mathrm{T}}^{\mathrm{ref}}$ distributions fitted with the Modified Poisson function are shown in Fig. 28.

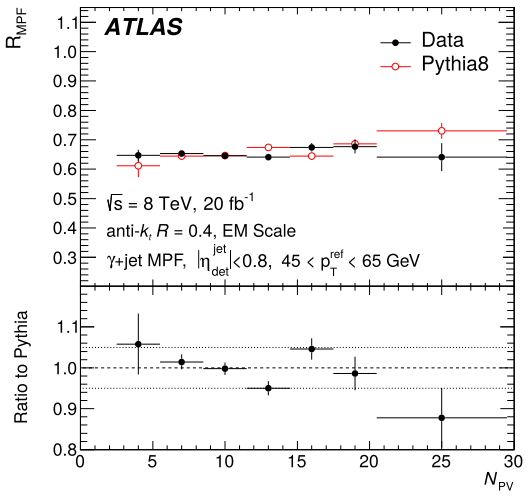

(a) N_{PV} dependence, $45\,\mathrm{GeV} \leq p_{\mathrm{T}}^{\mathrm{ref}} < 65\,\mathrm{GeV}$

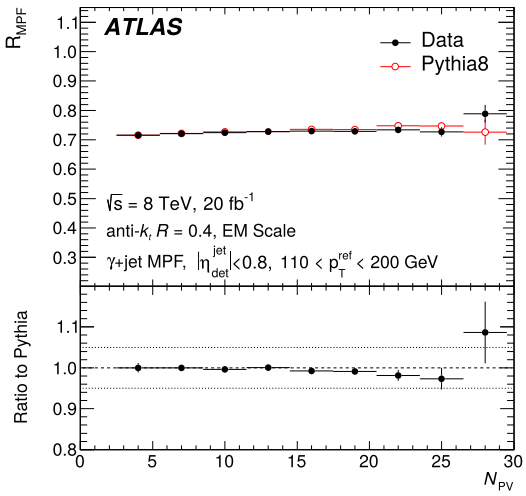

(b) N_{PV} dependence, $110\,\mathrm{GeV} \leq p_{\mathrm{T}}^{\mathrm{ref}} < 200\,\mathrm{GeV}$

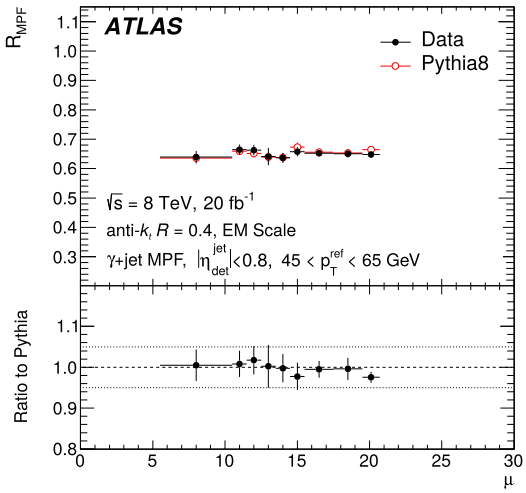

(c) μ dependence, $45\,\mathrm{GeV} \leq p_{\mathrm{T}}^{\mathrm{ref}} < 65\,\mathrm{GeV}$

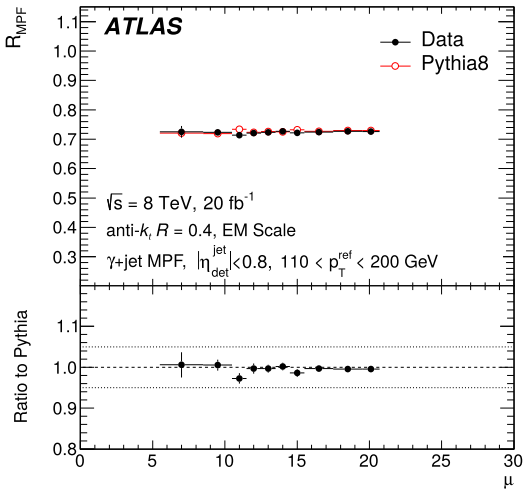

(d) μ dependence, $110\,\mathrm{GeV} \leq p_{\mathrm{T}}^{\mathrm{ref}} < 200\,\mathrm{GeV}$

Fig. 25 MPF response R_{MPF} in γ+jet events for jets calibrated at the EM scale for both data (black filled circles) and MC simulation (red empty circles), as a function of **a**, **b** N_{PV} and **c**, **d** μ for a reference p_{T} range of **a**, **c** $45\,\mathrm{GeV} \leq p_{\mathrm{T}}^{\mathrm{ref}} < 65\,\mathrm{GeV}$ and **b**, **d** $110\,\mathrm{GeV} \leq p_{\mathrm{T}}^{\mathrm{ref}} < 200\,\mathrm{GeV}$. Only statistical uncertainties are shown

Figure 29 presents R_{DB} as a function of $p_{\mathrm{T}}^{\mathrm{ref}}$ for large-R jets in two η_{det} ranges, both for data and MC simulations. The response in the central calorimeter region, $|\eta_{\mathrm{det}}| < 0.8$, is modelled within 1% by the simulation, with simulations tending to overestimate the response by ∼0.5%. For large-R jets with $0.8 < |\eta_{\mathrm{det}}| < 1.2$, this deviation grows to ∼2%. Rather than using this deviation as a calibration to correct for the difference between data and MC simulation, this difference is taken as an additional uncertainty. As detailed in Sect. 4.4, large-R jets do not receive any intercalibration c_η.

7.4.2 Systematic uncertainties

Most of the systematic uncertainties are evaluated in the same way as for small-R jets as detailed in Sect. 7.3.4. Additional uncertainties specific to large-R jets and changes to the evaluation of some of the uncertainty sources are detailed below.

- Rather than using the difference of the data-to-MC ratio of R_{DB} from unity as a calibration, it is instead taken as an uncertainty. This allows a straightforward combination with the procedure used to derive uncertainties outside of the kinematic range for which the γ + large-R jet R_{DB}

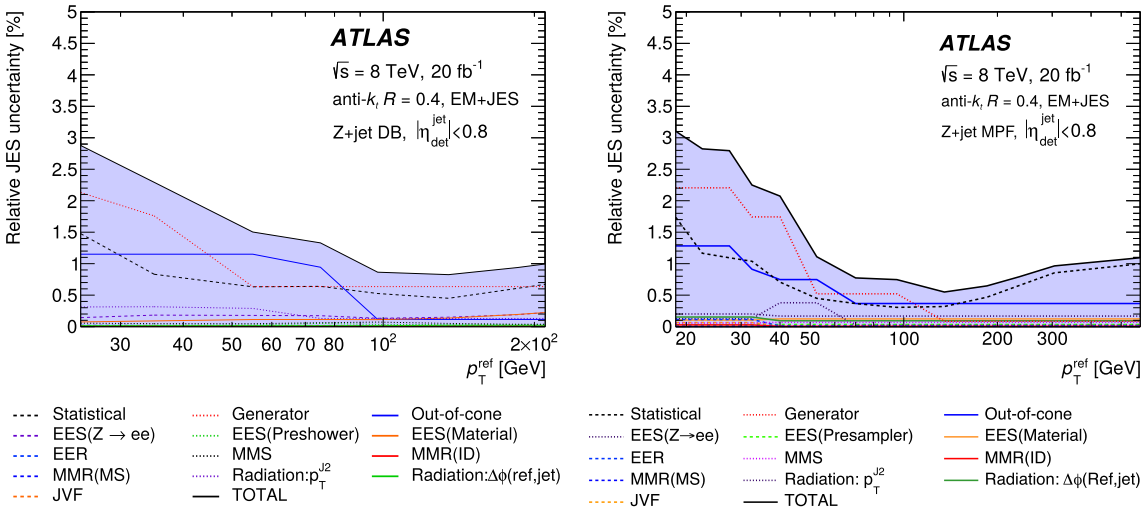

(a) Z+jet DB, anti-k_t $R = 0.4$, EM+JES **(b)** Z+jet MPF, anti-k_t $R = 0.4$, EM+JES

Fig. 26 Summary of the JES statistical and systematic uncertainties evaluated for the Z+jet **a** DB and **b** MPF analyses for anti-k_t jets with $R = 0.4$ and calibrated with the EM+JES scheme. The total uncertainty, shown as a shaded region, is obtained from the addition in quadrature of all uncertainty sources. EES/EER denotes the electron energy scale/resolution, while MMS/MMR denotes the muon momentum scale/resolution

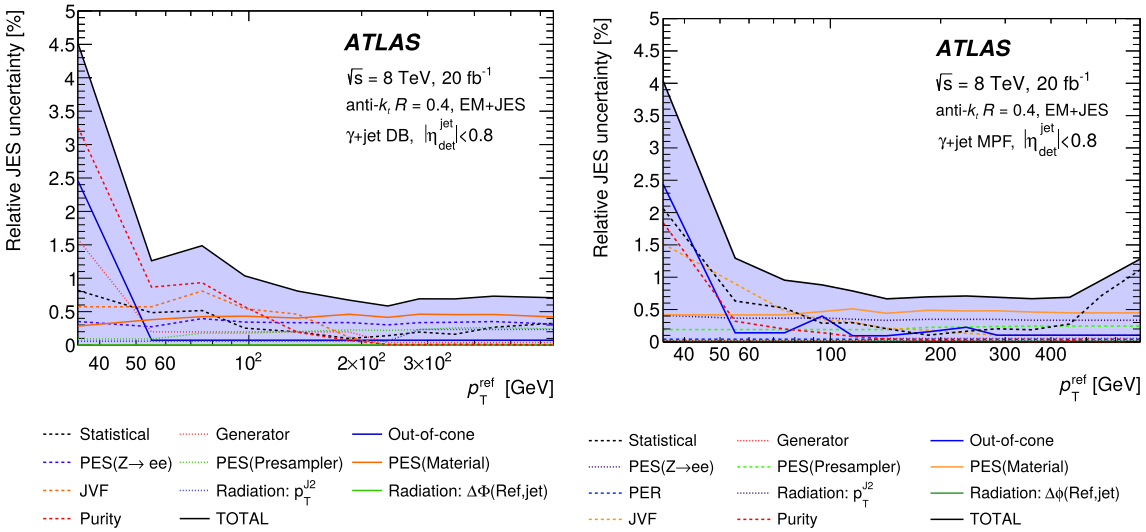

(a) γ+jet DB, anti-k_t $R = 0.4$, EM+JES **(b)** γ+jet MPF, anti-k_t $R = 0.4$, EM+JES

Fig. 27 Summary of the JES statistical and systematic uncertainties evaluated for the γ+jet **a** DB and **b** MPF analyses for anti-k_t jets with $R = 0.4$ and calibrated with the EM+JES scheme. The total uncertainty, shown as a shaded region, is obtained from the addition in quadrature of all uncertainty sources. PES denotes the photon energy scale, while PER denotes the photon energy resolution

can be derived. This is a significant uncertainty source, especially for jets with $0.8 \leq |\eta_{\text{det}}| < 1.2$.

- The OOC uncertainty is evaluated only for large-R jets with $|\eta_{\text{det}}| < 0.8$, since for other η_{det} bins the large-R jets are not always fully contained within the tracking acceptance. The uncertainty derived in this central η_{det} range is also applied to the more forward $|\eta_{\text{det}}|$ bins. Due to the large radius ($R = 1.0$), out-of-cone effects are very small, and the uncertainty is negligible for $p_{\text{T}} > 100$ GeV.
- As mentioned in Sect. 7.2.3, the subleading jet (labelled "j2") that is used to suppress additional QCD radiation is required to have an angular separation of $\Delta R(\text{j1}, \text{j2}) > 0.8$ from the large-R jet ("j1"). Since the leading jet has

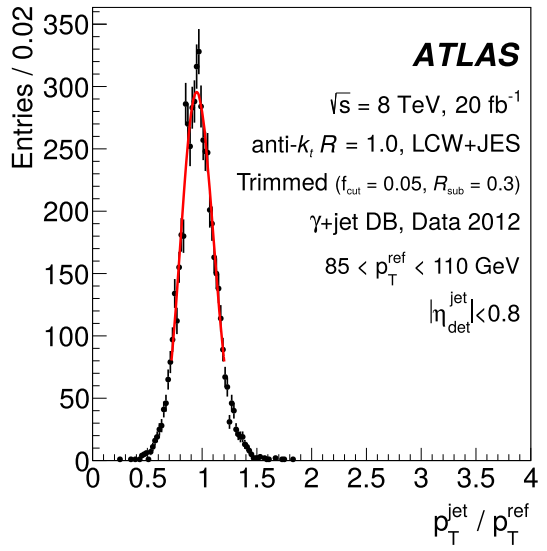

(a) $85\,\text{GeV} \leq p_{\text{T}}^{\text{ref}} < 110\,\text{GeV}$

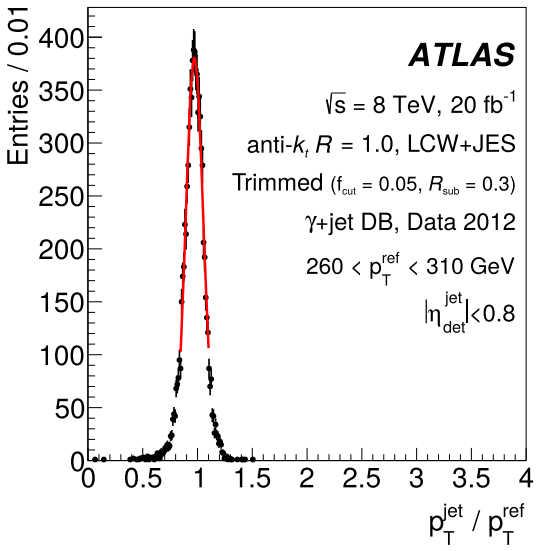

(b) $260\,\text{GeV} \leq p_{\text{T}}^{\text{ref}} < 310\,\text{GeV}$

Fig. 28 $p_{\text{T}}^{\text{j1}}/p_{\text{T}}^{\text{ref}}$ distributions for events with **a** $85\,\text{GeV} \leq p_{\text{T}}^{\text{ref}} < 110\,\text{GeV}$ and **b** $260\,\text{GeV} \leq p_{\text{T}}^{\text{ref}} < 310\,\text{GeV}$ for trimmed anti-k_t jets with $R = 1.0$ calibrated with the LCW+JES scheme in data. The lines present fits to the data of a Modified Poisson function (Eq. (20)). The markers show data with error bars corresponding to the statistical uncertainties

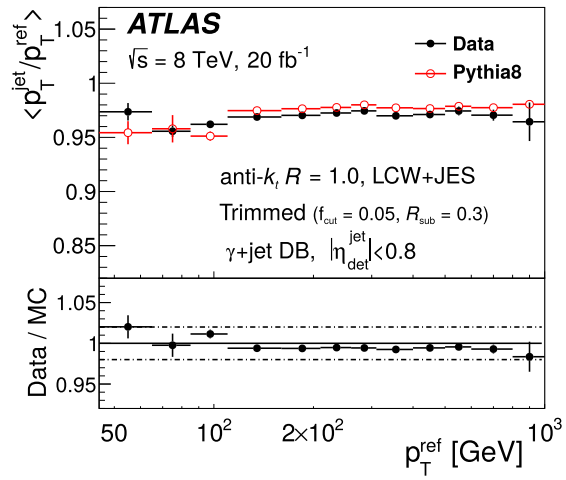

(a) R_{DB} vs p_{T}, $|\eta_{\text{det}}| < 0.8$

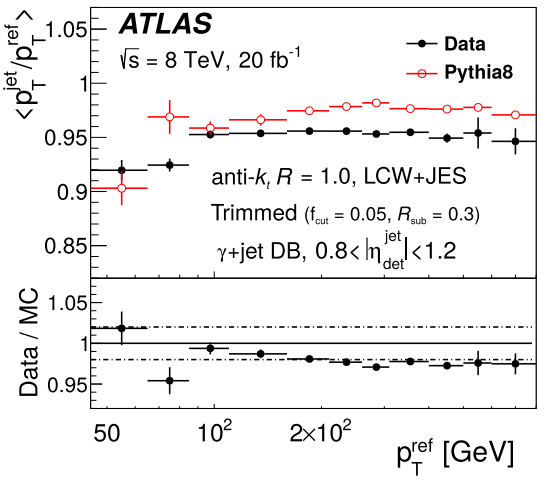

(b) R_{DB} vs p_{T}, $0.8 \leq |\eta_{\text{det}}| < 1.2$

Fig. 29 R_{DB} for trimmed anti-k_t jets with $R = 1.0$ calibrated with the LCW+JES scheme for **a** $|\eta_{\text{det}}| < 0.8$ and **b** $0.8 \leq |\eta_{\text{det}}| < 1.2$ for both data (filled circles) and MC simulation (empty circles), as a function of the $p_{\text{T}}^{\text{ref}}$. Only statistical uncertainties are shown

$R = 1.0$ while the subleading jet has $R = 0.4$, this means that there is a significant overlap in terms of solid angle, but since the p_{T} profile of jets tend to be narrow (see the $\mathcal{W}_{\text{trk}}$ distribution of Figs. 6 and 7), the amount of energy sharing is still expected to be small. The assigned uncertainty component is evaluated by changing the ΔR requirement from 0.8 to 1.4 to ensure that there is strictly no overlap between the two jets.

- Since the small-R jets are reconstructed independently of the large-R jets using the same topo-clusters as input, a large-R jet will sometimes contain two small-R jets close to the large-R jet axis. It is possible that events with such topologies have additional uncertainties due to the QCD modelling. To assess this effect, an alternative subleading jet selection was applied in which "j2" is defined simply as the subleading $R = 0.4$ jet, without any restriction based on the angle to the large-R jet. This means that "j2" will sometimes be within the large-R jet and sometimes not (the leading $R = 0.4$ jet tends to be aligned very close to the large-R jet axis). With this definition, the

event selection $p_{\mathrm{T}}^{\mathrm{j2}} < 0.1\, p_{\mathrm{T}}^{\mathrm{ref}}$ was applied in place of the standard $p_{\mathrm{T}}^{\mathrm{j2}}$ selection, and an uncertainty component was derived from the impact of this variation.
- An additional dependence of the jet response for large-R jets on the ratio of the jet mass to the p_{T}, m/p_{T}, is observed, particularly for large $|\eta_{\mathrm{det}}|$. A systematic uncertainty is assigned to account for this dependence, derived as a triple ratio. The data/MC ratios of the R_{DB} ratios are evaluated in the two m/p_{T} ranges shown in Fig. 30, corresponding to $m/p_{\mathrm{T}} < 0.15$ and $m/p_{\mathrm{T}} > 0.15$. The systematic uncertainty is given by the ratio of the double ratios obtained for the two m/p_{T} ranges.

7.4.3 Pile-up uncertainty for large-R jets

As discussed in Sect. 4.1, large-R jets do not receive any pile-up correction. Due to the trimming algorithm applied, large-R jets are significantly less sensitive to pile-up than standard small-R jets. To study the impact of pile-up on the large-R jet p_{T}, it is measured as a function of N_{PV} and μ in bins of p_{T} of track jets that are matched to the large-R jets being probed. Track jets are resilient to pile-up since they are built from inner-detector tracks that are matched only to the primary vertex, and do not contain contributions (tracks) from pile-up vertices (in most cases). The track jets are reconstructed using the same algorithm as the calorimeter large-R jets (trimmed anti-k_t $R = 1.0$).

Within a given track jet p_{T} bin, the large-R jets are expected to have a similar truth-particle jet p_{T}. The reconstructed p_{T} is studied as a function of N_{PV} and μ. The results for a representative track jet p_{T} bin is presented in Fig. 31. As expected (Eq. (2) and Ref. [6]) there is a linear dependence of the jet p_{T} on both N_{PV} and μ. For each track jet p_{T} bin, the "gradients" $\partial p_{\mathrm{T}}/\partial N_{\mathrm{PV}}$ and $\partial p_{\mathrm{T}}/\partial \mu$ are extracted from the slopes of a linear fits of p_{T} vs N_{PV} and p_{T} vs μ (Fig. 31). Figure 32 shows these gradients as a function of the average p_{T} of the large-R jets. Both of these graphs are well described with a function of the form $a + b \log(p_{\mathrm{T}}/p_{\mathrm{T},0})$, where the parameters a and b are extracted from a fit and $p_{\mathrm{T},0}$ is a constant chosen to be 50 GeV.

Based on the p_{T} parameterization of the gradients from the fits to data described in the previous paragraph (Fig. 32), two uncertainty components are derived that have the following impact on the jet p_{T}

$$\Delta_{N_{\mathrm{PV}}} = (\partial p_{\mathrm{T}}/\partial N_{\mathrm{PV}}) \left(N_{\mathrm{PV}} - N_{\mathrm{PV}}^{\mathrm{ref}}\right) \quad \text{and}$$
$$\Delta_{\mu} = (\partial p_{\mathrm{T}}/\partial \mu)(\mu - \mu^{\mathrm{ref}}), \tag{21}$$

where $\partial p_{\mathrm{T}}/\partial N_{\mathrm{PV}}$ and $\partial p_{\mathrm{T}}/\partial \mu$ are the gradients parameterized as a function of large-R jet p_{T} according to the fitted functions, μ is the average number of interaction per bunch crossing, and N_{PV} is the number of primary vertices of the event, and $\mu^{\mathrm{ref}} = 20.7$ and $N_{\mathrm{PV}}^{\mathrm{ref}} = 11.8$ are the average values for the full 2012 γ+jet dataset. As can be seen from Eq. (21), the impact on the jet p_{T} from the two uncertainty components can change sign depending on the amount of pile-up, and become zero for jets produced in events with pile-up conditions matching the 2012 average values. The resulting fractional p_{T} uncertainties are presented for two values of large-R jet p_{T} in Fig. 33.

7.4.3.1 Summary of systematic uncertainties Figure 34 presents a summary of the statistical and systematic uncertainties in the large-R jet p_{T} from the DB analysis, including a detailed breakdown of the uncertainty components that are in common with the small-R jet γ+jet measurements presented in Sect. 7.3.4, while the additional uncertainty sources specific to large-R jets are presented in Sect. 7.4.2. The total uncertainty for $|\eta| < 0.8$ is found to be ∼1% above 150 GeV, rising to ∼2% at 1 TeV. At larger $|\eta|$, the uncertainty increases to ∼2% at low $p_{\mathrm{T}}^{\mathrm{ref}}$, rising to ∼3% at 1 TeV. The uncertainties are dominated by the photon energy scale uncertainty, the uncertainty coming from the large-R jet response dependence on the ratio of m/p_{T}, and the difference of the data-to-MC R_{DB} from unity. The generator systematic uncertainty becomes dominant for $|\eta| > 1.2$.

7.5 Measurement of the jet energy resolution using the DB method

The width of the DB distribution in a given $p_{\mathrm{T}}^{\mathrm{ref}}$ bin is used to probe the JER. The detector resolution of the reference object is negligible compared with that of the jet, so the method to measure the JER using Z+jet and γ+jet events is significantly simpler than that for dijets described in Sect. 6. The event selection and binning is the same as for the R_{DB} measurements, but instead of determining the mean R_{DB} of the $p_{\mathrm{T}}^{\mathrm{j1}}/p_{\mathrm{T}}^{\mathrm{ref}}$ distribution within each $p_{\mathrm{T}}^{\mathrm{ref}}$ bin, the width $\sigma_{\mathrm{DB}}^{\mathrm{reco}}$ is extracted as the standard deviation of the same Modified Poisson fit. The relative JER σ_E/E is then estimated using

$$\frac{\sigma_E}{E} = \frac{\sigma_{p_{\mathrm{T}}}}{p_{\mathrm{T}}} = \sigma_{\mathrm{DB}}^{\mathrm{reco}} \ominus \sigma_{\mathrm{DB}}^{\mathrm{truth}}, \tag{22}$$

where the first equality holds to a good approximation since the contribution from the angular resolution is negligible, and the second relation follows from the same reasoning as for Eq. (14) (Sect. 6.1). The parameter $\sigma_{\mathrm{DB}}^{\mathrm{truth}}$ is obtained using a fit to the $p_{\mathrm{T}}^{\mathrm{truth}}/p_{\mathrm{T}}^{\mathrm{ref}}$ distribution extracted using MC simulation with same selection (applied to reconstructed jets) as for the DB measurement. For each simulated event, $p_{\mathrm{T}}^{\mathrm{truth}}$ is defined from the truth-particle jet that is ghost-matched (Sect. 4.2) to the leading reconstructed jet. The simulated JER is also extracted from the MC samples with fits to $p_{\mathrm{T}}^{\mathrm{reco}}/p_{\mathrm{T}}^{\mathrm{truth}}$ (Sect. 4.2).

Figure 35 presents a MC-based comparison between the relative JER obtained using the in situ technique applied to the simulated events (Eq. (22)) and the relative JER extracted

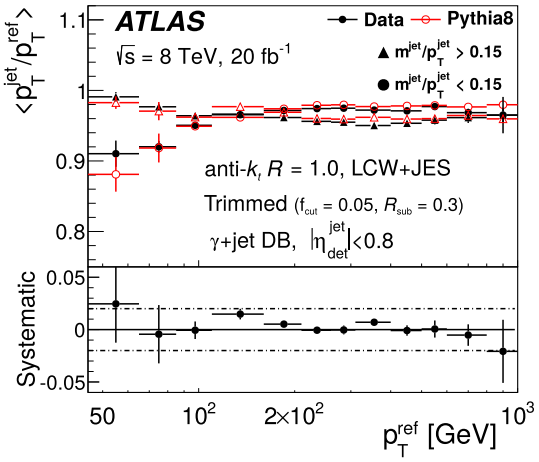

(a) Large-R jet mass dependence, $|\eta_{\text{det}}| < 0.8$

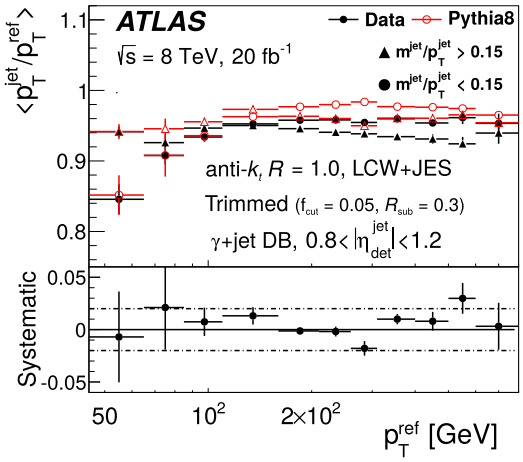

(b) Large-R jet mass dependence, $0.8 \leq |\eta_{\text{det}}| < 1.2$

Fig. 30 R_{DB} as a function of $p_{\text{T}}^{\text{ref}}$ measured for trimmed anti-k_t jets with $R = 1.0$ in γ+jet events shown separately for jets with **a** $|\eta_{\text{det}}| < 0.8$ and **b** $0.8 \leq |\eta_{\text{det}}| < 1.2$. Separate results are shown for jets with $m/p_{\text{T}} < 0.15$ and $m/p_{\text{T}} > 0.15$, displayed with circles and triangles, respectively. Measurements in data are shown as filled markers and MC predictions as open makers. Statistical uncertainties are shown for each point. The lower parts of the figures show the systematic uncertainty evaluated as the data-to-MC ratio of the ratios of R_{DB} extracted in the two m/p_{T} ranges

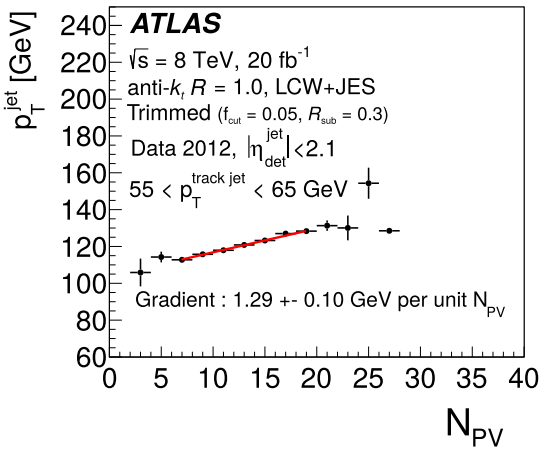

(a) Large-R jet p_{T} vs N_{PV}

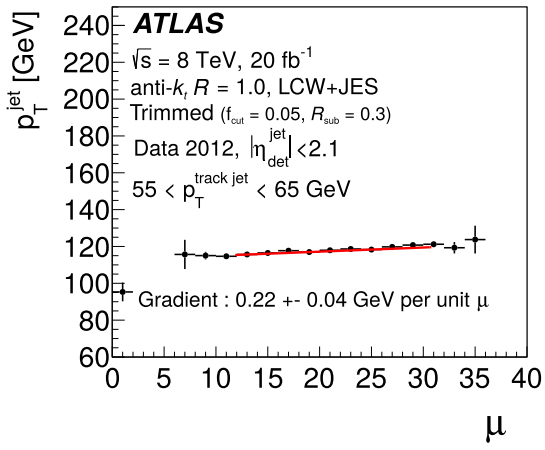

(b) Large-R jet p_{T} vs μ

Fig. 31 Large-R jet p_{T} as a function of **a** N_{PV} in γ+jet events with $20 < \mu < 22$, and as a function of **b** μ in events with $10 < N_{\text{PV}} < 12$. The $p_{\text{T}}^{\text{trackjet}}$ is required to be within $55 < p_{\text{T}}^{\text{trackjet}} < 65$ GeV. The lines are linear fits. The markers show data with error bars corresponding to the statistical uncertainties. The lowest point shown in **b** corresponds to special data-taking conditions, and is thus not expected to match the other points on the plot

from truth-particle jet matching. Over most of the p_{T} range probed, the in situ extracted JER agrees with the expectation from simulation within 10%, but for the first and last bins probed, the agreement is worse (20–40%). The difference between the measured and expected JER is taken as a "non-closure" systematic uncertainty.

The truth-particle jet DB width $\sigma_{\text{DB}}^{\text{truth}}$, used in the JER measurement (Eq. (22)) depends on details of the physics model implemented in the MC generator. A systematic "generator" uncertainty is evaluated to assess this dependence through taking the difference between the extracted JER using different MC generators. Other systematic uncertainty sources considered for the JER measurement are the same as those considered for the JES measurements discussed in Sect. 7.3.4 and are derived for the JER analogously. Figure 36 presents the resulting JER uncertainties for anti-k_t $R = 0.4$ jets and also the relative data-to-MC difference of the JER measurement. Results are reported as a function of $p_{\text{T}}^{\text{ref}}$, separately for the measurements performed using the Z+jet and γ+jet datasets. The total, relative JER uncertainty

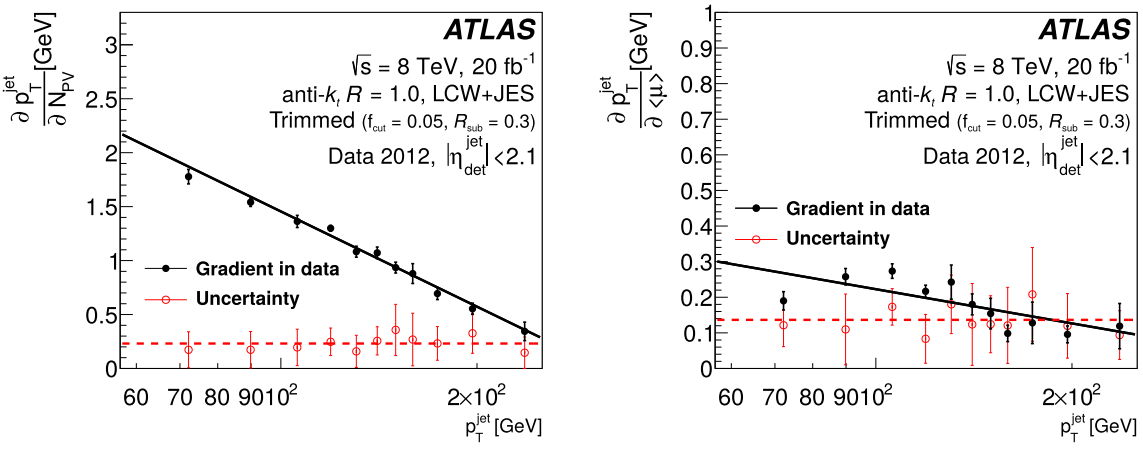

(a) $\partial p_{\mathrm{T}}/\partial N_{\mathrm{PV}}$ vs large-R jet p_{T} **(b)** $\partial p_{\mathrm{T}}/\partial \mu$ vs large-R jet p_{T}

Fig. 32 The gradients **a** $\partial p_{\mathrm{T}}/\partial N_{\mathrm{PV}}$ and **b** $\partial p_{\mathrm{T}}/\partial \mu$ extracted in γ + jet data (filled circles) and the difference of the gradients measured in data and MC simulations (empty circles) as functions of the large-R calorimeter jet p_{T}. The lines correspond to fits of a constant to the uncertainty (red dashed line) and a function of the form $a + b \log(p_{\mathrm{T}}/p_{\mathrm{T},0})$ with $p_{\mathrm{T},0} = 50$ GeV for the gradients vs p_{T} (black solid line). The error bars shown on the markers reflect the statistical uncertainty

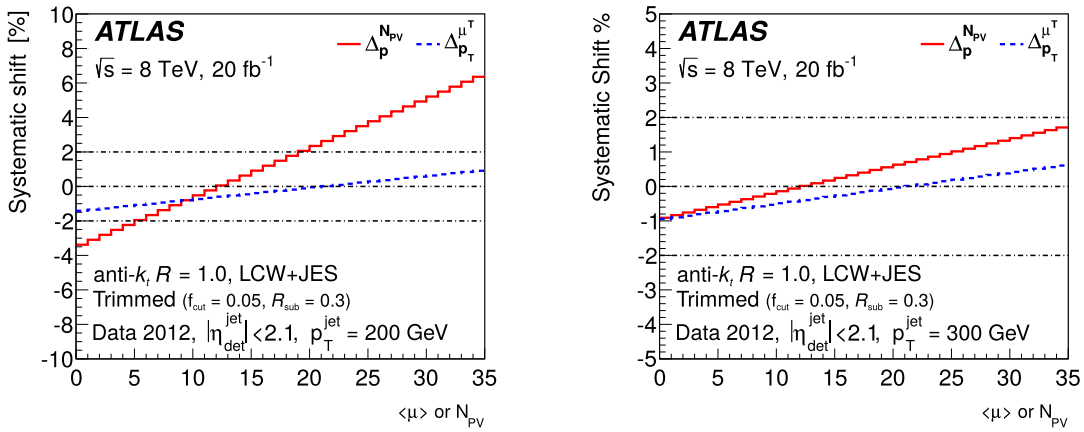

(a) Large-R jet pile-up uncertainties, $p_{\mathrm{T}} = 200$ GeV **(b)** Large-R jet pile-up uncertainties, $p_{\mathrm{T}} = 300$ GeV

Fig. 33 Systematic uncertainties due to the N_{PV} and μ dependence of the large-R jet p_{T} presented in percentage as functions of μ (dashed lines) and N_{PV} (solid lines) for large-R jets with **a** $p_{\mathrm{T}} = 200$ GeV and **b** $p_{\mathrm{T}} = 300$ GeV. Horizontal lines are added at 0% and ±2% to guide the eye

evaluated for the Z + jet JER measurements varies between 20 and 40%, depending on the algorithm and $p_{\mathrm{T}}^{\mathrm{ref}}$ values. Dominant sources of uncertainties include the choice of MC generator for the modelling of $\sigma_{\mathrm{DB}}^{\mathrm{truth}}$, the non-closure, and limited statistics. The JER uncertainty of the γ + jet measurement is slightly smaller than that from Z + jet events, varying between 10 and 30%. The dominant sources of systematic uncertainties are the choice of MC generator and the suppression of additional radiation. For $p_{\mathrm{T}}^{\mathrm{ref}} < 50$ GeV, the data-to-MC differences can be as large as ∼40%.

8 High-p_{T}-jet calibration using multijet balance

The Z + jet and γ + jet analyses described in the previous section probe the jet calibration in the range 17 GeV $\leq p_{\mathrm{T}} <$ 800 GeV. For jets with p_{T} above 800 GeV, there are an insufficient number of Z + jet and γ + jet events, and the multijet balance (MJB) technique is used instead. This method exploits the p_{T} balance of events in which the leading (highest-p_{T}) jet is produced back-to-back with a recoil system composed of multiple lower-p_{T} jets. The jets in the recoil system are fully calibrated including the in situ corrections described in the previous sections, while the leading jet, which is being

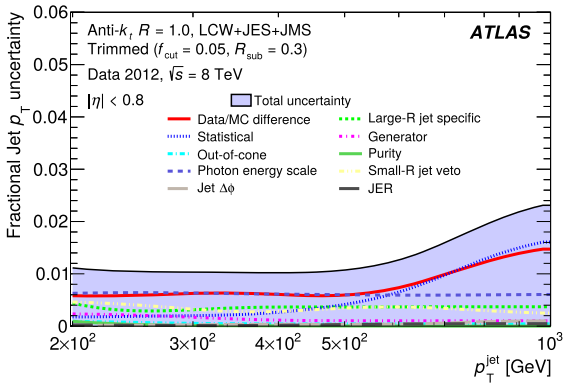

(a) Large-R jet JES uncertainty, $|\eta_{\text{det}}| < 0.8$

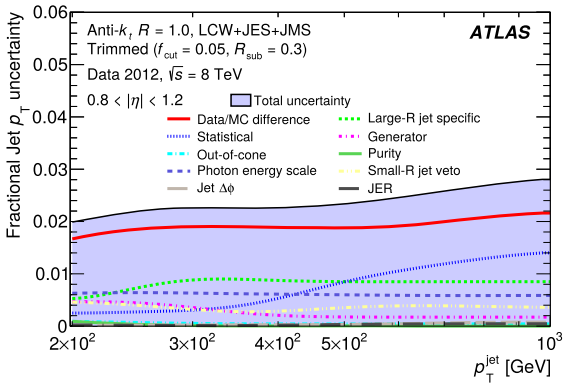

(b) Large-R jet JES uncertainty, $0.8 \leq |\eta_{\text{det}}| < 1.2$

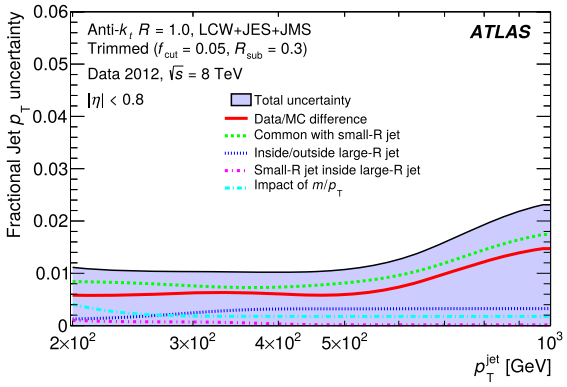

(c) Large-R jet JES uncertainty, $|\eta_{\text{det}}| < 0.8$

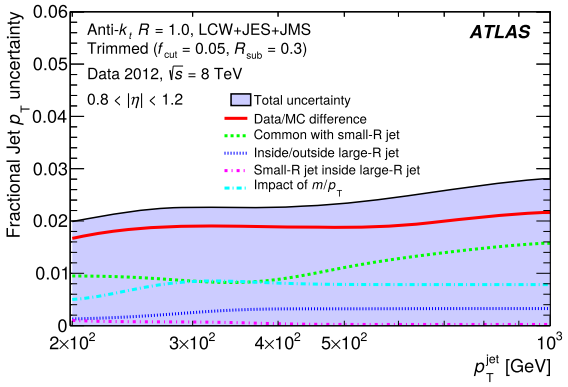

(d) Large-R jet JES uncertainty, $0.8 \leq |\eta_{\text{det}}| < 1.2$

Fig. 34 Statistical and systematic uncertainties in the data-to-MC ratio of R_{DB} for trimmed $R = 1.0$ anti-k_t jets calibrated with the LCW+JES scheme with **a**, **c** $|\eta_{\text{det}}| < 0.8$ and **b**, **d** $0.8 \leq |\eta_{\text{det}}| < 1.2$. The uncertainties are evaluated in bins of $p_{\text{T}}^{\text{ref}}$, converted to jet p_{T}, and translated into a function using a Gaussian kernel smoothing. **a**, **b** highlight the systematic uncertainty components derived analogously (and hence due to the same effects) to those for small-R jets (Fig. 27). In **c** and **d**, these uncertainties are added in quadrature, and the uncertainties specific to large-R jets are instead displayed separately. In all figures, the difference of the data-to-MC R_{DB} from unity is taken as an additional uncertainty rather than being applied as a calibration; this uncertainty is shown as a solid line

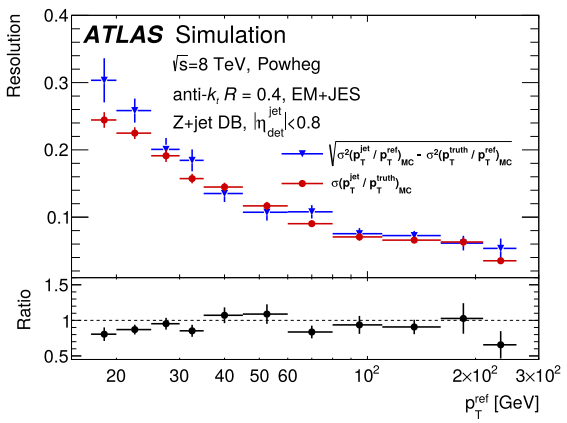

(a) Z+jet

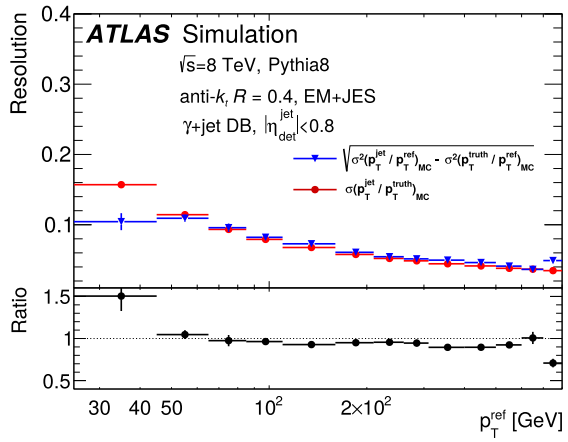

(b) γ+jet

Fig. 35 Comparison of the jet energy resolution determined in situ (triangles) with the MC jet energy resolution (circles) measured for anti-k_t EM+JES jets with $R = 0.4$, in **a** Z+jet and **b** γ+jet events. The bottom frame shows the ratio of the two

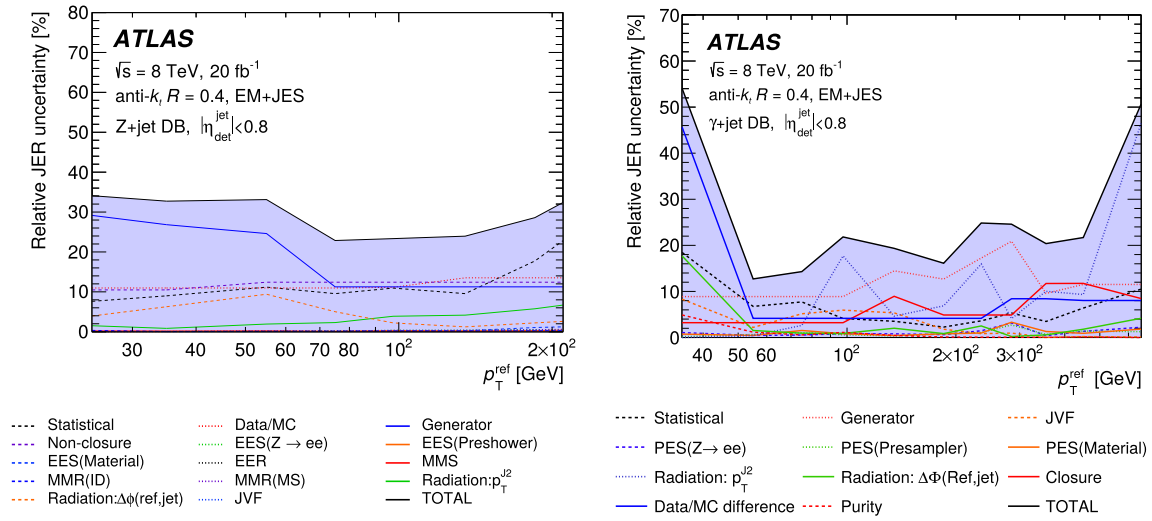

(a) Z+jet, anti-k_t $R = 0.4$, EM+JES

(b) γ+jet, anti-k_t $R = 0.4$, EM+JES

Fig. 36 Summary of systematic uncertainties of the JER measured using the DB method in **a** Z+jet and **b** γ+jet events for anti-k_t jets with $R = 0.4$ calibrated with the EM+JES scheme. The difference between the JER measured in data and MC simulation is presented as an uncertainty ("data/MC difference"). The total uncertainty, shown as a shaded area, is obtained by addition in quadrature of all uncertainty components (including the data-to-MC difference). EES/EER denotes the electron energy scale/resolution, MMS/MMR denotes the muon momentum scale/resolution, and PES denotes the photon energy scale

probed, is calibrated with all corrections except the absolute in situ correction (Sect. 7).

The multijet balance observable R_{MJB} is defined as:

$$R_{\mathrm{MJB}} = \left\langle \frac{p_{\mathrm{T}}^{\mathrm{j1}}}{p_{\mathrm{T}}^{\mathrm{recoil}}} \right\rangle,$$

where $p_{\mathrm{T}}^{\mathrm{j1}}$ is the p_{T} of the leading jet and $p_{\mathrm{T}}^{\mathrm{recoil}}$ is that from the vectorial sum of the subleading jet four-momenta. The parameter R_{MJB} is measured in both data and MC simulations in bins of $p_{\mathrm{T}}^{\mathrm{recoil}}$. The multijet balance observable R_{MJB} is not an unbiased estimator of the leading jet response. It has a value below unity even at particle level due to the effects of soft quark/gluon emission outside of the jets. The largest deviation is at low p_{T}, with data and MC simulations exhibiting similar dependence. This underlying bias is reduced in the double ratio $R_{\mathrm{MJB}}^{\mathrm{data}}/R_{\mathrm{MJB}}^{\mathrm{MC}}$, allowing the response of high-p_{T} jets to be estimated. Mis-modelling in the simulation is evaluated as a systematic uncertainty of the double ratio.

As mentioned above, the jets used in the construction of $p_{\mathrm{T}}^{\mathrm{recoil}}$ are fully calibrated, including all in situ calibrations. However, the in situ corrections from the Z/γ + jet analyses are only available for $p_{\mathrm{T}} < 800$ GeV (Sect. 7). An iterative procedure is used to calibrate all jets that are used in the calculation of $p_{\mathrm{T}}^{\mathrm{recoil}}$. For the first iteration of the MJB, an upper limit is imposed on the p_{T} of the recoil jets such that the second highest-p_{T} jet in the event has a $p_{\mathrm{T}} < 800$ GeV. This initial selection allows corrections to R_{MJB} to be derived, but limits the overall statistical accuracy of the measurements at high p_{T}. To improve the statistical accuracy, R_{MJB} is recalculated after the application of the correction factors from the first iteration to jets in the recoil system with $p_{\mathrm{T}} > 800$ GeV.

8.1 Event selection

Multijet events were obtained using single-jet triggers that are fully efficient for a given bin of $p_{\mathrm{T}}^{\mathrm{recoil}}$. The triggers used for 300 GeV $< p_{\mathrm{T}}^{\mathrm{recoil}} < 600$ GeV were prescaled, whereas a non-prescaled jet trigger was used for $p_{\mathrm{T}}^{\mathrm{recoil}} > 600$ GeV. Events are required to contain at least three jets with $p_{\mathrm{T}} > 25$ GeV. The leading jet is required to have $|\eta_{\mathrm{det}}| < 1.2$, and the subleading jets that constitute the recoil system are required to have $|\eta_{\mathrm{det}}| < 2.8$. To select non-dijet events, the leading jet in the recoil system $p_{\mathrm{T}}^{\mathrm{j2}}$ is required to have less than 80% of the total p_{T} of the recoil system ($p_{\mathrm{T}}^{\mathrm{j2}}/p_{\mathrm{T}}^{\mathrm{recoil}} < 0.8$). Furthermore, the angle α in the azimuthal plane between the leading jet three-momentum and the vector defining the recoil system is required to satisfy $|\alpha - \pi| < 0.3$ radians, and the angle β in the azimuthal plane between the leading jet and the nearest jet from the recoil system is required to be greater than 1 radian.

8.2 Results

Figure 37 shows R_{MJB} for data and MC simulation using the EM+JES calibration scheme. The MJB method provides

inputs for the in situ jet calibration in the p_{T} range between 300 GeV and 1900 GeV. The data and MC simulation agree to within 1% across the p_{T} range probed, a feature that is reproduced by the Z/γ + jet analyses (Sect. 7).

8.3 Systematic uncertainties

Since the jets entering R_{MJB} have been calibrated using the other in situ approaches, the uncertainty in the energy scale of the jets in the recoil system is defined by the systematic and statistical uncertainties of each in situ procedure. To propagate the uncertainty to R_{MJB}, all input components are individually varied by $\pm 1\sigma$ and the full iterative analysis procedure is repeated for each such variation. Changes in R_{MJB} due to the statistical uncertainties of the γ + jet and Z + jet calibrations are typically much smaller than 1%.

Also, the event selection criteria and the modelling in the event generators affect the p_{T} balance R_{MJB}. The impact of the event selection is investigated by shifting each selection criterion up and down by a specified amount and observing the change in R_{MJB}. The p_{T} threshold for jets is shifted by ± 5 GeV, the requirement on the ratio $p_{\mathrm{T}}^{\mathrm{j2}}/p_{\mathrm{T}}^{\mathrm{recoil}}$ is shifted by ± 0.1, the angle α by ± 0.1, and the angle β by ± 0.5. The uncertainty due to MC modelling of multijet events is estimated from the symmeterized envelope of MJB corrections obtained by comparing the nominal results obtained from SHERPA with those obtained from POWHEG + PYTHIA8, PYTHIA8, and HERWIG++.

The unknown flavour of each jet is also a source of systematic uncertainty. The uncertainty in R_{MJB} due to the jet flavour response is evaluated using a correlated propagation of the jet flavour response uncertainties, i.e. all jets in the recoil system are shifted simultaneously. The jet flavour composition uncertainty is propagated to R_{MJB} for the first, second, and third recoil jets independently, with the final composition uncertainty obtained from the quadrature sum of the three variations. The total uncertainty due to the unknown parton flavour is taken as the sum in quadrature of the flavour response and composition uncertainties.

Examples of the impact of systematic uncertainties are shown in Fig. 37b for anti-k_t $R = 0.4$ jets using the EM + JES calibration scheme. The uncertainties are grouped together into in situ, event topology, physics modelling, and jet flavour categories. Uncertainties for anti-k_t $R = 0.6$ jets or the LCW + JES scheme are comparable.

The uncertainty accounting for the difference of the jet energy resolution between data and simulation was not propagated to the recoil system of the multi-jet balance as the scale was derived before the resolution. However, the impact of this effect on the multi-jet balance was checked after the resolution was derived, and was found to introduce per-mille level differences on the extraction of the scale. This effect is therefore negligible compared to the existing uncertainties on the multi-jet balance shown in Fig. 37b.

9 Final jet energy calibration and its uncertainty

As detailed in Sects. 7 and 8, response observables that are directly proportional to the JES are constructed using in situ techniques by exploiting the transverse momentum balance in γ + jet, Z + jet, and multijet events. These response observables are determined in both data and MC simulations. The final residual jet calibration c_{abs}, which accounts for effects not captured by the MC calibration, is defined through the ratio of the responses measured in data and MC simulation by

$$\frac{1}{c_{\mathrm{abs}}} = \frac{R_{\mathrm{data}}}{R_{\mathrm{MC}}}. \tag{23}$$

As explained in Sect. 4.3, the absolute in situ correction c_{abs} is applied last in the calibration chain following the origin, pile-up, MC-based, and dijet in situ calibrations. Just as for the dijet intercalibration (Sect. 6), the absolute correction is applied only to data to remove any residual differences in the jet response following the MC calibration. The dijet η intercalibration is referred to as a relative in situ calibration, as it quantifies the balance between a pair of jets in different detector regions without evaluating the absolute scale of either jet. The absolute calibration is done for the Z + jet, γ + jet, and MJB techniques, which all balance the probe jet against a well-known reference quantity, thus providing a measure of the absolute scale of the jet and are known as absolute in situ calibrations.

Figure 38 summarizes the results of the Z + jet, γ + jet, and multijet balance analyses, showing the ratio of jet response in data to jet response in MC simulations. In the p_{T} range 20−2000 GeV, the response agrees between MC simulations and data at the 1% level. The deviation of the response from unity defines the absolute in situ calibration which is applied to jets in data. There is good agreement and little tension between the three different in situ methods in the regions of phase space where they overlap.

9.1 Combination of absolute in situ measurements

The separate measurements from Z + jet, γ + jet, and multijet balance are combined using the procedure outlined in Ref. [6]. For the Z + jet and γ + jet measurements, the method giving the smallest overall uncertainty is used, corresponding to the DB approach for Z + jet and the MPF approach for γ + jet (see Sect. 7 for details on the methods). The choice of DB for Z + jet is a compromise between the precision of the $R = 0.4$ and $R = 0.6$ jet calibrations in the low p_{T} regime where the Z + jet final state is most relevant: it was found

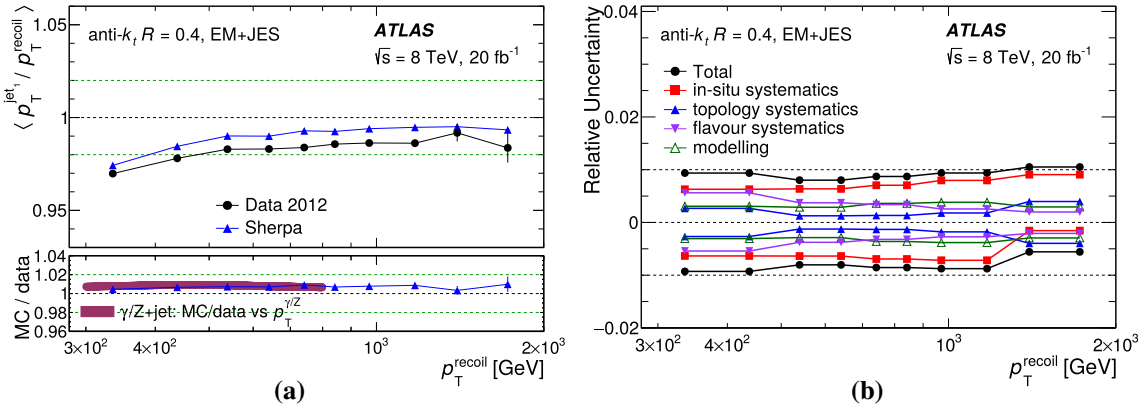

Fig. 37 **a** Multijet balance R_{MJB} in data (circles) and MC simulation (triangles) for anti-k_t $R = 0.4$ jets calibrated with the EM+JES scheme. The bottom frame compares $R_{\mathrm{MJB}}^{\mathrm{MC}} / R_{\mathrm{MJB}}^{\mathrm{data}}$ (triangles) with the corresponding γ/Z+jet results (magenta solid line). **b** The impact of in situ, event selection (topology), physics modelling, and jet flavour systematic uncertainties on R_{MJB}. The error bars on the R_{MJB} measurements only show statistical uncertainties

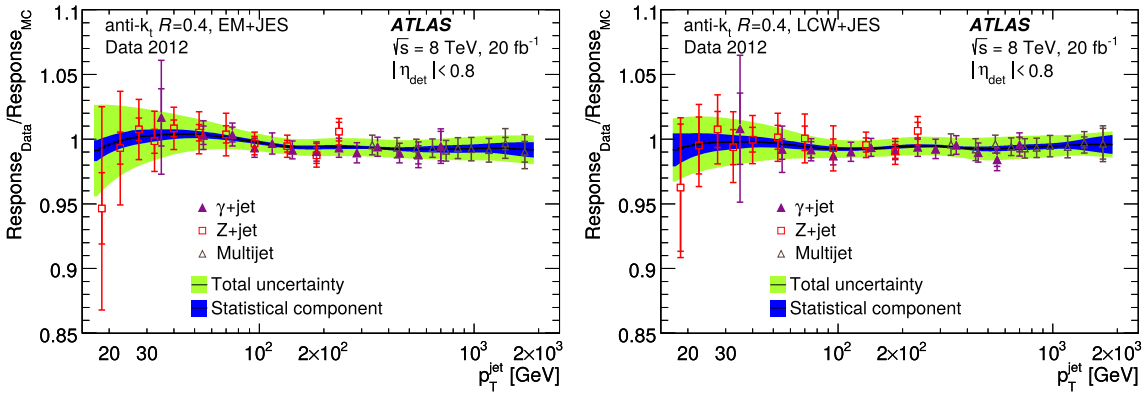

Fig. 38 Ratio of response measured in data to response measured in MC samples for Z+jet (empty squares), γ+jet (filled triangles) and multijet balance (empty triangles) in situ analyses. The method giving the smallest overall uncertainty is used, corresponding to the DB approach for Z+jet and the MPF approach for γ+jet. Each measurement has two error bars: the smaller interval corresponds to the statistical uncertainty, while the outer error interval corresponds to the total uncertainty. Also shown is the combined correction (line) with its associated total uncertainty (wider band) and statistical uncertainty (narrower band) as discussed in Sect. 9.1

that the DB and MPF techniques give similar uncertainties for $R = 0.4$ jets, while the DB technique provides improved precision for $R = 0.6$ jets. In contrast, the MPF technique is used for γ+jet events as it is found to generally provide better uncertainties across its kinematic range of relevance. This combination uses the compatibility of the three in situ measurements and their associated systematic uncertainties to produce a combined measurement of the response ratio with associated uncertainties.

Table 3 presents the 26 systematic uncertainty sources that affect c_{abs}. These are evaluated as detailed in Sects. 7.3.4 and 8.3. The electron and photon energy scale uncertainties are each split into four sources that are fully correlated. These are treated as four e/γ energy scale sources, yielding a list of 22 systematic uncertainty components. Each source is further classified into one of the following four categories:

- detector description (det.),
- physics modelling (model),
- statistics and method (stat./meth.), and
- mixed detector and modelling (mixed).

The combination is carried out using the absolute in situ measurements (Eq. (23)) in bins of $p_{\mathrm{T}}^{\mathrm{ref}}$ and evaluated at $\langle p_{\mathrm{T}}^{\mathrm{ref}} \rangle$. The data-to-MC response ratio is defined in fine $p_{\mathrm{T}}^{\mathrm{ref}}$ bins for each method using interpolating second-order polynomial splines. The combination is then carried out using a weighted average of the absolute in situ measurements based

Table 3 Summary of the uncertainty components propagated through to the combination of absolute in situ jet energy scale measurements from Z+jet, γ+jet, and multijet balance studies. These are discussed in more detail in Sects. 6 and 7

Name	Description	Category
Z+jet		
e E-scale material	Material uncertainty in electron energy scale	Det.
e E-scale presampler	Presampler uncertainty in electron energy scale	Det.
e E-scale baseline	Baseline uncertainty in electron energy scale	Mixed
e E-scale smearing	Uncertainty in electron energy smearing	Mixed
μ E-scale baseline	Baseline uncertainty in muon energy scale	Det.
μ E-scale smearing ID	Uncertainty in muon ID momentum smearing	Det.
μ E-scale smearing MS	Uncertainty in muon MS momentum smearing	Det.
MC generator	Difference between MC generators	Model
JVF	JVF choice	Mixed
$\Delta\phi$	Extrapolation in $\Delta\phi$	Model
Out-of-cone	Contribution of particles outside the jet cone	Model
Subleading jet veto	Variation in subleading jet veto	Model
Statistical components	Statistical uncertainty	Stat./meth.
γ+jet		
γ E-scale material	Material uncertainty in photon energy scale	Det.
γ E-scale presampler	Presampler uncertainty in photon energy scale	Det.
γ E-scale baseline	Baseline uncertainty in photon energy scale	Det.
γ E-scale smearing	Uncertainty in photon energy smearing	Det.
MC generator	Difference between MC generators	Model
$\Delta\phi$	Extrapolation in $\Delta\phi$	Model
Out-of-cone	Contribution of particles outside the jet cone	Model
Subleading jet veto	Variation in subleading jet veto	Model
Photon purity	Purity of sample in γ+jets	Det.
Statistical components	Statistical uncertainty	Stat./meth.
Multijet balance		
α selection	Angle between leading jet and recoil system	Model
β selection	Angle between leading et and closest subleading jet	Model
MC generator	Difference between MC generators (fragmentation)	Mixed
p_{T} asymmetry selection	Asymmetry selection between leading and subleading jet	Model
Jet p_{T} threshold	Jet p_{T} threshold	Mixed
Statistical components	Statistical uncertainty	Stat./meth.

on a χ^2-minimization. This local χ^2 is used to define the level of agreement between measurements.

Each uncertainty source in the combination is treated as being fully correlated across p_{T} and η and independent of one another. All the uncertainty components are propagated to the combined results using pseudo-experiments [5]. To determine the correlations between different phase-space regions, it is necessary to understand the contribution of each uncertainty component to the final uncertainty. Therefore, each individual source is propagated separately to the combined result by coherently shifting all the correction factors by one standard deviation. Comparison of this shifted combination result with the nominal result provides an estimate of the propagated systematic uncertainty.

One exception is the jet flavour uncertainty of the recoil in the multijet balance method (Sect. 8). It is correlated in a non-trivial way with the additional uncertainties due to flavour composition and response considered in analyses. Including this uncertainty does not change the overall absolute in situ uncertainty by a significant amount after combination with the other in situ methods, so it is dropped.

To take tensions between measurements into account, each uncertainty source is increased by rescaling it by $\sqrt{\chi^2/n_{\mathrm{dof}}}$ if χ^2/n_{dof} is larger than unity [66], where n_{dof} is the number of degrees of freedom. The number of degrees of freedom

varies with p_{T} and corresponds to the number of in situ methods $n_{\text{in-situ}}$ that contribute to the combination minus one, i.e. $n_{\text{dof}} = n_{\text{in-situ}} - 1$. The local $\sqrt{\chi^2/n_{\text{dof}}}$ of the final combination (Fig. 39) for both jet collections is below unity for most of the p_{T} range and barely exceeds 2 anywhere. The combined in situ factor is the final calibration factor to be applied to data after reducing statistical fluctuations using a sliding Gaussian kernel.

Figure 40 shows the uncertainty sources for the three absolute in situ analyses used in the combination as a function of p_{T}. In the combination, the Z+jet measurement is most important at low p_{T}, the γ+jet measurement at medium p_{T}, and the multijet balance at high p_{T}.

The combined jet response, shown as a line in Fig. 38, is observed to have a general offset of 0.5% between data and MC simulation (with data below the MC prediction). The total uncertainty from the combination of absolute in situ techniques is shown as the wider band around the measured response and is about 3.5% (2.5%) for jets with $p_{\mathrm{T}} \approx 25$ GeV for EM (LCW) jets and decreases to about 1% (1%) for p_{T} above 200 GeV.

As mentioned a spline-based combination procedure, with a local averaging within fine p_{T} intervals followed by a global smoothing, is used for the in-situ JES combination. This method avoids assumptions on the jet energy response dependence that are implicitly present in procedures based on global fits using a functional form, which can further reduce the uncertainties (see e.g. Ref. [67]).

9.2 Jet energy scale uncertainties

In addition to the uncertainties coming from the combination of in situ methods detailed above, there are several other uncertainties that account for other potential systematic effects or expand the kinematic reach. These additional uncertainties are described below, and summarized in Sect. 9.2.4

9.2.1 Single-hadron response

The jet energy response measured by the in situ methods can also be compared with results from a method where the jet energy scale is estimated from the calorimeter response to single hadrons measured in test beam studies. This provides a cross-check of the direct balance in situ methods, albeit with a larger uncertainty, and also allows the extension of the in situ measurements of the jet energy scale to higher energies beyond the reach of balance methods due to limited data. In this "single hadron" method, jets are treated as a superposition of the individual energy deposits of their constituent particles [68]. In some cases, highly energetic jets contain constituents beyond test-beam energies. When this occurs, a constant 10% uncertainty is applied to each of these constituents.

In the previous jet energy scale measurements based on data taken in 2011 [6], the absolute in situ methods and the single-hadron response studies gave consistent results, indicating that MC simulation overestimated the jet response in data by approximately 2%. However, since the in situ methods are more precise (approximately 2% uncertainty compared to 5%) the single-particle response method is only used at high p_{T} (> 1500 GeV) where the statistical power of in situ methods becomes limited. The single-hadron response measurements from the 2011 data [6] are propagated to high p_{T} jets to provide an uncertainty where it is beyond the reach of the absolute in situ analyses.

9.2.2 Pile-up uncertainties

There are four uncertainties sources associated with the mitigation of the pile-up contributions to the jet momentum (Eq. (2)) that are evaluated by comparing data with simulation using in situ techniques. Two of the uncertainties are in the values of the slope parameters α and β that determine the dependence on the number of reconstructed pile-up vertices and the average interactions per crossing, respectively. The third uncertainty accounts for jet p_{T} dependence of the α and β parameters. These uncertainties are evaluated using momentum balance in Z+jet events. The fourth uncertainty is associated with a topology dependence of the event p_{T}-density ρ. It is evaluated as the largest difference in measured average p_{T} density $\langle\rho\rangle$ at a given pile-up condition μ between dijet, γ+jet, and Z+jet events. As shown in Eq. (2), this uncertainty is directly proportional to the jet area and is larger by approximately a factor of $0.6^2/0.4^2 = 2.25$ for $R = 0.6$ jets compared with $R = 0.4$ jets. For $R = 0.6$ jets, this tends to be the dominant uncertainty component with a typical magnitude of 2% for jets with p_{T} around 40 GeV. For $R = 0.4$ jets in events with moderate pile-up, the N_{PV}-dependent uncertainty component tends to be largest for jets in the central calorimeter region while the μ component is largest in the forward calorimeter region ($|\eta_{\text{det}}| > 2.8$).

9.2.3 Flavour-based uncertainties

The in situ methods used to derive final corrections and uncertainties of the jet energy scale make use of event samples with particular fractions of jets initiated by quarks and gluons. The event samples in physics analyses may have jet flavour compositions which differ from that of the calibration sample.

The response for quark-initiated jets is considerably higher than that for gluon-initiated jets (Sect. 5.5). Therefore, if the flavour composition of final states in a given analysis is unknown, it has an impact on the JES uncertainty. The degree to which the flavour of jets is known in an analysis

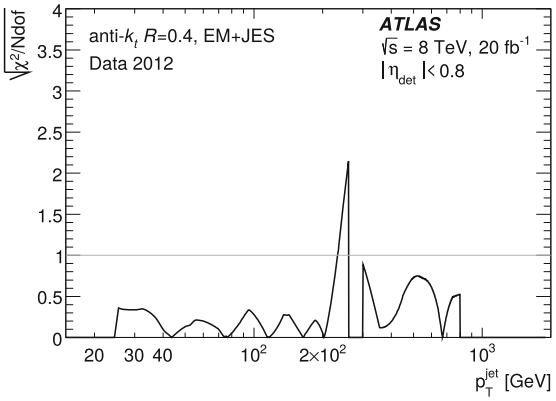

(a) EM+JES

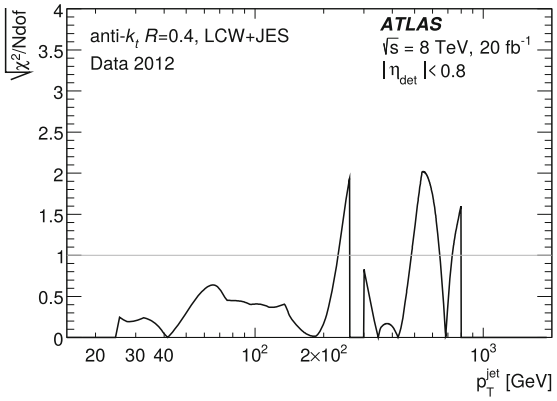

(b) LCW+JES

Fig. 39 χ^2/n_{dof} for the combination of absolute in situ measurements illustrating the compatibility of the included in situ calibrations as a function of jet p_{T}. At any given point, there are at most two in situ results being combined: Z+jet and γ+jet at low p_{T}, or γ+jet and MJB at high p_{T}, which means that the number of degrees of freedom n_{dof} is equal to one. For a small p_{T} range near 300 GeV, only one measurement (γ+jet) contributes, and there is a gap ($n_{\mathrm{dof}} = 0$). The points where the curve touches zero correspond to where the two in situ calibrations cross

can be specified in order to evaluate the corresponding uncertainty. Alternatively, analyses can be conservative and use a completely unknown flavour composition.

While the response for light-quark-initiated jets is found to be in good agreement between different generators, shifts are seen in the gluon jet response for different generators due to differences in the jet fragmentation. There is therefore an additional uncertainty for gluon-initiated jets, which is subdominant in the Z+jet and γ+jet regions used to constrain the uncertainty, as defined by the difference between the gluon jet response in PYTHIA8 and HERWIG++. These differences are typically reduced using LCW topo-clusters as inputs, and this is visible in the central region of the detector when comparing to jets built using EM topo-clusters. However, this is less true in the forward region of the detector where the LCW correction is less robust due to the different properties of the more forward calorimeters.

Further details of this uncertainty are given in Ref. [6], and additional discussion of how the GS correction reduces the jet flavour uncertainties are presented in Sects. 5.5 and 5.7.

9.2.4 *Summary of jet energy scale uncertainties*

The total jet energy scale uncertainty is compiled from multiple sources:

- 22 systematic sources from absolute in situ methods,
- 34 statistical sources from absolute in situ methods,
- a single-hadron response uncertainty which only affects the highest-p_{T} jets beyond the reach of in situ techniques (Sect. 9.2.1),
- two η-intercalibration uncertainties (one systematic, one statistical),
- four sources from uncertainties associated with the pile-up corrections:
  - μ-dependent uncertainty in the pile-up correction,
  - N_{PV}-dependent uncertainty in the pile-up correction,
  - p_{T} dependence of pile-up corrections, and
  - ρ topology dependence,

  as outlined in Ref. [51] (Sect. 9.2.2), and
- two sources due to jet flavour (Sect. 9.2.3).

The last two terms are assumed to be independent, resulting in a jet energy scale uncertainty defined in terms of 65 components (nuisance parameters). The resulting, total jet energy scale uncertainty is shown as a function of jet p_{T} in Fig. 41 and versus jet η in Fig. 42.

9.2.5 *Uncertainties in fast simulation*

All uncertainties discussed in the previous section apply to MC samples produced using either the full or fast simulation. However, a small non-closure of the jet calibration was observed in fast simulation compared with full simulation. To account for this, an additional systematic uncertainty must be included in analyses using fast simulation since relative and absolute in situ methods are not used to validate this simulation. The size of this uncertainty compared with other systematic uncertainties is generally small for $R = 0.4$ jets (Fig. 43). However, as shown in Fig. 44, this uncertainty becomes sizeable for $R = 0.6$ jets.

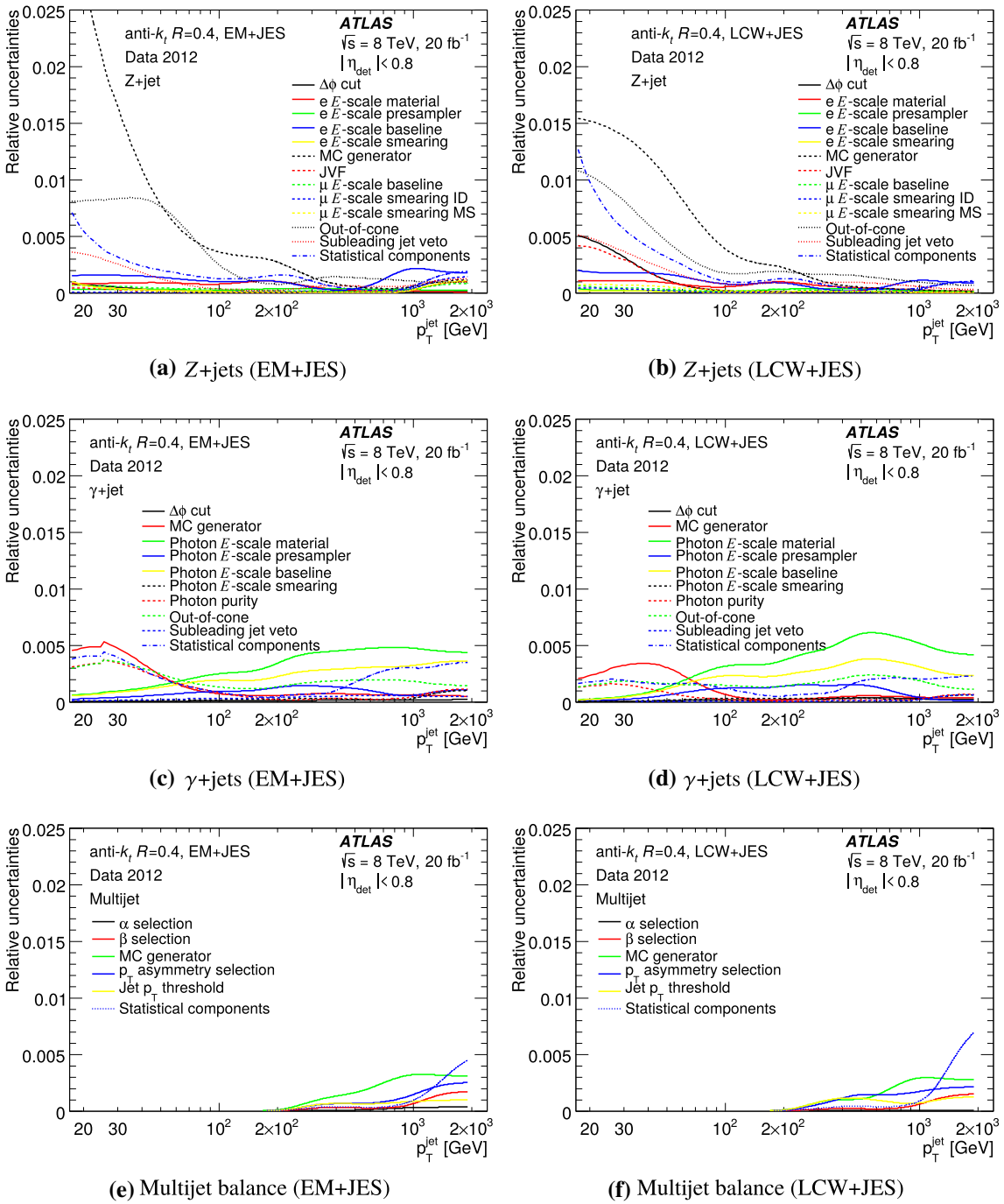

(a) Z+jets (EM+JES) **(b)** Z+jets (LCW+JES)

(c) γ+jets (EM+JES) **(d)** γ+jets (LCW+JES)

(e) Multijet balance (EM+JES) **(f)** Multijet balance (LCW+JES)

Fig. 40 Individual uncertainty sources used in the combination for the three absolute in situ calibration methods. The systematic uncertainties displayed correspond to those in Table 3

9.3 Simplified description of uncertainty correlations

The list of uncertainties described in Sect. 9.2.4 requires an analysis to propagate a total of 65 JES uncertainty terms to correctly account for all correlations in the jet calibration. For many analyses it is preferable to describe such correlations using a reduced set of uncertainty components (nuisance parameters).

As detailed in Ref. [6], the total covariance matrix of the JES correction factors including all the in situ sources can be diagonalized, and then a new set of independent uncertainty sources can be derived from the eigenvectors and eigenvalues. A good approximation of the covariance matrix is

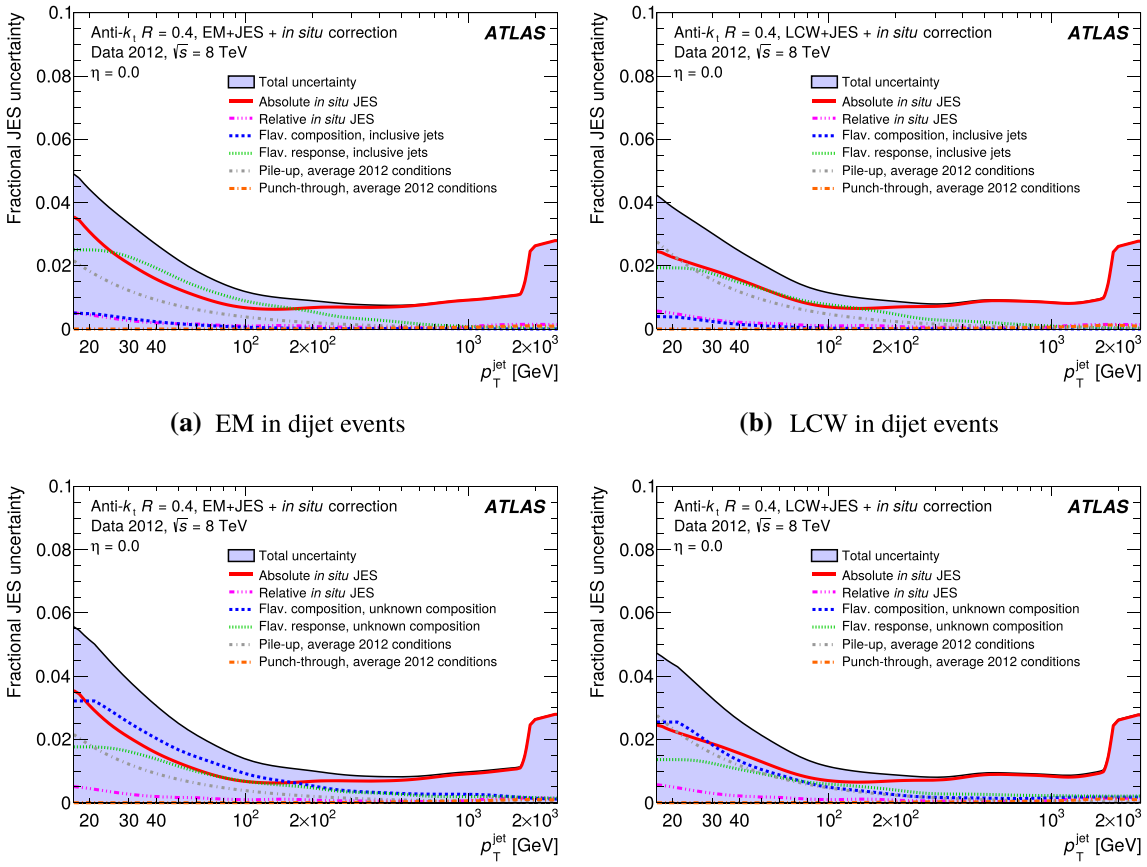

(a) EM in dijet events **(b)** LCW in dijet events

(c) EM in unknown composition events **(d)** LCW in unknown composition events

Fig. 41 The total jet energy scale uncertainty as a function of p_T for central jets. Two flavour compositions are shown, one for dijet events, where the quark/gluon composition is taken from MC simulations and an associated uncertainty from generator comparisons, and one for an unknown flavour composition (assuming 50:50 quark:gluon jets with a 100% uncertainty). "Absolute in situ JES" refers to the uncertainty arising from Z+jet, γ+jet, and multijet measurements, including also the single-hadron response uncertainty at high p_T. "Relative in situ JES" refers to the uncertainty arising from the dijet η intercalibration. "Punch-through" refers to the uncertainty in the final (muon-based) stage of the global sequential correction

then obtained by selecting a subset of the new uncertainty sources (those with the largest eigenvalues) and combining the remaining nuisance parameters into a residual term. Figure 45 demonstrates this procedure, showing the nominal correlation matrix and the difference between this and a similar matrix derived from a reduced set of nuisance parameters. Only uncertainties depending on a single parameter (in this case p_T) are combined in this way and any uncertainties with dependencies on other parameters are left separate. Including such uncertainty components with additional parameter dependencies in the combination would not result in any significant reduction of the correlation information into fewer nuisance parameters, as such components require additional dimensions to represent their correlations.

Two reduction schemes are provided. The first scheme reduces the number of central absolute in situ nuisance parameters, those shown in Fig. 40 and the statistical components of the γ + jet, Z + jet, and multijet balance, from 56 to 6 ("standard"). To preserve some knowledge of the uncertainty source in this procedure, a second scheme is provided where the reduction is done within categories (statistical, detector, modelling, or mixed). This "category based" reduction reduces the number of central absolute in situ parameters from 56 to 15. Retaining the separation of detector, statistical, and modelling components allows the correlation between experiments and different data-taking years to be assessed in combinations of measurements. No reduction is done for the other terms, and in addition to the 6 (15) nuisance parameters, nine additional parameters are required, resulting in 15 (24) parameters. This procedure gives a simpler propagation of the correlations and uncertainties associated with the jet energy scale with very little loss of information about the correlations.

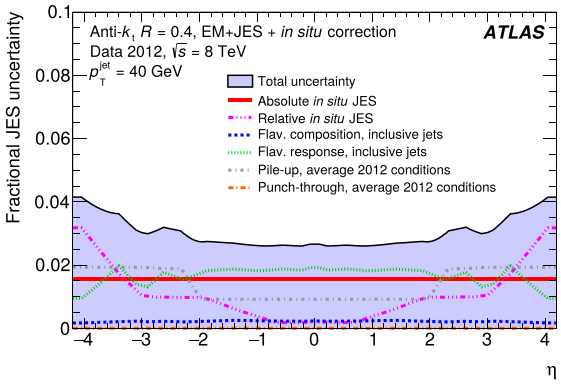

(a) EM in dijet events

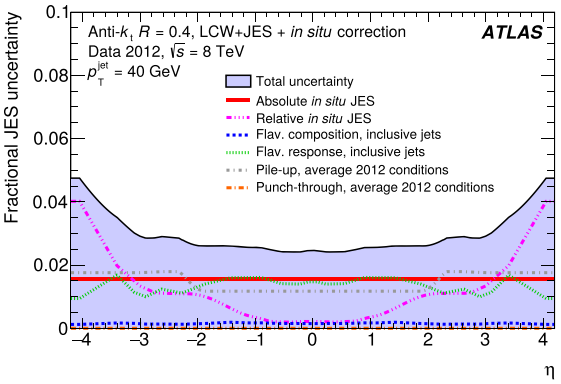

(b) LCW in dijet events

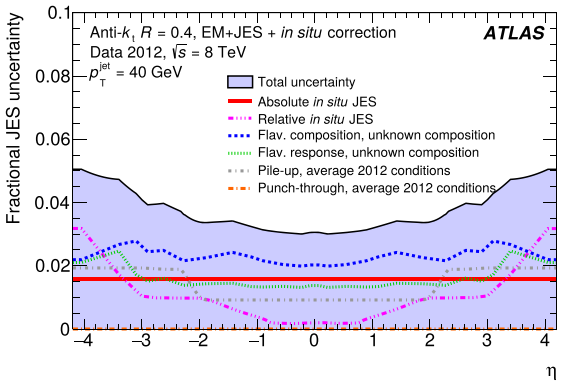

(c) EM in unknown composition events

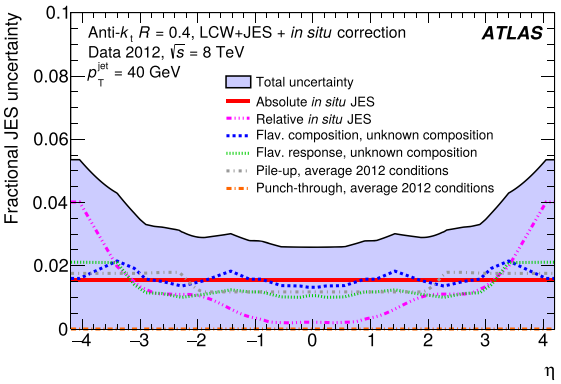

(d) LCW in unknown composition events

Fig. 42 The total jet energy scale uncertainty as a function of $|\eta|$ for $p_T = 40$ GeV jets. Two flavour compositions are shown, one for dijet events, where the quark/gluon composition is taken from MC simulations and an associated uncertainty from generator comparisons, and one for an unknown flavour composition (assuming 50:50 quark:gluon jets with a 100% uncertainty). "Absolute in situ JES" refers to the uncertainty arising from Z + jet, γ + jet, and multijet measurements. "Relative in situ JES" refers to the uncertainty arising from the dijet η intercalibration. "Punch-through" refers to the uncertainty in the final (muon-based) stage of the global sequential correction

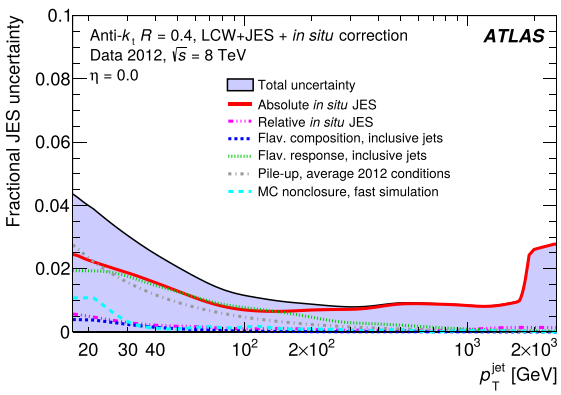

(a) Uncertainty vs p_T

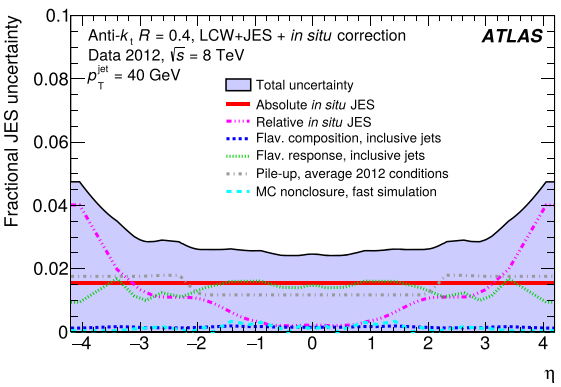

(b) Uncertainty vs η

Fig. 43 Total uncertainty in the calibration of anti-k_t, $R = 0.4$ jets in fast simulation as a function of p_T and η. "Absolute in situ JES" refers to the uncertainty arising from Z + jet, γ + jet, and multijet measurements. "Relative in situ JES" refers to the uncertainty arising from the dijet η intercalibration. "MC non-closure, fast simulation" refers to the additional non-closure observed in fast simulation when comparing with full simulation

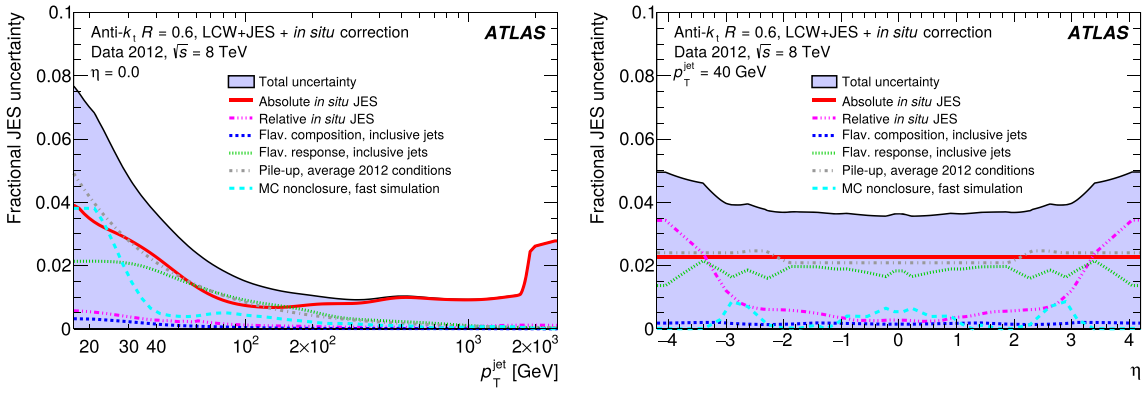

(a) Uncertainty vs p_T **(b)** Uncertainty vs η

Fig. 44 Total uncertainty in the calibration of anti-k_t, $R = 0.6$ jets in fast simulation as a function of p_T and η. The large "MC non-closure" term demonstrates the limitations of using $R = 0.6$ jets in fast simulation. "Absolute in situ JES" refers to the uncertainty arising from Z + jet, γ + jet, and multijet measurements. "Relative in situ JES" refers to the uncertainty arising from the dijet η intercalibration

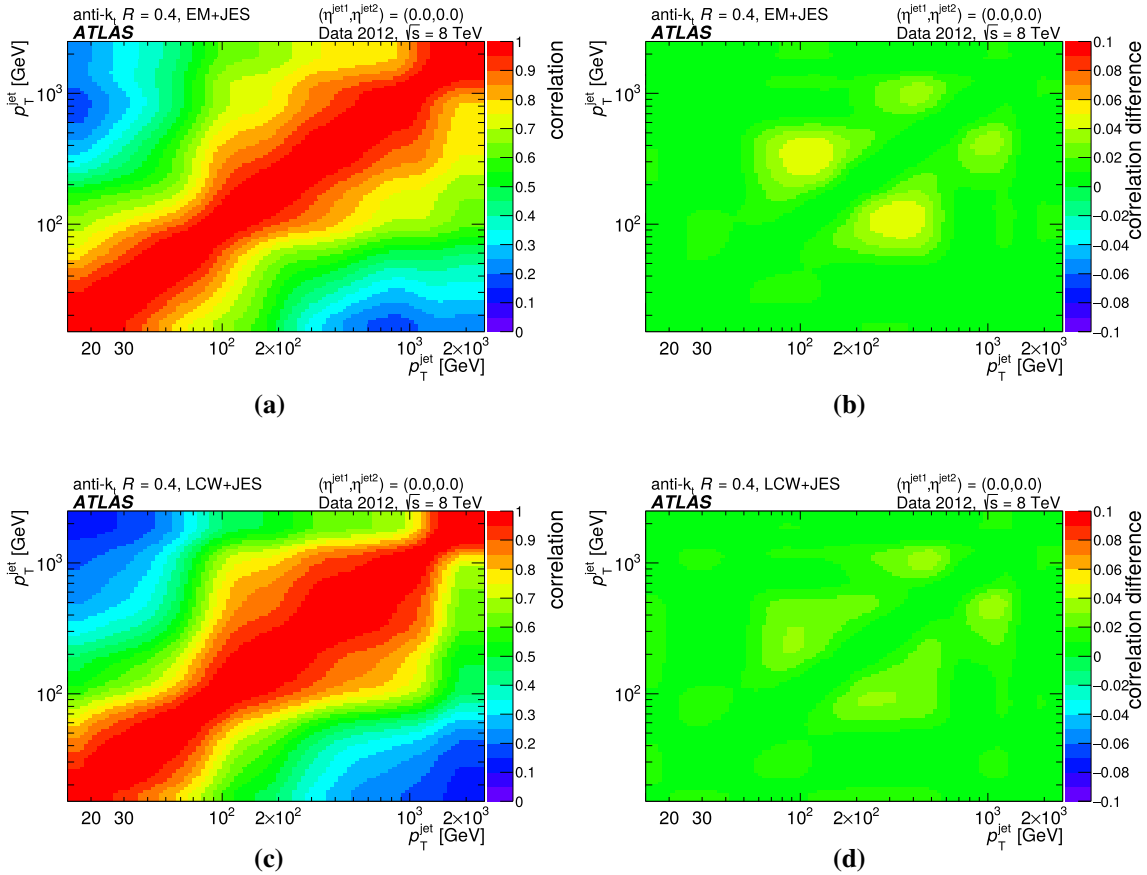

Fig. 45 The **a**, **c** JES correlation matrix and **b**, **d** difference between the full correlation matrix and that derived from a reduced number (6) of absolute in situ uncertainty components for anti-k_t $R = 0.4$ jets calibrated with the **a**, **b** EM+JES and **c**, **d** LCW+JES schemes

A method has been developed for evaluating the correlations between the full set of 56 in situ JES uncertainty terms and a reduced set. This is especially useful for evaluating the correlations between the uncertainties obtained for two physics analyses that use different uncertainty configurations (e.g. the full set and a reduced set of JES uncertainty terms). In this method, each JES uncertainty term in the full set is projected, in the space of uncertainties, onto the direction of each uncertainty term in the reduced set. The corresponding projection coefficients allow expression of the uncertainties propagated by one analysis using a given configuration in terms of the components corresponding to another configuration. Therefore, this allows correlations to be assessed between analyses using different uncertainty configurations.

9.4 Alternative uncertainty configurations

Many physics analyses use "profiling" of uncertainties in the statistical analysis, such as the profile log-likelihood method, which improves the precision of the associated physics results. These methods may make significant use of the uncertainty amplitudes and correlation in different kinematic regions, and the exact parameterization of the JES systematic uncertainties might impact the result. Since the correlation between uncertainty sources often is unknown, the nominal uncertainty parameterization discussed in the previous sections corresponds to a "best guess". Certain analyses could erroneously benefit from somewhat arbitrary choices made during the construction of this uncertainty scheme. To allow analyses to test if their results depend on these choices, two alternative uncertainty parameterizations are provided, one that results in stronger JES uncertainty correlations and one that gives weaker correlations. These are constructed by making alternative assumptions about the correlation between different effects and by employing a different rebinning prescription when propagating absolute in situ derived uncertainties to the combination.

In both the strong and weak correlation scenarios, a change is made in the rebinning procedure described in Sect. 6.4. The condition for stopping the merging of bins is altered such that the stronger (weaker) correlation scenario has more (less) bins merged. The effect of this procedure is particularly noticeable at low p_{T} and results in a reduction of the absolute in situ uncertainties for the stronger correlation scenario. In addition, both alternatives use a slower turn-on of the interpolation between multijet balance and single-particle uncertainties at $p_{\mathrm{T}} \approx 1.7$ TeV (Fig. 41).

For the strong correlations alternative, certain uncertainty components that are treated as being uncorrelated with each other in the nominal parametrization are combined into a correlated component. This is only done for components that are suspected to have some correlation. The flavour composition uncertainty is also switched from using PYTHIA8 to derive the quark/gluon response to using HERWIG++ to fully encompass generator dependence.

For the weak correlation alternative, several "2-point" systematic uncertainties are split into two subcomponents [69]. The term 2-point systematic uncertainties refers to uncertainties evaluated by comparison of the nominal result with only one alternative, e.g. a comparison between the predictions from two MC generators. The two constructed uncertainty components are defined such that their sum in quadrature equals the original component, thus the total uncertainty is retained. The split is performed by multiplying the original component by a factor varying linearly from 0 to 1 in either $|\eta|$ or $\log p_{\mathrm{T}}$, forming the first subcomponent, while the second subcomponent is formed as the quadrature complement. Components treated this way in the alternative configurations include the η-intercalibration modelling term and flavour components.

9.5 Large-R jet uncertainties

Uncertainties in the large-R jet calibration are determined using in situ methods with the same principle as for $R = 0.4$ and $R = 0.6$ jets. Jet energy scale uncertainties are derived by combining direct balance measurements (Eq. (17)) performed in γ+jet events and are combined with uncertainties with track jets as reference objects. Uncertainties for the jet mass scale are derived only using track jets as reference objects. The track jet double-ratio method is discussed below along with an additional topological uncertainty similar to the flavour composition uncertainty in small-R jets. The γ+jet studies and uncertainties are discussed in Sect. 7.

Track jet double-ratio method

In the double-ratio method, track jets are used as reference objects since charged-particle tracks are both well measured and independent of the calorimeter and are associated with calorimeter jets using a geometrical matching in the η–ϕ plane. This method assumes that energy fluctuations measured using the calorimeter are independent of the charge-to-neutral fraction of the particle-level jet's constituents. This is only approximately true because the calorimeter response is different for charged and neutral particles. The precision of the method requires that the track jet momentum resolution is much smaller than the calorimeter jet energy resolution, an excellent approximation for calorimeter jet momenta up to several hundred GeV.

This approach was widely used in the measurement of the jet mass and substructure properties of jets in the 2011 data [45]. Performance studies [70] have shown that there is excellent agreement between the measured positions of clusters and tracks in data, indicating no systematic misalignment between the calorimeter and the inner detector.

However, the use of track jets as reference objects is limited to a precision in the jet mass scale of around 3–7% in the central detector region due to systematic uncertainties arising from the inner-detector tracking efficiency [71] and confidence in MC modelling of the charged and neutral components of jets. The track jet double ratio is compared for two different MC generators: PYTHIA8 and HERWIG++, and the larger disagreement between data and MC prediction is taken as the uncertainty. Figure 46 shows the jet mass scale uncertainty for anti-k_t $R = 1.0$ trimmed jets in different detector regions. The uncertainties are derived in bins of p_{T}, $|\eta|$, and m/p_{T}, and two examples are shown.

Topological uncertainty

Similarly to the jet flavour composition uncertainty for small-R jets, an uncertainty in the jet energy response for different mixtures of quark/gluon jets, boosted top jets, and W jets is derived for large-R jets. Simulated $t\bar{t}$ events are used to account for the different hard substructure and energy distributions within the W or top jets compared with quark/gluons jets which are taken from W+jet samples requiring exactly one lepton. The uncertainties are derived for anti-k_t $R = 1.0$ trimmed jets. Figure 47 shows the p_{T} dependance of the jet response in three η regions for four different kinds of jets: "full top" jets have the three quarks from the top decay contained within $\Delta R = 0.8$ of the jet axis; "W-only" jets have the quarks from the W decay within $\Delta R = 0.8$ of the jet axis but any b-quark must have $\Delta R > 1.2$; "non-top" jets have the top quark separated from the jet axis by $\Delta R > 2.0$; and, "QCD jets" are jets from a leptonically decaying W+jets sample. The topological uncertainty (Fig. 47) is determined by the envelope of the responses of these different types of jets.

Combination

The jet p_{T} scale uncertainties are available within $|\eta| < 2.0$ but the available data at high p_{T} ($p_{\mathrm{T}} > 800$ GeV) is limited for the direct γ+jet p_{T} balance method. By contrast, the uncertainties from the track jet double ratios cover $p_{\mathrm{T}} > 800$ GeV. To benefit from the drastically reduced p_{T} scale uncertainties derived with γ+jet events, a linear interpolation is performed around $p_{\mathrm{T}} = 800$ GeV between the two methods. The uncertainty arising from the topological composition of the jet is added in quadrature to form the total uncertainty. This total uncertainty and its components are shown as a function of p_{T} in Fig. 48.

10 Final jet energy resolution and its uncertainty

The measurement of the jet energy resolution (JER) in data is a multi-step process. As detailed in Sects. 6 and 7, the analyses employed to measure the JER are essentially the same as for the jet calibration, but the observable of interest is not the mean of the response observable but is its width. For the central rapidity region, the JER is measured with good precision using γ+jet and Z+jet events. In the forward pseudorapidity region and for high p_{T}, dijet events provide the most precise determination of the JER. For very low p_{T} jets there is a significant contribution to the jet energy resolution from pile-up particles and electronic noise. Using the data taken in 2012, new methods have been developed to measure the pile-up component.

The jet energy resolution is parameterized as a function of three terms [7],

$$\frac{\sigma_{p_{\mathrm{T}}}}{p_{\mathrm{T}}} = \frac{N}{p_{\mathrm{T}}} \oplus \frac{S}{\sqrt{p_{\mathrm{T}}}} \oplus C \,, \tag{24}$$

where N parameterizes the effect of noise (electronic and pile-up), S parameterizes the stochastic effect arising from the sampling nature of the calorimeters, and C is a p_{T}-independent constant term. It is the determination of these terms in data that is the subject of this section.

In Sect. 10.1, the MC simulated jet energy resolution is discussed, followed by the determination of the noise term in data in Sect. 10.2. The combination of the measurements of the noise term and the Z+jet, γ+jet, and dijet measurements, described in Sects. 7 and 6, respectively, is detailed in Sect. 10.3. The uncertainty in the measurement of the jet energy resolution arising from the various in situ methods is propagated through the fit to the p_{T} dependence of the jet energy resolution.

10.1 JER in simulation

The jet energy resolution is measured in simulated event samples as described in Sect. 4.2, i.e. it is defined as the width parameter σ of a Gaussian fit to the jet energy response distribution restricted to the range $\pm 1.5\,\sigma$ around the mean. Figure 49 shows the resolution determined using PYTHIA8 dijet MC samples both with full GEANT4 detector simulation and with fast simulation. The two simulations generally agree very well, although there are some discrepancies in the very forward regions. The distribution is shown both with and without the GS correction, which significantly improves the resolution (decreasing the resolution of $R = 0.4$ EM+JES jets from 10% to 7% at 100 GeV), particularly for jets built from EM-scale clusters. The resolution is shown as functions of $p_{\mathrm{T}}^{\mathrm{truth}}$ and $|\eta_{\mathrm{det}}|$. As expected, the resolution improves quickly with increasing $p_{\mathrm{T}}^{\mathrm{truth}}$. The resolution for a fixed value

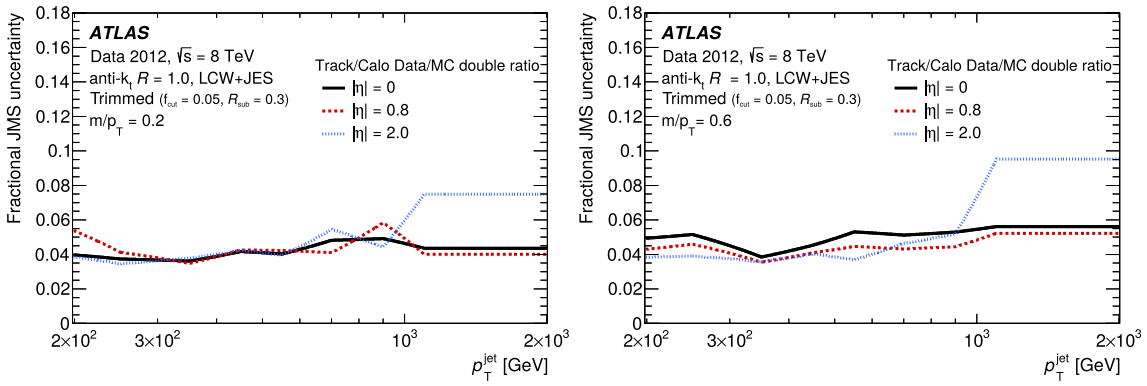

(a) $m/p_{\mathrm{T}} = 0.2$ **(b)** $m/p_{\mathrm{T}} = 0.6$

Fig. 46 Jet mass scale (JMS) uncertainties for anti-k_t $R = 1.0$ trimmed jets ($f_{\mathrm{cut}} = 0.05$ and $R_{\mathrm{sub}} = 0.3$) in different detector regions for **a** $m/p_{\mathrm{T}} = 0.2$ and **b** $m/p_{\mathrm{T}} = 0.6$

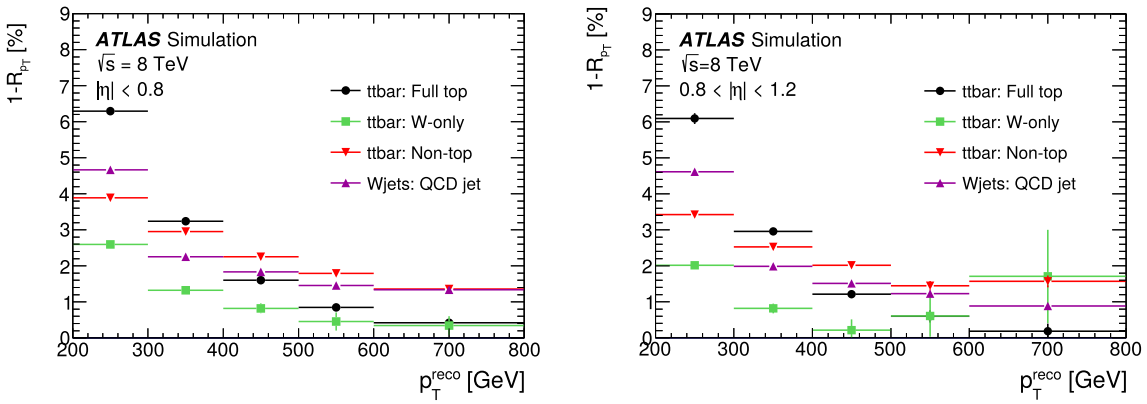

(a) $0.0 < |\eta| < 0.8$ **(b)** $0.8 < |\eta| < 1.2$

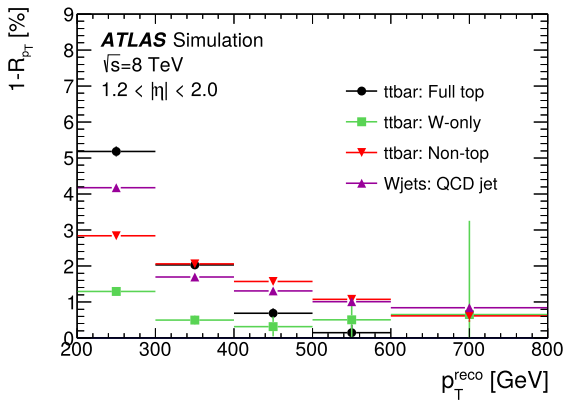

(c) $1.2 < |\eta| < 2.0$

Fig. 47 One minus the jet p_{T} response ($\langle p_{\mathrm{T}}^{\mathrm{truth}} - p_{\mathrm{T}}^{\mathrm{reco}} \rangle / p_{\mathrm{T}}^{\mathrm{truth}} = 1 - \mathcal{R}_{p_{\mathrm{T}}}$) for anti-$k_t$ $R = 1.0$ trimmed jets with different flavour composition for **a** $0.0 < |\eta| < 0.8$, **b** $0.8 < |\eta| < 1.2$, **c** $1.2 < |\eta| < 2.0$. The categories in the plot are defined by (1) "$t\bar{t}$ full top" jets (circles) that represent jets for which the three quarks from a hadronic top quark decay are contained within $\Delta R = 0.8$ of the jet axis; (2) "$t\bar{t}$ W-only" jets (squares), for which the quarks from the W boson decay are within $\Delta R = 0.8$ of the jet axis while the b-quark fulfils $\Delta R > 1.2$; (3) "$t\bar{t}$ non-top" jets (lower triangles) that represent jets for which the top quark is $\Delta R > 2.0$ from the jet; and, (4) "Wjets QCD" jets (upper triangles) representing jets from a leptonically decaying W boson in a W+jets MC sample. These are plotted as a function of reconstructed jet p_{T} ($p_{\mathrm{T}}^{\mathrm{reco}}$), but due to the large bin size compared with the p_{T} resolution, the choice of plotting $p_{\mathrm{T}}^{\mathrm{reco}}$ or $p_{\mathrm{T}}^{\mathrm{truth}}$ is of little significance

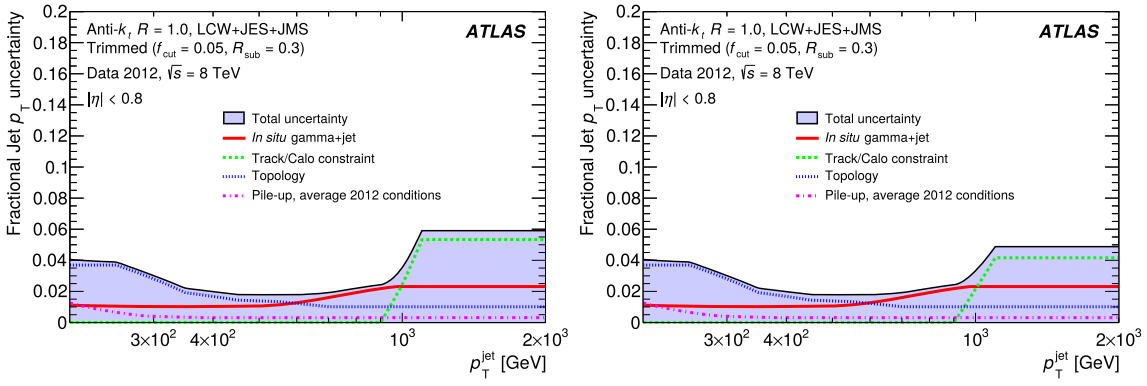

(a) $m/p_T = 0.2$ **(b)** $m/p_T = 0.6$

Fig. 48 Combination of the uncertainties in the jet p_T scale for anti-k_t $R = 1.0$ trimmed jets for $|\eta| = 0$ and two values of m/p_T: **a** $m/p_T = 0.20$ and **b** $m/p_T = 0.60$

of p_T gets better towards more forward regions (this is not the case for constant jet energy).

10.2 Determination of the noise term in data

Noise, both from the calorimeter electronics and from pile-up, forms a significant component of the JER at low p_T. The noise term is not evaluated for $R = 1.0$ trimmed jets, as they are only used for $p_T > 200$ GeV at which point the noise term is negligible. It is quite challenging to measure the JER at low p_T with in situ techniques (Sect. 10.3) as uncertainties increase at low p_T and the stochastic and noise terms are correlated at intermediate p_T. Two alternative methods have hence been developed to target the noise term. These attempt to extract the noise at the constituent scale (the scale of the input topo-clusters) as explained in Sects. 10.2.1 and 10.2.2. They are translated into the effect on the jet resolution at the calibrated scale in Sect. 10.2.3. Good agreement is found between the methods, and a closure test is performed using MC simulations in Sect. 10.2.4, leading to a final value for the noise term in the jet energy resolution.

The JER noise term receives contributions from the cells inside the topo-clusters created by the actual truth-particle jet as well as from pile-up. The noise term is significantly affected by the topo-cluster formation threshold as jets will contain a varying fraction of particles that have enough energy to form a topo-cluster. The noise term in data without pile-up is denoted $N^{\mu=0}$. As just mentioned, this term will be affected by a contribution corresponding to the number of constituent particles produced without enough energy to produce topo-clusters or that have been swept out of the cone by the magnetic field, and also by the electronic noise from the cells inside the topo-clusters. Pile-up particles can result in increased noise of topo-clusters seeded by the truth-particle jet particles, and also create new topo-clusters that are included in the jet. The latter effects is assumed to dominate, and its contribution to the JER noise term is denoted N^{PU}. A third source of noise are topo-clusters created solely from electronic noise in the entire calorimeter. This is assumed to be a negligible effect as the topo-clusters require a calorimeter cell with $4\,\sigma$ energy over noise, which is also confirmed in data from events without collisions. The following sections present two different measurements of N^{PU}.

10.2.1 Pile-up noise measured using random cones in zero-bias data

In the random cone method, a cone of given size is formed at a random values of η and ϕ in zero-bias data, and the energies of all clusters (at either EM or LCW scale) that fall within this cone are combined. The data was collected using a zero-bias trigger that records events occurring one LHC revolution after an event is accepted by a L1 electron/photon trigger. The total p_T of a random cone is hence expected to only capture contributions from pile-up interactions. Since jets formed with the anti-k_t algorithm tend to be circular (Fig. 3a), fluctuations of the p_T in a random cone can be considered a measure of the expected pile-up fluctuations that are captured by an anti-k_t jet with a radius parameter equal to the cone size.

The η of the cone is randomly sampled within the range for which the noise is being probed, and the random cone method proceeds by forming a second cone at $\phi + \pi$ ("back-to-back" in azimuth to the first cone) but at a new random η, also restricted to the η range probed. The effect of the noise in these cones is expected to be the same on average[6], and the difference in the random cone p_T, Δp_T, is plotted. The difference between two cones is used to remove any absolute offset present as the jet calibration would remove any abso-

[6] The noise is η dependent, but since both η values are sampled randomly within the probe region, the noise will be the same on average.

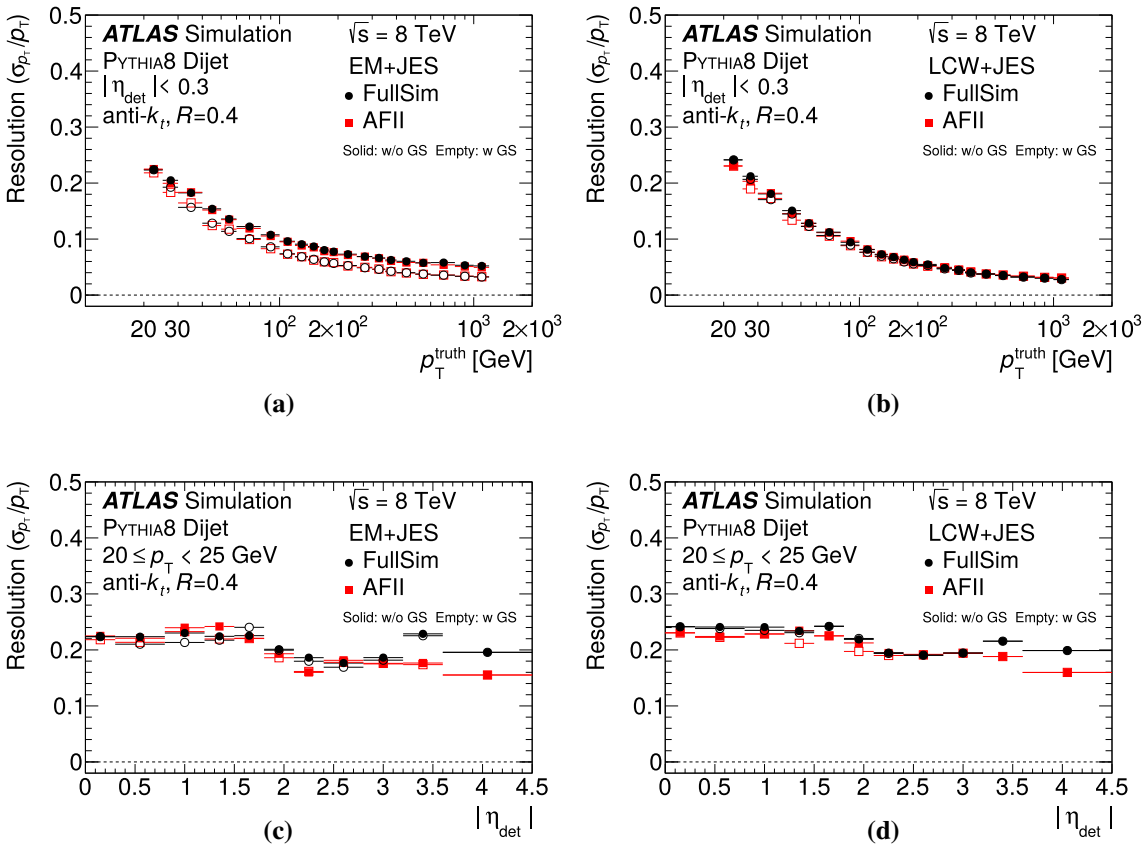

Fig. 49 Jet energy resolution measured in dijet MC samples as a function of $p_{\mathrm{T}}^{\mathrm{truth}}$ for **a** EM+JES and **b** LCW+JES jets (filled markers). The resolution in both events simulated with the full GEANT4 toolkit (circles) and with fast simulation (squares) are shown. Additionally the improvement from the global sequential correction is shown (empty markers). Figures **c** and **d** show the dependence of the resolution on $|\eta_{\mathrm{det}}|$ for low-p_{T} (20–25 GeV) jets and the level of agreement between full simulation (circles) and fast simulation (squares)

lute bias affecting the jets. The noise is studied as a function of η by restricting the $|\eta|$ values that can be chosen for the random cones as previously mentioned. Since the topo-clusters that enter the random cone have no origin correction applied (Sect. 4.3.1), the η of the random cone corresponds to η_{det} of a jet. An example of the distribution of this noise in data is shown in Fig. 50. Due to the random nature of the pile-up energy deposits with significant energy over noise, the Δp_{T} distribution is not expected to be Gaussian. The 68% confidence interval of this distribution is defined as the width. Since Δp_{T} gives the fluctuations of two cones, this value is divided by $\sqrt{2}$ to give an estimate of the noise term due to pile-up N^{PU} at the constituent scale for a given jet.

The growth of this noise term at the constituent scale as a function of the average number of interactions per bunch crossing is shown in Fig. 51 separately for $|\eta| < 0.8$ and $3.2 < |\eta| < 4.5$. From these results, it is clear that the MC simulations overestimate the influence of pile-up events, and this effect is increased in the forward region. Also, the noise term at constituent scale is larger for LCW than EM topo-clusters, because the LCW weighting acts to increase the energy scale of the topo-clusters, which also increases the constituent-level noise term. The EM- and LCW-scale noise terms can only be fairly compared after applying the jet calibration factor, which is done later in Sect. 10.2.3. Figure 52 shows the average pile-up noise fluctuations expected in different jets in 2012 for the different $|\eta|$ regions. The data–MC agreement deteriorates in the more forward regions of the detector. This is likely to arise from poor modelling of the pile-up being exacerbated in this region due to the change in detector granularity and noise thresholds.

To extract the pile-up noise term for average 2012 conditions, the noise term in random cones is extracted from the total 2012 zero-bias dataset. To ensure that the μ distribution used in other in situ measurements (dijet, Z+jet, and γ+jet) is identical to that in the zero-bias dataset, a reweighting is applied dependent on the μ distribution. This reweighting has a very small effect as the zero-bias trigger and prescales are designed to produce a dataset which mimics the μ distribution of the full dataset used for physics. In addition, to enable a direct comparison between data and MC simulations, the simulated μ distribution is reweighted to that of the data.

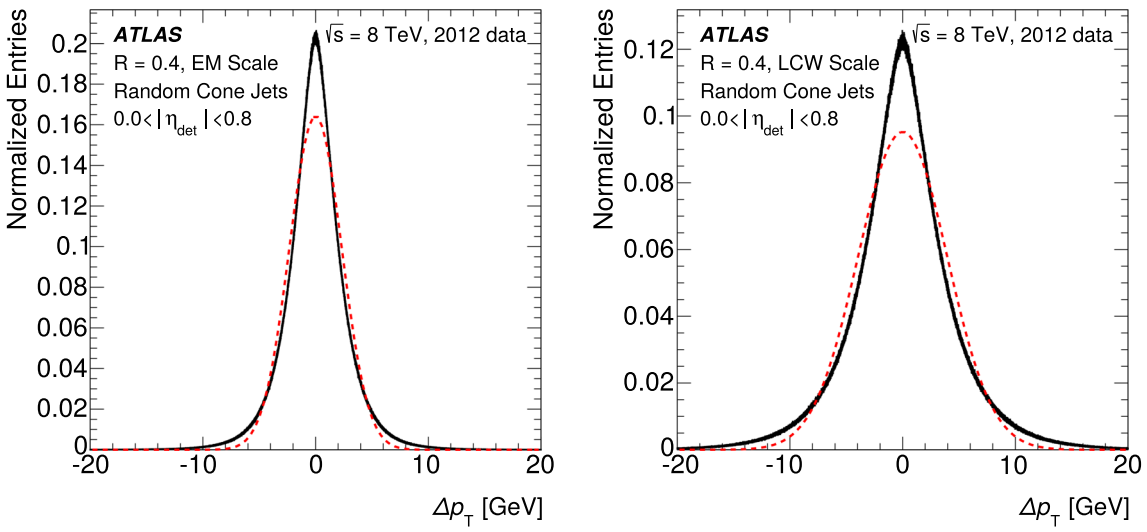

(a) EM **(b)** LCW

Fig. 50 The balance of random cones of size 0.4 ($\Delta p_{\mathrm{T}} = p_{\mathrm{T}}^{1} - p_{\mathrm{T}}^{2}$) in the central region $|\eta| < 0.8$ in 2012 zero-bias data using EM and LCW clusters. The non-Gaussian shape of this distribution is demonstrated by the inclusion of a Gaussian fit (dashed lines) to the data (solid lines)

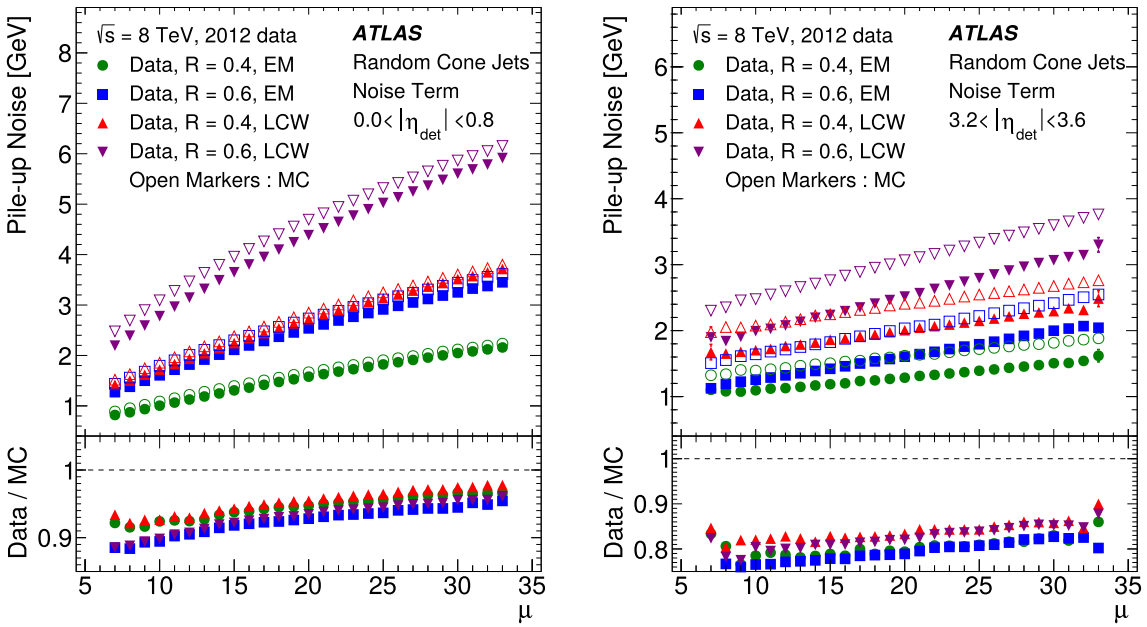

(a) $0.0 < |\eta| < 0.8$ **(b)** $3.2 < |\eta| < 3.6$

Fig. 51 The magnitude of the expected fluctuations in different jet radii at the constituent scale derived using the random cone procedure as a function of μ, for data (filled markers) and MC simulations (open markers). The results are shown for $R = 0.4$ and $R = 0.6$ cones and at both the EM and LCW scales probing two calorimeter $|\eta|$ regions, one central ($|\eta| < 0.8$) and one forward ($3.2 < |\eta| < 3.6$). A scale factor of 1.09 has been applied to μ in the MC simulations to correct for extra activity observed in the minimum-bias tune

10.2.2 Pile-up noise term measurements using the soft jet momentum method

As explained in Sect. 4.3.2, the event p_{T}-density ρ is obtained by reconstructing jets using the k_t algorithm without applying any jet p_{T} threshold and defining ρ to be the median of the jet p_{T}-density p_{T}/A, where A is the area of the jet. Starting from this quantity, the noise term of the JER due to pile-up N^{PU} is extracted by defining a new observable σ_ρ that is a measure of the fluctuations in p_{T} per unit area assuming a stochastic model of noise. Due to using the median (rather than the mean) in its definition, ρ is to first order insensitive

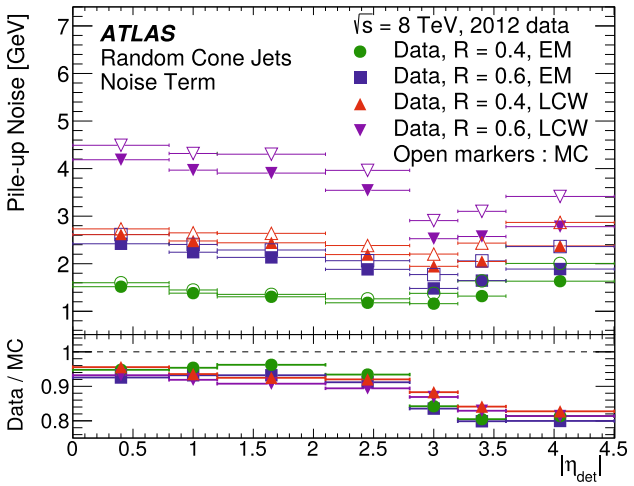

Fig. 52 The magnitude of the expected fluctuations within different jet radii at the constituent scale as a function of $|\eta|$ for data (filled markers) and MC simulations (open markers). The results are shown for $R = 0.4$ and $R = 0.6$ cones and at both the EM and LCW scales

to the hard process. Any type of data can in principle be used for the measurement. The results presented in this section are based on $Z \to \mu\mu$ data. The following steps are performed:

- Jets are reconstructed using the Cambridge–Aachen algorithm [72] with $R = 0.6$ and required to have $|\eta| < 2.1$. No p_{T} threshold is applied, and the jet p_{T} extends down to zero.
- For each jet, the quantity $r = (p_{\mathrm{T}} - \rho\, A)/\sqrt{A}$ is calculated, where A is the jet area defined using the Voronoi procedure [54]. Since no jet p_{T} threshold is applied, many jets will be built from noise only. The distribution of r is expected to be centred at zero since after subtracting $\rho\, A$ there should be as many jets above the p_{T} density as below.
- The observable σ_ρ is defined event-by-event from the width of the r distribution of all jets in the event. To avoid complications of non-Gaussianity and the hard-scatter event biasing the upper side tail, σ_ρ is defined by half the difference between the 84% and 16% quantile points.

The size of the expected fluctuations at the constituent scale of a given jet is given by $\sigma_\rho \sqrt{A}$. The distributions of σ_ρ for EM-scale and LCW-scale clusters in $Z \to \mu\mu$ data and PYTHIA8 samples are shown in Fig. 53. $Z \to \mu\mu$ events are used to select an unbiased set of events for data-to-MC comparison, thus avoiding the use of any jet-based trigger which would bias the jet distributions. As in the random cone method (Fig. 51), the pile-up noise is overestimated in the MC simulations. An estimate of the noise term due to pile-up is obtained by scaling the mean value of the σ_ρ distribution by $\sqrt{\pi R^2}$.

10.2.3 *Comparison of methods and construction of the noise term*

As described in the previous two sections, the random cone and the soft jet momentum methods can both be used to measure the noise term of the jet energy resolution. It is useful to compare their results and to contrast the two methods. As well as using different data samples, these methods make quite different assumptions about the underlying physics:

- The soft jet momentum method implicitly assumes the pile-up noise is stochastic (such that it grows with $\sqrt{A}$).
- The random cone method measures the noise in several η-bins, while the soft jet momentum method does not consider any η-dependence of the noise within the probed detector region $|\eta| < 2.1$.
- The symmetry assumption of the two cones back-to-back in azimuth in the zero bias events is not required by the soft jet momentum method.

Further, while the soft jet momentum method gives an estimate of the noise term in each event (as is done for the calculation of ρ), the random cone method gives the noise term over an event sample. Table 4 compares the measured noise term at the constituent scale using the two methods. The two sets of measurements agree at the level of 20%.

10.2.4 *Closure test of the pile-up noise measurement in MC simulation*

A closure test is performed on the pile-up noise measurements by comparing the random cone result with the pile-up noise extracted using truth-particle jets in MC simulation. The pile-up noise in MC simulations is extracted by measuring the MC JER (Sect. 4.2) in two PYTHIA8 dijet samples: one without pile-up and one sample with 2012 pile-up conditions. By subtracting the JER measured in the sample without pile-up from the JER measured in the sample with pile-up, the contribution from the pile-up noise is isolated and can be compared with the measurement of the noise term using the random cone method. However, this comparison cannot be done directly since the random cone measures the noise at constituent scale (EM or LCW), while the JER is measured at the fully calibrated scale (EM+JES or LCW+JES). To account for this mismatch in scale, the random cone measurements are scaled by the average MC calibration factor $\langle c_{\mathrm{JES}} \rangle$ evaluated for the jets in the kinematic region of interest. The results of these tests are shown in Fig. 54 as a function of p_{T} for both EM and LCW jets. The relevant comparison is that of the estimated noise term N^{PU} and the quadrature difference of the MC JER measurements with and without pile-up. In the central region $|\eta| < 0.8$, good closure is observed, both for EM+JES and LCW+JES. In

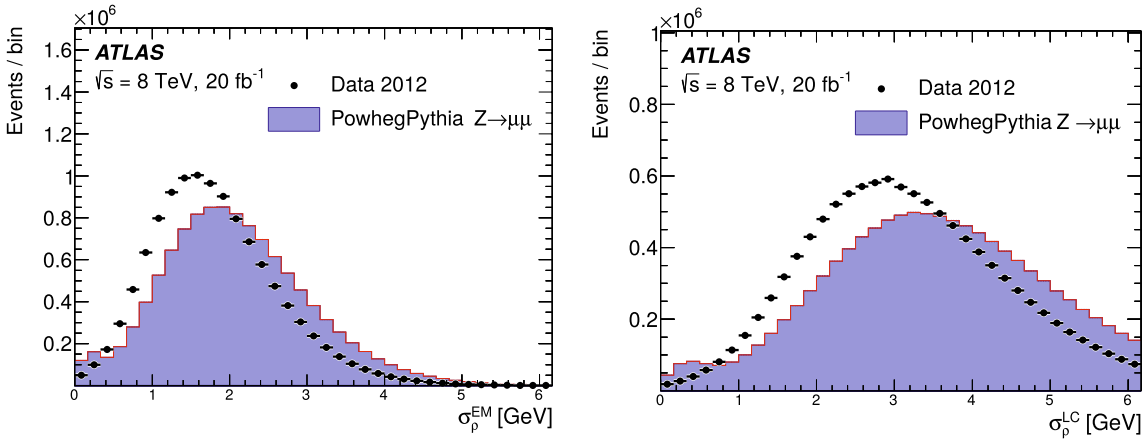

Fig. 53 Extracted values of σ_ρ in data (points) and MC simulations (histogram) for a sample of $Z \to \mu\mu$ events at the EM scale (left) and the LCW scale (right). This observable quantifies the fluctuations of the p_{T} density ρ, i.e. the p_{T} per area in (y, ϕ)-space

Table 4 Measurements of $\langle\sigma_\rho\rangle$ and $\langle\sigma_\rho\rangle\sqrt{A}$, where $\langle\sigma_\rho\rangle$ is the mean of the σ_ρ distribution, and the random cone results, both using data and MC simulations. The area is defined by $A = \pi R^2$, where R is the radius parameter. The $\sigma_\rho\sqrt{A}$ results, which is a noise term measurement from the soft jet momentum method, is extracted using the region $|\eta| < 2.1$ while the noise term measurement using the random cone method is extracted for jet $|\eta| < 0.8$. Statistical uncertainties of both measurements are negligible

	EM $R = 0.4$	LCW $R = 0.4$	EM $R = 0.6$	LCW $R = 0.6$
$\langle\sigma_\rho\rangle$ ($Z \to \mu\mu$, data) (GeV)	1.81	3.25	1.81	3.25
$\langle\sigma_\rho\rangle$ ($Z \to \mu\mu$, MC) (GeV)	2.09	3.72	2.09	3.72
$\langle\sigma_\rho\rangle\sqrt{A}$ ($Z \to \mu\mu$, data) (GeV)	1.28	2.30	1.92	3.46
Random cone, data (GeV)	1.52	2.61	2.42	4.19
Difference (%)	16	12	21	17
$\langle\sigma_\rho\rangle\sqrt{A}$ ($Z \to \mu\mu$, MC) (GeV)	1.48	2.64	2.22	3.96
Random cone, MC (GeV)	1.60	2.73	2.61	4.49
Difference (%)	7.5	4.4	15	12

this region, the calorimeters have high granularity, and as a consequence energy clusters from pile-up and from the hard-scatter signal tend to form separately with little overlap. Slightly larger non-closure is observed towards the more forward regions, which is expected due to the coarser angular granularity and higher noise thresholds, which result in a larger overlap between energy deposits from pile-up and the hard scatter.

The same closure test was performed for the N^{PU} measured with the soft jet momentum method, and the difference between the results is taken as a systematic uncertainty due to the arbitrariness of the selection of method. Additionally, the degree of non-closure of the method is taken as a systematic uncertainty.

10.2.5 Noise term in the no pile-up scenario

The random cone and soft jet momentum methods provide measurements of the part of the noise term arising from pile-up activity N^{PU}. In the dijet MC sample without pile-up, for which $\mu = 0$, the noise term does not have any pile-up contribution but does include other effects such as electronic noise on the signal clusters and threshold effects. To get a handle on the additional noise terms not included in the random cone or soft jet methods, the $\mu = 0$ MC simulated resolution is fitted with the standard N, S and C parameterization of Eq. (24) to extract the no pile-up noise term $N^{\mu=0}$. The result of such fits are presented in Table 5.

The total jet energy resolution (Eq. (24)) was measured in 2010 and agreed between data and MC simulations within 10% for jet p_{T} in the range 30 GeV $< p_{\mathrm{T}} <$ 500 GeV [7]. For $p_{\mathrm{T}} = 30$ GeV in the central region, the noise term is responsible for more than half of the total resolution. Given that the dominant resolution source leads to a total resolution modelled to the level of 10%, this implies that the noise term itself agrees between data and MC simulation to the level of 20% in simulated samples without pile-up. This conclusion is also supported by single-particle measurements [68].

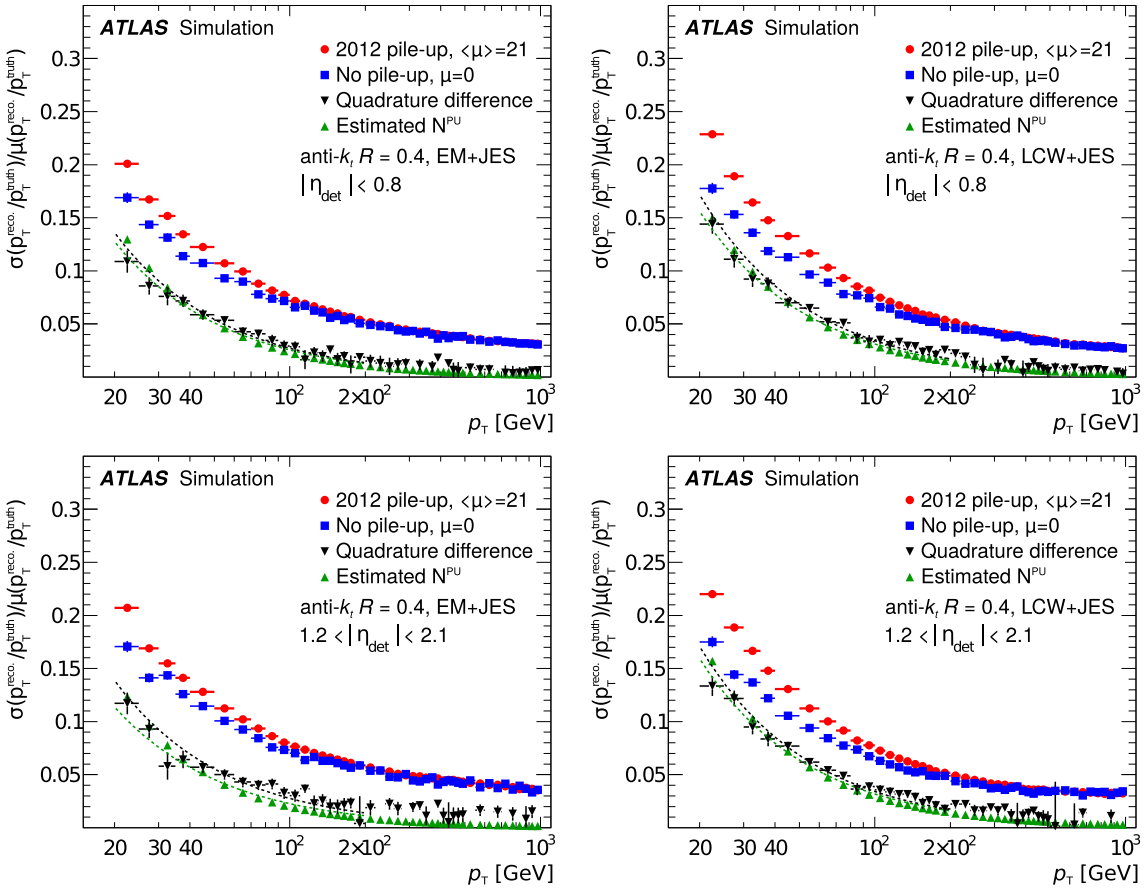

Fig. 54 Comparison between the pile-up noise term N^{PU} extracted using the random cone method (upward triangles) with the expectation from MC simulation (downward triangles). Results are shown for jets built from EM (left) and LC (right) topo-clusters, for jets with $|\eta_{\mathrm{det}}| < 0.8$ (top) and $1.2 < |\eta_{\mathrm{det}}| < 2.1$ (bottom). The expected N^{PU} is obtained by quadrature subtraction of the JER obtained from MC simulation of events with nominal pile-up (circles) from that of events with no pile-up (squares). Fits performed to the measured and expected pile-up noise data are displayed as dotted curves. Quadrature differences corresponding to points where, due to statistical fluctuations, the resolution is worse in the no pile-up scenario are not displayed

Table 5 The noise term $N^{\mu=0}$ in GeV extracted in a dijet MC sample without pile-up. The values and uncertainties are extracted from a fit. For data, an additional 20% uncertainty is assigned, based on the 2010 measurements [7]

	EM+JES R= 0.4	LCW+JES R= 0.4	EM+JES R= 0.6	LCW+JES R= 0.6
$\lvert\eta\rvert < 0.8$	2.28 ± 0.13	2.66 ± 0.09	1.83 ± 0.12	2.54 ± 0.09
$0.8 < \lvert\eta\rvert < 1.2$	1.95 ± 0.25	2.14 ± 0.17	1.29 ± 0.25	2.34 ± 0.15
$1.2 < \lvert\eta\rvert < 2.1$	2.52 ± 0.18	2.99 ± 0.09	0.90 ± 0.28	2.94 ± 0.09
$2.1 < \lvert\eta\rvert < 2.8$	2.25 ± 0.30	2.19 ± 0.13	0 ± 0.95	2.24 ± 0.11

This extrapolation includes some additional assumptions in the MC modelling of the detector as several settings changed between 2010 and 2012, most notably the topo-cluster noise thresholds; however, 20% is considered a conservative estimate of the uncertainty in this component.

The total JER noise term N is defined by combining the noise term extracted in the no pile-up sample with that originating from pile-up (measured above) using a sum in quadrature, i.e. $N = N^{\mathrm{PU}} \oplus N^{\mu=0}$.

10.3 Combined in situ jet energy resolution measurement

The JER measurements based on the bisector method in dijet events reported in Sect. 6.6 and the vector boson plus jet balance reported in Sect. 7.5 are statistically combined using a chi-squared minimization of the function in Eq. (24). In this fit, the noise term is held at the central value found in the previous section, while measurements of the S and C terms are extracted. The uncertainties in each term are evaluated in the same way they were in the JES determination in Sect. 9.1,

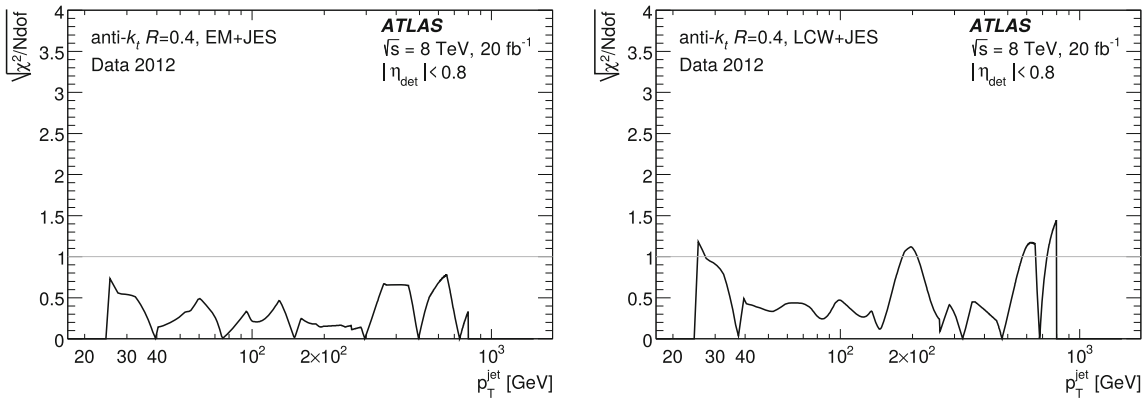

(a) EM+JES **(b)** LCW+JES

Fig. 55 The χ^2 per degree of freedom for the jet energy resolution showing the compatibility of the three in situ measurements of the jet energy resolution (dijet asymmetry, Z+jet balance, and γ+jet balance) for jets calibrated with the **a** EM+JES and **b** LCW+JES schemes

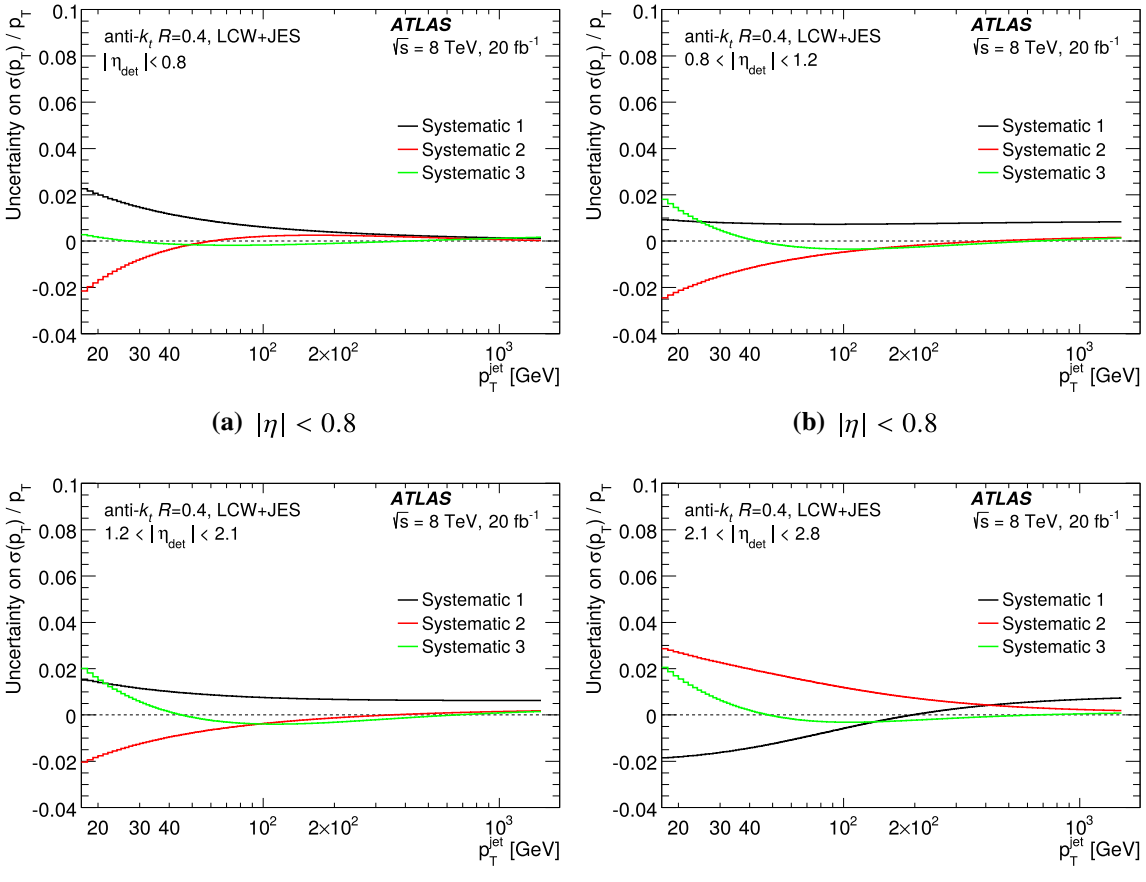

(a) $|\eta| < 0.8$ **(b)** $|\eta| < 0.8$

(c) $1.2 < |\eta| < 2.1$ **(d)** $2.1 < |\eta| < 2.8$

Fig. 56 The three eigenvectors after the eigenvector reduction of the nuisance parameters in the jet energy resolution measurement for LCW+JES $R = 0.4$ jets for four different $|\eta|$ bins. These nuisance parameters fully describe the correlations

i.e. by re-evaluating the JER measurement after a 1σ shifts of each individual uncertainty source. The degree of agreement between the three in situ measurements is in Fig. 55, which shows the χ^2 per degree of freedom as a function of p_{T}. The low values of the χ^2 per degree of freedom across the p_{T} range demonstrates that the in situ methods agree well. As expected, there is a large anti-correlation between the S and C parameters of -0.25 (-0.44) for EM+JES (LCW+JES) calibrated jets, and the χ^2 per degree of freedom for the fit to find N, S and C is 8/35 (15/35) when correlations are not

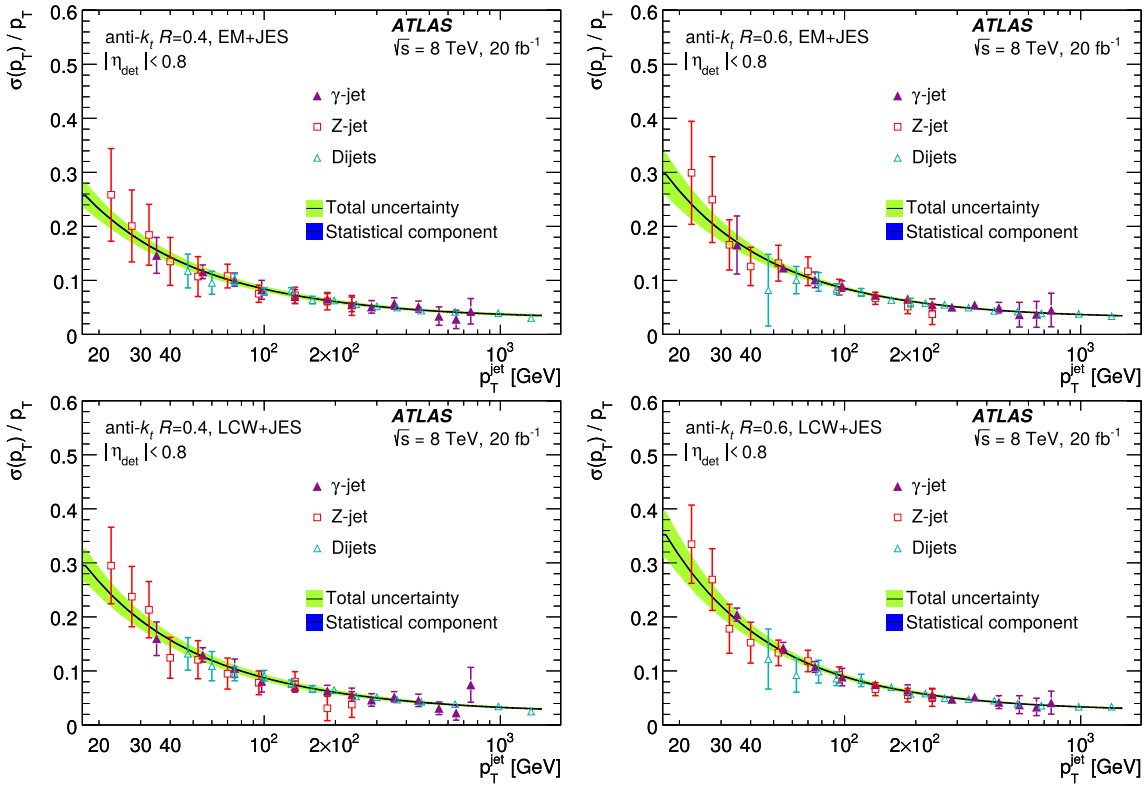

Fig. 57 The jet resolution as a function of p_{T} for the four different jet collections in the central region. The three in situ inputs to the measurement, namely Z+jet (empty squares), γ+jet (filled triangles), and dijet balance (empty triangles) are shown displaying the compatibility of the measurements. The final fit using the function in Eq. (24) is included with its associated statistical and total uncertainty

considered, and 71/35 (58/35) when correlations are considered. The relatively large size of the χ^2 per degree of freedom when correlations are considered indicates a limitation in the fitting function used. It is a possible indication of the need for higher-order terms in the series to better describe the resolution dependence on p_{T}. A similar effect is seen when looking at the fit to these three parameters in MC simulations.

When propagating the uncertainty in the noise term to the fit the resulting changes in the fitted values of N, S and C for anti-k_t $R = 0.4$ EM+JES (LCW+JES) jets are $^{+0.63}_{-0.63}$, $^{-0.038}_{+0.030}$, $^{+0.001}_{-0.001}$ $\left(^{+0.74}_{-0.74}, ^{-0.048}_{+0.039}, ^{+0.002}_{-0.002}\right)$. Again, correlations between the different components are observed, namely increasing N results in a reduced S and increased C.

To reduce the number of parameters which need to be propagated, the full set of eigenvectors is built according to the total effect on the JER measurement of each uncertainty component (rather than the effect of each component on the N, S and C terms individually). These uncertainty sources can then be reduced in number by using an eigenvector decomposition (diagonalization) as was done for the JES. This allows the full correlations to be retained and propagated to analyses. Figure 56 shows the three eigenvectors after this diagonalization. Combining in quadrature the results from varying N and propagating the in situ uncertainties gives $N = 3.33 \pm 0.63$ (4.12 ± 0.74) GeV, $S = 0.71 \pm 0.07$ (0.74 ± 0.10) $\sqrt{\mathrm{GeV}}$, and $C = 0.030 \pm 0.003$ (0.023 ± 0.003) for anti-k_t $R = 0.4$ EM+JES (LCW+JES) jets. Figure 57 shows the individual measurements of the resolution in the central region, the result of the combination, and the associated uncertainty. The uncertainty in the jet energy resolution for anti-k_t $R = 0.4$ jets is less than 0.03 at 20 GeV and below 0.01 above 100 GeV.

When considering the more forward $|\eta|$ bins, the large statistical uncertainty in Z+jet and γ+jet events means that only dijet measurements are useful. These are combined with the measured noise term in data in the same way as in the central region. For LCW+JES anti-k_t $R = 0.4$ jets all the different regions are shown in Fig. 58 and the extracted N, S, and C parameters for all jet collections are shown in Tables 6 and 7.

Finally, to account for correlations between the measurements at different $|\eta|$ a correlation matrix as a function of p_{T} and $|\eta|$ is built. The systematic uncertainties of the noise term and dijet balance results are assumed to be correlated between $|\eta|$ regions. The eigenvector reduction is performed, which results in, at most, 12 uncertainty components required

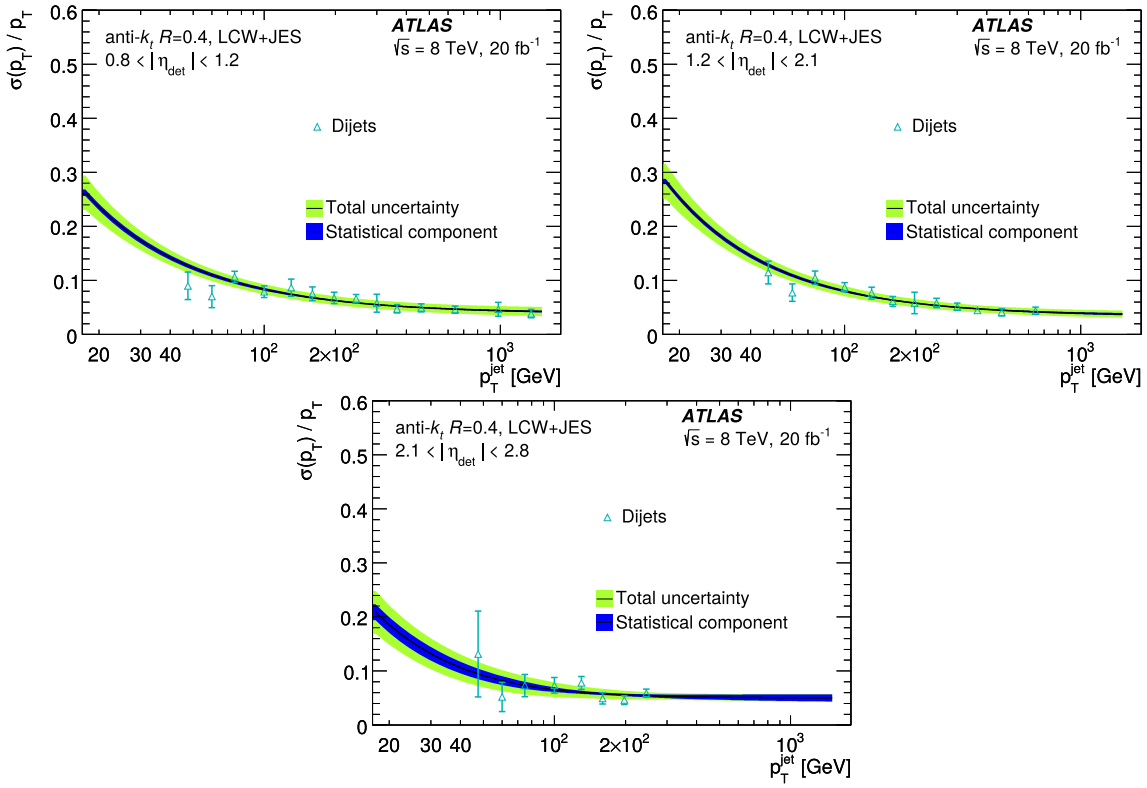

Fig. 58 The jet resolution as a function of p_{T} for LCW+JES anti-k_t $R = 0.4$ jets in three more-forward regions. The dijet in situ inputs (empty triangles) to the measurement are shown. The final fit using the function in Eq. (24) is included with its associated statistical and total uncertainty

Table 6 Extracted values of the N, S, and C terms from a combined fit to the jet energy resolution measurements for $R = 0.4$ and $R = 0.6$ jets, both calibrated with the EM+JES scheme. The quoted uncertainties of the N, S, and C terms are highly correlated with each other

$\lvert\eta\rvert$ Range	EM+JES, $R = 0.4$			EM+JES, $R = 0.6$		
	N (GeV)	S (GeV$^{0.5}$)	C	N (GeV)	S (GeV$^{0.5}$)	C
(0, 0.8)	3.33 ± 0.63	0.71 ± 0.07	0.030 ± 0.003	4.34 ± 0.93	0.67 ± 0.08	0.030 ± 0.003
(0.8, 1.2)	3.04 ± 0.70	0.69 ± 0.13	0.036 ± 0.003	4.06 ± 0.93	0.76 ± 0.10	0.031 ± 0.003
(1.2, 2.1)	3.34 ± 0.80	0.61 ± 0.16	0.044 ± 0.008	3.96 ± 0.91	0.56 ± 0.14	0.042 ± 0.007
(2.1, 2.8)	2.9 ± 1.0	0.46 ± 0.30	0.053 ± 0.011	3.41 ± 0.84	0.48 ± 0.27	0.049 ± 0.012

Table 7 Extracted values of the N, S, and C terms from a combined fit to the jet energy resolution measurements for $R = 0.4$ and $R = 0.6$ jets, both calibrated with the LCW+JES scheme. The uncertainties shown are highly correlated between the N, S, and C terms

$\lvert\eta\rvert$ Range	LCW+JES, $R = 0.4$			LCW+JES, $R = 0.6$		
	N (GeV)	S (GeV$^{0.5}$)	C	N (GeV)	S (GeV$^{0.5}$)	C
(0, 0.8)	4.12 ± 0.74	0.74 ± 0.10	0.023 ± 0.003	5.50 ± 0.99	0.66 ± 0.12	0.026 ± 0.004
(0.8, 1.2)	3.66 ± 0.75	0.64 ± 0.13	0.039 ± 0.009	5.40 ± 0.98	0.78 ± 0.15	0.032 ± 0.005
(1.2, 2.1)	4.27 ± 0.75	0.58 ± 0.15	0.034 ± 0.007	5.7 ± 1.0	0.62 ± 0.16	0.031 ± 0.006
(2.1, 2.8)	3.38 ± 0.65	0.26 ± 0.36	0.050 ± 0.010	5.2 ± 1.0	0.51 ± 0.38	0.028 ± 0.019

to capture all the correlations between the p_{T} and $|\eta|$ regions covered by the in situ studies.

11 Conclusions

This article describes the determination of the jet energy scale (JES) and jet energy resolution (JER) for data recorded by the ATLAS experiment in 2012 at $\sqrt{s} = 8$ TeV.

The calibration scheme used for anti-k_t jets reconstructed using radius parameter $R = 0.4$ or $R = 0.6$ corrects for pile-up and the location of the primary interaction point before performing a calibration based on MC simulation. These initial steps in the calibration provide stability of the calibration as a function of pile-up and improve the angular resolution of jets. Following the MC-simulation-derived baseline calibration, a global sequential correction is performed. It is also derived from MC simulations using information about how the jet deposits energy in the calorimeter, the tracks associated with the jet, and the activity in the muon chambers behind the jet (particularly important for high-p_{T} jets). This improves the resolution of jets and reduces the difference in energy scale between quark- and gluon-initiated jets.

Following these MC-based calibration steps, the data taken in 2012 are used to perform a residual calibration that constrains the uncertainties. This is performed for anti-k_t jets with $R = 0.4$ and $R = 0.6$ calibrated with both the EM+JES and LCW+JES schemes. Dijet events are used to calibrate jets in the forward region relative to the central region as a function of jet transverse momentum and pseudorapidity. The uncertainties of this calibration step have been significantly reduced compared with previous results primarily though the use of event generators with improved modelling of multijet production. The total uncertainties are typically below 1% for central jets, rising to 3.5% for low-p_{T} jets at high absolute pseudorapidity. Central jets are calibrated by exploiting the balance between jets recoiling against either a photon or a Z boson. In the pseudorapidity region $0.8 \leq |\eta_{\mathrm{det}}| < 2.8$, the jet energy scale is validated with Z+jet events using the direct p_{T} balance technique. The jet energy scale calibration for central jets with high p_{T} is determined using events in which an isolated high-p_{T} jet recoils against a system of lower-p_{T} jets. The final calibration is obtained through a statistical combination of the different measurements. This results in a correction at the level of 0.5% to the JES in data with an associated uncertainty of less than 1% for central anti-k_t $R = 0.4$ jets with $100 < p_{\mathrm{T}} < 1500$ GeV. At higher p_{T}, the uncertainty is about 3% as in situ measurements become statistically limited, and instead the calibration relies on single-hadron response studies.

The jet energy scale of trimmed anti-k_t jets with $R = 1.0$ is derived using MC simulation in the same way as for $R = 0.4$ and $R = 0.6$ jets, thus calibrating the jets to the LCW+JES scale. In an additional step, a dedicated calibration of the jet mass for the $R = 1.0$ jets is derived. The MC-derived calibration is tested in situ using the direct balance method with γ+jet events. These studies are used to evaluate uncertainties in the calibration. The total uncertainty for $|\eta_{\mathrm{det}}| < 0.8$ is found to be around 3% for jets with low p_{T}, falling to about 1% for jets with $p_{\mathrm{T}} \geq 150$ GeV. At larger $|\eta_{\mathrm{det}}|$, the uncertainty increases to 4−5% at low jet p_{T}, decreasing to 1−2% for $p_{\mathrm{T}} > 150$ GeV.

The JER is measured in 2012 data using several in situ methods. The JER pile-up noise term is determined using novel techniques that exploit the increased level of pile-up interactions in the 2012 data. Three measurements of the JER as a function of jet p_{T} and η_{det} are performed using γ+jet, Z+jet and dijet data. A final measurement of the JER is obtained using a statistical combination of these measurements, using a methodology similar to that used for the JES calibration. The different in situ inputs are found to be consistent with each other over the kinematic regions where they overlap. For anti-k_t $R = 0.4$ jets in the central calorimeter region $|\eta| < 0.8$ calibrated with the EM+JES calibration scheme, the JER resolution parameters are measured to be $N = 3.33 \pm 0.63$ GeV, $S = 0.71 \pm 0.07$ $\sqrt{\mathrm{GeV}}$, and $C = 0.030 \pm 0.003$, which corresponds to a relative JER of $\sigma_{p_{\mathrm{T}}}/p_{\mathrm{T}} = (23 \pm 2)\%$ for $p_{\mathrm{T}} = 20$ GeV and $\sigma_{p_{\mathrm{T}}}/p_{\mathrm{T}} = (8.4 \pm 0.6)\%$ for $p_{\mathrm{T}} = 100$ GeV. The jet energy resolution in data is generally well reproduced by the MC simulation. In certain kinematic regions, the simulated jets have a slightly smaller resolution than jets in data. In physics analyses, the p_{T} of the simulated jets is corrected by random smearing to match the resolution observed in data. The required amount of smearing is of similar order of magnitude as the jet energy resolution uncertainties.

Acknowledgements We thank CERN for the very successful operation of the LHC, as well as the support staff from our institutions without whom ATLAS could not be operated efficiently. We acknowledge the support of ANPCyT, Argentina; YerPhI, Armenia; ARC, Australia; BMWFW and FWF, Austria; ANAS, Azerbaijan; SSTC, Belarus; CNPq and FAPESP, Brazil; NSERC, NRC and CFI, Canada; CERN; CONICYT, Chile; CAS, MOST and NSFC, China; COLCIENCIAS, Colombia; MSMT CR, MPO CR and VSC CR, Czech Republic; DNRF and DNSRC, Denmark; IN2P3-CNRS and CEA-DRF/IRFU, France; SRNSFG, Georgia; BMBF, HGF and MPG, Germany; GSRT, Greece; RGC and Hong Kong SAR, China; ISF and Benoziyo Center, Israel; INFN, Italy; MEXT and JSPS, Japan; CNRST, Morocco; NWO, Netherlands; RCN, Norway; MNiSW and NCN, Poland; FCT, Portugal; MNE/IFA, Romania; MES of Russia and NRC KI, Russia Federation; JINR; MESTD, Serbia; MSSR, Slovakia; ARRS and MIZŠ, Slovenia; DST/NRF, South Africa; MINECO, Spain; SRC and Wallenberg Foundation, Sweden; SERI, SNSF and Cantons of Bern and Geneva, Switzerland; MOST, Taiwan; TAEK, Turkey; STFC, United Kingdom; DOE and NSF, United States of America. In addition, individual groups and members have received support from BCKDF, CANARIE, Compute Canada and CRC, Canada; ERC, ERDF, Horizon 2020, Marie Skłodowska-Curie Actions and COST, European Union;

Investissements d'Avenir Labex, Investissements d'Avenir Idex and ANR, France; DFG and AvH Foundation, Germany; Herakleitos, Thales and Aristeia programmes co-financed by EU-ESF and the Greek NSRF, Greece; BSF-NSF and GIF, Israel; CERCA Programme Generalitat de Catalunya and PROMETEO Programme Generalitat Valenciana, Spain; Göran Gustafssons Stiftelse, Sweden; The Royal Society and Leverhulme Trust, United Kingdom.
The crucial computing support from all WLCG partners is acknowledged gratefully, in particular from CERN, the ATLAS Tier-1 facilities at TRIUMF (Canada), NDGF (Denmark, Norway, Sweden), CC-IN2P3 (France), KIT/GridKA (Germany), INFN-CNAF (Italy), NL-T1 (Netherlands), PIC (Spain), ASGC (Taiwan), RAL (UK) and BNL (USA), the Tier-2 facilities worldwide and large non-WLCG resource providers. Major contributors of computing resources are listed in Ref. [73].

Data Availability Statement This manuscript has no associated data or the data will not be deposited. [Authors' comment: All ATLAS scientific output is published in journals, and preliminary results are made available in Conference Notes. All are openly available, without restriction on use by external parties beyond copyright law and the standard conditions agreed by CERN. Data associated with journal publications are also made available: tables and data from plots (e.g. cross section values, likelihood profiles, selection efficiencies, cross section limits, ...) are stored in appropriate repositories such as HEPDATA (http://hepdata.cedar.ac.uk/). ATLAS also strives to make additional material related to the paper available that allows a reinterpretation of the data in the context of new theoretical models. For example, an extended encapsulation of the analysis is often provided for measurements in the framework of RIVET (http://rivet.hepforge.org/)." This information is taken from the ATLAS Data Access Policy, which is a public document that can be downloaded from http://opendata.cern.ch/record/413 [opendata.cern.ch].

Funded by SCOAP[3].

References

1. ATLAS Collaboration, The ATLAS Experiment at the CERN Large Hadron Collider. JINST **3**, S08003 (2008)
2. M. Cacciari, G.P. Salam, G. Soyez, The anti-k(t) jet clustering algorithm. JHEP **04**, 063 (2008). arXiv:0802.1189 [hep-ph]
3. ATLAS Collaboration, Topological cell clustering in the ATLAS calorimeters and its performance in LHC Run 1. Eur. Phys. J. C **77**, 490 (2017). arXiv:1603.02934 [hep-ex]
4. ATLAS Collaboration, Measurement of inclusive jet and dijet cross sections in proton–proton collisions at 7 TeV centre-of-mass energy with the ATLAS detector. Eur. Phys. J. C **71**, 1512 (2011). arXiv:1009.5908 [hep-ex]
5. ATLAS Collaboration, Jet energy measurement with the ATLAS detector in proton–proton collisions at $\sqrt{s} = 7$ TeV. Eur. Phys. J. C **73**, 2304 (2013). arXiv:1112.6426 [hep-ex]
6. ATLAS Collaboration, Jet energy measurement and its systematic uncertainty in proton–proton collisions at $\sqrt{s} = 7$ TeV with the ATLAS detector. Eur. Phys. J. C **75**, 17 (2015). arXiv:1406.0076 [hep-ex]
7. ATLAS Collaboration, Jet energy resolution in proton-proton collisions at $\sqrt{s} = 7$ TeV recorded in 2010 with the ATLAS detector. Eur. Phys. J. C **73**, 2306 (2013). arXiv:1210.6210 [hep-ex]
8. ATLAS Collaboration, Jet energy scale measurements and their systematic uncertainties in proton–proton collisions at $\sqrt{s} =$ 13 TeV with the ATLAS detector. Phys. Rev. D **96**, 072002 (2017). arXiv:1703.09665 [hep-ex]
9. ATLAS Collaboration, In situ calibration of large-radius jet energy and mass in 13 TeV proton–proton collisions with the ATLAS detector. Eur. Phys. J. C **79**, 135 (2019). arXiv:1807.09477 [hep-ex]
10. ATLAS Collaboration, Performance of the ATLAS Trigger System in 2010. Eur. Phys. J. C **72**, 1849 (2012). arXiv:1110.1530 [hep-ex]
11. ATLAS Collaboration, The performance of the jet trigger for the ATLAS detector during 2011 data taking. Eur. Phys. J. C **76**, 526 (2016). arXiv:1606.07759 [hep-ex]
12. ATLAS Collaboration, Luminosity determination in pp collisions at $\sqrt{s} = 8$ TeV using the ATLAS detector at the LHC. Eur. Phys. J. C **76**, 653 (2016). arXiv:1608.03953 [hep-ex]
13. ATLAS Collaboration, Drift Time Measurement in the ATLAS Liquid Argon Electromagnetic Calorimeter using Cosmic Muons. Eur. Phys. J. C **70**, 755 (2010). arXiv:1002.4189 [physics.ins-det]
14. H. Abreu et al., Performance of the electronic readout of the ATLAS liquid argon calorimeters. JINST **5**, P09003 (2010)
15. A. Buckley et al., General-purpose event generators for LHC physics. Phys. Rept. **504**, 145 (2011). arXiv:1101.2599 [hep-ph]
16. H.-L. Lai et al., New parton distributions for collider physics. Phys. Rev. D **82**, 074024 (2010). arXiv:1007.2241 [hep-ph]
17. ATLAS Collaboration, New ATLAS event generator tunes to 2010 data, ATL-PHYS-PUB-2011-008 (2011). https://cds.cern.ch/record/1345343
18. P.M. Nadolsky et al., Implications of CTEQ global analysis for collider observables. Phys. Rev. D **78**, 013004 (2008). arXiv:0802.0007 [hep-ph]
19. S. Gieseke, C. Rohr, A. Siodmok, Colour reconnections in Herwig++. Eur. Phys. J. C **72**, 2225 (2012). arXiv:1206.0041 [hep-ph]
20. ATLAS Collaboration, Further ATLAS tunes of Pythia 6 and Pythia 8, ATL-PHYS-PUB-2011-014 (2011). https://cds.cern.ch/record/1400677
21. T. Sjöstrand, M. van Zijl, A multiple interaction model for the event structure in hadron collisions. Phys. Rev. D **36**, 2019 (1987)
22. A. Martin, W. Stirling, R. Thorne, G. Watt, Parton distributions for the LHC. Eur. Phys. J. C **63**, 189 (2009). arXiv:0901.0002 [hep-ph]
23. ATLAS Collaboration, Summary of ATLAS Pythia 8 tunes, ATL-PHYS-PUB-2012-003 (2012). https://cds.cern.ch/record/1474107
24. T. Sjöstrand, S. Mrenna, P.Z. Skands, A brief introduction to PYTHIA 8.1. Comput. Phys. Commun. **178**, 852 (2008). arXiv:0710.3820 [hep-ph]
25. B. Andersson, G. Gustafson, G. Ingelman, T. Sjöstrand, Parton fragmentation and string dynamics. Phys. Rept. **97**, 31 (1983)
26. G. Corcella et al., HERWIG 6: An event generator for hadron emission reactions with interfering gluons (including supersymmetric processes). JHEP **01**, 010 (2001). arXiv:hep-ph/0011363
27. M. Bahr et al., Herwig++ physics and manual. Eur. Phys. J. C **58**, 639 (2008). arXiv:0803.0883 [hep-ph]
28. T. Gleisberg et al., Event generation with SHERPA 1.1. JHEP **02**, 007 (2009). arXiv:0811.4622 [hep-ph]
29. S. Catani, F. Krauss, R. Kuhn, B.R. Webber, QCD matrix elements + parton showers. JHEP **11**, 063 (2001). arXiv:hep-ph/0109231

30. J.-C. Winter, F. Krauss, G. Soff, A modified cluster-hadronization model. Eur. Phys. J. C **36**, 381 (2004). arXiv:hep-ph/0311085
31. P. Nason, A new method for combining NLO QCD with shower Monte Carlo algorithms. JHEP **11**, 040 (2004). arXiv:hep-ph/0409146
32. S. Frixione, P. Nason, C. Oleari, Matching NLO QCD computations with parton shower simulations: the POWHEG method. JHEP **11**, 070 (2007). arXiv:0709.2092
33. S. Alioli, P. Nason, C. Oleari, E. Re, A general framework for implementing NLO calculations in shower Monte Carlo programs: the POWHEG BOX. JHEP **06**, 043 (2010). arXiv:1002.2581 [hep-ph]
34. S. Alioli, K. Hamilton, P. Nason, C. Oleari, E. Re, Jet pair production in POWHEG. JHEP **04**, 081 (2011). arXiv:1012.3380 [hep-ph]
35. ATLAS Collaboration, The ATLAS simulation infrastructure. Eur. Phys. J. C **70**, 823 (2010). arXiv:1005.4568 [physics.ins-det]
36. S. Agostinelli et al., GEANT4 – a Simulation toolkit. Nucl. Instrum. Methods A **506**, 250 (2003)
37. G. Folger, J. Wellisch, String Parton Models in GEANT4, MOMT007 (2003). arXiv:nucl-th/0306007
38. ATLAS Collaboration, The simulation principle and performance of the ATLAS fast calorimeter simulation FastCaloSim, tech. rep. ATL-PHYS-PUB-2010-013 (2010)
39. M. Cacciari, G.P. Salam, Dispelling the N^3 myth for the k_t jet-finder. Phys. Lett. B **641**, 57 (2006). arXiv:hep-ph/0512210
40. M. Cacciari, G.P. Salam, G. Soyez, FastJet user manual. Eur. Phys. J. C **72**, 1896 (2012). arXiv:1111.6097 [hep-ph]
41. M. Aharrouche et al., Measurement of the response of the ATLAS liquid argon barrel calorimeter to electrons at the 2004 combined test-beam. Nucl. Instrum. Methods A **614**, 400 (2010)
42. M. Aharrouche et al., Response uniformity of the ATLAS liquid argon electromagnetic calorimeter. Nucl. Instrum. Methods A **582**, 429 (2007). arXiv:0709.1094 [physics.ins-det]
43. M. Aharrouche et al., Energy linearity and resolution of the ATLAS electromagnetic barrel calorimeter in an electron test-beam. Nucl. Instrum. Methods A **568**, 601 (2006). arXiv:physics/0608012
44. ATLAS Collaboration, Electron performance measurements with the ATLAS detector using the 2010 LHC proton–proton collision data. Eur. Phys. J. C **72**, 1909 (2012). arXiv:1110.3174 [hep-ex]
45. ATLAS Collaboration, Performance of jet substructure techniques for large-R jets in proton–proton collisions at $\sqrt{s} = 7$ TeV using the ATLAS detector. JHEP **09**, 076 (2013). arXiv:1306.4945 [hep-ex]
46. ATLAS Collaboration, Jet mass and substructure of inclusive jets in $\sqrt{s} = 7$ TeV pp collisions with the ATLAS experiment. JHEP **05**, 128 (2012). arXiv:1203.4606 [hep-ex]
47. ATLAS Collaboration, Identification of boosted, hadronically decaying W bosons and comparisons with ATLAS data taken at $\sqrt{s} = 8$ TeV. Eur. Phys. J. C **76**, 154 (2016). arXiv:1510.05821 [hep-ex]
48. ATLAS Collaboration, Identification of high transverse momentum top quarks in pp collisions at $\sqrt{s} = 8$ TeV with the ATLAS detector. JHEP **06**, 093 (2016). arXiv:1603.03127 [hep-ex]
49. D. Krohn, J. Thaler, L.-T. Wang, Jet Trimming. JHEP **02**, 084 (2010). arXiv:0912.1342 [hep-ph]
50. S. Catani, Y.L. Dokshitzer, M.H. Seymour, B.R. Webber, Longitudinally-invariant k_t-clustering algorithms for hadron hadron collisions. Nucl. Phys. B **406**, 187 (1993)
51. ATLAS Collaboration, Performance of pile-up mitigation techniques for jets in pp collisions at $\sqrt{s} = 8$ TeV using the ATLAS detector. Eur. Phys. J. C **76**, 581 (2016). arXiv:1510.03823 [hep-ex]
52. ATLAS Collaboration, Measurement of Higgs boson production in the diphoton decay channel in pp collisions at center-of-mass energies of 7 and 8 TeV with the ATLAS detector. Phys. Rev. D **90**, 112015 (2014). arXiv:1408.7084 [hep-ex]
53. M. Cacciari, G.P. Salam, Pileup subtraction using jet areas. Phys. Lett. B **659**, 119 (2008). arXiv:0707.1378 [hep-ph]
54. M. Cacciari, G.P. Salam, G. Soyez, The catchment area of jets. JHEP **04**, 005 (2008). arXiv:0802.1188 [hep-ph]
55. ATLAS Collaboration, Measurement of the muon reconstruction performance of the ATLAS detector using 2011 and 2012 LHC proton-proton collision data. Eur. Phys. J. C **74**, 3130 (2014). arXiv:1407.3935 [hep-ex]
56. ATLAS Collaboration, Light-quark and gluon jet discrimination in pp collisions at $\sqrt{s} = 7$ TeV with the ATLAS detector. Eur. Phys. J. C **74**, 3023 (2014). arXiv:1405.6583 [hep-ex]
57. V. Lendermann et al., Combining Triggers in HEP data analysis. Nucl. Instrum. Methods A **604**, 707 (2009). arXiv:0901.4118 [hep-ex]
58. G. Bohm, G. Zech, Introduction to statistics and data analysis for physicists. Verl. Dt. Elektronen-Synchrotron (2010). http://dx.doi.org/10.3204/PUBDB-2017-08987
59. ATLAS Collaboration, Measurement of the muon reconstruction performance of the ATLAS detector using 2011 and 2012 LHC proton–proton collision data. Eur. Phys. J. C **74**, 3130 (2014). arXiv:1407.3935 [hep-ex]
60. D0 Collaboration, Determination of the absolute jet energy scale in the D0 calorimeters. Nucl. Instrum. Methods A **424**, 352 (1999). arXiv:hep-ex/9805009
61. ATLAS Collaboration, Performance of algorithms that reconstruct missing transverse momentum in $\sqrt{s} = 8$ TeV proton-proton collisions in the ATLAS detector. Eur. Phys. J. C **77**, 241 (2017). arXiv:1609.09324 [hep-ex]
62. ATLAS Collaboration, Measurement of the photon identification efficiencies with the ATLAS detector using LHC Run-1 data. Eur. Phys. J. C **76**, 666 (2016). arXiv:1606.01813 [hep-ex]
63. ATLAS Collaboration, Performance of the electron and photon trigger in pp collisions at $\sqrt{s} = 7$ TeV with the ATLAS Detector at the LHC, ATLAS-CONF-2011-114 (2011). https://cds.cern.ch/record/1375551
64. ATLAS Collaboration, Performance of the ATLAS muon trigger in pp collisions at $\sqrt{s} = 8$ TeV. Eur. Phys. J. C **75**, 120 (2015). arXiv:1408.3179 [hep-ex]
65. ATLAS Collaboration, Electron efficiency measurements with the ATLAS detector using 2012 LHC proton–proton collision data. Eur. Phys. J. C **77**, 195 (2017). arXiv:1612.01456 [hep-ex]
66. J. Beringer et al., Review of particle physics. Phys. Rev. D **86**, 010001 (2012)
67. CMS Collaboration, Jet energy scale and resolution in the CMS experiment in pp collisions at 8 TeV. JINST **12**, P02014 (2017). arXiv:1607.03663 [hep-ex]
68. ATLAS Collaboration, Single hadron response measurement and calorimeter jet energy scale uncertainty with the ATLAS detector at the LHC. Eur. Phys. J. C **73**, 2305 (2013). arXiv:1203.1302 [hep-ex]
69. ATLAS Collaboration, A method for the construction of strongly reduced representations of ATLAS experimental uncertainties and the application thereof to the jet energy scale, ATL-PHYS-PUB-2015-014 (2015). https://cds.cern.ch/record/2037436
70. ATLAS Collaboration, Measurement of Dijet Azimuthal Decorrelations in pp Collisions at $\sqrt{s} = 7$ TeV. Phys. Rev. Lett. **106**, 172002 (2011). arXiv:1102.2696 [hep-ex]
71. ATLAS Collaboration, Charged-particle multiplicities in pp interactions measured with the ATLAS detector at the LHC. New J. Phys. **13**, 053033 (2011). arXiv:1012.5104 [hep-ex]
72. G.P. Salam, Towards jetography. Eur. Phys. J. C **67**, 637 (2010). arXiv:0906.1833 [hep-ph]
73. ATLAS Collaboration, ATLAS Computing Acknowledgements, ATL-GEN-PUB-2016-002 (2016). https://cds.cern.ch/record/2202407

ATLAS Collaboration

M. Aaboud[35d], G. Aad[101], B. Abbott[128], O. Abdinov[13,*], B. Abeloos[64], S. H. Abidi[167], O. S. AbouZeid[145], N. L. Abraham[155], H. Abramowicz[161], H. Abreu[160], Y. Abulaiti[6], B. S. Acharya[66a,66b,p], S. Adachi[163], C. Adam Bourdarios[64], L. Adamczyk[83a], J. Adelman[120], M. Adersberger[113], T. Adye[143], A. A. Affolder[145], Y. Afik[160], C. Agheorghiesei[27c], J. A. Aguilar-Saavedra[139a,139f], F. Ahmadov[79,ai], G. Aielli[73a,73b], S. Akatsuka[85], T. P. A. Åkesson[96], E. Akilli[53], A. V. Akimov[110], G. L. Alberghi[23a,23b], J. Albert[176], P. Albicocco[50], M. J. Alconada Verzini[88], S. Alderweireldt[118], M. Aleksa[36], I. N. Aleksandrov[79], C. Alexa[27b], G. Alexander[161], T. Alexopoulos[10], M. Alhroob[128], B. Ali[141], G. Alimonti[68a], J. Alison[37], S. P. Alkire[147], C. Allaire[64], B. M. M. Allbrooke[155], B. W. Allen[131], P. P. Allport[21], A. Aloisio[69a,69b], A. Alonso[40], F. Alonso[88], C. Alpigiani[147], A. A. Alshehri[56], M. I. Alstaty[101], B. Alvarez Gonzalez[36], D. Álvarez Piqueras[174], M. G. Alviggi[69a,69b], B. T. Amadio[18], Y. Amaral Coutinho[80b], L. Ambroz[134], C. Amelung[26], D. Amidei[105], S. P. Amor Dos Santos[139a,139c], S. Amoroso[36], C. S. Amrouche[53], C. Anastopoulos[148], L. S. Ancu[53], N. Andari[21], T. Andeen[11], C. F. Anders[60b], J. K. Anders[20], K. J. Anderson[37], A. Andreazza[68a,68b], V. Andrei[60a], S. Angelidakis[38], I. Angelozzi[119], A. Angerami[39], A. V. Anisenkov[121a,121b], A. Annovi[71a], C. Antel[60a], M. T. Anthony[148], M. Antonelli[50], D. J. A. Antrim[171], F. Anulli[72a], M. Aoki[81], L. Aperio Bella[36], G. Arabidze[106], Y. Arai[81], J. P. Araque[139a], V. Araujo Ferraz[80b], R. Araujo Pereira[80b], A. T. H. Arce[48], R. E. Ardell[93], F. A. Arduh[88], J-F. Arguin[109], S. Argyropoulos[77], A. J. Armbruster[36], L. J. Armitage[92], O. Arnaez[167], H. Arnold[119], M. Arratia[32], O. Arslan[24], A. Artamonov[123,*], G. Artoni[134], S. Artz[99], S. Asai[163], N. Asbah[45], A. Ashkenazi[161], E. M. Asimakopoulou[172], L. Asquith[155], K. Assamagan[29], R. Astalos[28a], R. J. Atkin[33a], M. Atkinson[173], N. B. Atlay[150], K. Augsten[141], G. Avolio[36], R. Avramidou[59a], B. Axen[18], M. K. Ayoub[15a], G. Azuelos[109,ax], A. E. Baas[60a], M. J. Baca[21], H. Bachacou[144], K. Bachas[67a,67b], M. Backes[134], P. Bagnaia[72a,72b], M. Bahmani[84], H. Bahrasemani[151], A. J. Bailey[174], J. T. Baines[143], M. Bajic[40], O. K. Baker[183], P. J. Bakker[119], D. Bakshi Gupta[95], E. M. Baldin[121a,121b], P. Balek[180], F. Balli[144], W. K. Balunas[136], E. Banas[84], A. Bandyopadhyay[24], Sw. Banerjee[181,j], A. A. E. Bannoura[182], L. Barak[161], W. M. Barbe[38], E. L. Barberio[104], D. Barberis[54a,54b], M. Barbero[101], T. Barillari[114], M.-S. Barisits[36], J. Barkeloo[131], T. Barklow[152], N. Barlow[32], R. Barnea[160], S. L. Barnes[59c], B. M. Barnett[143], R. M. Barnett[18], Z. Barnovska-Blenessy[59a], A. Baroncelli[74a], G. Barone[26], A. J. Barr[134], L. Barranco Navarro[174], F. Barreiro[98], J. Barreiro Guimarães da Costa[15a], R. Bartoldus[152], A. E. Barton[89], P. Bartos[28a], A. Basalaev[137], A. Bassalat[64,ar], R. L. Bates[56], S. J. Batista[167], S. Batlamous[35e], J. R. Batley[32], M. Battaglia[145], M. Bauce[72a,72b], F. Bauer[144], K. T. Bauer[171], H. S. Bawa[31,n], J. B. Beacham[126], M. D. Beattie[89], T. Beau[135], P. H. Beauchemin[170], P. Bechtle[24], H. C. Beck[52], H. P. Beck[20,s], K. Becker[51], M. Becker[99], C. Becot[124], A. Beddall[12d], A. J. Beddall[12a], V. A. Bednyakov[79], M. Bedognetti[119], C. P. Bee[154], T. A. Beermann[36], M. Begalli[80b], M. Begel[29], A. Behera[154], J. K. Behr[45], A. S. Bell[94], G. Bella[161], L. Bellagamba[23b], A. Bellerive[34], M. Bellomo[160], K. Belotskiy[111], N. L. Belyaev[111], O. Benary[161,*], D. Benchekroun[35a], M. Bender[113], N. Benekos[10], Y. Benhammou[161], E. Benhar Noccioli[183], J. Benitez[77], D. P. Benjamin[48], M. Benoit[53], J. R. Bensinger[26], S. Bentvelsen[119], L. Beresford[134], M. Beretta[50], D. Berge[45], E. Bergeaas Kuutmann[172], N. Berger[5], L. J. Bergsten[26], J. Beringer[18], S. Berlendis[57], N. R. Bernard[102], G. Bernardi[135], C. Bernius[152], F. U. Bernlochner[24], T. Berry[93], P. Berta[99], C. Bertella[15a], G. Bertoli[44a,44b], I. A. Bertram[89], C. Bertsche[45], G. J. Besjes[40], O. Bessidskaia Bylund[44a,44b], M. Bessner[45], N. Besson[144], A. Bethani[100], S. Bethke[114], A. Betti[24], A. J. Bevan[92], J. Beyer[114], R. M. Bianchi[138], O. Biebel[113], D. Biedermann[19], R. Bielski[100], K. Bierwagen[99], N. V. Biesuz[71a,71b], M. Biglietti[74a], T. R. V. Billoud[109], M. Bindi[52], A. Bingul[12d], C. Bini[72a,72b], S. Biondi[23a,23b], T. Bisanz[52], C. Bittrich[47], D. M. Bjergaard[48], J. E. Black[152], K. M. Black[25], R. E. Blair[6], T. Blazek[28a], I. Bloch[45], C. Blocker[26], A. Blue[56], U. Blumenschein[92], S. Blunier[146a], G. J. Bobbink[119], V. S. Bobrovnikov[121a,121b], S. S. Bocchetta[96], A. Bocci[48], C. Bock[113], D. Boerner[182], D. Bogavac[113], A. G. Bogdanchikov[121a,121b], C. Bohm[44a], V. Boisvert[93], P. Bokan[172,52], T. Bold[83a], A. S. Boldyrev[112], A. E. Bolz[60b], M. Bomben[135], M. Bona[92], J. S. Bonilla[131], M. Boonekamp[144], A. Borisov[122], G. Borissov[89], J. Bortfeldt[36], D. Bortoletto[134], V. Bortolotto[62b,62c,73a,73b], D. Boscherini[23b], M. Bosman[14], J. D. Bossio Sola[30], J. Boudreau[138], E. V. Bouhova-Thacker[89], D. Boumediene[38], S. K. Boutle[56], A. Boveia[126], J. Boyd[36], I. R. Boyko[79], A. J. Bozson[93], J. Bracinik[21], N. Brahimi[101], A. Brandt[8], G. Brandt[182], O. Brandt[60a], F. Braren[45], U. Bratzler[164], B. Brau[102], J. E. Brau[131], W. D. Breaden Madden[56], K. Brendlinger[45], A. J. Brennan[104], L. Brenner[45], R. Brenner[172], S. Bressler[180], B. Brickwedde[99], D. L. Briglin[21], T. M. Bristow[49], D. Britton[56], D. Britzger[60b], I. Brock[24], R. Brock[106], G. Brooijmans[39], T. Brooks[93], W. K. Brooks[146c], E. Brost[120], J. H. Broughton[21], P. A. Bruckman de Renstrom[84], D. Bruncko[28b], A. Bruni[23b], G. Bruni[23b], L. S. Bruni[119], S. Bruno[73a,73b], B. H. Brunt[32], M. Bruschi[23b], N. Bruscino[138], P. Bryant[37], L. Bryngemark[45], T. Buanes[17], Q. Buat[36], P. Buchholz[150], A. G. Buckley[56], I. A. Budagov[79], M. K. Bugge[133], F. Bührer[51], O. Bulekov[111], D. Bullock[8], T. J. Burch[120], S. Burdin[90], C. D. Burgard[119], A. M. Burger[5], B. Burghgrave[120], S. Burke[143], I. Burmeister[46], J. T. P. Burr[134], D. Büscher[51], V. Büscher[99], E. Buschmann[52], P. J. Bussey[56], J. M. Butler[25], C. M. Buttar[56], J. M. Butterworth[94], P. Butti[36], W. Buttinger[36],

A. Buzatu[157], A. R. Buzykaev[121a,121b], G. Cabras[23b,23a], S. Cabrera Urbán[174], D. Caforio[141], H. Cai[173], V. M. M. Cairo[2], O. Cakir[4a], N. Calace[53], P. Calafiura[18], A. Calandri[101], G. Calderini[135], P. Calfayan[65], G. Callea[41a,41b], L. P. Caloba[80b], S. Calvente Lopez[98], D. Calvet[38], S. Calvet[38], T. P. Calvet[154], M. Calvetti[71a,71b], R. Camacho Toro[37], S. Camarda[36], P. Camarri[73a,73b], D. Cameron[133], R. Caminal Armadans[102], C. Camincher[57], S. Campana[36], M. Campanelli[94], A. Camplani[68a,68b], A. Campoverde[150], V. Canale[69a,69b], M. Cano Bret[59c], J. Cantero[129], T. Cao[161], Y. Cao[173], M. D. M. Capeans Garrido[36], I. Caprini[27b], M. Caprini[27b], M. Capua[41b,41a], R. M. Carbone[39], R. Cardarelli[73a], F. Cardillo[51], I. Carli[142], T. Carli[36], G. Carlino[69a], B. T. Carlson[138], L. Carminati[68a,68b], R. M. D. Carney[44a,44b], S. Caron[118], E. Carquin[146c], S. Carrá[68a,68b], G. D. Carrillo-Montoya[36], D. Casadei[33c], M. P. Casado[14,f], A. F. Casha[167], M. Casolino[14], D. W. Casper[171], R. Castelijn[119], V. Castillo Gimenez[174], N. F. Castro[139a,139e], A. Catinaccio[36], J. R. Catmore[133], A. Cattai[36], J. Caudron[24], V. Cavaliere[29], E. Cavallaro[14], D. Cavalli[68a], M. Cavalli-Sforza[14], V. Cavasinni[71a,71b], E. Celebi[12b], F. Ceradini[74a,74b], L. Cerda Alberich[174], A. S. Cerqueira[80a], A. Cerri[155], L. Cerrito[73a,73b], F. Cerutti[18], A. Cervelli[23a,23b], S. A. Cetin[12b], A. Chafaq[35a], D. Chakraborty[120], S. K. Chan[58], W. S. Chan[119], Y. L. Chan[62a], P. Chang[173], J. D. Chapman[32], D. G. Charlton[21], C. C. Chau[34], C. A. Chavez Barajas[155], S. Che[126], A. Chegwidden[106], S. Chekanov[6], S. V. Chekulaev[168a], G. A. Chelkov[79,aw], M. A. Chelstowska[36], C. Chen[59a], C. H. Chen[78], H. Chen[29], J. Chen[59a], J. Chen[39], S. Chen[136], S. J. Chen[15c], X. Chen[15b,av], Y. Chen[82], Y-H. Chen[45], H. C. Cheng[105], H. J. Cheng[15a], A. Cheplakov[79], E. Cheremushkina[122], R. Cherkaoui El Moursli[35e], E. Cheu[7], K. Cheung[63], L. Chevalier[144], V. Chiarella[50], G. Chiarelli[71a], G. Chiodini[67a], A. S. Chisholm[36], A. Chitan[27b], I. Chiu[163], Y. H. Chiu[176], M. V. Chizhov[79], K. Choi[65], A. R. Chomont[64], S. Chouridou[162], Y. S. Chow[119], V. Christodoulou[94], M. C. Chu[62a], J. Chudoba[140], A. J. Chuinard[103], J. J. Chwastowski[84], L. Chytka[130], D. Cinca[46], V. Cindro[91], I. A. Cioară[24], A. Ciocio[18], F. Cirotto[69a,69b], Z. H. Citron[180,l], M. Citterio[68a], A. Clark[53], M. R. Clark[39], P. J. Clark[49], R. N. Clarke[18], C. Clement[44a,44b], Y. Coadou[101], M. Cobal[66a,66c], A. Coccaro[54b], J. Cochran[78], A. E. C. Coimbra[180], L. Colasurdo[118], B. Cole[39], A. P. Colijn[119], J. Collot[57], P. Conde Muiño[139a], E. Coniavitis[51], S. H. Connell[33c], I. A. Connelly[100], S. Constantinescu[27b], F. Conventi[69a,ay], A. M. Cooper-Sarkar[134], F. Cormier[175], K. J. R. Cormier[167], M. Corradi[72a,72b], E. E. Corrigan[96], F. Corriveau[103,ag], A. Cortes-Gonzalez[36], M. J. Costa[174], D. Costanzo[148], G. Cottin[32], G. Cowan[93], B. E. Cox[100], J. Crane[100], K. Cranmer[124], S. J. Crawley[56], R. A. Creager[136], G. Cree[34], S. Crépé-Renaudin[57], F. Crescioli[135], M. Cristinziani[24], V. Croft[124], G. Crosetti[41a,41b], A. Cueto[98], T. Cuhadar Donszelmann[148], A. R. Cukierman[152], M. Curatolo[50], J. Cúth[99], S. Czekierda[84], P. Czodrowski[36], M. J. Da Cunha Sargedas De Sousa[59b,139b], C. Da Via[100], W. Dabrowski[83a], T. Dado[28a,aa], S. Dahbi[35e], T. Dai[105], O. Dale[17], F. Dallaire[109], C. Dallapiccola[102], M. Dam[40], G. D'amen[23b,23a], J. R. Dandoy[136], M. F. Daneri[30], N. P. Dang[181,j], N. S. Dann[100], M. Danninger[175], V. Dao[36], G. Darbo[54b], O. Dartsi[5], A. Dattagupta[131], T. Daubney[45], S. D'Auria[56], W. Davey[24], C. David[45], T. Davidek[142], D. R. Davis[48], E. Dawe[104], I. Dawson[148], K. De[8], R. De Asmundis[69a], A. De Benedetti[128], S. De Castro[23a,23b], S. De Cecco[135], N. De Groot[118], P. de Jong[119], H. De la Torre[106], F. De Lorenzi[78], A. De Maria[52,u], D. De Pedis[72a], A. De Salvo[72a], U. De Sanctis[73a,73b], A. De Santo[155], K. De Vasconcelos Corga[101], J. B. De Vivie De Regie[64], C. Debenedetti[145], D. V. Dedovich[79], N. Dehghanian[3], A. M. Deiana[105], M. Del Gaudio[41a,41b], J. Del Peso[98], D. Delgove[64], F. Deliot[144], C. M. Delitzsch[7], M. Della Pietra[69a,69b], D. Della Volpe[53], A. Dell'Acqua[36], L. Dell'Asta[25], M. Delmastro[5], C. Delporte[64], P. A. Delsart[57], D. A. DeMarco[167], S. Demers[183], M. Demichev[79], S. P. Denisov[122], D. Denysiuk[119], L. D'Eramo[135], D. Derendarz[84], J. E. Derkaoui[35d], F. Derue[135], P. Dervan[90], K. Desch[24], C. Deterre[45], K. Dette[167], M. R. Devesa[30], P. O. Deviveiros[36], A. Dewhurst[143], S. Dhaliwal[26], F. A. Di Bello[53], A. Di Ciaccio[73a,73b], L. Di Ciaccio[5], W. K. Di Clemente[136], C. Di Donato[69a,69b], A. Di Girolamo[36], B. Di Micco[74a,74b], R. Di Nardo[36], K. F. Di Petrillo[58], A. Di Simone[51], R. Di Sipio[167], D. Di Valentino[34], C. Diaconu[101], M. Diamond[167], F. A. Dias[40], T. Dias Do Vale[139a], M. A. Diaz[146a], J. Dickinson[18], E. B. Diehl[105], J. Dietrich[19], S. Díez Cornell[45], A. Dimitrievska[18], J. Dingfelder[24], F. Dittus[36], F. Djama[101], T. Djobava[159b], J. I. Djuvsland[60a], M. A. B. Do Vale[80c], M. Dobre[27b], D. Dodsworth[26], C. Doglioni[96], J. Dolejsi[142], Z. Dolezal[142], M. Donadelli[80d], J. Donini[38], A. D'onofrio[92], M. D'Onofrio[90], J. Dopke[143], A. Doria[69a], M. T. Dova[88], A. T. Doyle[56], E. Drechsler[52], E. Dreyer[151], T. Dreyer[52], M. Dris[10], Y. Du[59b], J. Duarte-Campderros[161], F. Dubinin[110], A. Dubreuil[53], E. Duchovni[180], G. Duckeck[113], A. Ducourthial[135], O. A. Ducu[109,z], D. Duda[119], A. Dudarev[36], A. C. Dudder[99], E. M. Duffield[18], L. Duflot[64], M. Dührssen[36], C. Dülsen[182], M. Dumancic[180], A. E. Dumitriu[27b,d], A. K. Duncan[56], M. Dunford[60a], A. Duperrin[101], H. Duran Yildiz[4a], M. Düren[55], A. Durglishvili[159b], D. Duschinger[47], B. Dutta[45], D. Duvnjak[1], M. Dyndal[45], B. S. Dziedzic[84], C. Eckardt[45], K. M. Ecker[114], R. C. Edgar[105], T. Eifert[36], G. Eigen[17], K. Einsweiler[18], T. Ekelof[172], M. El Kacimi[35c], R. El Kosseifi[101], V. Ellajosyula[101], M. Ellert[172], F. Ellinghaus[182], A. A. Elliot[176], N. Ellis[36], J. Elmsheuser[29], M. Elsing[36], D. Emeliyanov[143], Y. Enari[163], J. S. Ennis[178], M. B. Epland[48], J. Erdmann[46], A. Ereditato[20], S. Errede[173], M. Escalier[64], C. Escobar[174], B. Esposito[50], O. Estrada Pastor[174], A. I. Etienvre[144], E. Etzion[161], H. Evans[65], A. Ezhilov[137], M. Ezzi[35e], F. Fabbri[23a,23b], L. Fabbri[23a,23b], V. Fabiani[118], G. Facini[94], R. M. Faisca Rodrigues Pereira[139a], R. M. Fakhrutdinov[122], S. Falciano[72a], P. J. Falke[5], S. Falke[5], J. Faltova[142], Y. Fang[15a], M. Fanti[68a,68b], A. Farbin[8],

A. Farilla[74a], E. M. Farina[70a,70b], T. Farooque[106], S. Farrell[18], S. M. Farrington[178], P. Farthouat[36], F. Fassi[35e], P. Fassnacht[36], D. Fassouliotis[9], M. Faucci Giannelli[49], A. Favareto[54a,54b], W. J. Fawcett[53], L. Fayard[64], O. L. Fedin[137,r], W. Fedorko[175], M. Feickert[42], S. Feigl[133], L. Feligioni[101], C. Feng[59b], E. J. Feng[36], M. Feng[48], M. J. Fenton[56], A. B. Fenyuk[122], L. Feremenga[8], J. Ferrando[45], A. Ferrari[172], P. Ferrari[119], R. Ferrari[70a], D. E. Ferreira de Lima[60b], A. Ferrer[174], D. Ferrere[53], C. Ferretti[105], F. Fiedler[99], A. Filipčič[91], F. Filthaut[118], M. Fincke-Keeler[176], K. D. Finelli[25], M. C. N. Fiolhais[139a,139c,a], L. Fiorini[174], C. Fischer[14], J. Fischer[182], W. C. Fisher[106], N. Flaschel[45], I. Fleck[150], P. Fleischmann[105], R. R. M. Fletcher[136], T. Flick[182], B. M. Flierl[113], L. Flores[136], L. R. Flores Castillo[62a], N. Fomin[17], G. T. Forcolin[100], A. Formica[144], F. A. Förster[14], A. C. Forti[100], A. G. Foster[21], D. Fournier[64], H. Fox[89], S. Fracchia[148], P. Francavilla[71a,71b], M. Franchini[23a,23b], S. Franchino[60a], D. Francis[36], L. Franconi[133], M. Franklin[58], M. Frate[171], M. Fraternali[70a,70b], D. Freeborn[94], S. M. Fressard-Batraneanu[36], B. Freund[109], W. S. Freund[80b], D. Froidevaux[36], J. A. Frost[134], C. Fukunaga[164], T. Fusayasu[115], J. Fuster[174], O. Gabizon[160], A. Gabrielli[23b,23a], A. Gabrielli[18], G. P. Gach[83a], S. Gadatsch[53], S. Gadomski[53], P. Gadow[114], G. Gagliardi[54a,54b], L. G. Gagnon[109], C. Galea[27b], B. Galhardo[139a,139c], E. J. Gallas[134], B. J. Gallop[143], P. Gallus[141], G. Galster[40], R. Gamboa Goni[92], K. K. Gan[126], S. Ganguly[180], Y. Gao[90], Y. S. Gao[31,n], C. García[174], J. E. García Navarro[174], J. A. García Pascual[15a], M. Garcia-Sciveres[18], R. W. Gardner[37], N. Garelli[152], V. Garonne[133], K. Gasnikova[45], A. Gaudiello[54a,54b], G. Gaudio[70a], I. L. Gavrilenko[110], A. Gavrilyuk[123], C. Gay[175], G. Gaycken[24], E. N. Gazis[10], C. N. P. Gee[143], J. Geisen[52], M. Geisen[99], M. P. Geisler[60a], K. Gellerstedt[44a,44b], C. Gemme[54b], M. H. Genest[57], C. Geng[105], S. Gentile[72a,72b], C. Gentsos[162], S. George[93], D. Gerbaudo[14], G. Gessner[46], S. Ghasemi[150], B. Giacobbe[23b], S. Giagu[72a,72b], N. Giangiacomi[23a,23b], P. Giannetti[71a], S. M. Gibson[93], M. Gignac[145], D. Gillberg[34], G. Gilles[182], D. M. Gingrich[3,ax], M. P. Giordani[66a,66c], F. M. Giorgi[23b], P. F. Giraud[144], P. Giromini[58], G. Giugliarelli[66a,66c], D. Giugni[68a], F. Giuli[134], M. Giulini[60b], S. Gkaitatzis[162], I. Gkialas[9,i], E. L. Gkougkousis[14], P. Gkountoumis[10], L. K. Gladilin[112], C. Glasman[98], J. Glatzer[14], P. C. F. Glaysher[45], A. Glazov[45], M. Goblirsch-Kolb[26], J. Godlewski[84], S. Goldfarb[104], T. Golling[53], D. Golubkov[122], A. Gomes[139a,139b], R. Goncalves Gama[80a], R. Gonçalo[139a], G. Gonella[51], L. Gonella[21], A. Gongadze[79], F. Gonnella[21], J. L. Gonski[58], S. González de la Hoz[174], S. Gonzalez-Sevilla[53], L. Goossens[36], P. A. Gorbounov[123], H. A. Gordon[29], B. Gorini[36], E. Gorini[67a,67b], A. Gorišek[91], A. T. Goshaw[48], C. Gössling[46], M. I. Gostkin[79], C. A. Gottardo[24], C. R. Goudet[64], D. Goujdami[35c], A. G. Goussiou[147], N. Govender[33c,b], C. Goy[5], E. Gozani[160], I. Grabowska-Bold[83a], P. O. J. Gradin[172], E. C. Graham[90], J. Gramling[171], E. Gramstad[133], S. Grancagnolo[19], V. Gratchev[137], P. M. Gravila[27f], C. Gray[56], H. M. Gray[18], Z. D. Greenwood[95], C. Grefe[24], K. Gregersen[94], I. M. Gregor[45], P. Grenier[152], K. Grevtsov[45], J. Griffiths[8], A. A. Grillo[145], K. Grimm[31,m], S. Grinstein[14,ac], Ph. Gris[38], J.-F. Grivaz[64], S. Groh[99], E. Gross[180], J. Grosse-Knetter[52], G. C. Grossi[95], Z. J. Grout[94], A. Grummer[117], L. Guan[105], W. Guan[181], J. Guenther[36], A. Guerguichon[64], F. Guescini[168a], D. Guest[171], O. Gueta[161], R. Gugel[51], B. Gui[126], T. Guillemin[5], S. Guindon[36], U. Gul[56], C. Gumpert[36], J. Guo[59c], W. Guo[105], Y. Guo[59a,t], Z. Guo[101], R. Gupta[42], S. Gupta[134], S. Gurbuz[12c], G. Gustavino[128], B. J. Gutelman[160], P. Gutierrez[128], N. G. Gutierrez Ortiz[94], C. Gutschow[94], C. Guyot[144], M. P. Guzik[83a], C. Gwenlan[134], C. B. Gwilliam[90], A. Haas[124], C. Haber[18], H. K. Hadavand[8], N. Haddad[35e], A. Hadef[101], S. Hageböck[24], M. Hagihara[169], H. Hakobyan[184,*], M. Haleem[177], J. Haley[129], G. Halladjian[106], G. D. Hallewell[101], K. Hamacher[182], P. Hamal[130], K. Hamano[176], A. Hamilton[33a], G. N. Hamity[148], K. Han[59a,ab], L. Han[59a], S. Han[15a], K. Hanagaki[81,x], M. Hance[145], D. M. Handl[113], B. Haney[136], R. Hankache[135], P. Hanke[60a], E. Hansen[96], J. B. Hansen[40], J. D. Hansen[40], M. C. Hansen[24], P. H. Hansen[40], E. C. Hanson[100], K. Hara[169], A. S. Hard[181], T. Harenberg[182], S. Harkusha[107], P. F. Harrison[178], N. M. Hartmann[113], Y. Hasegawa[149], A. Hasib[49], S. Hassani[144], S. Haug[20], R. Hauser[106], L. Hauswald[47], L. B. Havener[39], M. Havranek[141], C. M. Hawkes[21], R. J. Hawkings[36], D. Hayden[106], C. Hayes[154], C. P. Hays[134], J. M. Hays[92], H. S. Hayward[90], S. J. Haywood[143], M. P. Heath[49], V. Hedberg[96], L. Heelan[8], S. Heer[24], K. K. Heidegger[51], J. Heilman[34], S. Heim[45], T. Heim[18], B. Heinemann[45,as], J. J. Heinrich[113], L. Heinrich[124], C. Heinz[55], J. Hejbal[140], L. Helary[36], A. Held[175], S. Hellesund[133], S. Hellman[44a,44b], C. Helsens[36], R. C. W. Henderson[89], Y. Heng[181], S. Henkelmann[175], A. M. Henriques Correia[36], G. H. Herbert[19], H. Herde[26], V. Herget[177], Y. Hernández Jiménez[33e], H. Herr[99], G. Herten[51], R. Hertenberger[113], L. Hervas[36], T. C. Herwig[136], G. G. Hesketh[94], N. P. Hessey[168a], J. W. Hetherly[42], S. Higashino[81], E. Higón-Rodriguez[174], K. Hildebrand[37], E. Hill[176], J. C. Hill[32], K. H. Hiller[45], S. J. Hillier[21], M. Hils[47], I. Hinchliffe[18], M. Hirose[132], D. Hirschbuehl[182], B. Hiti[91], O. Hladik[140], D. R. Hlaluku[33e], X. Hoad[49], J. Hobbs[154], N. Hod[168a], M. C. Hodgkinson[148], A. Hoecker[36], M. R. Hoeferkamp[117], F. Hoenig[113], D. Hohn[24], D. Hohov[64], T. R. Holmes[37], M. Holzbock[113], M. Homann[46], S. Honda[169], T. Honda[81], T. M. Hong[138], A. Hönle[114], B. H. Hooberman[173], W. H. Hopkins[131], Y. Horii[116], P. Horn[47], A. J. Horton[151], L. A. Horyn[37], J-Y. Hostachy[57], A. Hostiuc[147], S. Hou[157], A. Hoummada[35a], J. Howarth[100], J. Hoya[88], M. Hrabovsky[130], J. Hrdinka[36], I. Hristova[19], J. Hrivnac[64], A. Hrynevich[108], T. Hryn'ova[5], P. J. Hsu[63], S.-C. Hsu[147], Q. Hu[29], S. Hu[59c], Y. Huang[15a], Z. Hubacek[141], F. Hubaut[101], M. Huebner[24], F. Huegging[24], T. B. Huffman[134], E. W. Hughes[39], M. Huhtinen[36], R. F. H. Hunter[34], P. Huo[154], A. M. Hupe[34], N. Huseynov[79,ai], J. Huston[106], J. Huth[58], R. Hyneman[105], G. Iacobucci[53],

G. Iakovidis[29], I. Ibragimov[150], L. Iconomidou-Fayard[64], Z. Idrissi[35e], P. Iengo[36], R. Ignazzi[40], O. Igonkina[119,ae,*], R. Iguchi[163], T. Iizawa[179], Y. Ikegami[81], M. Ikeno[81], D. Iliadis[162], N. Ilic[152], F. Iltzsche[47], G. Introzzi[70a,70b], M. Iodice[74a], K. Iordanidou[39], V. Ippolito[72a,72b], M. F. Isacson[172], N. Ishijima[132], M. Ishino[163], M. Ishitsuka[165], C. Issever[134], S. Istin[12c,ap], F. Ito[169], J. M. Iturbe Ponce[62a], R. Iuppa[75a,75b], A. Ivina[180], H. Iwasaki[81], J. M. Izen[43], V. Izzo[69a], S. Jabbar[3], P. Jacka[140], P. Jackson[1], R. M. Jacobs[24], V. Jain[2], G. Jäkel[182], K. B. Jakobi[99], K. Jakobs[51], S. Jakobsen[76], T. Jakoubek[140], D. O. Jamin[129], D. K. Jana[95], R. Jansky[53], J. Janssen[24], M. Janus[52], P. A. Janus[83a], G. Jarlskog[96], N. Javadov[79,ai], T. Javůrek[51], M. Javurkova[51], F. Jeanneau[144], L. Jeanty[18], J. Jejelava[159a,aj], A. Jelinskas[178], P. Jenni[51,c], J. Jeong[45], C. Jeske[178], S. Jézéquel[5], H. Ji[181], J. Jia[154], H. Jiang[78], Y. Jiang[59a], Z. Jiang[152], S. Jiggins[51], F. A. Jimenez Morales[38], J. Jimenez Pena[174], S. Jin[15c], A. Jinaru[27b], O. Jinnouchi[165], H. Jivan[33e], P. Johansson[148], K. A. Johns[7], C. A. Johnson[65], W. J. Johnson[147], K. Jon-And[44a,44b], R. W. L. Jones[89], S. D. Jones[155], S. Jones[7], T. J. Jones[90], J. Jongmanns[60a], P. M. Jorge[139a,139b], J. Jovicevic[168a], X. Ju[181], J. J. Junggeburth[114], A. Juste Rozas[14,ac], A. Kaczmarska[84], M. Kado[64], H. Kagan[126], M. Kagan[152], T. Kaji[179], E. Kajomovitz[160], C. W. Kalderon[96], A. Kaluza[99], S. Kama[42], A. Kamenshchikov[122], L. Kanjir[91], Y. Kano[163], V. A. Kantserov[111], J. Kanzaki[81], B. Kaplan[124], L. S. Kaplan[181], D. Kar[33e], M. J. Kareem[168b], E. Karentzos[10], S. N. Karpov[79], Z. M. Karpova[79], V. Kartvelishvili[89], A. N. Karyukhin[122], K. Kasahara[169], L. Kashif[181], R. D. Kass[126], A. Kastanas[153], Y. Kataoka[163], C. Kato[163], A. Katre[53], J. Katzy[45], K. Kawade[82], K. Kawagoe[87], T. Kawamoto[163], G. Kawamura[52], E. F. Kay[90], V. F. Kazanin[121a,121b], R. Keeler[176], R. Kehoe[42], J. S. Keller[34], E. Kellermann[96], J. J. Kempster[21], J. Kendrick[21], O. Kepka[140], S. Kersten[182], B. P. Kerševan[91], R. A. Keyes[103], M. Khader[173], F. Khalil-Zada[13], A. Khanov[129], A. G. Kharlamov[121a,121b], T. Kharlamova[121b,121a], A. Khodinov[166], T. J. Khoo[53], V. Khovanskiy[123,*], E. Khramov[79], J. Khubua[159b], S. Kido[82], M. Kiehn[53], C. R. Kilby[93], H. Y. Kim[8], S. H. Kim[169], Y. K. Kim[37], N. Kimura[66a,66c], O. M. Kind[19], B. T. King[90,*], D. Kirchmeier[47], J. Kirk[143], A. E. Kiryunin[114], T. Kishimoto[163], D. Kisielewska[83a], V. Kitali[45], O. Kivernyk[5], E. Kladiva[28b,*], T. Klapdor-Kleingrothaus[51], M. H. Klein[105], M. Klein[90], U. Klein[90], K. Kleinknecht[99], P. Klimek[120], A. Klimentov[29], R. Klingenberg[46,*], T. Klingl[24], T. Klioutchnikova[36], F. F. Klitzner[113], P. Kluit[119], S. Kluth[114], E. Kneringer[76], E. B. F. G. Knoops[101], A. Knue[51], A. Kobayashi[163], D. Kobayashi[87], T. Kobayashi[163], M. Kobel[47], M. Kocian[152], P. Kodys[142], T. Koffas[34], E. Koffeman[119], L. A. Kogan[134], N. M. Köhler[114], T. Koi[152], M. Kolb[60b], I. Koletsou[5], T. Kondo[81], N. Kondrashova[59c], K. Köneke[51], A. C. König[118], T. Kono[125,aq], R. Konoplich[124,am], N. Konstantinidis[94], B. Konya[96], R. Kopeliansky[65], S. Koperny[83a], K. Korcyl[84], K. Kordas[162], A. Korn[94], I. Korolkov[14], E. V. Korolkova[148], O. Kortner[114], S. Kortner[114], T. Kosek[142], V. V. Kostyukhin[24], A. Kotwal[48], A. Koulouris[10], A. Kourkoumeli-Charalampidi[70a,70b], C. Kourkoumelis[9], E. Kourlitis[148], V. Kouskoura[29], A. B. Kowalewska[84], R. Kowalewski[176], T. Z. Kowalski[83a], C. Kozakai[163], W. Kozanecki[144], A. S. Kozhin[122], V. A. Kramarenko[112], G. Kramberger[91], D. Krasnopevtsev[111], M. W. Krasny[135], A. Krasznahorkay[36], D. Krauss[114], J. A. Kremer[83a], J. Kretzschmar[90], K. Kreutzfeldt[55], P. Krieger[167], K. Krizka[18], K. Kroeninger[46], H. Kroha[114], J. Kroll[140], J. Kroll[136], J. Kroseberg[24], J. Krstic[16], U. Kruchonak[79], H. Krüger[24], N. Krumnack[78], M. C. Kruse[48], T. Kubota[104], S. Kuday[4b], J. T. Kuechler[182], S. Kuehn[36], A. Kugel[60a], F. Kuger[177], T. Kuhl[45], V. Kukhtin[79], R. Kukla[101], Y. Kulchitsky[107], S. Kuleshov[146c], Y. P. Kulinich[173], M. Kuna[57], T. Kunigo[85], A. Kupco[140], T. Kupfer[46], O. Kuprash[161], H. Kurashige[82], L. L. Kurchaninov[168a], Y. A. Kurochkin[107], M. G. Kurth[15a,15d], E. S. Kuwertz[176], M. Kuze[165], J. Kvita[130], T. Kwan[176], A. La Rosa[114], J. L. La Rosa Navarro[80d], L. La Rotonda[41a,41b], F. La Ruffa[41a,41b], C. Lacasta[174], F. Lacava[72a,72b], J. Lacey[45], D. P. J. Lack[100], H. Lacker[19], D. Lacour[135], E. Ladygin[79], R. Lafaye[5], B. Laforge[135], S. Lai[52], S. Lammers[65], W. Lampl[7], E. Lançon[29], U. Landgraf[51], M. P. J. Landon[92], M. C. Lanfermann[53], V. S. Lang[45], J. C. Lange[14], R. J. Langenberg[36], A. J. Lankford[171], F. Lanni[29], K. Lantzsch[24], A. Lanza[70a], A. Lapertosa[54a,54b], S. Laplace[135], J. F. Laporte[144], T. Lari[68a], F. Lasagni Manghi[23b,23a], M. Lassnig[36], T. S. Lau[62a], A. Laudrain[64], A. T. Law[145], P. Laycock[90], M. Lazzaroni[68a,68b], B. Le[104], O. Le Dortz[135], E. Le Guirriec[101], E. P. Le Quilleuc[144], M. LeBlanc[7], T. LeCompte[6], F. Ledroit-Guillon[57], C. A. Lee[29], G. R. Lee[146a], L. Lee[58], S. C. Lee[157], B. Lefebvre[103], G. Lefebvre[135], M. Lefebvre[176], F. Legger[113], C. Leggett[18], G. Lehmann Miotto[36], W. A. Leight[45], A. Leisos[162,y], M. A. L. Leite[80d], R. Leitner[142], D. Lellouch[180,*], B. Lemmer[52], K. J. C. Leney[94], T. Lenz[24], B. Lenzi[36], R. Leone[7], S. Leone[71a], C. Leonidopoulos[49], G. Lerner[155], C. Leroy[109], R. Les[167], A. A. J. Lesage[144], C. G. Lester[32], M. Levchenko[137], J. Levêque[5], D. Levin[105], L. J. Levinson[180], D. Lewis[92], B. Li[59a,t], C-Q. Li[59a,al], H. Li[59b], L. Li[59c], Q. Li[15a,15d], Q. Y. Li[59a], S. Li[59c,59d], X. Li[59c], Y. Li[150], Z. Liang[15a], B. Liberti[73a], A. Liblong[167], K. Lie[62c], S. Liem[119], A. Limosani[156], C. Y. Lin[32], K. Lin[106], S. C. Lin[158], T. H. Lin[99], R. A. Linck[65], B. E. Lindquist[154], A. L. Lionti[53], E. Lipeles[136], A. Lipniacka[17], M. Lisovyi[60b], T. M. Liss[173,au], A. Lister[175], A. M. Litke[145], J. D. Little[8], B. Liu[78], B. L. Liu[6], H. B. Liu[29], H. Liu[105], J. B. Liu[59a], J. K. K. Liu[134], K. Liu[135], M. Liu[59a], P. Liu[18], Y. L. Liu[59a], Y. W. Liu[59a], M. Livan[70a,70b], A. Lleres[57], J. Llorente Merino[15a], S. L. Lloyd[92], C. Y. Lo[62b], F. Lo Sterzo[42], E. M. Lobodzinska[45], P. Loch[7], F. K. Loebinger[100], K. M. Loew[26], T. Lohse[19], K. Lohwasser[148], M. Lokajicek[140], B. A. Long[25], J. D. Long[173], R. E. Long[89], L. Longo[67a,67b], K. A. Looper[126], J. A. Lopez[146c], D. Lopez Mateos[58], I. Lopez Paz[14], A. Lopez Solis[135], J. Lorenz[113], N. Lorenzo Martinez[5], M. Losada[22],

P. J. Lösel[113], A. Lösle[51], X. Lou[45], X. Lou[15a], A. Lounis[64], J. Love[6], P. A. Love[89], J. J. Lozano Bahilo[174], H. Lu[62a], N. Lu[105], Y. J. Lu[63], H. J. Lubatti[147], C. Luci[72a,72b], A. Lucotte[57], C. Luedtke[51], F. Luehring[65], I. Luise[135], W. Lukas[76], L. Luminari[72a], B. Lund-Jensen[153], M. S. Lutz[102], P. M. Luzi[135], D. Lynn[29], R. Lysak[140], E. Lytken[96], F. Lyu[15a], V. Lyubushkin[79], H. Ma[29], L. L. Ma[59b], Y. Ma[59b], G. Maccarrone[50], A. Macchiolo[114], C. M. Macdonald[148], J. Machado Miguens[136,139b], D. Madaffari[174], R. Madar[38], W. F. Mader[47], A. Madsen[45], N. Madysa[47], J. Maeda[82], S. Maeland[17], T. Maeno[29], A. S. Maevskiy[112], V. Magerl[51], C. Maidantchik[80b], T. Maier[113], A. Maio[139a,139b,139d], K. Maj[84], O. Majersky[28a], S. Majewski[131], Y. Makida[81], N. Makovec[64], B. Malaescu[135], Pa. Malecki[84], V. P. Maleev[137], F. Malek[57], U. Mallik[77], D. Malon[6], C. Malone[32], S. Maltezos[10], S. Malyukov[36], J. Mamuzic[174], G. Mancini[50], I. Mandić[91], J. Maneira[139a], L. Manhaes de Andrade Filho[80a], J. Manjarres Ramos[47], K. H. Mankinen[96], A. Mann[113], A. Manousos[76], B. Mansoulie[144], J. D. Mansour[15a], R. Mantifel[103], M. Mantoani[52], S. Manzoni[68a,68b], G. Marceca[30], L. March[53], L. Marchese[134], G. Marchiori[135], M. Marcisovsky[140], C. A. Marin Tobon[36], M. Marjanovic[38], D. E. Marley[105], F. Marroquim[80b], Z. Marshall[18], M. U. F. Martensson[172], S. Marti-Garcia[174], C. B. Martin[126], T. A. Martin[178], V. J. Martin[49], B. Martin dit Latour[17], M. Martinez[14,ac], V. I. Martinez Outschoorn[102], S. Martin-Haugh[143], V. S. Martoiu[27b], A. C. Martyniuk[94], A. Marzin[36], L. Masetti[99], T. Mashimo[163], R. Mashinistov[110], J. Masik[100], A. L. Maslennikov[121a,121b], L. H. Mason[104], L. Massa[73a,73b], P. Mastrandrea[5], A. Mastroberardino[41a,41b], T. Masubuchi[163], P. Mättig[182], J. Maurer[27b], B. Maček[91], S. J. Maxfield[90], D. A. Maximov[121a,121b], R. Mazini[157], I. Maznas[162], S. M. Mazza[145], N. C. Mc Fadden[117], G. Mc Goldrick[167], S. P. Mc Kee[105], T. G. McCarthy[114], L. I. McClymont[94], E. F. McDonald[104], J. A. Mcfayden[36], M. A. McKay[42], K. D. McLean[176], S. J. McMahon[143], P. C. McNamara[104], C. J. McNicol[178], R. A. McPherson[176,ag], J. E. Mdhluli[33e], Z. A. Meadows[102], S. Meehan[147], T. Megy[51], S. Mehlhase[113], A. Mehta[90], T. Meideck[57], B. Meirose[43], D. Melini[174,g], B. R. Mellado Garcia[33e], J. D. Mellenthin[52], M. Melo[28a], F. Meloni[20], A. Melzer[24], S. B. Menary[100], L. Meng[90], X. T. Meng[105], A. Mengarelli[23a,23b], S. Menke[114], E. Meoni[41a,41b], S. Mergelmeyer[19], C. Merlassino[20], P. Mermod[53], L. Merola[69a,69b], C. Meroni[68a], F. S. Merritt[37], A. Messina[72a,72b], J. Metcalfe[6], A. S. Mete[171], C. Meyer[136], J. Meyer[160], J-P. Meyer[144], H. Meyer Zu Theenhausen[60a], F. Miano[155], R. P. Middleton[143], L. Mijović[49], G. Mikenberg[180], M. Mikestikova[140], M. Mikuž[91], M. Milesi[104], A. Milic[167], D. A. Millar[92], D. W. Miller[37], A. Milov[180], D. A. Milstead[44a,44b], A. A. Minaenko[122], I. A. Minashvili[159b], A. I. Mincer[124], B. Mindur[83a], M. Mineev[79], Y. Minegishi[163], Y. Ming[181], L. M. Mir[14], A. Mirto[67a,67b], K. P. Mistry[136], T. Mitani[179], J. Mitrevski[113], V. A. Mitsou[174], A. Miucci[20], P. S. Miyagawa[148], A. Mizukami[81], J. U. Mjörnmark[96], T. Mkrtchyan[184], M. Mlynarikova[142], T. Moa[44a,44b], K. Mochizuki[109], P. Mogg[51], S. Mohapatra[39], S. Molander[44a,44b], R. Moles-Valls[24], M. C. Mondragon[106], K. Mönig[45], J. Monk[40], E. Monnier[101], A. Montalbano[151], J. Montejo Berlingen[36], F. Monticelli[88], S. Monzani[68a], R. W. Moore[3], N. Morange[64], D. Moreno[22], M. Moreno Llácer[36], P. Morettini[54b], M. Morgenstern[119], S. Morgenstern[36], D. Mori[151], T. Mori[163], M. Morii[58], M. Morinaga[179], V. Morisbak[133], A. K. Morley[36], G. Mornacchi[36], J. D. Morris[92], L. Morvaj[154], P. Moschovakos[10], M. Mosidze[159b], H. J. Moss[148], J. Moss[31,o], K. Motohashi[165], R. Mount[152], E. Mountricha[29], E. J. W. Moyse[102], S. Muanza[101], F. Mueller[114], J. Mueller[138], R. S. P. Mueller[113], D. Muenstermann[89], P. Mullen[56], G. A. Mullier[20], F. J. Munoz Sanchez[100], P. Murin[28b], W. J. Murray[143,178], A. Murrone[68a,68b], M. Muškinja[91], C. Mwewa[33a], A. G. Myagkov[122,an], J. Myers[131], M. Myska[141], B. P. Nachman[18], O. Nackenhorst[46], K. Nagai[134], R. Nagai[125], K. Nagano[81], Y. Nagasaka[61], K. Nagata[169], M. Nagel[51], E. Nagy[101], A. M. Nairz[36], Y. Nakahama[116], K. Nakamura[81], T. Nakamura[163], I. Nakano[127], F. Napolitano[60a], R. F. Naranjo Garcia[45], R. Narayan[11], D. I. Narrias Villar[60a], I. Naryshkin[137], T. Naumann[45], G. Navarro[22], R. Nayyar[7], H. A. Neal[105,*], P. Y. Nechaeva[110], T. J. Neep[144], A. Negri[70a,70b], M. Negrini[23b], S. Nektarijevic[118], C. Nellist[52], M. E. Nelson[134], S. Nemecek[140], P. Nemethy[124], M. Nessi[36,e], M. S. Neubauer[173], M. Neumann[182], P. R. Newman[21], T. Y. Ng[62c], Y. S. Ng[19], H. D. N. Nguyen[101], T. Nguyen Manh[109], E. Nibigira[38], R. B. Nickerson[134], R. Nicolaidou[144], J. Nielsen[145], N. Nikiforou[11], V. Nikolaenko[122,an], I. Nikolic-Audit[135], K. Nikolopoulos[21], P. Nilsson[29], Y. Ninomiya[81], A. Nisati[72a], N. Nishu[59c], R. Nisius[114], I. Nitsche[46], T. Nitta[179], T. Nobe[163], Y. Noguchi[85], M. Nomachi[132], I. Nomidis[34], M. A. Nomura[29], T. Nooney[92], M. Nordberg[36], N. Norjoharuddeen[134], T. Novak[91], O. Novgorodova[47], R. Novotny[141], M. Nozaki[81], L. Nozka[130], K. Ntekas[171], E. Nurse[94], F. Nuti[104], F. G. Oakham[34,ax], H. Oberlack[114], T. Obermann[24], J. Ocariz[135], A. Ochi[82], I. Ochoa[39], J. P. Ochoa-Ricoux[146a], K. O'Connor[26], S. Oda[87], S. Odaka[81], A. Oh[100], S. H. Oh[48], C. C. Ohm[153], H. Ohman[172], H. Oide[54a,54b], H. Okawa[169], Y. Okazaki[85], Y. Okumura[163], T. Okuyama[81], A. Olariu[27b], L. F. Oleiro Seabra[139a], S. A. Olivares Pino[146a], D. Oliveira Damazio[29], J. L. Oliver[1], M. J. R. Olsson[37], A. Olszewski[84], J. Olszowska[84], D. C. O'Neil[151], A. Onofre[139a,139e], K. Onogi[116], P. U. E. Onyisi[11], H. Oppen[133], M. J. Oreglia[37], Y. Oren[161,*], D. Orestano[74a,74b], N. Orlando[62b], A. A. O'Rourke[45], R. S. Orr[167], B. Osculati[54a,54b,*], V. O'Shea[56], R. Ospanov[59a], G. Otero y Garzon[30], H. Otono[87], M. Ouchrif[35d], F. Ould-Saada[133], A. Ouraou[144], Q. Ouyang[15a], M. Owen[56], R. E. Owen[21], V. E. Ozcan[12c], N. Ozturk[8], K. Pachal[151], A. Pacheco Pages[14], L. Pacheco Rodriguez[144], C. Padilla Aranda[14], S. Pagan Griso[18], M. Paganini[183], G. Palacino[65], S. Palazzo[41a,41b],

S. Palestini[36], M. Palka[83b], D. Pallin[38], I. Panagoulias[10], C. E. Pandini[53], J. G. Panduro Vazquez[93], P. Pani[36], L. Paolozzi[53], T. D. Papadopoulou[10], K. Papageorgiou[9,i], A. Paramonov[6], D. Paredes Hernandez[62b], B. Parida[59c], A. J. Parker[89], K. A. Parker[45], M. A. Parker[32], F. Parodi[54a,54b], J. A. Parsons[39], U. Parzefall[51], V. R. Pascuzzi[167], J. M. P. Pasner[145], E. Pasqualucci[72a], S. Passaggio[54b], F. Pastore[93], P. Pasuwan[44a,44b], S. Pataraia[99], J. R. Pater[100], A. Pathak[181], T. Pauly[36], B. Pearson[114], S. Pedraza Lopez[174], R. Pedro[139a,139b], S. V. Peleganchuk[121a,121b], O. Penc[140], C. Peng[15a], H. Peng[59a], J. Penwell[65], B. S. Peralva[80a], M. M. Perego[144], A. P. Pereira Peixoto[139a], D. V. Perepelitsa[29], F. Peri[19], L. Perini[68a,68b], H. Pernegger[36], S. Perrella[69a,69b], V. D. Peshekhonov[79,*], K. Peters[45], R. F. Y. Peters[100], B. A. Petersen[36], T. C. Petersen[40], E. Petit[57], A. Petridis[1], C. Petridou[162], P. Petroff[64], E. Petrolo[72a], M. Petrov[134], F. Petrucci[74a,74b], N. E. Pettersson[102], A. Peyaud[144], R. Pezoa[146c], T. Pham[104], F. H. Phillips[106], P. W. Phillips[143], G. Piacquadio[154], E. Pianori[178], A. Picazio[102], M. A. Pickering[134], R. Piegaia[30], J. E. Pilcher[37], A. D. Pilkington[100], M. Pinamonti[73a,73b], J. L. Pinfold[3], M. Pitt[180], M.-A. Pleier[29], V. Pleskot[142], E. Plotnikova[79], D. Pluth[78], P. Podberezko[121a,121b], R. Poettgen[96], R. Poggi[70a,70b], L. Poggioli[64], I. Pogrebnyak[106], D. Pohl[24], I. Pokharel[52], G. Polesello[70a], A. Poley[45], A. Policicchio[41a,41b], R. Polifka[36], A. Polini[23b], C. S. Pollard[45], V. Polychronakos[29], D. Ponomarenko[111], L. Pontecorvo[72a], G. A. Popeneciu[27d], D. M. Portillo Quintero[135], S. Pospisil[141], K. Potamianos[45], I. N. Potrap[79], C. J. Potter[32], H. Potti[11], T. Poulsen[96], J. Poveda[36], M. E. Pozo Astigarraga[36], P. Pralavorio[101], S. Prell[78], D. Price[100], M. Primavera[67a], S. Prince[103], N. Proklova[111], K. Prokofiev[62c], F. Prokoshin[146c], S. Protopopescu[29], J. Proudfoot[6], M. Przybycien[83a], A. Puri[173], P. Puzo[64], J. Qian[105], Y. Qin[100], A. Quadt[52], M. Queitsch-Maitland[45], A. Qureshi[1], S. K. Radhakrishnan[154], P. Rados[104], F. Ragusa[68a,68b], G. Rahal[97], J. A. Raine[100], S. Rajagopalan[29], T. Rashid[64], S. Raspopov[5], M. G. Ratti[68a,68b], D. M. Rauch[45], F. Rauscher[113], S. Rave[99], B. Ravina[148], I. Ravinovich[180], J. H. Rawling[100], M. Raymond[36], A. L. Read[133], N. P. Readioff[57], M. Reale[67a,67b], D. M. Rebuzzi[70a,70b], A. Redelbach[177], G. Redlinger[29], R. Reece[145], R. G. Reed[33e], K. Reeves[43], L. Rehnisch[19], J. Reichert[136], A. Reiss[99], C. Rembser[36], H. Ren[15a], M. Rescigno[72a], S. Resconi[68a], E. D. Resseguie[136], S. Rettie[175], E. Reynolds[21], O. L. Rezanova[121a,121b], P. Reznicek[142], R. Richter[114], S. Richter[94], E. Richter-Was[83b], O. Ricken[24], M. Ridel[135], P. Rieck[114], C. J. Riegel[182], O. Rifki[45], M. Rijssenbeek[154], A. Rimoldi[70a,70b], M. Rimoldi[20], L. Rinaldi[23b], G. Ripellino[153], B. Ristić[36], E. Ritsch[36], I. Riu[14], J. C. Rivera Vergara[146a], F. Rizatdinova[129], E. Rizvi[92], C. Rizzi[14], R. T. Roberts[100], S. H. Robertson[103,ag], A. Robichaud-Veronneau[103], D. Robinson[32], J. E. M. Robinson[45], A. Robson[56], E. Rocco[99], C. Roda[71a,71b], Y. Rodina[101,ad], S. Rodriguez Bosca[174], A. Rodriguez Perez[14], D. Rodriguez Rodriguez[174], A. M. Rodríguez Vera[168b], S. Roe[36], C. S. Rogan[58], O. Røhne[133], R. Röhrig[114], C. P. A. Roland[65], J. Roloff[58], A. Romaniouk[111], M. Romano[23b,23a], E. Romero Adam[174], N. Rompotis[90], M. Ronzani[124], L. Roos[135], S. Rosati[72a], K. Rosbach[51], P. Rose[145], N-A. Rosien[52], E. Rossi[69a,69b], L. P. Rossi[54b], L. Rossini[68a,68b], J. H. N. Rosten[32], R. Rosten[147], M. Rotaru[27b], J. Rothberg[147], D. Rousseau[64], D. Roy[33e], A. Rozanov[101], Y. Rozen[160], X. Ruan[33e], F. Rubbo[152], F. Rühr[51], A. Ruiz-Martinez[34], Z. Rurikova[51], N. A. Rusakovich[79], H. L. Russell[103], J. P. Rutherfoord[7], N. Ruthmann[36], E. M. Rüttinger[45,k], Y. F. Ryabov[137,*], M. Rybar[173], G. Rybkin[64], S. Ryu[6], A. Ryzhov[122], G. F. Rzehorz[52], P. Sabatini[52], G. Sabato[119], S. Sacerdoti[64], H.F-W. Sadrozinski[145], R. Sadykov[79], F. Safai Tehrani[72a], P. Saha[120], M. Sahinsoy[60a], M. Saimpert[45], M. Saito[163], T. Saito[163], H. Sakamoto[163], A. Sakharov[124,am], D. Salamani[53], G. Salamanna[74a,74b], J. E. Salazar Loyola[146c], D. Salek[119], P. H. Sales De Bruin[172], D. Salihagic[114,*], A. Salnikov[152], J. Salt[174], D. Salvatore[41a,41b], F. Salvatore[155], A. Salvucci[62a,62b,62c], A. Salzburger[36], D. Sammel[51], D. Sampsonidis[162], D. Sampsonidou[162], J. Sánchez[174], A. Sanchez Pineda[66a,66c], H. Sandaker[133], C. O. Sander[45], M. Sandhoff[182], C. Sandoval[22], D. P. C. Sankey[143], M. Sannino[54a,54b], Y. Sano[116], A. Sansoni[50], C. Santoni[38], H. Santos[139a], I. Santoyo Castillo[155], A. Sapronov[79], J. G. Saraiva[139a,139d], O. Sasaki[81], K. Sato[169], E. Sauvan[5], P. Savard[167,ax], N. Savic[114], R. Sawada[163], C. Sawyer[143], L. Sawyer[95,ak], C. Sbarra[23b], A. Sbrizzi[23a], T. Scanlon[94], D. A. Scannicchio[171], J. Schaarschmidt[147], P. Schacht[114], B. M. Schachtner[113], D. Schaefer[37], L. Schaefer[136], J. Schaeffer[99], S. Schaepe[36], U. Schäfer[99], A. C. Schaffer[64], D. Schaile[113], R. D. Schamberger[154], N. Scharmberg[100], V. A. Schegelsky[137], D. Scheirich[142], F. Schenck[19], M. Schernau[171], C. Schiavi[54b,54a], S. Schier[145], L. K. Schildgen[24], Z. M. Schillaci[26], E. J. Schioppa[36], M. Schioppa[41a,41b], K. E. Schleicher[51], S. Schlenker[36], K. R. Schmidt-Sommerfeld[114], K. Schmieden[36], C. Schmitt[99], S. Schmitt[45], S. Schmitz[99], U. Schnoor[51], L. Schoeffel[144], A. Schoening[60b], E. Schopf[24], M. Schott[99], J. F. P. Schouwenberg[118], J. Schovancova[36], S. Schramm[53], N. Schuh[99], A. Schulte[99], H-C. Schultz-Coulon[60a], M. Schumacher[51], B. A. Schumm[145], Ph. Schune[144], A. Schwartzman[152], T. A. Schwarz[105], H. Schweiger[100], Ph. Schwemling[144], R. Schwienhorst[106], A. Sciandra[24], G. Sciolla[26], M. Scornajenghi[41a,41b], F. Scuri[71a], F. Scutti[104], L. M. Scyboz[114], J. Searcy[105], C. D. Sebastiani[72a,72b], P. Seema[24], S. C. Seidel[117], A. Seiden[145], J. M. Seixas[80b], G. Sekhniaidze[69a], K. Sekhon[105], S. J. Sekula[42], N. Semprini-Cesari[23a,23b], S. Senkin[38], C. Serfon[133], L. Serin[64], L. Serkin[66a,66b], M. Sessa[74a,74b], H. Severini[128], T. Šfiligoj[91], F. Sforza[170], A. Sfyrla[53], E. Shabalina[52], J. D. Shahinian[145], N. W. Shaikh[44a,44b], L. Y. Shan[15a], R. Shang[173], J. T. Shank[25], M. Shapiro[18], A. Sharma[134], A. S. Sharma[1], P. B. Shatalov[123], K. Shaw[66a,66b], S. M. Shaw[100],

A. Shcherbakova[137], C. Y. Shehu[155], Y. Shen[128], N. Sherafati[34], A. D. Sherman[25], P. Sherwood[94], L. Shi[157,at], S. Shimizu[82], C. O. Shimmin[183], M. Shimojima[115], I. P. J. Shipsey[134], S. Shirabe[87], M. Shiyakova[79], J. Shlomi[180], A. Shmeleva[110], D. Shoaleh Saadi[109], M. J. Shochet[37], J. Shojaii[104], D. R. Shope[128], S. Shrestha[126], E. Shulga[111], P. Sicho[140], A. M. Sickles[173], P. E. Sidebo[153], E. Sideras Haddad[33e], O. Sidiropoulou[177], A. Sidoti[23a,23b], F. Siegert[47], Dj. Sijacki[16], J. Silva[139a], M. Jr. Silva[181], S. B. Silverstein[44a], L. Simic[79], S. Simion[64], E. Simioni[99], B. Simmons[94], M. Simon[99], P. Sinervo[167], N. B. Sinev[131], M. Sioli[23a,23b], G. Siragusa[177], I. Siral[105], S. Yu. Sivoklokov[112], J. Sjölin[44a,44b], M. B. Skinner[89], P. Skubic[128], M. Slater[21], T. Slavicek[141], M. Slawinska[84], K. Sliwa[170], R. Slovak[142], V. Smakhtin[180], B. H. Smart[5], J. Smiesko[28a], N. Smirnov[111], S. Yu. Smirnov[111], Y. Smirnov[111], L. N. Smirnova[112,v], O. Smirnova[96], J. W. Smith[52], M. N. K. Smith[39], R. W. Smith[39], M. Smizanska[89], K. Smolek[141], A. A. Snesarev[110], I. M. Snyder[131], S. Snyder[29], R. Sobie[176,ag], F. Socher[47], A. M. Soffa[171], A. Soffer[161], A. Søgaard[49], D. A. Soh[157], G. Sokhrannyi[91], C. A. Solans Sanchez[36], M. Solar[141], E. Yu. Soldatov[111], U. Soldevila[174], A. A. Solodkov[122], A. Soloshenko[79], O. V. Solovyanov[122], V. Solovyev[137], P. Sommer[148], H. Son[170], W. Song[143], A. Sopczak[141], F. Sopkova[28b], D. Sosa[60b], C. L. Sotiropoulou[71a,71b], S. Sottocornola[70a,70b], R. Soualah[66a,66c,h], A. M. Soukharev[121a,121b], D. South[45], B. C. Sowden[93], S. Spagnolo[67a,67b], M. Spalla[114], M. Spangenberg[178], F. Spanò[93], D. Sperlich[19], F. Spettel[114], T. M. Spieker[60a], R. Spighi[23b], G. Spigo[36], L. A. Spiller[104], M. Spousta[142], A. Stabile[68a,68b], R. Stamen[60a], S. Stamm[19], E. Stanecka[84], R. W. Stanek[6], C. Stanescu[74a], M. M. Stanitzki[45], B. Stapf[119], S. Stapnes[133], E. A. Starchenko[122], G. H. Stark[37], J. Stark[57], S. H. Stark[40], P. Staroba[140], P. Starovoitov[60a], S. Stärz[36], R. Staszewski[84], M. Stegler[45], P. Steinberg[29], B. Stelzer[151], H. J. Stelzer[36], O. Stelzer-Chilton[168a], H. Stenzel[55], T. J. Stevenson[92], G. A. Stewart[36], M. C. Stockton[131], G. Stoicea[27b], P. Stolte[52], S. Stonjek[114], A. Straessner[47], J. Strandberg[153], S. Strandberg[44a,44b], M. Strauss[128], P. Strizenec[28b], R. Ströhmer[177], D. M. Strom[131], R. Stroynowski[42], A. Strubig[49], S. A. Stucci[29], B. Stugu[17], J. Stupak[128], N. A. Styles[45], D. Su[152], J. Su[138], S. Suchek[60a], Y. Sugaya[132], M. Suk[141], V. V. Sulin[110], D. M. S. Sultan[53], S. Sultansoy[4c], T. Sumida[85], S. Sun[105], X. Sun[3], K. Suruliz[155], C. J. E. Suster[156], M. R. Sutton[155], S. Suzuki[81], M. Svatos[140], M. Swiatlowski[37], S. P. Swift[2], A. Sydorenko[99], I. Sykora[28a], T. Sykora[142], D. Ta[99], K. Tackmann[45], J. Taenzer[161], A. Taffard[171], R. Tafirout[168a], E. Tahirovic[92], N. Taiblum[161], H. Takai[29], R. Takashima[86], E. H. Takasugi[114], K. Takeda[82], T. Takeshita[149], Y. Takubo[81], M. Talby[101], A. A. Talyshev[121a,121b], J. Tanaka[163], M. Tanaka[165], R. Tanaka[64], R. Tanioka[82], B. B. Tannenwald[126], S. Tapia Araya[146c], S. Tapprogge[99], A. Tarek Abouelfadl Mohamed[135], S. Tarem[160], G. Tarna[27b,d], G. F. Tartarelli[68a], P. Tas[142], M. Tasevsky[140], T. Tashiro[85], E. Tassi[41a,41b], A. Tavares Delgado[139a,139b], Y. Tayalati[35e], A. C. Taylor[117], A. J. Taylor[49], G. N. Taylor[104], P. T. E. Taylor[104], W. Taylor[168b], A. S. Tee[89], P. Teixeira-Dias[93], D. Temple[151], H. Ten Kate[36], P. K. Teng[157], J. J. Teoh[132], F. Tepel[182], S. Terada[81], K. Terashi[163], J. Terron[98], S. Terzo[14], M. Testa[50], R. J. Teuscher[167,ag], S. J. Thais[183], T. Theveneaux-Pelzer[45], F. Thiele[40], J. P. Thomas[21], A. S. Thompson[56], P. D. Thompson[21], L. A. Thomsen[183], E. Thomson[136], Y. Tian[39], R. E. Ticse Torres[52], V. O. Tikhomirov[110,ao], Yu. A. Tikhonov[121a,121b], S. Timoshenko[111], P. Tipton[183], S. Tisserant[101], K. Todome[165], S. Todorova-Nova[5], S. Todt[47], J. Tojo[87], S. Tokár[28a], K. Tokushuku[81], E. Tolley[126], M. Tomoto[116], L. Tompkins[152], B. Tong[58], P. Tornambe[51], E. Torrence[131], H. Torres[47], E. Torró Pastor[147], C. Tosciri[134], J. Toth[101,af], F. Touchard[101], D. R. Tovey[148], C. J. Treado[124], T. Trefzger[177], F. Tresoldi[155], A. Tricoli[29], I. M. Trigger[168a], S. Trincaz-Duvoid[135], M. F. Tripiana[14], W. Trischuk[167], B. Trocmé[57], A. Trofymov[45], C. Troncon[68a], M. Trovatelli[176], F. Trovato[155], L. Truong[33c], M. Trzebinski[84], A. Trzupek[84], F. Tsai[45], K. W. Tsang[62a], J.C-L. Tseng[134], P. V. Tsiareshka[107], N. Tsirintanis[9], S. Tsiskaridze[14], V. Tsiskaridze[154], E. G. Tskhadadze[159a], I. I. Tsukerman[123], V. Tsulaia[18], S. Tsuno[81], D. Tsybychev[154], Y. Tu[62b], A. Tudorache[27b], V. Tudorache[27b], T. T. Tulbure[27a], A. N. Tuna[58], S. Turchikhin[79], D. Turgeman[180], I. Turk Cakir[4b,w], R. T. Turra[68a], P. M. Tuts[39], G. Ucchielli[23a,23b], I. Ueda[81], M. Ughetto[44a,44b], F. Ukegawa[169], G. Unal[36], A. Undrus[29], G. Unel[171], F. C. Ungaro[104], Y. Unno[81], K. Uno[163], J. Urban[28b], P. Urquijo[104], P. Urrejola[99], G. Usai[8], J. Usui[81], L. Vacavant[101], V. Vacek[141], B. Vachon[103], K. O. H. Vadla[133], A. Vaidya[94], C. Valderanis[113], E. Valdes Santurio[44a,44b], M. Valente[53], S. Valentinetti[23a,23b], A. Valero[174], L. Valéry[45], R. A. Vallance[21], A. Vallier[5], J. A. Valls Ferrer[174], T. R. Van Daalen[14], W. Van Den Wollenberg[119], H. Van der Graaf[119], P. Van Gemmeren[6], J. Van Nieuwkoop[151], I. Van Vulpen[119], M. C. van Woerden[119], M. Vanadia[73a,73b], W. Vandelli[36], A. Vaniachine[166], P. Vankov[119], G. Vardanyan[184], R. Vari[72a], E. W. Varnes[7], C. Varni[54a,54b], T. Varol[42], D. Varouchas[64], A. Vartapetian[8], K. E. Varvell[156], G. A. Vasquez[146c], J. G. Vasquez[183], F. Vazeille[38], D. Vazquez Furelos[14], T. Vazquez Schroeder[103], J. Veatch[52], V. Vecchio[74a,74b], L. M. Veloce[167], F. Veloso[139a,139c], S. Veneziano[72a], A. Ventura[67a,67b], M. Venturi[176], N. Venturi[36], V. Vercesi[70a], M. Verducci[74a,74b], W. Verkerke[119], A. T. Vermeulen[119], J. C. Vermeulen[119], M. C. Vetterli[151,ax], N. Viaux Maira[146c], O. Viazlo[96], I. Vichou[173,*], T. Vickey[148], O. E. Vickey Boeriu[148], G. H. A. Viehhauser[134], S. Viel[18], L. Vigani[134], M. Villa[23a,23b], M. Villaplana Perez[68a,68b], E. Vilucchi[50], M. G. Vincter[34], V. B. Vinogradov[79], A. Vishwakarma[45], C. Vittori[23a,23b], I. Vivarelli[155], S. Vlachos[10], M. Vogel[182], P. Vokac[141], G. Volpi[14], S. E. von Buddenbrock[33e], E. Von Toerne[24], V. Vorobel[142], K. Vorobev[111], M. Vos[174], J. H. Vossebeld[90], N. Vranjes[16], M. Vranjes Milosavljevic[16],

V. Vrba[141], M. Vreeswijk[119], R. Vuillermet[36], I. Vukotic[37], P. Wagner[24], W. Wagner[182], J. Wagner-Kuhr[113], H. Wahlberg[88], S. Wahrmund[47], K. Wakamiya[82], J. Walder[89], R. Walker[113], W. Walkowiak[150], V. Wallangen[44a,44b], A. M. Wang[58], C. Wang[59b,d], F. Wang[181], H. Wang[18], H. Wang[3], J. Wang[156], J. Wang[60b], P. Wang[42], Q. Wang[128], R.-J. Wang[135], R. Wang[59a], R. Wang[6], S. M. Wang[157], T. Wang[39], W. Wang[157,q], W. X. Wang[59a,ah], Y. Wang[59a,al], Z. Wang[59c], C. Wanotayaroj[45], A. Warburton[103], C. P. Ward[32], D. R. Wardrope[94], A. Washbrook[49], P. M. Watkins[21], A. T. Watson[21], M. F. Watson[21], G. Watts[147], S. Watts[100], B. M. Waugh[94], A. F. Webb[11], S. Webb[99], C. Weber[183], M. S. Weber[20], S. A. Weber[34], S. M. Weber[60a], J. S. Webster[6], A. R. Weidberg[134], B. Weinert[65], J. Weingarten[52], M. Weirich[99], C. Weiser[51], P. S. Wells[36], T. Wenaus[29], T. Wengler[36], S. Wenig[36], N. Wermes[24], M. D. Werner[78], P. Werner[36], M. Wessels[60a], T. D. Weston[20], K. Whalen[131], N. L. Whallon[147], A. M. Wharton[89], A. S. White[105], A. White[8], M. J. White[1], R. White[146c], D. Whiteson[171], B. W. Whitmore[89], F. J. Wickens[143], W. Wiedenmann[181], M. Wielers[143], C. Wiglesworth[40], L. A. M. Wiik-Fuchs[51], A. Wildauer[114], F. Wilk[100], H. G. Wilkens[36], H. H. Williams[136], S. Williams[32], C. Willis[106], S. Willocq[102], J. A. Wilson[21], I. Wingerter-Seez[5], E. Winkels[155], F. Winklmeier[131], O. J. Winston[155], B. T. Winter[24], M. Wittgen[152], M. Wobisch[95], A. Wolf[99], T. M. H. Wolf[119], R. Wolff[101], M. W. Wolter[84], H. Wolters[139a,139c], V. W. S. Wong[175], N. L. Woods[145], S. D. Worm[21], B. K. Wosiek[84], K. W. Woźniak[84], K. Wraight[56], M. Wu[37], S. L. Wu[181], X. Wu[53], Y. Wu[59a], T. R. Wyatt[100], B. M. Wynne[49], S. Xella[40], Z. Xi[105], L. Xia[15b], D. Xu[15a], H. Xu[59a,d], L. Xu[29], T. Xu[144], W. Xu[105], B. Yabsley[156], S. Yacoob[33a], K. Yajima[132], D. P. Yallup[94], D. Yamaguchi[165], Y. Yamaguchi[165], A. Yamamoto[81], T. Yamanaka[163], F. Yamane[82], M. Yamatani[163], T. Yamazaki[163], Y. Yamazaki[82], Z. Yan[25], H. J. Yang[59c,59d], H. T. Yang[18], S. Yang[77], Y. Yang[163], Y. Yang[157], Z. Yang[17], W-M. Yao[18], Y. C. Yap[45], Y. Yasu[81], E. Yatsenko[5], K. H. Yau Wong[24], J. Ye[42], S. Ye[29], I. Yeletskikh[79], E. Yigitbasi[25], E. Yildirim[99], K. Yorita[179], K. Yoshihara[136], C. J. S. Young[36], C. Young[152], J. Yu[78], J. Yu[8], X. Yue[60a], S. P. Y. Yuen[24], I. Yusuff[32], B. Zabinski[84], G. Zacharis[10], R. Zaidan[14], A. M. Zaitsev[122,an], N. Zakharchuk[45], J. Zalieckas[17], S. Zambito[58], D. Zanzi[36], C. Zeitnitz[182], G. Zemaityte[134], J. C. Zeng[173], Q. Zeng[152], O. Zenin[122], T. Ženiš[28a], D. Zerwas[64], M. Zgubič[134], D. F. Zhang[59b], D. Zhang[105], F. Zhang[181], G. Zhang[59a,ah], H. Zhang[15c], J. Zhang[6], L. Zhang[51], L. Zhang[59a], M. Zhang[173], P. Zhang[15c], R. Zhang[59a,d], R. Zhang[24], X. Zhang[59b], Y. Zhang[15a,15d], Z. Zhang[64], X. Zhao[42], Y. Zhao[59b,64,ab], Z. Zhao[59a], A. Zhemchugov[79], B. Zhou[105], C. Zhou[181], L. Zhou[42], M. S. Zhou[15a,15d], M. Zhou[154], N. Zhou[59c], Y. Zhou[7], C. G. Zhu[59b], H. L. Zhu[59a], H. Zhu[15a], J. Zhu[105], Y. Zhu[59a], X. Zhuang[15a], K. Zhukov[110], V. Zhulanov[121a,121b], A. Zibell[177], D. Zieminska[65], N. I. Zimine[79], S. Zimmermann[51], Z. Zinonos[114], M. Zinser[99], M. Ziolkowski[150], L. Živković[16], G. Zobernig[181], A. Zoccoli[23b,23a], K. Zoch[52], T. G. Zorbas[148], R. Zou[37], M. Zur Nedden[19], L. Zwalinski[36]

[1] Department of Physics, University of Adelaide, Adelaide, Australia
[2] Physics Department, SUNY Albany, Albany, NY, USA
[3] Department of Physics, University of Alberta, Edmonton, AB, Canada
[4] [(a)]Department of Physics, Ankara University, Ankara, Turkey; [(b)]Istanbul Aydin University, Istanbul, Turkey; [(c)]Division of Physics, TOBB University of Economics and Technology, Ankara, Turkey
[5] LAPP, Université Grenoble Alpes, Université Savoie Mont Blanc, CNRS/IN2P3, Annecy, France
[6] High Energy Physics Division, Argonne National Laboratory, Argonne, IL, USA
[7] Department of Physics, University of Arizona, Tucson, AZ, USA
[8] Department of Physics, University of Texas at Arlington, Arlington, TX, USA
[9] Physics Department, National and Kapodistrian University of Athens, Athens, Greece
[10] Physics Department, National Technical University of Athens, Zografou, Greece
[11] Department of Physics, University of Texas at Austin, Austin, TX, USA
[12] [(a)]Bahcesehir University, Faculty of Engineering and Natural Sciences, Istanbul, Turkey; [(b)]Istanbul Bilgi University, Faculty of Engineering and Natural Sciences, Istanbul, Turkey; [(c)]Department of Physics, Bogazici University, Istanbul, Turkey; [(d)]Department of Physics Engineering, Gaziantep University, Gaziantep, Turkey
[13] Institute of Physics, Azerbaijan Academy of Sciences, Baku, Azerbaijan
[14] Institut de Física d'Altes Energies (IFAE), Barcelona Institute of Science and Technology, Barcelona, Spain
[15] [(a)]Institute of High Energy Physics, Chinese Academy of Sciences, Beijing, China; [(b)]Physics Department, Tsinghua University, Beijing, China; [(c)]Department of Physics, Nanjing University, Nanjing, China; [(d)]University of Chinese Academy of Science (UCAS), Beijing, China
[16] Institute of Physics, University of Belgrade, Belgrade, Serbia

[17] Department for Physics and Technology, University of Bergen, Bergen, Norway
[18] Physics Division, Lawrence Berkeley National Laboratory and University of California, Berkeley, CA, USA
[19] Institut für Physik, Humboldt Universität zu Berlin, Berlin, Germany
[20] Albert Einstein Center for Fundamental Physics and Laboratory for High Energy Physics, University of Bern, Bern, Switzerland
[21] School of Physics and Astronomy, University of Birmingham, Birmingham, UK
[22] Facultad de Ciencias y Centro de Investigaciónes, Universidad Antonio Nariño, Bogota, Colombia
[23] [(a)]Dipartimento di Fisica, INFN Bologna and Universita' di Bologna, Bologna, Italy; [(b)]INFN Sezione di Bologna, Bologna, Italy
[24] Physikalisches Institut, Universität Bonn, Bonn, Germany
[25] Department of Physics, Boston University, Boston, MA, USA
[26] Department of Physics, Brandeis University, Waltham, MA, USA
[27] [(a)]Transilvania University of Brasov, Brasov, Romania; [(b)]Horia Hulubei National Institute of Physics and Nuclear Engineering, Bucharest, Romania; [(c)]Department of Physics, Alexandru Ioan Cuza University of Iasi, Iasi, Romania; [(d)]National Institute for Research and Development of Isotopic and Molecular Technologies, Physics Department, Cluj-Napoca, Romania; [(e)]University Politehnica Bucharest, Bucharest, Romania; [(f)]West University in Timisoara, Timisoara, Romania
[28] [(a)]Faculty of Mathematics, Physics and Informatics, Comenius University, Bratislava, Slovakia; [(b)]Department of Subnuclear Physics, Institute of Experimental Physics of the Slovak Academy of Sciences, Kosice, Slovak Republic
[29] Physics Department, Brookhaven National Laboratory, Upton, NY, USA
[30] Departamento de Física, Universidad de Buenos Aires, Buenos Aires, Argentina
[31] California State University, Long Beach, CA, USA
[32] Cavendish Laboratory, University of Cambridge, Cambridge, UK
[33] [(a)]Department of Physics, University of Cape Town, Cape Town, South Africa; [(b)]iThemba Labs, Western Cape, South Africa; [(c)]Department of Mechanical Engineering Science, University of Johannesburg, Johannesburg, South Africa; [(d)]University of South Africa, Department of Physics, Pretoria, South Africa; [(e)]School of Physics, University of the Witwatersrand, Johannesburg, South Africa
[34] Department of Physics, Carleton University, Ottawa, ON, Canada
[35] [(a)]Faculté des Sciences Ain Chock, Réseau Universitaire de Physique des Hautes Energies, Université Hassan II, Casablanca, Morocco; [(b)]Faculté des Sciences, Université Ibn-Tofail, Kénitra, Morocco; [(c)]Faculté des Sciences Semlalia, Université Cadi Ayyad, LPHEA, Marrakech, Morocco; [(d)]Faculté des Sciences, Université Mohamed Premier and LPTPM, Oujda, Morocco; [(e)]Faculté des sciences, Université Mohammed V, Rabat, Morocco
[36] CERN, Geneva, Switzerland
[37] Enrico Fermi Institute, University of Chicago, Chicago, IL, USA
[38] LPC, Université Clermont Auvergne, CNRS/IN2P3, Clermont-Ferrand, France
[39] Nevis Laboratory, Columbia University, Irvington, NY, USA
[40] Niels Bohr Institute, University of Copenhagen, Copenhagen, Denmark
[41] [(a)]Dipartimento di Fisica, Università della Calabria, Rende, Italy; [(b)]INFN Gruppo Collegato di Cosenza, Laboratori Nazionali di Frascati, Frascati, Italy
[42] Physics Department, Southern Methodist University, Dallas, TX, USA
[43] Physics Department, University of Texas at Dallas, Richardson, TX, USA
[44] [(a)]Department of Physics, Stockholm University, Sweden; [(b)]Oskar Klein Centre, Stockholm, Sweden
[45] Deutsches Elektronen-Synchrotron DESY, Hamburg and Zeuthen, Germany
[46] Lehrstuhl für Experimentelle Physik IV, Technische Universität Dortmund, Dortmund, Germany
[47] Institut für Kern- und Teilchenphysik, Technische Universität Dresden, Dresden, Germany
[48] Department of Physics, Duke University, Durham, NC, USA
[49] SUPA, School of Physics and Astronomy, University of Edinburgh, Edinburgh, UK
[50] INFN e Laboratori Nazionali di Frascati, Frascati, Italy
[51] Physikalisches Institut, Albert-Ludwigs-Universität Freiburg, Freiburg, Germany
[52] II. Physikalisches Institut, Georg-August-Universität Göttingen, Göttingen, Germany
[53] Département de Physique Nucléaire et Corpusculaire, Université de Genève, Genève, Switzerland
[54] [(a)]Dipartimento di Fisica, Università di Genova, Genoa, Italy; [(b)]INFN Sezione di Genova, Genoa, Italy
[55] II. Physikalisches Institut, Justus-Liebig-Universität Giessen, Giessen, Germany

[56] SUPA, School of Physics and Astronomy, University of Glasgow, Glasgow, UK
[57] LPSC, Université Grenoble Alpes, CNRS/IN2P3, Grenoble INP, Grenoble, France
[58] Laboratory for Particle Physics and Cosmology, Harvard University, Cambridge, MA, USA
[59] [(a)]Department of Modern Physics and State Key Laboratory of Particle Detection and Electronics, University of Science and Technology of China, Hefei, China; [(b)]Institute of Frontier and Interdisciplinary Science and Key Laboratory of Particle Physics and Particle Irradiation (MOE), Shandong University, Qingdao, China; [(c)]School of Physics and Astronomy, Shanghai Jiao Tong University, KLPPAC-MoE, SKLPPC, Shanghai, China; [(d)]Tsung-Dao Lee Institute, Shanghai, China
[60] [(a)]Kirchhoff-Institut für Physik, Ruprecht-Karls-Universität Heidelberg, Heidelberg, Germany; [(b)]Physikalisches Institut, Ruprecht-Karls-Universität Heidelberg, Heidelberg, Germany
[61] Faculty of Applied Information Science, Hiroshima Institute of Technology, Hiroshima, Japan
[62] [(a)]Department of Physics, Chinese University of Hong Kong, Shatin, NT, Hong Kong; [(b)]Department of Physics, University of Hong Kong, Hong Kong, China; [(c)]Department of Physics and Institute for Advanced Study, Hong Kong University of Science and Technology, Clear Water Bay, Kowloon, Hong Kong
[63] Department of Physics, National Tsing Hua University, Hsinchu, Taiwan
[64] IJCLab, Université Paris-Saclay, CNRS/IN2P3, 91405 Orsay, France
[65] Department of Physics, Indiana University, Bloomington, IN, USA
[66] [(a)]INFN Gruppo Collegato di Udine, Sezione di Trieste, Udine, Italy; [(b)]ICTP, Trieste, Italy; [(c)]Dipartimento Politecnico di Ingegneria e Architettura, Università di Udine, Udine, Italy
[67] [(a)]INFN Sezione di Lecce, Lecce, Italy; [(b)]Dipartimento di Matematica e Fisica, Università del Salento, Lecce, Italy
[68] [(a)]INFN Sezione di Milano, Milan, Italy; [(b)]Dipartimento di Fisica, Università di Milano, Milan, Italy
[69] [(a)]INFN Sezione di Napoli, Naples, Italy; [(b)]Dipartimento di Fisica, Università di Napoli, Naples, Italy
[70] [(a)]INFN Sezione di Pavia, Pavia, Italy; [(b)]Dipartimento di Fisica, Università di Pavia, Pavia, Italy
[71] [(a)]INFN Sezione di Pisa, Pisa, Italy; [(b)]Dipartimento di Fisica E. Fermi, Università di Pisa, Pisa, Italy
[72] [(a)]INFN Sezione di Roma, Rome, Italy; [(b)]Dipartimento di Fisica, Sapienza Università di Roma, Rome, Italy
[73] [(a)]INFN Sezione di Roma Tor Vergata, Rome, Italy; [(b)]Dipartimento di Fisica, Università di Roma Tor Vergata, Rome, Italy
[74] [(a)]INFN Sezione di Roma Tre, Rome, Italy; [(b)]Dipartimento di Matematica e Fisica, Università Roma Tre, Rome, Italy
[75] [(a)]INFN-TIFPA, Trento, Italy; [(b)]Università degli Studi di Trento, Trento, Italy
[76] Institut für Astro- und Teilchenphysik, Leopold-Franzens-Universität, Innsbruck, Austria
[77] University of Iowa, Iowa City, IA, USA
[78] Department of Physics and Astronomy, Iowa State University, Ames, IA, USA
[79] Joint Institute for Nuclear Research, Dubna, Russia
[80] [(a)]Departamento de Engenharia Elétrica, Universidade Federal de Juiz de Fora (UFJF), Juiz de Fora, Brazil; [(b)]Universidade Federal do Rio De Janeiro COPPE/EE/IF, Rio de Janeiro, Brazil; [(c)]Universidade Federal de São João del Rei (UFSJ), São João del Rei, Brazil; [(d)]Instituto de Física, Universidade de São Paulo, São Paulo, Brazil
[81] KEK, High Energy Accelerator Research Organization, Tsukuba, Japan
[82] Graduate School of Science, Kobe University, Kobe, Japan
[83] [(a)]AGH University of Science and Technology, Faculty of Physics and Applied Computer Science, Kraków, Poland; [(b)]Marian Smoluchowski Institute of Physics, Jagiellonian University, Kraków, Poland
[84] Institute of Nuclear Physics Polish Academy of Sciences, Kraków, Poland
[85] Faculty of Science, Kyoto University, Kyoto, Japan
[86] Kyoto University of Education, Kyoto, Japan
[87] Research Center for Advanced Particle Physics and Department of Physics, Kyushu University, Fukuoka, Japan
[88] Instituto de Física La Plata, Universidad Nacional de La Plata and CONICET, La Plata, Argentina
[89] Physics Department, Lancaster University, Lancaster, UK
[90] Oliver Lodge Laboratory, University of Liverpool, Liverpool, UK
[91] Department of Experimental Particle Physics, Jožef Stefan Institute and Department of Physics, University of Ljubljana, Ljubljana, Slovenia
[92] School of Physics and Astronomy, Queen Mary University of London, London, UK
[93] Department of Physics, Royal Holloway University of London, Egham, UK
[94] Department of Physics and Astronomy, University College London, London, UK
[95] Louisiana Tech University, Ruston, LA, USA

[96] Fysiska institutionen, Lunds universitet, Lund, Sweden
[97] Centre de Calcul de l'Institut National de Physique Nucléaire et de Physique des Particules (IN2P3), Villeurbanne, France
[98] Departamento de Física Teorica C-15 and CIAFF, Universidad Autónoma de Madrid, Madrid, Spain
[99] Institut für Physik, Universität Mainz, Mainz, Germany
[100] School of Physics and Astronomy, University of Manchester, Manchester, UK
[101] CPPM, Aix-Marseille Université, CNRS/IN2P3, Marseille, France
[102] Department of Physics, University of Massachusetts, Amherst, MA, USA
[103] Department of Physics, McGill University, Montreal, QC, Canada
[104] School of Physics, University of Melbourne, Parkville, VIC, Australia
[105] Department of Physics, University of Michigan, Ann Arbor, MI, USA
[106] Department of Physics and Astronomy, Michigan State University, East Lansing, MI, USA
[107] B.I. Stepanov Institute of Physics, National Academy of Sciences of Belarus, Minsk, Belarus
[108] Research Institute for Nuclear Problems of Byelorussian State University, Minsk, Belarus
[109] Group of Particle Physics, University of Montreal, Montreal, QC, Canada
[110] P.N. Lebedev Physical Institute of the Russian Academy of Sciences, Moscow, Russia
[111] National Research Nuclear University MEPhI, Moscow, Russia
[112] D.V. Skobeltsyn Institute of Nuclear Physics, M.V. Lomonosov Moscow State University, Moscow, Russia
[113] Fakultät für Physik, Ludwig-Maximilians-Universität München, Munich, Germany
[114] Max-Planck-Institut für Physik (Werner-Heisenberg-Institut), Munich, Germany
[115] Nagasaki Institute of Applied Science, Nagasaki, Japan
[116] Graduate School of Science and Kobayashi-Maskawa Institute, Nagoya University, Nagoya, Japan
[117] Department of Physics and Astronomy, University of New Mexico, Albuquerque, NM, USA
[118] Institute for Mathematics, Astrophysics and Particle Physics, Radboud University Nijmegen/Nikhef, Nijmegen, Netherlands
[119] Nikhef National Institute for Subatomic Physics and University of Amsterdam, Amsterdam, The Netherlands
[120] Department of Physics, Northern Illinois University, DeKalb, IL, USA
[121] [(a)]Budker Institute of Nuclear Physics and NSU, SB RAS, Novosibirsk, Russia; [(b)]Novosibirsk State University Novosibirsk, Novosibirsk, Russia
[122] Institute for High Energy Physics of the National Research Centre Kurchatov Institute, Protvino, Russia
[123] Institute for Theoretical and Experimental Physics named by A.I. Alikhanov of National Research Centre "Kurchatov Institute", Moscow, Russia
[124] Department of Physics, New York University, New York, NY, USA
[125] Ochanomizu University, Otsuka, Bunkyo-ku, Tokyo, Japan
[126] Ohio State University, Columbus, OH, USA
[127] Faculty of Science, Okayama University, Okayama, Japan
[128] Homer L. Dodge Department of Physics and Astronomy, University of Oklahoma, Norman, OK, USA
[129] Department of Physics, Oklahoma State University, Stillwater, OK, USA
[130] Palacký University, RCPTM, Joint Laboratory of Optics, Olomouc, Czech Republic
[131] Center for High Energy Physics, University of Oregon, Eugene, OR, USA
[132] Graduate School of Science, Osaka University, Osaka, Japan
[133] Department of Physics, University of Oslo, Oslo, Norway
[134] Department of Physics, Oxford University, Oxford, UK
[135] LPNHE, Sorbonne Université, Université de Paris, CNRS/IN2P3, Paris, France
[136] Department of Physics, University of Pennsylvania, Philadelphia, PA, USA
[137] Konstantinov Nuclear Physics Institute of National Research Centre "Kurchatov Institute", PNPI, St. Petersburg, Russia
[138] Department of Physics and Astronomy, University of Pittsburgh, Pittsburgh, PA, USA
[139] [(a)]Laboratório de Instrumentação e Física Experimental de Partículas, LIP, Lisbon, Portugal; [(b)]Departamento de Física, Faculdade de Ciências, Universidade de Lisboa, Lisbon, Portugal; [(c)]Departamento de Física, Universidade de Coimbra, Coimbra, Portugal; [(d)]Centro de Física Nuclear da Universidade de Lisboa, Lisbon, Portugal; [(e)]Departamento de Física, Universidade do Minho, Braga, Portugal; [(f)]Departamento de Física Teórica y del Cosmos, Universidad de Granada, Granada, Spain; [(g)]Dep Física and CEFITEC of Faculdade de Ciências e Tecnologia, Universidade Nova de Lisboa, Caparica, Portugal; [(h)]Instituto Superior Técnico, Universidade de Lisboa, Lisbon, Portugal

[140] Institute of Physics of the Czech Academy of Sciences, Prague, Czech Republic
[141] Czech Technical University in Prague, Prague, Czech Republic
[142] Charles University, Faculty of Mathematics and Physics, Prague, Czech Republic
[143] Particle Physics Department, Rutherford Appleton Laboratory, Didcot, UK
[144] IRFU, CEA, Université Paris-Saclay, Gif-sur-Yvette, France
[145] Santa Cruz Institute for Particle Physics, University of California Santa Cruz, Santa Cruz, CA, USA
[146] [(a)]Departamento de Física, Pontificia Universidad Católica de Chile, Santiago, Chile; [(b)]Universidad Andres Bello, Department of Physics, Santiago, Chile; [(c)]Departamento de Física, Universidad Técnica Federico Santa María, Valparaíso, Chile
[147] Department of Physics, University of Washington, Seattle, WA, USA
[148] Department of Physics and Astronomy, University of Sheffield, Sheffield, UK
[149] Department of Physics, Shinshu University, Nagano, Japan
[150] Department Physik, Universität Siegen, Siegen, Germany
[151] Department of Physics, Simon Fraser University, Burnaby, BC, Canada
[152] SLAC National Accelerator Laboratory, Stanford, CA, USA
[153] Physics Department, Royal Institute of Technology, Stockholm, Sweden
[154] Departments of Physics and Astronomy, Stony Brook University, Stony Brook, NY, USA
[155] Department of Physics and Astronomy, University of Sussex, Brighton, UK
[156] School of Physics, University of Sydney, Sydney, Australia
[157] Institute of Physics, Academia Sinica, Taipei, Taiwan
[158] Academia Sinica Grid Computing, Institute of Physics, Academia Sinica, Taipei, Taiwan
[159] [(a)]E. Andronikashvili Institute of Physics, Iv. Javakhishvili Tbilisi State University, Tbilisi, Georgia; [(b)]High Energy Physics Institute, Tbilisi State University, Tbilisi, Georgia
[160] Department of Physics, Technion, Israel Institute of Technology, Haifa, Israel
[161] Raymond and Beverly Sackler School of Physics and Astronomy, Tel Aviv University, Tel Aviv, Israel
[162] Department of Physics, Aristotle University of Thessaloniki, Thessaloniki, Greece
[163] International Center for Elementary Particle Physics and Department of Physics, University of Tokyo, Tokyo, Japan
[164] Graduate School of Science and Technology, Tokyo Metropolitan University, Tokyo, Japan
[165] Department of Physics, Tokyo Institute of Technology, Tokyo, Japan
[166] Tomsk State University, Tomsk, Russia
[167] Department of Physics, University of Toronto, Toronto, ON, Canada
[168] [(a)]TRIUMF, Vancouver, BC, Canada; [(b)]Department of Physics and Astronomy, York University, Toronto, ON, Canada
[169] Division of Physics and Tomonaga Center for the History of the Universe, Faculty of Pure and Applied Sciences, University of Tsukuba, Tsukuba, Japan
[170] Department of Physics and Astronomy, Tufts University, Medford, MA, USA
[171] Department of Physics and Astronomy, University of California Irvine, Irvine, CA, USA
[172] Department of Physics and Astronomy, University of Uppsala, Uppsala, Sweden
[173] Department of Physics, University of Illinois, Urbana, IL, USA
[174] Instituto de Física Corpuscular (IFIC), Centro Mixto Universidad de Valencia - CSIC, Valencia, Spain
[175] Department of Physics, University of British Columbia, Vancouver, BC, Canada
[176] Department of Physics and Astronomy, University of Victoria, Victoria, BC, Canada
[177] Fakultät für Physik und Astronomie, Julius-Maximilians-Universität Würzburg, Würzburg, Germany
[178] Department of Physics, University of Warwick, Coventry, UK
[179] Waseda University, Tokyo, Japan
[180] Department of Particle Physics, Weizmann Institute of Science, Rehovot, Israel
[181] Department of Physics, University of Wisconsin, Madison, WI, USA
[182] Fakultät für Mathematik und Naturwissenschaften, Fachgruppe Physik, Bergische Universität Wuppertal, Wuppertal, Germany
[183] Department of Physics, Yale University, New Haven, CT, USA
[184] Yerevan Physics Institute, Yerevan, Armenia

[a] Also at Borough of Manhattan Community College, City University of New York, New York, NY, USA
[b] Also at Centre for High Performance Computing, CSIR Campus, Rosebank, Cape Town; South Africa

[c] Also at CERN, Geneva, Switzerland
[d] Also at CPPM, Aix-Marseille Université, CNRS/IN2P3, Marseille, France
[e] Also at Département de Physique Nucléaire et Corpusculaire, Université de Genève, Genève, Switzerland
[f] Also at Departament de Fisica de la Universitat Autonoma de Barcelona, Barcelona, Spain
[g] Also at Departamento de Física Teórica y del Cosmos, Universidad de Granada, Granada, Spain
[h] Also at Department of Applied Physics and Astronomy, University of Sharjah, Sharjah, United Arab Emirates
[i] Also at Department of Financial and Management Engineering, University of the Aegean, Chios, Greece
[j] Also at Department of Physics and Astronomy, University of Louisville, Louisville, KY, USA
[k] Also at Department of Physics and Astronomy, University of Sheffield, Sheffield, UK
[l] Also at Department of Physics, Ben Gurion University of the Negev, Beer Sheva, Israel
[m] Also at Department of Physics, California State University, East Bay, USA
[n] Also at Department of Physics, California State University, Fresno, USA
[o] Also at Department of Physics, California State University, Sacramento, USA
[p] Also at Department of Physics, King's College London, London, UK
[q] Also at Department of Physics, Nanjing University, Nanjing, China
[r] Also at Department of Physics, St. Petersburg State Polytechnical University, St. Petersburg, Russia
[s] Also at Department of Physics, University of Fribourg, Fribourg, Switzerland
[t] Also at Department of Physics, University of Michigan, Ann Arbor, MI, USA
[u] Also at Dipartimento di Fisica E. Fermi, Università di Pisa, Pisa, Italy
[v] Also at Faculty of Physics, M.V. Lomonosov Moscow State University, Moscow, Russia
[w] Also at Giresun University, Faculty of Engineering, Giresun, Turkey
[x] Also at Graduate School of Science, Osaka University, Osaka, Japan
[y] Also at Hellenic Open University, Patras, Greece
[z] Also at Horia Hulubei National Institute of Physics and Nuclear Engineering, Bucharest, Romania
[aa] Also at II. Physikalisches Institut, Georg-August-Universität Göttingen, Göttingen, Germany
[ab] Also at IJCLab, Université Paris-Saclay, CNRS/IN2P3, 91405, Orsay, France
[ac] Also at Institucio Catalana de Recerca i Estudis Avancats, ICREA, Barcelona, Spain
[ad] Also at Institut de Física d'Altes Energies (IFAE), Barcelona Institute of Science and Technology, Barcelona, Spain
[ae] Also at Institute for Mathematics, Astrophysics and Particle Physics, Radboud University Nijmegen/Nikhef, Nijmegen, The Netherlands
[af] Also at Institute for Particle and Nuclear Physics, Wigner Research Centre for Physics, Budapest, Hungary
[ag] Also at Institute of Particle Physics (IPP), Vancouver, Canada
[ah] Also at Institute of Physics, Academia Sinica, Taipei, Taiwan
[ai] Also at Institute of Physics, Azerbaijan Academy of Sciences, Baku, Azerbaijan
[aj] Also at Institute of Theoretical Physics, Ilia State University, Tbilisi, Georgia
[ak] Also at Louisiana Tech University, Ruston, LA, USA
[al] Also at LPNHE, Sorbonne Université, Université de Paris, CNRS/IN2P3, Paris, France
[am] Also at Manhattan College, New York, NY, USA
[an] Also at Moscow Institute of Physics and Technology State University, Dolgoprudny, Russia
[ao] Also at National Research Nuclear University MEPhI, Moscow, Russia
[ap] Also at Near East University, Nicosia, North Cyprus, Mersin, Turkey
[aq] Also at Ochadai Academic Production, Ochanomizu University, Tokyo, Japan
[ar] Also at Physics Department, An-Najah National University, Nablus, Palestine
[as] Also at Physikalisches Institut, Albert-Ludwigs-Universität Freiburg, Freiburg, Germany
[at] Also at School of Physics, Sun Yat-sen University, Guangzhou, China
[au] Also at The City College of New York, New York, NY, USA

[av] Also at The Collaborative Innovation Center of Quantum Matter (CICQM), Beijing, China
[aw] Also at Tomsk State University, Tomsk, and Moscow Institute of Physics and Technology State University, Dolgoprudny, Russia.
[ax] Also at TRIUMF, Vancouver, BC, Canada
[ay] Also at Universita di Napoli Parthenope, Naples, Italy.
*Deceased